IECO

Volume 9 No 1 Year 2026

■ Volume 9

■ No 1

■ Year 2026

University of Sistan and Baluchestan

Iranian Association of Electrical and Electronics Engineers

International Journal Of

Industrial Electronics Control and Optimization

In This Issue:

Research Articles:

IECO

International Journal Of
Industrial Electronics Control and Optimization

Editor-in-Chief's Message

International Journal of Industrial Electronics, Control and Optimization (IECO)*Volume 9, No. 1, 2026

It is my pleasure to present Volume 9, Issue 1 (2026) of the *International Journal of Industrial Electronics, Control and Optimization (IECO)*.

This issue reflects the evolving landscape of industrial electronics, advanced control systems, and optimization methodologies. The published articles span key domains including power converter topologies, intelligent diagnostics, optimal control techniques, antenna design, and stability analysis of power systems. Together, they illustrate the strong interplay between rigorous mathematical modeling, engineering design, and emerging data-driven approaches.

A notable trend across several contributions is the integration of artificial intelligence and computational intelligence techniques into classical engineering problems. Such developments are reshaping how industrial systems are analyzed, optimized, and monitored, enhancing both efficiency and reliability.

IECO remains committed to maintaining high scholarly standards through a transparent peer-review process and to fostering international academic collaboration. We sincerely thank our authors, reviewers, and editorial board members for their dedication and professionalism.

We look forward to continued contributions that advance both theoretical insight and practical innovation in industrial electronics, control, and optimization.

Prof. S. Masoud Barakati

Editor-in-Chief

International Journal of Industrial Electronics, Control and Optimization

About Journal

The University of Sistan and Baluchestan entered into strategic partnership with Iranian Association of Electrical and Electronic Engineers (IAEEE) to publish the **International Journal of Industrial Electronics Control and Optimization (IECO)**. The IECO is a refereed international journal which presents to the international scientific community important results of work in these fields, whether in the form of modeling simulation, analysis, fundamental research, development, application, design or real-time implementation. The scope of IECO is broad, encompassing all aspects of Industrial Electronics, Control and Optimization.

Note: International Journal of Industrial Electronics, Control and Optimization (IECO) has qualified to **ACADEMIC RESEARCH JOURNAL (ELMI-PAJOHESHI)** status certified by the ministry of Science, Research and Technology of Iran (No. 231566/3/18 dated 1396/10/09), and is published by the University of Sistan and Baluchestan through a formal partnership (No. 952/2/1500 dated 1395/11/04) with Iranian Association of Electrical and electronic Engineers (IAEEE) in order to develop scientific and research cooperation.

Aims and Scope

International Journal of Industrial Electronics, Control and Optimization (IECO) is a Peer reviewed journal of advanced and state-of-the-art in the science and engineering of Industrial Electronics, Control and Optimization. Its Scope encompasses the applications of Industrial Electronics, power systems, control, optimization and computational intelligence for the enhancement of industrial and manufacturing system and processes. The scope of the journal include the following:

I. Industrial Electronics

- Low and high-power converters
- Renewable energy
- Drive control techniques
- Techniques for advanced power semiconductor devices
- Power quality and utility applications
- Communications
- Flexible AC Transmission Systems (FACTS)
- Control in power electronics
- Electromagnetic and thermal performance of electronic power converters
- Motion control, robotics, sensors and actuators
- Fault detection and diagnosis

- Power systems
- Factory automation, communication, and computer networks

II. Control

- Adaptive control
- Control of process systems
- Control theory
- Data processing
- Design of control systems
- Hybrid systems
- Identification and observation
- Intelligent systems
- Model-predictive control
- Optimal control
- Robust control
- Fractional order systems

III. Optimization

- Ant Colony
- Chaos Theory
- Evolutionary Computing
- Fuzzy Computing
- Hybrid Methods
- Immunological Computing
- Neuro Computing
- Particle Swarm
- Probabilistic Computing
- Rough Sets
- Wavelet

International Journal Of
Industrial Electronics Control and Optimization
Print ISSN: 3517-2645
Online ISSN: 3568-2645
Homepage: https://ieco.usb.ac.ir/

A Single-Phase Boost AC-AC Converter with Inherent Commutation and Step-Changed Frequency Operation

Babak Fathipour[1] | Ramin Kheyri[1] | Ebrahim Babaei[1] | Samuel Nii Tackie[2]

[1]Faculty of Electrical and Computer Engineering, University of Tabriz, Tabriz, Iran.
[2]Engineering Faculty, Near East University, 99138 Nicosia, North Cyprus, Mersin 10, Turkey
Corresponding author's email: e-babaei@tabrizu.ac.ir

Article Info

Article type:
Research Article

Article history:
Received: 2-February-2025
Received in revised form: 19-May-2025
Accepted: 25-May-2025
Published online:21-March-2026

Keywords:
AC-AC Power Conversion, Inherent commutation, Continuous Input Current, Step-Changed Frequency operation.

ABSTRACT

In this paper, a single-phase boost AC-AC converter with inherent commutation and step-changed frequency operation is proposed. Distinct from conventional AC-AC converters, the proposed design achieves output voltage regulation utilizing one high-frequency switch. The inherent commutation feature of the converter negates the necessity for additional snubber circuits or complex commutation strategies, thereby simplifying the control method for adjusting the output voltage amplitude and frequency. The continuous input current of the proposed converter eliminates the requirement for a bulky LC filter. A straightforward and adaptable switching strategy is implemented to produce output frequency variations. The approach of preventing the conduction of the body diode in power MOSFETs mitigates issues associated with poor reverse recovery, enabling high-speed switching. The operating principles of the converter are elucidated across various modes of operation, with key equations derived and analyzed. To substantiate the validity of the proposed design, simulation results obtained using PSCAD/EMTDC software at frequencies of 25Hz, 50Hz, and 100Hz are presented.

I. Introduction

In various power applications, the demand for reliable and efficient AC-AC power converters is paramount. These converters can be classified into two main categories: indirect and direct AC-AC converters. Indirect AC-AC converters [1, 2], commonly referred to as AC-DC-AC converters, operate through two conversion stages to produce an output waveform with the desired voltage amplitude and frequency. Nonetheless, the process of converting the AC input voltage to a DC voltage, followed by inversion, inevitably introduces harmonic distortion into the power grid. On the other hand, direct AC-AC converters encompass matrix converters [3, 4] and AC-AC pulse width modulation (PWM) converters [5, 6]. Matrix converters are capable of varying both the voltage amplitude and frequency at the output without the need for energy storage components; however, they necessitate the integration of input and output filters and are limited to operating as voltage buck converters. In contemporary power electronic applications, there is an increasing requirement for output voltage boosting. Furthermore, these converters must navigate challenges related to commutation, with a safe commutation strategy proposed in [7] to mitigate such issues. Direct PWM AC-AC converters are often viewed as more suitable for applications where only adjustments to output voltage amplitude are necessary. These converters offer the advantages of single-stage conversion, enhanced efficiency and reliability, and reduced costs [8]. Nevertheless, they are unable to facilitate frequency changes, which have become essential for a wide range of industrial applications. Z-source AC-AC converters are categorized under direct PWM AC-AC converters. Following the introduction of the traditional Z-source inverter (ZSI) in [9], extensive research has been conducted to explore the application of the Z-source network across various power conversion types, including DC-AC [10, 11], AC-DC [12], DC-DC [13, 14], and AC-AC [15], owing to its distinctive features such as boost capability and enhanced reliability compared to voltage source inverters. The initial Z-source AC-AC converter was presented in [15], exhibiting both boost capabilities in-phase and buck/boost functionalities out-of-phase. However, this design was less

reliable than the conventional ZSI, primarily due to the non-ideal characteristics of the complementary bidirectional switches and the inherent delays in their gate drivers. These issues led to unintended overlap or dead times between the switches, resulting in current and voltage spikes, as documented in [16]. Furthermore, the input current in [15] is discontinuous, necessitating the incorporation of an LC filter. A potential solution to the commutation challenges faced by AC-AC converters involves the application of an RC snubber circuit, albeit with significant losses. While the authors of [19, 20] advocate for a complex safe commutation strategy as an alternative to the snubber circuit, this approach is not devoid of shortcomings, as it entails higher costs and increased control complexity. A concept known as "switching cells" was introduced in [17]. This approach involves partitioning the circuit architecture into two identical cells, allowing for the substitution of bidirectional switches with unidirectional switches combined with diodes. To effectively address the commutation challenges posed by the converter using switching cells, precise sensing of the input voltage-particularly in the vicinity of zero-is essential. The modulation of pulse-width modulation (PWM) is dependent on the polarity of the input voltage. Within a switching cell circuit framework, only one high-frequency switch is activated during each half-cycle, with the other remaining inactive until the following half-cycle. If the input voltage polarity is inaccurately sensed, it may result in improper operation of the switches. Therefore, accurate sensing of the input voltage polarity is crucial for the converter's proper functionality. A direct AC-AC converter utilizing four bidirectional power switches was innovated in [18]. This converter features a π-shaped circuit design formed by the power switches and other components, allowing for simultaneous regulation of the output voltage's phase and magnitude. However, it encounters challenges such as commutation difficulties, limited voltage gain, and pulsating input current. Conversely, high-gain Z-source boost AC-AC converters [19, 20] mitigate these issues by implementing a reliable commutation strategy that eliminates the necessity for snubber circuits; however, they do not facilitate inverting operations and involve complex control techniques. Furthermore, a boost AC-AC converter with variable frequency was presented in [21], though it suffers from drawbacks such as the requirement for a bulky input LC filter and low voltage gain. In [22], an asymmetric bipolar output voltage is provided at output. By preventing body diode conduction in MOSFETs, the issues associated with poor reverse recovery are addressed, enabling the implementation of high-speed power MOSFETs. However, the presence of series diodes with all switches increases the total number of semiconductor devices, leading to higher conduction losses and reduced efficiency. In non-inverting operation, the converter can function in boost mode; however, in inverting operation, it is limited to buck-boost mode. This buck-boost operation results in greater voltage and current stresses on the switches compared to boost converters, consequently increasing both switching and conduction losses. While the boost AC-AC converter discussed in [23] facilitates step-changed frequency operation with continuous input current, it is characterized by a low voltage gain. Additionally, this configuration necessitates precise input voltage sensing, which may lead to interface complications in the switches, particularly when the input voltage approaches zero and is not accurately detected. The topology presented in [24] offers both step-changed frequency and bipolar step-up amplitude operations; however, it is hindered by commutation issues and requires dead times between complementary power switches. Furthermore, the inherent connections of the body diodes in the switches contribute to operational challenges. The effective functioning of high-frequency switches in this converter demands exact input voltage sensing, which adds to the complexity of control, increases costs, and contributes to additional losses. In contrast, the converter presented in [25] proposes a single-phase AC-AC configuration that addresses commutation challenges while also ensuring continuous input current. Nevertheless, this design involves a considerable number of high-frequency switches and energy storage components, thereby enhancing its overall complexity. A family of single-phase boost AC-AC converters utilizing impedance network cells with symmetric bipolar operation is introduced in [26]. In this study, output voltage regulation and frequency variation are achieved with the use of only four switches. However, the increased number of diodes results in higher conduction losses, and the input current is quasi-continuous, necessitating the incorporation of a compact input LC filter. The converter outlined in [27] employs switched capacitor cells to achieve high voltage gain; however, it also suffers from commutation challenges, lacks the capability for frequency adjustment, and entails a high number of power switches, ultimately leading to increased implementation costs.

To address the aforementioned challenges, this article proposes a single-phase boost AC-AC converter with inherent commutation and step-changed frequency operation. The proposed converter employs only five switches, which is a reduced count in comparison to other existing converters. In this design, a single high-frequency switch is modulated using a high-frequency PWM signal throughout both half-cycles of the input voltage. This approach obviates the need for precise sensing of input voltage polarity and facilitates the implementation of a straightforward switching strategy. The output frequency can be varied as a multiple or fraction of the input frequency, rendering this converter particularly suitable for applications such as high-gain AC-DC rectifiers, inductive power transmission systems, and traction systems. Unlike indirect AC-DC-AC converters [1, 2], the proposed converter facilitates a single-stage direct AC-AC power conversion and requires only a minimal capacitance of a few microfarads (greater than 1μF). This requirement represents a significant

reduction from the substantially larger dc-link capacitors (greater than 1mF) typically employed in indirect AC-DC-AC converters. As a result, the proposed converter enables the use of a dependable (long lifespan), efficient (characterized by low equivalent series resistance losses), and compact film capacitor.

Moreover, the converter achieves inherent commutation without necessitating the division of the circuit into positive and negative switching cells, thereby enhancing the simplicity of its switching strategy. The input current maintains continuity without the need for a substantial filter on the input side. The prevention of body diode conduction in power MOSFETs mitigates issues related to poor reverse recovery, allowing the use of MOSFETs and enabling selection of a high switching frequency. Consequently, this reduces the size of passive components. The proposed converter has been thoroughly analyzed across various operational modes. To validate the theoretical equations and assess the precision of its performance, simulation results obtained using PSCAD/EMTDC software are presented.

II. Proposed Single-phase AC-AC Converter

The configuration of the proposed AC-AC converter is illustrated in Fig. 1. This converter comprises one high-frequency switch (S), four low-frequency switches (S_1, S_2, S_3, S_4), one inductor (L), seven diodes (D_{p1}, D_{p2}, D_{n1}, D_{n2}, D_1, D_2, D_3), and three capacitors (C_1, C_2, C_3). The low-frequency switches determine the output voltage polarity in relation to the input voltage source (v_i), allowing operations in both non-inverted and inverted modes. Capacitors are integrated into the design to store energy and provide a freewheeling path for the current flowing through the inductor, thereby enabling the proposed AC-AC converter to utilize an inherent commutation strategy. Consequently, there is no requirement for an additional safe commutation strategy or snubber circuit.

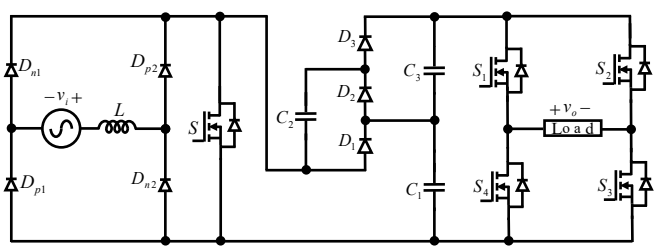

Fig. 1. The configuration of the proposed converter.

A. Switching Strategies of proposed converter

Fig. 2 illustrates the switching strategy employed by the proposed AC-AC converter to generate three distinct output frequencies: $f_i/2$, f_i, and $2f_i$. As depicted, the colored waveforms of the output voltage enhance the interpretation of states 1, 2, 3, and 4 across the various frequencies. These states (1-4) are determined by the conditions of the positive and negative input voltage sources during each half-cycle and the activation of the positive switch pairs (S_1, S_3) and negative switch pairs (S_2, S_4). State 1 is realized when the input voltage source is within its positive half-cycle and is conveyed to the output via the positive switch pairs, resulting in an in-phase output, referred to as non-inverting. In contrast, state 2 is achieved when the input voltage remains in its positive half-cycle and the negative switch pairs are engaged, leading to an out-of-phase output, thus termed inverting. States 3 and 4 occur during the negative half-cycle of the input voltage, depending on whether S_1 and S_3 or S_2 and S_4 are activated, resulting in inverting and non-inverting configurations with respect to the output, respectively. These four states facilitate the generation of varying output frequencies. The proposed converter is capable of producing frequencies $f_o=kf_i$ and $f_o=f_i/k$ where k=1,2, 3, … at the output.

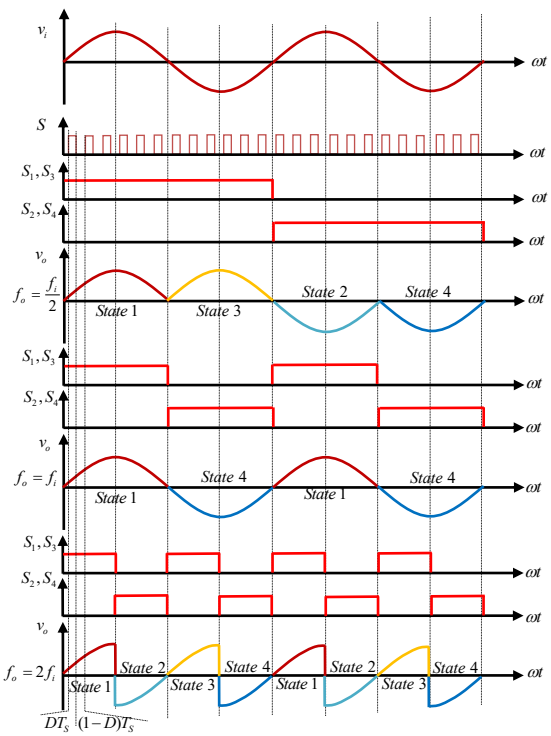

Fig. 2. The switching strategy of the proposed converter.

B. Analysis of proposed converter

The proposed AC-AC converter is examined in two operational states: state 1, characterized by a positive input and a corresponding positive output, and state 4, marked by a negative input producing a negative output, for the purpose of generating an output frequency of $f_o=f_i$. Similarly, an analysis of the converter in states 2 and 3 can be conducted to yield frequencies of $f_o=f_i/2$ and $f_o=2f_i$. The converter has been studied in two distinct operational modes: DT_s and $(1-D)T_s$ intervals. Key equations have been established concerning the voltage stress experienced by components, the current flowing through them, and the voltage gain of the converter. Prior to the analysis, the following assumptions are made: 1) The converter operates under continuous conduction mode; 2) The switching

frequency (f_s) is significantly greater than the input source frequency (f_i); and 3) All components are treated as ideal.

State 1: In state 1, the positive switch pairs S_1 and S_3 are activated, while switches S_2 and S_4 remain in the off position, resulting in non-inverting operation. During the positive half-cycle of the input voltage, diodes D_{p1} and D_{p2} are conducting, whereas diodes D_{n1} and D_{n2} are non-conductive in this state. The switch S operates during the intervals defined by DT_s and (1-D)T_s; as previously mentioned, switch S remains active throughout both half-cycles of the input voltage.

***DT*$_s$ interval:** Fig. 3(a) illustrates the equivalent circuit for this operational mode. The switch S is activated during the DT_s interval. The diodes D_1 and D_3 remain non-conductive due to the negative voltage present across them, resulting in the creation of a parallel configuration involving capacitors C_1, D_2, C_2, and S. Initially, the inductor L is charged through a loop that comprises the input voltage source, D_{p1}, D_{p2} and S, leading to an increase in the energy stored in the inductor. Subsequently, capacitor C_2 is charged via the established parallel loop, causing its voltage to rise. Ultimately, the voltage across capacitors C_1 and C_3 provides power to the load. The application of KVL in this operational mode can be expressed as follows:

$$v_L = v_i \tag{1}$$

$$v_{C1} = v_{C2} \tag{2}$$

$$v_o = v_{C3} + v_{C1} \tag{3}$$

(1-*D*)*T*$_s$ interval: Referring to the equivalent circuit depicted in Fig. 3(b), the S is turned off, resulting in D_2 not conducting during the interval of (1-D)T_s. C_1 is charged by the input voltage and L through the loop formed by D_1, D_{p1} and D_{p2}, leading to an increase in the energy stored within the C_1. Additionally, C_3 is charged by capacitor C_2. By applying KVL in this operational mode, the equation can be derived as follows:

$$v_L = v_i - v_{C1} \tag{4}$$

$$v_{C2} = v_{C3} \tag{5}$$

By employing the voltage-second balance principle for inductor L, the voltage across the capacitors can be expressed as follows:

$$v_{C1-C3} = +\frac{v_i}{1-D} \tag{6}$$

By substituting equation (6) into equation (3), the voltage gain (G) of the proposed converter in state 1 is derived as follows:

$$G = \frac{v_o}{v_i} = +\frac{2}{1-D} \tag{7}$$

State 4: In state 4, the negative switch pairs S_2 and S_4, along with D_{n1} and D_{n2}, are activated during the negative half-cycle of the input voltage source, facilitating non-inverting operation.

***DT*$_s$ interval:** The equivalent circuit for this operational mode is presented in Fig. 3(c). During this mode, the S is activated. Diodes D_1 and D_3 are reverse biased and do not conduct. The energy stored in the inductor L is increased through a loop that comprises the input voltage source, D_{n1}, D_{n2} and S. The energy stored in capacitor C_1 also serves to charge capacitor C_2, while the load is supplied by capacitors C_1 and C_3. The application of KVL in this operational mode can be expressed as follows:

$$v_L = v_i \tag{8}$$

$$v_{C1} = v_{C2} \tag{9}$$

$$v_o = v_{C3} + v_{C1} \tag{10}$$

(1-*D*)*T*$_s$ interval: The equivalent circuit for this mode is illustrated in Fig. 3(d). The S is deactivated during in (1-D)T_s interval. C_1 is charged via the loop formed by the input voltage source v_i, L, D_{n1}, D_{n2}, and D_1. With a positive voltage applied across D_1, and D_3, these diodes become conductive, providing a pathway for the energy stored in the inductor L to discharge into C_1, C_3, and the load. The application of KVL in this operational mode can be articulated as follows:

$$v_L = v_i - v_{C1} \tag{11}$$

$$v_{C2} = v_{C3} \tag{12}$$

By employing the voltage-second balance principle for inductor L, the voltage across the capacitors in state 4 can be expressed as follows:

$$v_{C1-C3} = +\frac{v_i}{1-D} \tag{13}$$

By substituting equation (13) into equation (10), the voltage

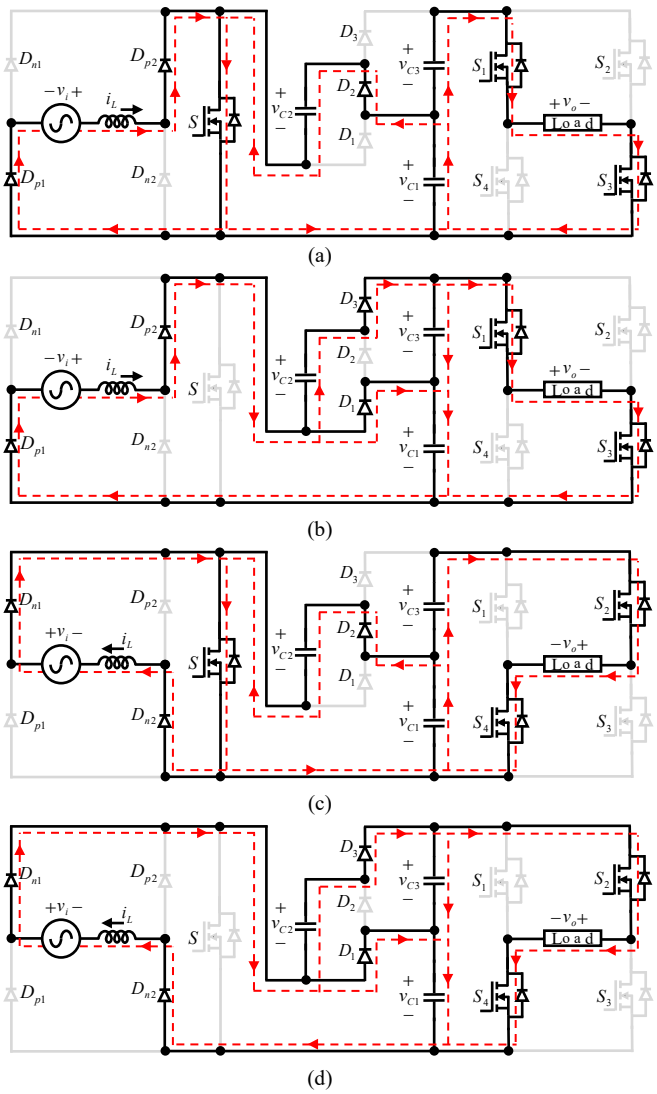

Fig. 3. Equivalent circuits of the proposed converter (a) DT_s interval of state 1. (b) (1-D)T_s interval of state 1. (c) DT_s interval of state 4. (d) (1-D)T_s interval of state 4.

gain of the proposed converter in state 4 is derived as follows:

$$G = \frac{v_o}{v_i} = +\frac{2}{1-D} \quad (14)$$

Based on the equations presented in equation (7) and equation (14), when the signs of the input voltage and output voltage are identical (either both positive or both negative) during a half-cycle, the voltage gain is positive (as seen in states 1 and 4). This indicates a non-inverting output relative to the input voltage. Conversely, when the input voltage is positive while the output voltage is negative, or vice versa (as observed in states 2 and 3), the voltage gain exhibits a negative sign, indicating that the output is inverted in relation to the input voltage.

III. Parameter Design

A. Active Components Selection

Semiconductor devices must be selected to withstand the maximum peak voltage and current values without sustaining damage. Therefore, it is imperative to ascertain the maximum voltage and current specifications for the switches and diodes. The peak voltage stresses experienced by the switches and diodes can be calculated using the following equations:

$$\begin{cases} V_{S(peak)} \\ V_{D1-D3(peak)} \\ V_{D1p,n(peak)} \\ V_{D2p,n(peak)} \end{cases} = \sqrt{2}\frac{1}{(1-D)}V_{i(rms)} \qquad V_{S1-S4(peak)} = \sqrt{2}\frac{2}{(1-D)}V_{i(rms)} \quad (15)$$

The peak current flowing through the switches, diodes, and inductor, as well as the root mean square (RMS) currents of the switches, inductor, and capacitors, and the average currents of the switches and diodes over a complete line cycle are calculated and presented in Table 1.

TABLE 1: THE CURRENT EQUATIONS OF COMPONENTS

Switches/$I_{o(rms)}$		
Peak	RMS	Average
$\boldsymbol{I_S = \frac{\sqrt{2}(1+D)}{D(1-D)}}$	$I_S = \frac{1+D}{(1-D)\sqrt{D}}$	$I_S = \frac{2\sqrt{2}(1+D)}{\pi(1-D)}$
$\boldsymbol{I_{S3-S6} = \sqrt{2}}$	$I_{S1-S4} = \frac{1}{\sqrt{2}}$	$I_{S1-S4} = \frac{\sqrt{2}}{\pi}$
Diodes/$I_{o(rms)}$		
Peak		Average
$\boldsymbol{I_{\substack{D1p,n \\ D2p,n}} = \frac{2\sqrt{2}}{(1-D)}}$, $\boldsymbol{I_{D1,D3} = \frac{\sqrt{2}}{(1-D)}}$		$I_{\substack{D1p,n \\ D2p,n}} = \frac{2\sqrt{2}}{\pi(1-D)}$, $I_{D1-D3} = \frac{2\sqrt{2}}{\pi}$
$\boldsymbol{I_{D2} = \frac{\sqrt{2}}{D}}$		
Inductor/$I_{o(rms)}$		
Peak		RMS
$\boldsymbol{I_L = \frac{2\sqrt{2}}{(1-D)}}$		$I_L = \frac{2}{(1-D)}$
Capacitors/$I_{o(rms)}$		
RMS		
$\boldsymbol{i_{C1} = \frac{(1+D)}{\sqrt{D(1-D)}}}$, $\boldsymbol{i_{C2} = \sqrt{\frac{1}{D(1-D)}}}$, $\boldsymbol{i_{C3} = \sqrt{\frac{D}{1-D}}}$		

B. Passive Components Design

The required inductance value can be determined using the following equation:

$$L = \frac{|V_L|DT_S}{|\Delta I_L|} \quad (16)$$

In the previous equation, the voltage applied across the inductor during $\Delta T = DT_S$ is represented by $|V_L|$. The maximum permissible current ripple, denoted as ΔI_L, has been established as $\Delta I_L = x\%I_{L(peak)}$, where $I_{L(peak)}$ represents the peak current stress experienced by the inductor, as indicated in Table 1. Consequently, the necessary inductance value for the proposed converter can be derived using the following equation:

$$L = \frac{DV_{i(rms)}^2}{x\%f_sP_o} \quad (17)$$

The required capacitance value is determined through a methodology analogous to that used for calculating inductance values. Consequently, the necessary capacitance can be expressed as follows:

$$C = \frac{|I_C|DT_S}{|\Delta V_C|} \quad (18)$$

In this context, $|I_C|$ represents the current flowing the capacitor during the DT_s interval, $\Delta V_C = y\%V_{C(peak)}$ denotes the maximum permissible voltage ripple, and $V_{C(peak)}$ signifies the peak voltage across the capacitor. Therefore, the necessary capacitance value for the proposed converter can be computed as follows:

$$\begin{cases} C_1 = \frac{(1+D)(1-D)^2P_o}{2y\%f_sV_{i(rms)}^2} \\ C_2 = \frac{(1-D)^2P_o}{2y\%f_sV_{i(rms)}^2} \\ C_3 = \frac{D(1-D)^2P_o}{2y\%f_sV_{i(rms)}^2} \end{cases} \quad (19)$$

IV. Control Block Diagram for Output Voltage Regulation

The control block diagram for the proposed converter is shown in Fig. 4. In order to regulate the operation of the switch pairs S_1,S_3 and S_2,S_4, which operate at line frequency, a comparator is employed to assess the polarity of the input voltage. The peak output voltage is calculated using the methodology outlined in [29], as illustrated in the block diagram in Fig. 5, and is acquired as follows:

$$\sqrt{[v_o\,sin(\omega t)]^2 + [v_o\,cos(\omega t)]^2} = V_{o(peak)} \quad (20)$$

The incorporation of low-pass filters (LPFs) at both inputs of the peak voltage detector is intended to attenuate high-frequency noise, thereby decreasing the potential for erroneous switch activations. The detected peak output voltage ($V_{o(peak)}$) is then compared to the reference voltage ($V_{o(ref)}$), resulting in the generation of an error signal ($v_e(t)$). This error signal is processed by a proportional-integral (PI) controller, which computes the duty cycle ($D(t)$) necessary to adjust the output voltage to the desired reference level. The operation of the PI controller is characterized by the

proportional gain (k_p) and the integral gain (k_i), as depicted in Fig. 4. Ultimately, the control signals consist of a high-frequency PWM pulse for switch S, in addition to four low-frequency PWM pulses (operating at line frequency) for switches S_1-S_4, which are subsequently sent to the converter.

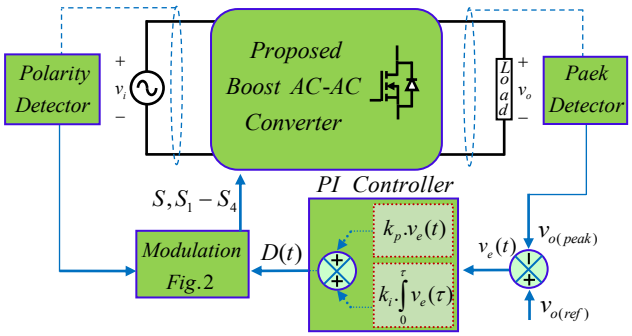

Fig. 4. The control block diagram of the proposed converter.

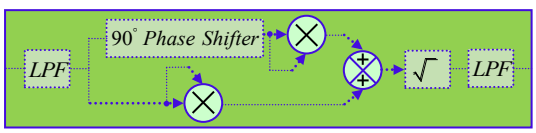

Fig. 5. The block diagram of the peak voltage detector.

V. Comparative Analysis

Table 2 presents a comparative analysis between the proposed converter and various other single-phase boost AC-AC converters. The voltage gain relative to the duty cycle for the proposed converter, alongside the gains of other converters, is illustrated in Fig. 6(a). The voltage gain of the proposed converter is found to be comparable to that of the converter presented in [27], while exceeding the gains of most other converters. As shown in Table 2, the proposed topology features the fewest switches in its design, second only to the converter in [26], which utilizes four active switches but additionally requires nine external diodes and exhibits a discontinuous input current. Moreover, converters [20, 24, 27] face commutation issues that necessitate dead or overlap times to avoid short circuits in capacitors and open circuits in inductors, negatively impacting the quality of the output voltage waveform. Although the converter discussed in [25] addresses commutation challenges, it does so at the cost of employing a significant number of active and passive components while yielding a low voltage gain. The proposed converter, along with those in [23-26], provides symmetrical voltage gain and enables step-changed frequency operation, making them particularly suitable for high-gain AC-DC rectifiers and traction systems. The converters detailed in [20] and [22-27] depend on precise input voltage polarity sensing, as the operation of their high-frequency switches is contingent upon accurate detection of this polarity. Such dependence can lead to interface complications, especially when the input voltage is close to zero and its polarity cannot be precisely identified. In contrast, the proposed converter mitigates this issue by employing a single high-frequency switch that operates across both half-cycles of the input voltage, independent of voltage polarity sensing. Furthermore, converters [20, 24, 27] experience challenges due to high-frequency conduction of the body diode in the switching devices, along with associated reverse recovery problems.

Fig. 6(b) and 6(c) illustrate a reduction in both the total voltage stress across the switches and the current that flows through them in the proposed converter. While converters [20, 22, 26, and 27] also exhibit reductions in voltage stress for various voltage gains (G) when compared to the proposed converter, they are associated with significant issues, including commutation challenges, increased complexity in control and switching patterns, a higher number of high-frequency switches, and conduction through the body diode of the switching devices. The switching device peak power (SDP_{peak}), which is directly correlated to the overall power rating and cost of the switching devices, as well as the average power (SDP_{ave}), which is related to losses and the thermal requirements of the devices [28], are defined for the proposed converter as follows:

$$SDP_{peak} = \sum_{n=1}^{N} V_{n(peak)} I_{n(peak)} = \frac{2+18D-8D^2}{D(1-D)} P_o \quad (21)$$

$$SDP_{ave} = \sum_{n=1}^{N} V_{n(peak)} I_{n(ave)} = \frac{24-12D}{\pi(1-D)} P_o \quad (22)$$

In equations (21) and (22), $V_{n(peak)}$, $I_{n(peak)}$, and $I_{n(ave)}$ represent the peak voltage, peak current, and average current of the *nth* device, respectively. The normalized values for peak power (SDP_{peak}) and average power (SDP_{ave}) of both the proposed converter and its counterparts are presented in Fig. 7 as a function of voltage gain. It is evident that the proposed converter demonstrates the lowest peak and average power ratings for the switching devices when compared to converters [20, 22, 23, 25, 26]. This suggests that the proposed converter requires a reduced total power rating, lower cost, diminished losses, and minimized heatsink requirements.

VI. Simulation Results and Loss Analysis

A. Simulation Results

To validate the effectiveness and ensure the reliability of the proposed converter, simulation results are presented using PSCAD/EMTDC software. The parameters employed in the simulation are outlined in Table 3. To demonstrate the capability of the proposed converter regarding step-changed frequency operation, performance evaluations have been conducted at three specific frequencies: 25Hz (stepped down), 50Hz (identical to the input voltage source), and 100Hz (stepped up), with a duty cycle (D) of 0.5. Fig. 8(a) illustrates the input voltage waveform (V_i), which exhibits a peak value of

TABLE 3: PARAMETERS USED IN THE SIMULATION

Parameters and Values						
$V_{i(peak)}$	f_S	D	f_i	$C_1 - C_3$	L	$load$
50 V	100KHZ	0.5	50HZ	4μF	400μH	80Ω

TABLE 2: COMPARISON OF THE PROPOSED CONVERTER WITH OTHER AC-AC CONVERTERS

Parameters	[20]	[22]	[23]	[24]	[25]	[26]	[27]	Proposed
Voltage gain	$\frac{1+(N-1)D}{1-D}$	$\frac{1}{1-D}$	$\frac{1}{1-D}$	$\frac{1}{1-D}$	$\frac{1}{1-D}$	$\frac{1+D}{1-D}$	$\frac{2}{1-D}$	$\frac{2}{1-D}$
No. of switches	4	6	6	8	8	4	8	5
No. of diodes	-	6	8	-	8	9	-	7
No. of inductors	1	1	1	2	6	2	1	1
No. of capacitors	2	2	2	3	3	1	3	3
Symmetrical voltage gain	No	No	Yes	Yes	Yes	Yes	No	Yes
Continuous input current	Yes	Yes	Yes	Yes	Yes	No	Yes	Yes
Step-changed frequency operation	No	No	Yes	Yes	Yes	Yes	No	Yes
Control complexity	High	Moderate	Moderate	Moderate	Moderate	Moderate	High	Low
Inherent commutation	No	Yes	Yes	No	Yes	Yes	No	Yes
Need dead or overlap time	Yes	No	No	Yes	No	No	Yes	No
Body diodes conduction	Yes	No	No	Yes	No	No	Yes	No

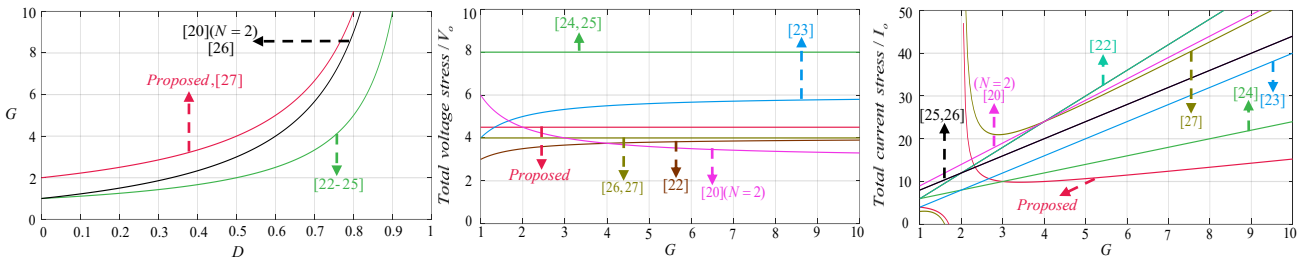

(a) (b) (c)

Fig. 6. Comparison plots, (a) Voltage gain, (b) Total switches voltage stress, (c) Total switches current stress.

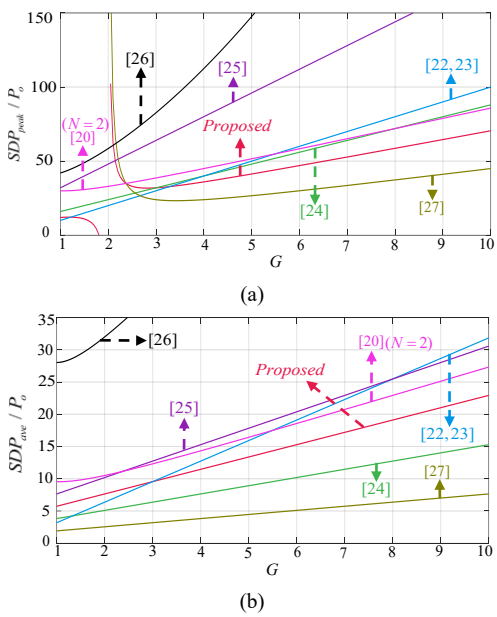

(a)

(b)

Fig. 7. Total switching devices power of the proposed converter and other converters, (a) SDP_{peak}. (b) SDP_{ave}.

$50V$. Fig. 8(b) presents the output voltage waveform (V_o) of the proposed converter at $25Hz$, revealing four distinct states corresponding to the signs of the input voltage source. The output voltage waveform (V_o) for the frequency of $50Hz$ is depicted in Fig. 8(c), where it can be observed that the output voltage is increased and remains entirely in phase with V_i. Based on equation (7), the maximum output voltage is calculated to be $200V$, which aligns well with the simulation results obtained. Subsequently, Fig. 8(d) shows the output voltage waveform of the proposed converter at f_o=$100Hz$, which also exhibits four states. As illustrated in Fig. 8(d), each half-cycle of the input voltage contains two states, which are either inverted or non-inverted based on the sign of the input voltage. The voltage stress on the capacitors, switches, and diodes with their zoomed-in waveforms is depicted in Figs. 9(a) to 10(d). The calculated voltage stress values on the capacitors, derived from (6), and those on the switches and diodes, calculated using (15), closely correlate with the simulation outcomes presented in Figs. 9(a) to 10(d). The zoomed-in waveforms illustrating the voltage stress across the semiconductors indicate the absence of short circuits or voltage spikes during the operation of the proposed converter, which is consistent with the analytical results obtained. Fig 11(a) and Fig. 11(b) presents the simulation results for the input and output voltage and current waveforms, along with their zoomed-in views, under an R-L load characterized by a resistance of R=80Ω and inductance L=$50mH$, operating at an output of $50Hz$.

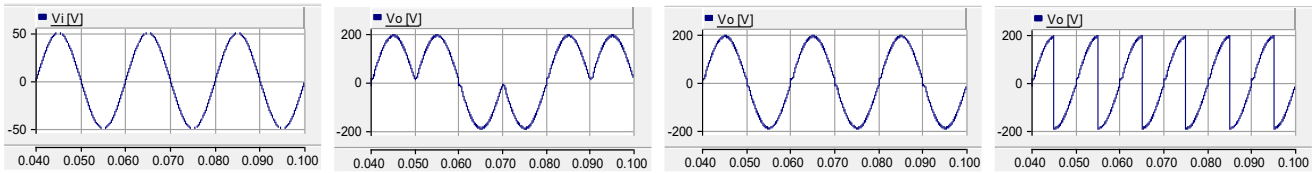

(a) (b) (c) (d)

Fig. 8. Simulation results of input and output waveforms for step-changed frequency operation. (a) Input voltage. (b) Output voltage for 25*Hz*. (c) Output voltage for 50*Hz*. (d) Output voltage for 100*Hz*.

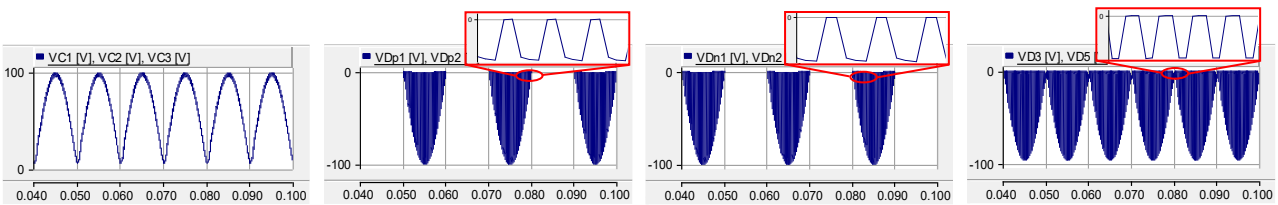

(a) (b) (c) (d)

Fig. 9. Simulation results of voltage stress waveforms. (a) Across capacitors. (b) Across D_{p1}, D_{p2}. (c) Across D_{n1}, D_{n2}. (d) Across D_3, D_5.

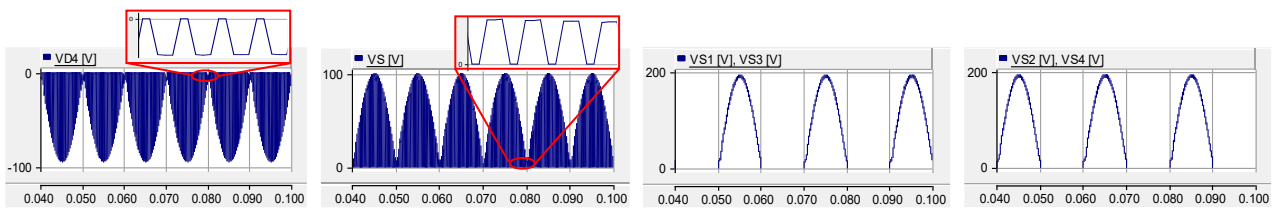

(a) (b) (c) (d)

Fig. 10. Simulation results of voltage stress waveforms. (a) Across D_4. (b) Across S. (c) Across S_1, S_3. (d) Across S_2, S_4.

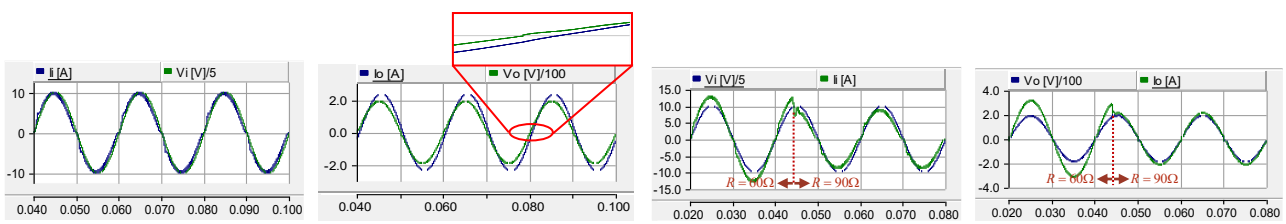

(a) (b) (c) (d)

Fig. 11. Simulation results, (a) Input waveforms under RL load, (b) Output waveforms under RL load, (c) Input waveforms under transient load, (d) Output waveforms under transient load.

This demonstrates the proposed converter's capability to manage non-unity load conditions. Additionally, the input and output waveforms of the proposed converter are depicted in Figs. 11(c) and 11(d), showcasing its performance as the load resistance varies from 60Ω to 90Ω. The waveform analysis reveals the converter's proficiency in sustaining inherent commutation while exhibiting the absence of voltage spikes during load transitions.

B. Loss Analysis

In non-ideal operating conditions, each component of the converter contributes to the overall power losses. These losses are primarily categorized into two types: conduction loss (P_{cond}) and switching loss ($P_{switching}$), which together constitute the total power loss of the converter (P_{Loss}). To obtain an accurate assessment of the total losses, it is essential to consider several key parameters, including the on-state resistance of the switches (r_S), the equivalent series resistance associated with the capacitors (r_C), the resistance of the inductor (r_L), the forward voltage drops across the diodes (V_F), the switching frequency (f_s), as well as the turn-on (t_r) and turn-off (t_f) times of the switches. The formulations for P_{cond}, $P_{switching}$, and P_{Loss} can be expressed as follows:

$$\begin{cases} P_{cond} = r_S(I^2_{S(rms)} + I^2_{S1-S4(rms)}) + r_L(I^2_{L(rms)}) + \\ V_F(I_{D1p,n(ave)} + I_{D3-D5(ave)}) + \\ \quad D2p,n(ave) \\ r_C(I^2_{C1(rms)} + I^2_{C2(rms)} + I^2_{C3(rms)}) \\ P_{switching} = \frac{1}{6} V_{S(rms)} I_{S(rms)} f_s (t_r + t_f) \\ P_{Loss} = P_{cond} + P_{switching} \end{cases} \quad (23)$$

It is presumed that the voltage and current fluctuations in the inductors and capacitors are insignificant. The switching losses are primarily associated with the high-frequency switch S. The

root mean square (RMS) values of the currents flowing through the capacitors, inductors, and switches, along with the average current values for the diodes, are computed over one line period and presented in Table 2. This can be formally expressed as follows:

$$\begin{cases} P_{Loss} = r_S\left[\left(\frac{1+D}{(1-D)\sqrt{D}}\right)^2 + \left(\sqrt{2}\right)^2\right] I_{o(rms)}^2 + \\ \frac{1}{6} V_{S(rms)} I_{S(rms)} f_S (t_r + t_f) + \\ V_F\left(\frac{8\sqrt{2}}{\pi(1-D)} + \frac{6\sqrt{2}}{\pi}\right) I_{o(rms)} + r_L\left(\frac{2}{1-D}\right)^2 I_{o(rms)}^2 + \\ r_C\left[\left(\frac{1+D}{\sqrt{D(1-D)}}\right)^2 + \left(\sqrt{\frac{1}{D(1-D)}}\right)^2 + \left(\sqrt{\frac{D}{1-D}}\right)^2\right] I_{o(rms)}^2 \end{cases} \quad (24)$$

Ultimately, the efficiency of the proposed converter can be evaluated as follows:

$$\eta = \frac{P_o}{P_o + P_{Loss}} \quad (25)$$

The non-ideal voltage gain (G') of the proposed converter can be expressed using the following equation:

$$G' = \frac{G}{1+(P_{Loss}/P_o)} \quad (26)$$

Fig. 12 presents the characteristics of conversion efficiency and voltage gain as a function of duty cycle (D) under the specified conditions: $v_{i(rms)}$=50V, V_F=0.7V, r_S=0.04Ω, t_r+t_f=100ns, f_s=100kHz, and R=80Ω. The analysis in Fig. 12 indicates that at high duty cycles, an increase in inductor resistance (r_L) and capacitors resistance ($r_{C1} = r_{C2} = r_{C3} \approx r_C$) can significantly impair both the voltage gain and efficiency of the converter.

Fig. 13 presents a comparison of the efficiency curves for the proposed converter alongside those of other converters [20, 22, 23, 26] under matched operating conditions, specifically at an output voltage of 140V_{rms} and a gain of 4, over a broad spectrum of output powers ranging from 50W to 450W. As depicted in Fig. 13, the proposed converter exhibits superior efficiency compared to the other converters throughout the entire output power range. The impressive efficiency attained by the proposed converter can be attributed to several factors, including the optimized use of a reduced number of switches

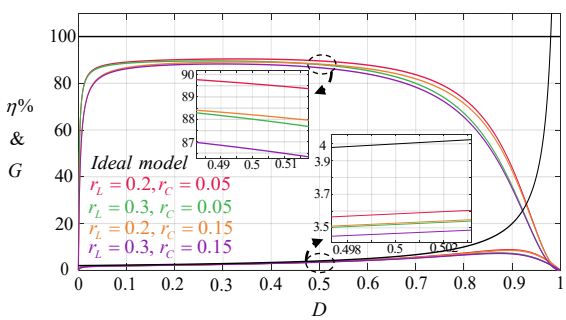

Fig. 12. The efficiency and non-ideal voltage gain curves.

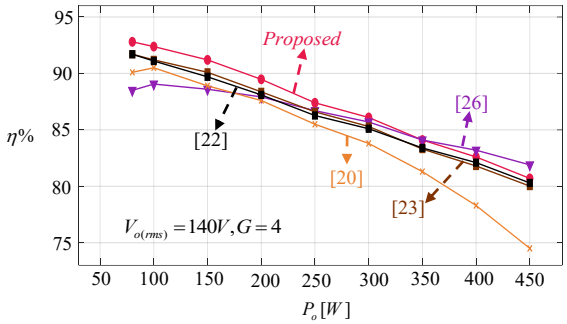

Fig. 13. The efficiency of the proposed converter.

and the effective mitigation of commutation issues, achieved without any overlap or dead time.

VII. Conclusion

This paper presents a single-phase boost AC-AC converter with inherent commutation and step-changed frequency operation. When compared to existing boost AC-AC converters, the proposed design exhibits a higher voltage gain and eliminates the necessity for bidirectional switches. Moreover, the commutation issue is addressed inherently, negating the need for division into two sub-circuits, which effectively reduces the number of components, overall costs, and size of the converter. As illustrated in Fig. 2, the proposed converter features a straightforward control method that involves turning a single high-frequency switch on and off during both half-cycles of the input voltage. This configuration helps minimize conduction losses and enhance overall efficiency. The simulation results validate these assertions across three frequencies: 25Hz, 50Hz, and 100Hz.

References

[1] L. Qin, P.C. Loh and F. Blaabjerg, "Modulation schemes with enhanced switch thermal distribution for single-phase ac-dc-ac reduced-switch converters," *IEEE Trans. Power Electron.*, vol. 31, no. 4, pp. 3302-3313, Apr. 2016.

[2] P. Alemi, Y.C. Jeung and D.C. Lee, "Dc-link capacitance minimization in T-type three-level ac/dc/ac PWM converters," *IEEE Trans. Ind. Electron.*, vol. 62, no. 3, pp. 1382-1391, Mar. 2015.

[3] A. Zuckerberger, D. Weinstock and A. Alexandrovitz, "Single-phase matrix converter," *IEE Proc. Elect. Power Appl.*, vol. 144, no. 4, pp. 235-240, 1997.

[4] P. Szcześniak and J. Kaniewski, "Hybrid transformer with matrix converter," *IEEE Trans. Power Del.*, vol. 31, no. 3, pp. 1388-1396, June 2016.

[5] A.A. Khan, H. Cha and H.G. Kim, "Magnetic integration of discrete coupled inductors in single-phase direct PWM ac-ac converters," *IEEE Trans. Power Electron.*, vol. 31, no. 3, pp. 2129-2138, Mar. 2016.

[6] S.M.J. Mousavi, D. Zargariafshar, E. Babaei and H.F. Ahmed, "A single-phase Z-source ac-ac converter with continuous input current and without commutation issue," *IEEE Trans. Ind. Electron.*, vol. 71, no. 11, pp. 14002-14010, Nov. 2024.

[7] Z. Idris, S.Z.M. Noor and M.K. Hamzah, "Safe commutation strategy in single phase matrix converter," *in Proc. Int. Conf. Power Electron. Drives Syst.*, 2005, pp. 886-

891.
[8] B. Fathipour, S.M.J. Mousavi and E. Babaei, "An extendable single-phase boost ac-ac converter with continuous input current and step-changed frequency operation," *Int. J. Circ. Theor. Appl*., pp. 1-15, Mar. 2025.
[9] F.Z .Peng, "Z-source inverter," *IEEE Trans. Ind. App.*, vol. 39, no. 2, pp. 504-510, March-April 2003.
[10] S. Laali and E. Babaei, "Developed quasi Z-source inverters based on diode-cells: analysis and implementation," *Int. J. Ind. Electron. Cont. Opt.*, vol. 5, no. 1, pp. 51-62, Mar. 2022.
[11] T. Ahmadzadeh, E. Babaei, M. Sabahi and T. Abedinzadeh, "PWM control methods based on mathematical equations for Z-source inverters," *Int. J. Ind. Electron. Cont. Opt.*, vol. 4, no. 2, pp. 167-179, Apr. 2021.
[12] M. Monfard, M. Babaei and S. Sharifi, "A Z-source network integrated buck-boost PFC rectifier," *Int. J. Ind. Electron. Cont. Opt.*, vol. 2, no. 4, pp. 289-296, Oct. 2019.
[13] H. Gholizadeh and S. Hasanpour, "A new quadratic cuk-based step-up dc/dc converter without right hand plane zero," *Int. J. Ind. Elec Cont. Opt.*, vol. 8, no. 1, pp. 25-35, Mar. 2025.
[14] S. Toofan, B. Fathipour and E. Babaei, "A single switch transformer-less dc-dc converter with continuous input current for photovoltaic applications," *Int. J. Ind. Electron. Cont. Opt.*, vol. 7, no. 4, pp. 281-290, Dec. 2024.
[15] M. Nguyen, Y. Jung, Y. Lim and Y. Kim, "A single-phase Z-source buck-boost matrix converter," *IEEE Trans. Power Electron.*, vol. 25, no. 2, pp. 453-462, Feb. 2010.
[16] B. Fathipour, R. Kheyri, S.M.J. Mousavi and E. Babaei, "A single-phase ac-ac converter with continuous input current and without commutation problem," *Int. J. Circ. Theor. Appl*., pp. 1-22, June 2024.
[17] H. Shin, H. Cha, H. Kim and D. Yoo, "Novel single-phase PWM ac-ac converters solving commutation problem using switching cell structure and coupled inductor," *IEEE Trans. Power Electron.*, vol. 30, no. 4, pp. 2137-2147, April 2015.
[18] Y. Zhang and X. Ruan, "π model ac-ac converter with controllable phase and amplitude," *IEEE Trans. Ind. Electron*., vol. 64, no. 8, pp. 6422-6431, Aug. 2017.
[19] A.L. Eshkevari, I. Abdoli., M.K. Hajiabadi and A. Mosallanejad, "High step-up direct ac-ac boost converter with optimal components counts based on sepic," *IET Power Electron.*, vol. 17, no. 9, pp. 1106-1118, 2024.
[20] I. Abdoli, M.K. Hajiabadi, A. Mosallanejad and A.L. Eshkevari, "A single-phase p-type ac-ac converter with reduced components count and high boost factor," *Int. J. Circ. Theory Appl.*, vol. 51, no. 1, pp. 360-378, Aug. 2023.
[21] T. Mishima, Y. Nakagawa and M. Nakaoka, "A bridgeless BHB ZVS-PWM ac-ac converter for high-frequency induction heating applications," *IEEE Trans. Ind. Appl.*, vol. 51, no. 4, pp. 3304-3315, July-Aug. 2015.
[22] H.F. Ahmed, H. Cha, A.A. Khan and H. Kim, "A novel buck-boost ac-ac converter with both inverting and noninverting operations and without commutation problem," *IEEE Trans. Power Electron.*, vol. 31, no. 6, pp. 4241-4251, June 2016.
[23] N. Ashraf, G. Abbas, N. Ullah, H.I.A. khammash and M. Zubair, "An improved bipolar voltage boost ac voltage controller with reduced switching transistors," *IEEE Access*, vol. 9, pp. 90402-90417, 2021.
[24] H.F. Ahmed, M.S.E Moursi, B. Zahawi, and K.A. Hosani, "High-efficiency single-phase matrix converter with diverse symmetric bipolar buck and boost operations," *IEEE Trans. Power Electron*., vol. 36, no. 4, pp. 4300-4315, April 2021.
[25] H.F. Ahmed, O. Alzaabi, M.S.E. Moursi, and K.H.A. Hosaini, "Highly-efficient dual-buck structured buck-boost ac-ac converter with versatile identical inverting/non-inverting operations," *IEEE Trans. Ind. Inf.*, vol. 19, no. 12, pp. 11403-11417, Dec. 2023.
[26] B. Fathipour, S.M.J. Mousavi and E. Babaei, "A family of single-phase boost ac-ac converters based on impedance network cells with symmetric bipolar operation," *Int. J. Circ. Theor. Appl*., vol. 53, no. 1, pp. 291-310, May 2024.
[27] M.S. Dall'Asta, I. Barbi and T.B. Lazzarin, "Ac-ac hybrid boost switched-capacitor converter," *IEEE Trans. Power Electron.*, vol. 35, no. 12, pp. 13115-13125, Dec. 2020.
[28] S. Sharifi, M. Monfared, M. Babaei and A. Pourfaraj, "Highly efficient single-phase buck-boost variable-frequency ac-ac converter with inherent commutation capability," *IEEE Trans. Ind. Electron.*, vol. 67, no. 7, pp. 3640-3649, May 2020.
[29] B.H. Kwon, G.Y. Jeong, S.H. Han and D.H. Lee, "Novel line conditioner with voltage up/down capability," *IEEE Trans. Ind. Appl.*, vol. 49, no. 5, pp. 1110-1119, Oct. 2002.

Babak Fathipour was born in Tabriz, Iran, in 1999. He received a B.Sc. degree in Electrical Power Engineering, and an M.Sc. degree in Power Electronics Engineering from University of Tabriz, Tabriz, Iran in 2021 and 2023, respectively. His current research interests include power electronic converters and renewable energy systems.

Ramin Kheyri received his B.Sc. in Electrical Engineering from Urmia University of Technology in 2006, his M.Sc. in Electrical Engineering from the University of Science and Research in 2009, and his Ph.D. in Electrical Engineering from Shahrood University of Technology in 2023. Dr. Kheyri's areas of interest include: Power Electronics, Power Electronics Control, Power Electronic Converters, Power Electronic Converter Modeling, and Electrical Energy Generation.

Ebrahim Babaei (M'10, SM'16) received the Ph.D. degree in Electrical Engineering from the University of Tabriz, in 2007. He is the author and co-author of one book and more than 720 journal and conference papers. He also holds 26 patents in the area of power electronics. His current research interests include the analysis, modelling, design, and control of Power Electronics Converters and their applications, Renewable Energy Sources, and FACTS Devices.Prof. Babaei has been the Editor-in-Chief of the Journal of Electrical Engineering of the University of Tabriz, since 2013. He was an Associate Editor of the IEEE Transactions on Industrial Electronics from 2015 to 2023. He is also currently an Associate Editor of the IEEE Transactions on Power Electronics, IEEE Open Journal of the Industrial Electronics Society, Iranian Journal of Science and Technology, Transactions of Electrical Engineering, and International Journal of Circuit Theory and Applications. He was selected by the Ministry of Science Research and Technology as the distinguished researcher of Iran in the field of engineering in 2022.

Samuel Nii Tackie received his MSc and PhD in Electrical and Electronic Engineering from Near East University in 2015 and 2021, respectively. He has a solid, young, demonstrable profession in both academia and engineering, incorporating teaching, research, supervision, and hands-on practice to advance the field of electrical and electronic engineering. Currently, his research area of interest includes: Power Electronics, Renewable Energy Sources, Generation of Electrical Energy, Custom Power Devices, and Power Electronic Converters.

IECO

This page intentionally left blank.

IECO International Journal Of Industrial Electronics Control and Optimization
Print ISSN: 3517-2645
Online ISSN: 3568-2645
Homepage: https://ieco.usb.ac.ir/

Improved Boost Topology According to the Voltage Lift Technique

Reza Hazratian | Ebrahim Afjei

Electrical Engineering Faculty, Shahid Beheshti University, Tehran, Iran.[1,2]
Corresponding author's email: E-Afjei@sbu.ac.ir

Article Info

Article type:
Research Article

Article history:
Received: 07-January-2025
Received in revised form: 06-May-2025
Accepted: 11-May-2025
Published online:21-March-2026

Keywords:
Boost converter,
multiplier cell,
HID lamps,
Luo .

ABSTRACT

This paper proposes a novel non-isolated DC-DC converter topology combining a super-lift Luo converter with inductor-capacitor voltage multipliers (VMCs) to achieve high voltage gain without extreme duty cycles. The proposed design offers seven key advantages. These are a continuous input current that reduces input capacitor stress, a common ground between source and load that mitigates EMI, enhanced voltage-lift effect via hybrid Luo-VMC stages, a semiconductor voltage stress that is significantly lower when compared to output voltage, a semiconductor current stress below input current, minimized current stress for most switches and a scalable voltage gain suitable for high-output applications. The converter is analyzed in both ideal and non-ideal modes with derived equations for continuous and discontinuous conduction modes (CCM/DCM). A 100W prototype (12 V input, 312 V output, 50% duty cycle) validated the design showing its efficacy for high-intensity discharge (HID) lamps and other high-gain applications.

Abbreviations

Vin	Input voltage source	$V_{C1} - V_{C7}$	capacitor voltage 1st to 7th
V_{CO}	Output capacitor voltage	$I_{L1} - I_{L3}$	inductor average current 1st to 3rd
$I_2 - I_8$	capacitor inrush current 2nd to 8th	$Vs1$	Voltage stress of the switch
$V_{D1} - V_{D10}$	Voltage stress of the 1st diode to 10th	$I_{D1} - I_{D10}$	Current stress of the 1st diode to 10th
I_{S1}	Current stress of the 1st switch	fs	Switching frequency
P_L	Conduction loss of the inductors	P_{SC}	Conduction loss of the switch
P_D	Conduction loss of the diodes	r_L	The equivalent resistance of the inductors
r_{SC}	The equivalent resistance of the switch	V_{DF}	Threshold voltage of the diodes
η	Efficiency	R	Load
D	Duty cycle	I_O	Output current
δ	The ratio of the activation time of the last diode over the switching period		

I. Introduction

Isolated and non-isolated topologies are the two main groups of DC-DC converters [1]. The isolated DC-DC converters use a high-frequency transformer to provide a high voltage gain [2]. Also, the provided isolation between load and input source protects the sensitive loads from the faults of the input side [3]. All these advantages are accompanied by some disadvantages. Using the transformers increases the volume and mass and decreases the power density of the converter [4]. Additionally, the leakage inductance of the coils leads to the existence of residual currents, which increases the voltage stress of the switch and requires the use of snubber circuits, which increases the complexity of the converter [5]. Consequently, non-isolated topologies can be used in applications that do not require the isolation of the load and input source [6]. Among the classic non-isolated step-up DC-DC converters, the boost and super lift Luo converters are the most popular ones [7]. These converters have a step-up behavior in all duty cycles. However, providing a ten times voltage gain requires using a high value of the duty cycle,

which is close to unity. Such a high value of the duty cycle leads to a poor efficiency, dramatic high semiconductor voltage stress and a reverse recovery time problem of the diodes [8]. Consequently, new and improved topologies are required.

[9]-[22] include recently proposed improved topologies. The presented topology in [9] uses a boost and buck-boost topology to provide a higher voltage gain than the classic converters. Additionally, the continuity of the input current is present. However, the output polarity is reversed. Additionally, the switch number becomes two and a voltage higher than the output voltage is applied to the last switch and diode. Notably, the voltage gain can cause high values as the duty cycle percentage approaches unity. The presented topologies in [10] and [11] use the same idea. Both topologies use a boost and a super lift Luo converter in their structure. Notably, the proposed topology in [10] is a single-switch form of [11]. The voltage gain provided by these topologies is higher than that of the cascaded boost converter while all the semiconductors' voltage stresses are less than the output voltage. Moreover, the continuity of the input current is maintained. Besides all these advantages, the voltage gain increase is not bold, and the difference between the output voltage and the highest voltage stress is not very significant. The proposed topology in [12] combines two boost topologies providing a higher voltage gain than the cascaded boost topology. Although the continuity of the input current is present, it has one more switch and last diode, and the switch in this topology experiences a voltage stress more than the output voltage compared with the cascaded boost topology. The presented topology in [13] is another two-switch topology, which uses a boost and super lift Luo converter. The voltage gain is more than the provided voltage gain by the cascaded connection of the boost and super lift Luo converter. However, this voltage gain is not significantly high and cannot be more than 10 times, while the duty cycle percentage is at low values. [14] presents a topology whose voltage gain is twice that of the cascaded boost topology. All the bold points and the drawbacks of the boost topology are present in this topology. The voltage gain provided in [15] is the same as that provided in [14], with a smaller number of inductors and all the advantages of the boost converter are present in this topology. However, similar to the boost converter, the highest voltage stress of the semiconductors is the same as the output voltage. The presented topologies in [17], [18] employ boost, super lift Luo, and inductor-based circuits to provide a high voltage gain. Both topologies provide a 10 times voltage gain as the duty cycle reaches 50%. All the positive characteristics of the sub topologies are present in the main topologies and all the semiconductors' voltage stress are less than the output voltage. However, the difference is not much significant. These advantages and disadvantages are repeated in [19]. The provided voltage gain by [19] is particularly higher than in [17], [18]. The presented topologies in [20], [21] are improved from of the presented topology in [12]. These converters can provide a voltage gain of more than 10 times while the duty cycle has low values. All the expressed bold points in [12] are present in [20], [21]. Additionally, the challenge of the semiconductors' voltage stress has been solved in [20], [21]. However, employing two switches in the power circuit is still a challenge. The presented topology in [22] is an improved form of the cascaded boost and Cuk converters. The voltage gain is well-increased while utilizing a single-switch structure. However, two problems arise in this topology, the first is the reversed output polarity of the converter and the second is the maximum voltage stress of the semiconductors, which becomes twice the output voltage.

This study presents a new topology of high gain, non-isolated DC-DC converters. The merits of this topology are: (I) the continuity of the input current is provided to reduce the current stress of the input filter capacitor; (II) the common ground of the load and the input source is present to reduce the electromagnetic interference (EMI) problems; (III) super lift Luo converter is used beside the inductor-based and capacitor-based voltage multiplier cells (VMC) to improve the voltage-lift technique; (IV) the voltage stress of the semiconductors is less than the output voltage with a bold difference; (V) the current stress of the semiconductors is less than the input current; (VI) most of the semiconductors experience the lowest current of the converter as their current stress; (VII) the voltage gain of the converter has increased appropriately that can easily provide the higher voltage gains without the high percentage of the duty cycle. The former characteristics makes this topology demanding for high-intensity discharge (HID) lamps and water electrolysis.

In the rest of this article, the proposed topology will be given in Section II. Section III represents operating modes' analysis. Section IV discuses non-ideal voltage gain and section V considers efficiency. Section VI includes comparative analysis and Section VII demonstrated the proposed topology application. Section VIII deals with small signal analysis and section IX experimental results. Finally, the conclusion is drawn in Section X.

II. Proposed Topology

A. Circuit Description & Operation Overview

In this section, the operation of the converter and its theoretical relations to the various parameters are discussed in the ideal and continuous conduction modes. As illustrated in Fig. 1, the positive output super lift Luo converter (POSLLC) represents an enhanced version of boost topology. This figure depicts the voltage lift process occurring between the input source and the initial capacitor. Essentially, the input source and the first capacitor are connected in parallel during the first operating phase. In the second phase, they are connected in series with the inductor, which increases the voltage gain. Although the voltage gain from this topology surpasses that of

a traditional boost converter, the enhancement is modest. Therefore, it is essential to amplify the impact of the voltage lift method. One effective approach to achieving this is through VMC. Figure 2 illustrates the integration of a VMC with POSLLC, where the VMC replaces the inductor in the POSLLC setup. Utilizing a VMC enhances the voltage gain of the sub-converter. Furthermore, employing inductor-based VMCs reduces the conduction losses by splitting a defined current across two inductors rather than a single one. Additionally, another VMC can be incorporated to achieve a higher voltage gain. As shown in Fig. 3, a diode-capacitor VMC can complement the configuration presented in Fig. 2. This type of VMC not only boosts voltage gain but also increases the separation between the switch and the output terminal, thereby reducing voltage stress on the semiconductors. The configuration in Fig. 3 offers the final iteration of the enhanced POSLLC, featuring two additional voltage-lift processes compared to the conventional POSLLC. However, this new configuration also raises the input current ripple. To address this issue, a boost topology is integrated into the design shown in Fig. 3. Figure 4 illustrates the proposed topology of this study. The inclusion of the boost converter at the start of the proposed configuration ensures continuous input current with minimal ripple. Additionally, the overall voltage gain of the topology takes a quadratic form, further supporting the voltage lift method. It is important to highlight that the entire design is centered around a switch with a straightforward drive structure. In the steady state, the system operates in two modes. During the first mode, as depicted in Fig. 5(a), the switch, diodes two through five, the seventh diode, and the ninth diode are engaged, resulting in a positive voltage being applied to the inductors. Consequently, the inductors become magnetized and store energy within their field.

In the second operating mode, the semiconductors that were active in the first mode turn off, while the remaining semiconductors are activated. Figure 5(b) illustrates the equivalent circuit for this mode. A negative voltage is applied to the inductors to cause demagnetization. It's important to highlight that in the first operating mode, the first through third capacitors are in parallel, along with the series connection of the third and fifth capacitors to the fourth capacitor and the series connection of the fourth, sixth and seventh capacitors to the output capacitor. In the second mode, the sixth capacitor becomes parallel with the seventh and the fourth through sixth capacitors are in series with the output capacitor. Based on the discussed concepts and the shown equivalent circuits, the equations for the inductors' voltage and the capacitors' current are as follows:

$$\begin{cases} V_{L1} = D\left(V_{in}\right) + \left(1-D\right)\left(V_{in} - V_{C1}\right) \\ V_{L2} = D\left(V_{C1}\right) + \left(1-D\right)\left(V_{C1} + V_{C2} - V'\right) \\ V_{L3} = D\left(V_{C1}\right) + \left(1-D\right)\left(V' + V_{C3} - V_{C4}\right) \end{cases} \quad (1)$$

$$V_{C1} = V_{C2} = V_{C3} \quad (2)$$

$$V_{C3} + V_{C5} = V_{C4} \quad (3)$$

$$V_{C6} = V_{C7} \quad (4)$$

$$V_o = V_{C4} + V_{C6} + V_{C7} \quad (5)$$

$$V_o = V_{C4} + V_{C5} + V_{C7} \quad (6)$$

$$\begin{cases} i_{C1} = D\left(-i_{L2} - i_{L3} - i_2 - i_3\right) + \left(1-D\right)\left(i_{L1} - i_{L2}\right) \\ i_{C2} = D\left(i_2\right) + \left(1-D\right)\left(-i_{L2}\right) \\ i_{C3} = D\left(i_3 + i_4 + i_8\right) + \left(1-D\right)\left(-i_{L2}\right) \\ i_{C4} = D\left(-i_4\right) + \left(1-D\right)\left(i_{L2} - i_5\right) \\ i_{C5} = D\left(i_4 + i_8\right) + \left(1-D\right)\left(-i_5\right) \\ i_{C6} = D\left(i_8\right) + \left(1-D\right)\left(i_7 - i_5\right) \\ i_{C7} = D\left(i_8\right) + \left(1-D\right)\left(-i_7\right) \\ i_{Co} = D\left(-i_8 - I_o\right) + \left(1-D\right)\left(i_5 - I_o\right) \end{cases} \quad (7)$$

Notably, the second and third inductors become series with each other in the second operating point. Consequently, their average current gets a relation as follows:

$$i_{L2} = i_{L3} \quad (8)$$

It is important to note that i2, i3, i4, i5, i7, and i8 are the capacitors' created inrush currents during their parallel connection.

Utilizing the voltage second balance in the inductors' voltage equation yields the average voltage of the capacitors as follows:

$$\begin{cases} V_{C1} = V_{C2} = V_{C3} = \dfrac{V_{in}}{1-D}, V' = \dfrac{2-D}{\left(1-D\right)^2} V_{in} \\ V_{C4} = \dfrac{3-D}{\left(1-D\right)^2} V_{in}, V_{C5} = V_{C6} = V_{C7} = \dfrac{2}{\left(1-D\right)^2} V_{in} \end{cases} \quad (9)$$

According to the expressed relations in (5), (6), and (9) the resulting voltage gain is as follows:

$$V_o = \frac{7-D}{\left(1-D\right)^2} V_{in} \quad (10)$$

the extracted voltage gain results from both the quadratic and voltage-lift methods. Furthermore, the voltage-lift The extracted voltage gain results from both the quadratic and voltage-lift methods. Furthermore, the voltage-lift technique is shown to have a threefold impact compared to the traditional POSLLC. Figure 6 illustrates a comparison between the voltage gain of the proposed topology and that of the classic boost converter. It is evident that the proposed topology achieves a higher voltage gain at lower duty cycle percentages than the boost topology does at higher duty cycle percentages. In other words, it is not required to use the higher percentages of the duty cycle to provide a significant value of the voltage gain. Notably, this point becomes bold, when the reverse recovery time of the semiconductors is an issue. This

achievement is the first one compared with the classic boost converter.

Using the current second balance in the capacitors' current equation results in the average current for the inductors and inrush currents as detailed below:

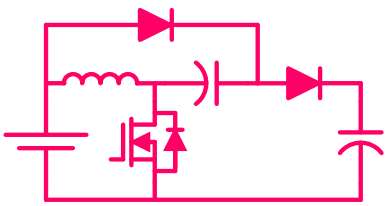

Fig. 1. Classic POSLLC.

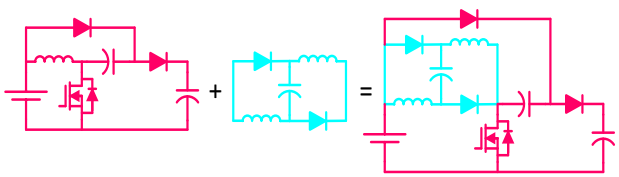

Fig. 2. Improving a classic POSLLC with an inductor-based VMC.

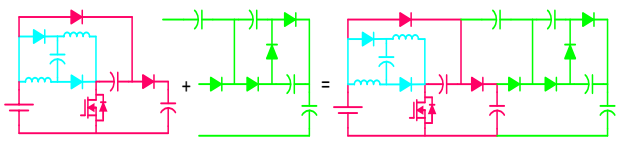

Fig. 3. Improving the modified POSLLC with a diode-capacitor VMC.

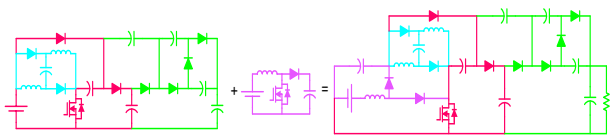

Fig. 4. Building procedure of the proposed topology.

$$\begin{cases} i_{L1}=\dfrac{7-D}{(1-D)^2}I_o, i_{L2}=i_{L3}=\dfrac{3}{1-D}I_o, i_2=\dfrac{3}{D}I_o \\ i_3=i_4=i_8=\dfrac{I_o}{D}, i_5=\dfrac{2}{1-D}I_o, i_7=\dfrac{I_o}{1-D} \end{cases} \quad (11)$$

Calculating the average current of inrush currents in inductors and capacitors helps define the current stresses in semiconductors.

$$\begin{cases} I_S=\dfrac{6+D-D^2}{(1-D)^2}I_o, I_{D1}=\dfrac{7-D}{1-D}I_o, I_{D2}=\dfrac{7D-D^2}{(1-D)^2}I_o \\ I_{D3}=I_{D4}=\dfrac{3}{1-D}I_o, I_{D5}=\ldots=I_{D10}=I_o \end{cases} \quad (12)$$

According to the expressed equations, 60% of the semiconductors experience the lowest current value as their current stress. Moreover, 80% of the semiconductors have a negligible current stress, which keeps the semiconductors' conduction loss at a desired low value. Notably, employing the diode-capacitor circuit at the end of the proposed topology leads to the equality of the current stress of 6 diodes to the output power. Such a feature is independent of the diodes' type. Calculating the average voltage across the capacitors is essential for assessing the voltage stress on the semiconductors, as outlined below:

$$\begin{cases} V_{D5}=V_{D6}=V_{D7}=V_{D8}=V_{D9}=V_{D10}=\dfrac{2}{(1-D)^2}V_{in}, V_S=\dfrac{2}{(1-D)^2}V_{in} \\ V_{D3}=V_{D4}=\dfrac{V_{in}}{(1-D)^2}, V_{D2}=\dfrac{1+D}{(1-D)^2}V_{in}, V_{D1}=\dfrac{V_{in}}{1-D} \end{cases} \quad (13)$$

The analyzed values indicate that semiconductors do not face a voltage exceeding the output voltage. Notably, the use of the diode-capacitor circuit at the end of the converter leads to a voltage stress, which is one-third of the output voltage on the switch and the last 5 diodes. Such a feature is independent of the diode types and based of the structure of the diode-capacitor circuit. Additionally, their current does not surpass the input current. Based on this, Figure 7 presents the semiconductors' normalized voltage/current stress. The figure indicates that the maximum normalized voltage stress for the semiconductors is 0.33. Furthermore, the maximum current stress is associated with the switch, which has a normalized voltage stress below one. Moreover, most diodes show a voltage stress of less than 0.1. These values illustrate that the semiconductors operate within acceptable limits in the proposed topology. Figure 8 presents the same analysis for the boost converter. According to this figure, the maximum of the normalized voltage stress of the semiconductors is the same as the unity. This result is not desired and has been solved in the proposed topology. Notably, 70 % of the semiconductors in the proposed topology has a normalized current stress less than 40% in all duty cycle percentages. However, such a bold point is absent in the classic boost converter.

The simplified form of the inductors' current ripple according to the inductors' voltage equation and capacitors'

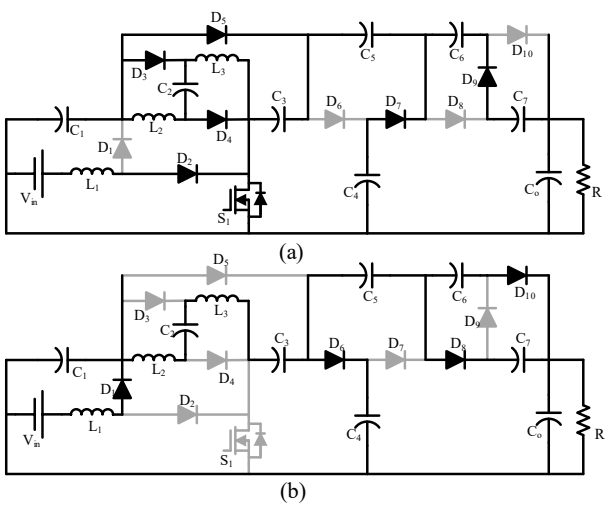

Fig. 5. Equivalent circuit of the proposed topology: (a) first mode, (b) second mode.

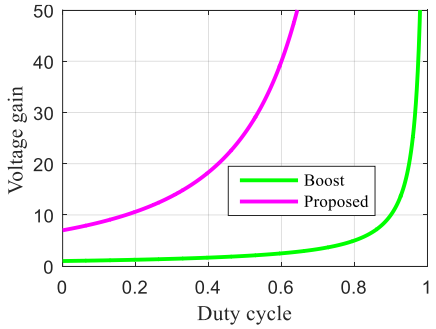

Fig. 6. Voltage gain comparison of the proposed topology and classic boost converter.

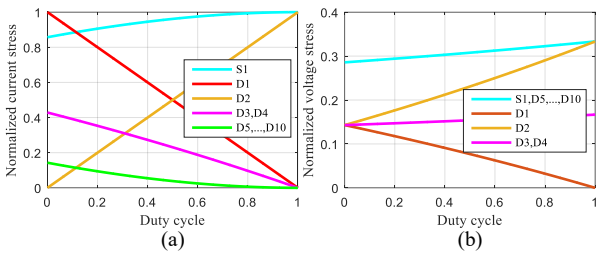

Fig. 7. Proposed converter's semiconductors normalized: (a) current stress, (b) voltage stress

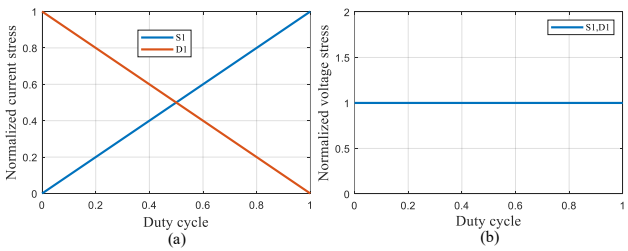

Fig. 8. Boost converter's semiconductors normalized: (a) current stress, (b) voltage stress

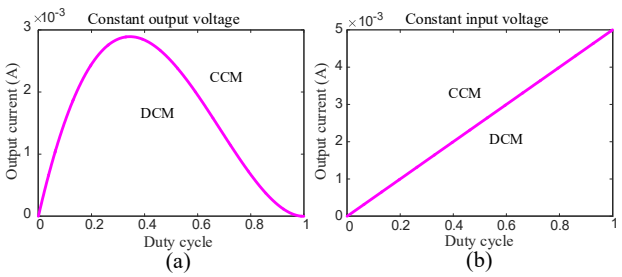

Fig. 9. The operational region of the converter between CCM and DCM is determined according to the output current and duty cycle, while (a) the output voltage is constant and (b) the input voltage is constant.

voltage ripple according to the capacitors' current equation are as follows:

$$\begin{cases} \Delta i_{L1}=\dfrac{DV_{in}}{L_1 f_s},\Delta i_{L2}=\dfrac{DV_{in}}{(1-D)L_2 f_s},\Delta i_{L3}=\dfrac{DV_{in}}{(1-D)L_3 f_s},\Delta v_{C1}=\dfrac{(4+2D)I_o}{(1-D)C_1 f_s},\Delta v_{C2}=\dfrac{3I_o}{C_2 f_s} \\ \Delta v_{C3}=\dfrac{3I_o}{C_3 f_s},\Delta v_{C4}=\dfrac{I_o}{C_4 f_s},\Delta v_{C5}=\dfrac{2I_o}{C_5 f_s},\Delta v_{C6}=\dfrac{I_o}{C_6 f_s},\Delta v_{C7}=\dfrac{I_o}{C_7 f_s},\Delta v_{Co}=\dfrac{(1+D)I_o}{C_o f_s} \end{cases} \quad (14)$$

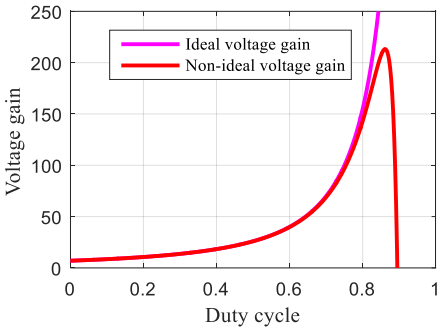

Fig. 10. Voltage gain comparison of the proposed topology in the ideal and non-ideal mode.

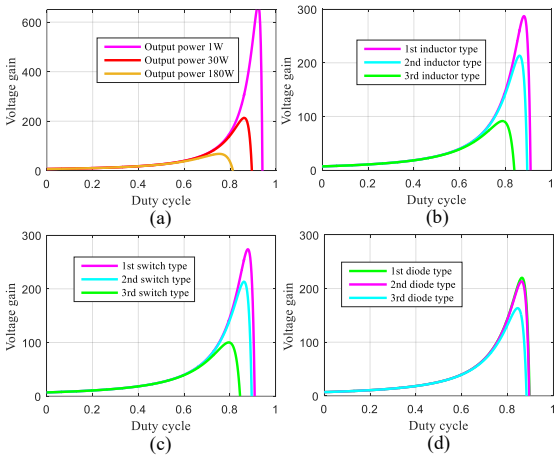

Fig. 11. Voltage gain of the proposed converter in the non-ideal mode according to the change of: (a) output power, (b) inductors' core type, (c) switch type, and (d) diodes' type.

III. Operating-Mode Analysis

The operation of the converter in the continuous and discontinuous conduction modes is not the same. Consequently, the effective factors in changing the continuous conduction mode to the discontinuous conduction mode are discussed. To maintain continuous conduction mode (CCM), the current ripple in the inductors must remain under twice the average current of each inductor. The value of the inductors directly influences their current ripple. Based on this criterion, the minimum inductor value necessary for sustaining CCM is as follows:

$$L_1 > \frac{D(1-D)^4 R}{2(7-D)^2 f_s}, L_2 > \frac{D(1-D)^2 R}{6(7-D) f_s}, L_3 > \frac{D(1-D)^2 R}{6(7-D) f_s} \quad (15)$$

Although the value of the inductors remains constant, their average current plays a crucial role in the converters' performance in CCM. To maintain CCM, the average current through the inductors needs to exceed half of their current ripple. This average current is determined by both the duty cycle and the average output current. Therefore, the converter's operational region between CCM and Discontinuous Conduction Mode (DCM), given constant input and output

voltages, can be represented as shown in Fig. 8, based on the equations provided below:

$$I_o = \frac{D(1-D)^2}{7-D}\frac{V_o}{6L_3 f_s} = D\frac{V_{in}}{6L_3 f_s} \tag{16}$$

All points above the presented curves are part of the CCM, while those below the curves refer to the DCM. The points on the curves represent the boundary condition.

The extracted voltage gain and average voltage of the capacitors in the DCM is as follows:

$$\begin{cases} V_{C1} = V_{C2} = V_{C3} = \dfrac{D+\delta}{\delta}V_{in} \\ V_{C4} = \dfrac{(D+\delta)(2D+3\delta)}{\delta^2}V_{in} \\ V_{C5} = V_{C6} = V_{C7} = 2\left(\dfrac{D+\delta}{\delta}\right)^2 V_{in} \\ \dfrac{V_o}{V_{in}} = \dfrac{(D+\delta)(6D+7\delta)}{\delta^2} \end{cases} \tag{17}$$

In this equation, D refers to the ratio of the activation time of the switch over the whole period of switching and δ refers to the ratio of the activation time of the last diode over the whole switching time period.

IV. Small Signal Analysis

In this section, the state space equations are discussed to extract a suitable compensator for the proposed topology in the closed-loop system. In order to analyze the stability of the proposed converter, the space state matrices have been presented in this section. It is good to note that the independent inductors are two as well as the independent capacitors. According to this concept, the space state matrices are as follows:

$$\frac{d}{dt}\begin{pmatrix} i_{L1} \\ i_{L2} \\ v_{C1} \\ v_{Co} \end{pmatrix} = \begin{pmatrix} 0 & 0 & \dfrac{D-1}{L_1} & 0 \\ 0 & 0 & \dfrac{3-D}{2L_2} & \dfrac{D-1}{3L_2} \\ \dfrac{1-D}{3C_1} & \dfrac{D-3}{3C_1} & 0 & \dfrac{-2}{3RC_1} \\ 0 & \dfrac{1-D}{2C_o} & 0 & \dfrac{-1}{2RC_o} \end{pmatrix}\begin{pmatrix} i_{L1} \\ i_{L2} \\ v_{C1} \\ v_{Co} \end{pmatrix} + \begin{pmatrix} \dfrac{V_{C1}}{L_1} \\ \dfrac{\frac{1}{3}V_{CO} - \frac{1}{2}V_{C1}}{L_2} \\ \dfrac{-I_{L1}+I_{L2}+4I_o}{C_1} \\ \dfrac{-I_{L2}}{C_o} \end{pmatrix} d$$

$$y = \begin{pmatrix} 0 & 0 & 0 & 1 \end{pmatrix}\begin{pmatrix} i_{L1} \\ i_{L2} \\ v_{C1} \\ v_{Co} \end{pmatrix}$$

According to these equations and using MATLAB, the bode diagram of the proposed topology have been extracted and presented in Fig. 12(a). It can be understood that the phase and gain margins are negative which stands from the non-minimum phase behavior of the proposed topology. Also, their multiplication is positive which shows the stability. In order to solve the non-minimum phase behavior, a suitable compensator must be designed. Using SISOTOOL of MATLAB leads to a compensator as follows:

$$G_C(s) = \frac{0.194}{s}$$

Applying this compensator to the plant leads to the positive phase/gain margins of the proposed topology according to Fig. 12(b).

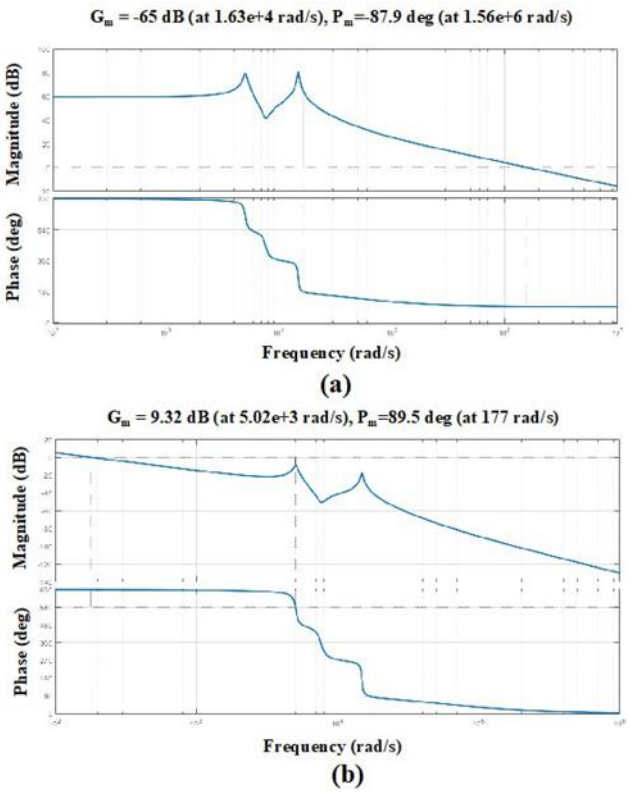

Fig. 12. Bode Diagram of the proposed topology: (a) before compensating (b) after compensating.

V. Performance Evaluation

A. Non-Ideal Voltage Gain

This sub-section considers the non-ideal analysis of the converter. The voltage gain extracted in the previous section corresponds to an ideal scenario where components are free from parasitic elements. However, this relationship cannot accurately forecast voltage gain behavior under varying conditions and differing component qualities. The parasitic elements of the inductors, switch, and diodes (r_L, r_S, and r_D) were considered to derive a more precise expression for non-ideal voltage gain. The simplified voltage gain relationship for the converter in non-ideal mode is as follows:

$$\frac{V_o}{V_{in}} = \frac{7-D}{(1-D)^2}\left(1 - \frac{r_L}{R}\frac{7-D}{(1-D)^4} - \frac{r_S}{R}\frac{D(7-D)}{(1-D)^4} - \frac{r_D}{R}\frac{7-D}{(1-D)^3}\right) \tag{18}$$

The extracted relation reveals additional components that are missing in the ideal mode's corresponding relation. These components contribute to the variations in voltage gains between the ideal and non-ideal modes. Figure 10 illustrates

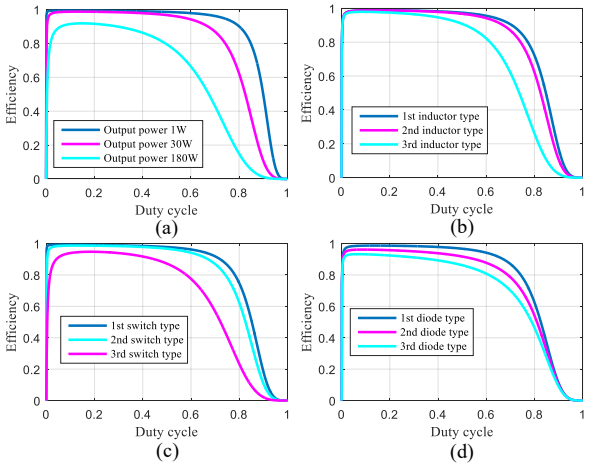

Fig. 13. Efficiency of the proposed converter in the non-ideal mode according to the change of: (a) output power, (b) inductors' core type, (c) switch type, and (d) diodes' type.

the voltage gain of the proposed topology in both the ideal and non-ideal component modes. Notably, the voltage gain of the converter peaks in the non-ideal mode, a feature absenting in its ideal model counterpart. The equation derived for the ideal mode indicates that higher duty cycle percentages correlate with increased voltage gain values. Conversely, the equation for the non-ideal mode does not support this expectation. Another significant observation from the figure is that both curves align at low duty cycle percentages, suggesting that higher voltage gains occur at lower duty cycles in both ideal and non-ideal conditions. Thus, the converter should be designed to deliver higher voltage gains at low-duty cycle percentages. Importantly, voltage gain characteristics vary under different conditions. Figure 11 demonstrates how voltage gain behaves based on output power and component quality variations. Figure 11(a) shows that lower output powers allow for a broader range of alignment between ideal and non-ideal voltage gains. Figures 11(b)-(d) illustrate that the sensitivity of voltage gain in the non-ideal mode remains consistent regardless of changes in inductor and switch types. Additionally, the sensitivity of voltage gain regarding diode-type changes is lower than the others.

B. *Efficiency*

Based on the analyzed relationships between the average current of inductors and the average voltage of capacitors, the input and output powers are equal, assuming ideal conditions for circuit components. However, in practical scenarios, the components are imperfect, resulting in lower output power than input power due to associated losses. This study accounts for the conduction losses of inductors (P_L), switches (P_{SC}), and diodes (P_D), while disregarding frequency losses related to low switching frequencies. The following is a summary of these simplified losses:

$$\begin{cases} P_L=\sum_{k=1}^{3} r_{L_k} i^2_{L_k}=\dfrac{67-50D+19D^2}{(1-D)^4}\dfrac{r_L}{R}P_o, P_{SC}=r_S i^2_S=\dfrac{\left(6+D-D^2\right)^2}{D(1-D)^4}\dfrac{r_S}{R}P_o \\ P_D=\sum_{k=1}^{3} V_{DF_k} i_{D_k}=\dfrac{18-18D+6D^2}{(1-D)^2}V_{DF}I_o, \eta=\dfrac{P_o}{P_o+P_L+P_{SC}+P_D} \\ Max\left\{r_{L_k}\right\}=r_L, Max\left\{V_{DF_k}\right\}=V_{DF} \end{cases} \quad (19)$$

The equations indicate that efficiency behavior is influenced by output power, component quality and duty cycle percentage. Figure 13 illustrates efficiency changes based on variations in the output power and the types of components. The most significant impact arises from changes in the output power. In the second stage, the type of switch holds the most essential effect. Following this, the third stage involves changes in diode types, while the least influence comes from changes in the inductor core type. Significantly, altering the diode type strongly affects the various component changes, even at low duty cycle percentages.

C. *Comparative Analysis*

In this sub-section, the bold features and achievements of the proposed topology are compared with the recently suggested converters. One of the outstanding features of the proposed topology is the high gain of voltage. As outlined in previous sections, this gain is achieved by integrating quadratic converters and voltage lift circuits. As a result, there's no need to utilize high-duty cycle to attain a substantial voltage gain. Figure 14 compares voltage gains among the proposed topology and the converters introduced in references [5]-[47] which indicates that the voltage gain from the proposed topology exceeds that of [5]-[47] across all duty cycle percentages including lower and higher duty cycles. This comparison highlights the considerable superiority of the proposed topology over currently suggested converters. Increasing the component number is achieved by providing a high value of the voltage gain. Therefore, the concept of the voltage gain density must be defined to see the voltage gain and the components number increase simultaneously. Figure 15(a) illustrates the voltage gain density over the whole number of components. According to this figure, the proposed topology in this study has the highest voltage gain density in all duty cycle percentages. Notably, such superiority is repeated in the voltage gain density over the inductor number (Fig. 15(b)), capacitor number (Fig15(c)), and switch number (Fig. 15(d)). In the case of voltage gain density over the diodes' number, the proposed topology is the second top converter among the recently proposed converters. Table 1 compares the number of components, voltage gain and the maximum value of the switch and diode voltage stress of the proposed topology with presented converters in [9]– [22]. According to this table, the proposed topology has the highest value of voltage gain. Additionally, the maximum voltage stress of the switch and diodes are much less than the output voltage. Notably, the

expressed data in column 1 to column 6 of this table, have been used in Fig. 15. To have a better view from the advantage of the proposed topology, the expressed voltage stresses in the seventh and eighth columns have been normalized by the expressed output voltages in the sixth column and relevant results have been presented in Fig. 16. According to Fig. 16 the proposed topology has the lowest normalized voltage stress. In other words, beside the high voltage gain of the proposed topology, the highest voltage stress of the semiconductors in this converter, is less than the output voltage with the highest difference. Such an advantage makes this converter suitable for high DC voltage applications.

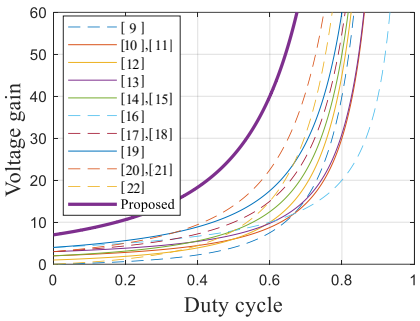

Fig. 14. Voltage gain comparing of the proposed topology with the presented topologies in [9]-[22].

TABLE 1 THE COMPARISON OF PROPOSED CONVERTER WITH THE STATE-OF-THE-ART CONVERTERS

	L	C	S	D	ALL	Voltage gain	Max (V_S)	Max (V_D)
[9]	2	3	2	3	10	$\frac{2D}{(1-D)^2}V_{in}$	$\frac{1+D}{(1-D)^2}V_{in}$	$\frac{1+D}{(1-D)^2}V_{in}$
[10]	2	3	1	4	10	$\frac{2-D}{(1-D)^2}V_{in}$	$\frac{V_{in}}{(1-D)^2}$	$\frac{V_{in}}{(1-D)^2}$
[11]	2	3	2	3	10	$\frac{2-D}{(1-D)^2}V_{in}$	$\frac{2-D}{(1-D)^2}V_{in}$	$\frac{2-D}{(1-D)^2}V_{in}$
[12]	2	3	2	3	10	$\frac{1+D}{(1-D)^2}V_{in}$	$\frac{1+D}{(1-D)^2}V_{in}$	$\frac{2}{(1-D)^2}V_{in}$
[13]	2	3	2	3	10	$\frac{3-3D+D^2}{(1-D)^2}V_{in}$	$\frac{V_{in}}{(1-D)^2}$	$\frac{2-D}{(1-D)^2}V_{in}$
[14]	3	5	1	5	14	$\frac{2}{(1-D)^2}V_{in}$	$\frac{V_{in}}{(1-D)^2}$	$\frac{V_{in}}{(1-D)^2}$
[15]	2	4	1	5	12	$\frac{2}{(1-D)^2}V_{in}$	$\frac{V_{in}}{(1-D)^2}$	$\frac{V_{in}}{(1-D)^2}$
[16]	2	4	2	4	12	$\frac{4}{(1-D)^2}V_{in}$	$\frac{2}{(1-D)^2}V_{in}$	$\frac{2}{(1-D)^2}V_{in}$
[17]	3	6	1	6	16	$\frac{3-D}{(1-D)^2}V_{in}$	$\frac{V_{in}}{(1-D)^2}$	$\frac{V_{in}}{(1-D)^2}$
[18]	3	4	1	6	14	$\frac{3-D}{(1-D)^2}V_{in}$	$\frac{2}{(1-D)^2}V_{in}$	$\frac{2}{(1-D)^2}V_{in}$
[19]	3	4	1	6	14	$\frac{2(2-D)}{(1-D)^2}V_{in}$	$\frac{2}{(1-D)^2}V_{in}$	$\frac{2}{(1-D)^2}V_{in}$
[20]	2	5	2	5	14	$\frac{3+D}{(1-D)^2}V_{in}$	$\frac{1+D}{(1-D)^2}V_{in}$	$\frac{2}{(1-D)^2}V_{in}$
[21]	2	5	2	5	14	$\frac{3+D}{(1-D)^2}V_{in}$	$\frac{1+D}{(1-D)^2}V_{in}$	$\frac{2}{(1-D)^2}V_{in}$
[22]	4	6	2	7	19	$\frac{4D}{(1-D)^2}V_{in}$	$\frac{4}{(1-D)^2}V_{in}$	$\frac{4}{(1-D)^2}V_{in}$
Proposed	3	8	1	10	22	$\frac{7-D}{(1-D)^2}V_{in}$	$\frac{2}{(1-D)^2}V_{in}$	$\frac{2}{(1-D)^2}V_{in}$

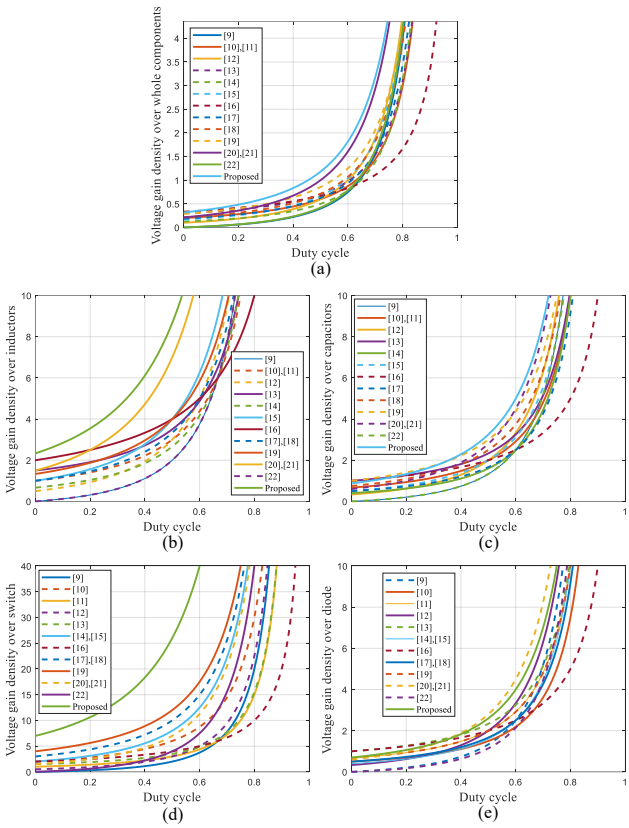

Fig. 15. Voltage gain density over:
(a) whole components, (b) inductors' number, (c) capacitors' number, (d) switches' number and (e) diodes' number.

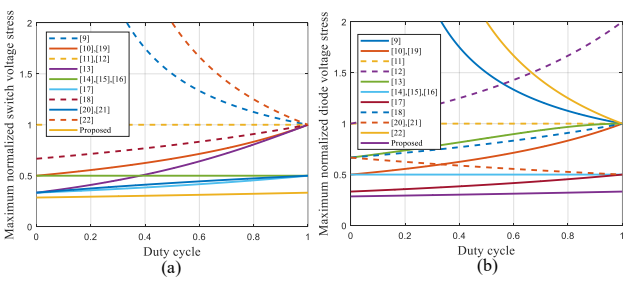

Fig. 16. Comparing the maximum normalized voltage stress of: (a) switches, (b) diodes.

VI. Application Case Studies

This section explains the suitable applications in which the proposed topology can be employed.

A. HID Lamps

According to the extracted voltage gain in the second section, providing a high voltage gain by the low duty cycle percentage is one of the bold achievements of the proposed topology. Such a high voltage gain can be used in applications such as HID lamps and Hydrogen extraction. HID lamps require a high voltage at their input side with a negligible input current. However, the accessible batteries in cars can provide a low voltage (12V) and high current. Consequently, a high-gain DC-DC converter (same as the proposed topology) can be

used according to Fig. 17 to provide the required input voltage of the HID lamps.

B. Hydrogen Extraction

It is good to note that the proposed topology can be used to electrolyze the water to extract the hydrogen as a clean fuel. Such a high voltage gain DC-DC converter can

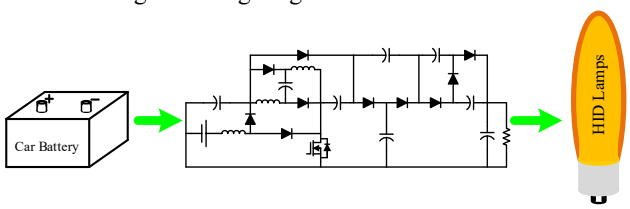

Fig. 17. Application of the proposed topology in HID lamps.

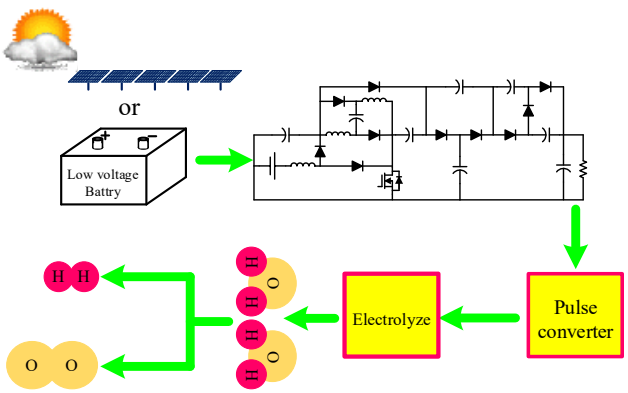

Fig. 18. Application of the proposed topology in hydrogen extraction from water electrolyzer.

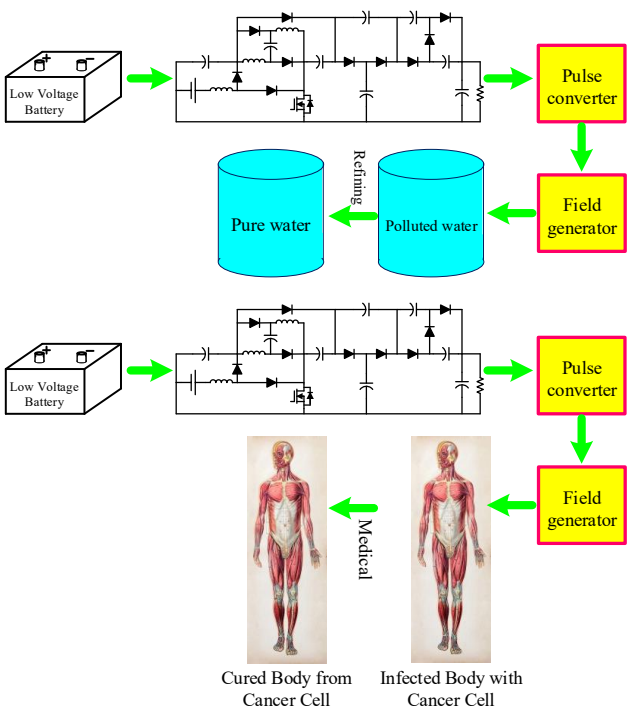

Fig. 19. Application of the proposed topology in medical procedures.

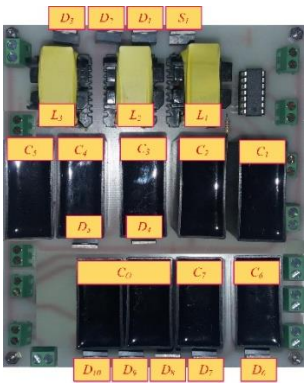

Fig. 20. The prototype of the proposed converter.

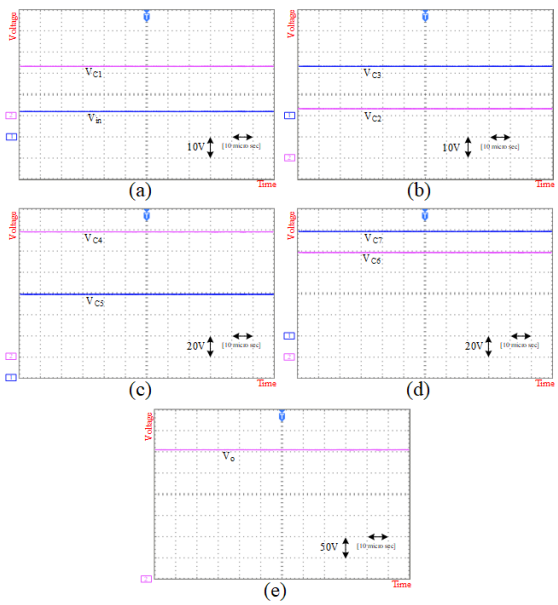

Fig. 21. Experimental outcomes.

increase the output voltage of the battery or photovoltaic panels to make it suitable for the input side of the pulsed power converter. At the next step, the provided pulsed waveform can be applied to the electrodes, which are surrounded by water and hydrogen and next oxygen can be produced and collected by membranes. Figure 18 presents the symbolic presentation of the mentioned procedure in water refinery applications.

C. Medical Procedures

With the aforementioned capability of this converter, beside the pulsed power converter, it can be used in medical procedures technologies. Same as the mentioned application, the same procedure can be employed in the medical applications in the same procedure as Fig. 19.

VII. Experimental Results (Prototype Measurement vs. Simulation)

This section discusses the validity of the extracted relations based on the experimental results. The results are obtained

using the prototype. To create the prototype, it is essential to identify the circuit components. The identification of these components involves defining their current and voltage characteristics. To establish the voltage and current characteristics of the components, one must specify the input voltage, output current and duty cycle. In this study, the parameters are defined in Table 2.

The input voltage value is the same as the car batteries' voltage. The converter's output current is determined according to the input current of the HID lamps. Considering these values and the current/voltage stress of the semiconductors is obtained as Table 3.

TABLE 2 DEFINED PARAMETERS

ITEM	PARAMETER	VALUE
1	V_{in}	12V
2	I_o	0.01A
3	D	0.5

TABLE 3 THE AVERAGE VALUES FOR INDUCTORS, CAPACITORS AND SEMI-CONDUCTORS

ITEM	VALUE	ITEM	VALUE	ITEM	VALUE
I_{L1}	260mA	V_o	312V	V_{D1}	24V
I_{L2}	60mA	V_{C1}	24V	V_{D2}	72V
I_{L3}	60mA	V_{C2}	24V	V_{D3}	48V
I_{S1}	250mA	V_{C3}	24V	V_{D4}	48V
I_{D1}	130mA	V_{C4}	120V	V_{D5} ... V_{D10}	96V
I_{D2}	130mA	V_{C5}	96V	V_S	96V
I_{D3}	60mA	V_{C6}	96V		
I_{D4}	60mA	V_{C7}	96V		
I_{D5}...I_{D10}	10 mA				

TABLE 4 MINIMUM VALUES FOR CAPACITORS AND INDUCTORS

ITEM	VALUE	ITEM	VALUE
L_1	1.5mH	C_3	500nF
L_2	13.3mH	C_4	33.3nF
L_3	13.3mH	C_5	83.3nF
C_o	19.2nF	C_6	41.6nF
C_1	1600nF	C_7	41.6nF
C_2	500nF		

Based on the voltage-current stress of the semiconductors, IRF640 may replace the switch, while FES8GT can be utilized for the diodes. Taking into account 30 percent current ripple for the inductors and 5 percent voltage ripple for the capacitors, the minimum values for the inductors and capacitors are determined as Table 4.

EC-type inductor cores are ideal for this project as they readily provide the required inductances. Additionally, MKT capacitors are perfect for high-frequency applications due to their negligible Equivalent Series Resistance (ESR) and excellent performance.

According to the expressed concepts, the prototype of the proposed topology has been displayed in Fig. 20. The extracted experimental results have been presented in Figs. 21-23. The presented waveforms in Fig. 21 are capacitors and input source voltage waveforms. The current waveform of the inductors, semiconductors and the load have been presented in Fig. 22. The voltage waveforms of the semiconductors have been presented in Fig. 23. Comparing the corresponding waveforms with the expressed values in Table 3, shows their compatibility and also validates the design criteria. Moreover, comparing the highest voltage stress of the semiconductors with the output voltage, demonstrates that the semiconductors' highest voltage stress is one-third of the output voltage. although in the boost converter, using the expressed relations in the second section, the average voltage of the capacitors, the average current of the inductors the highest voltage stress is the same as the output voltage.

Fig. 24 presents the prototype of the boost converter and Fig. 25 demonstrates the voltage waveforms of the capacitor and semiconductors in the boost converter.

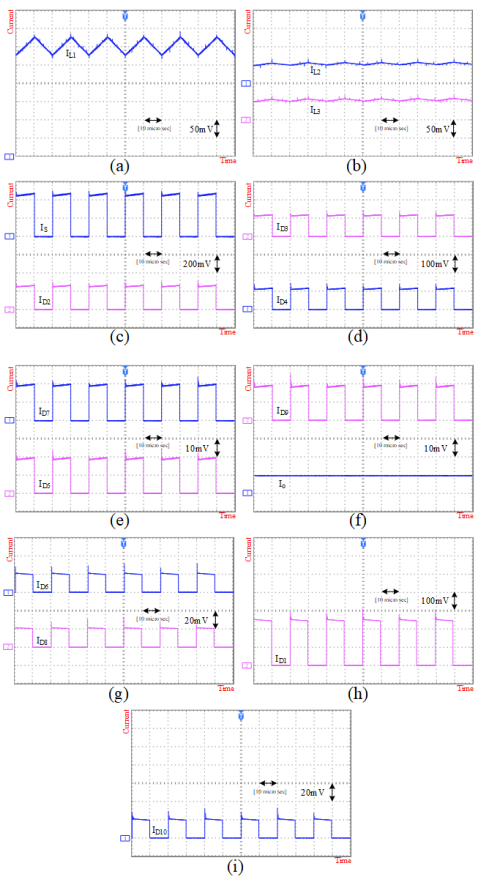

Fig. 22. Experimental outcomes.

Fig. 26 presents the extracted voltage gain of the converter according to the experimental results and the theoretical relation of the voltage gain. According to this figure, while the duty cycle is less than 70%, both curves are compatible with each other and their differences are negligible. While the duty cycle becomes more than 70%, the difference of the curves increases. The reason behind this is due to the employed approximations during the non-ideal voltage gain relation calculations. Notably, this region is not suggested due to the

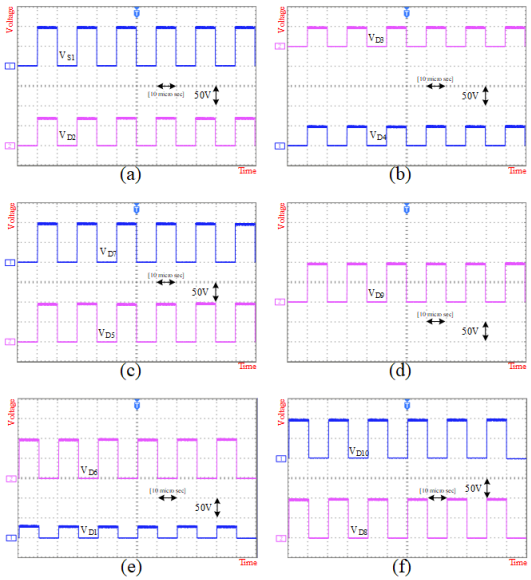

Fig. 23. Experimental outcomes.

low value of efficiency in this region. Fig. 27 presents the efficiency of the converter in a constant duty cycle (50%) and the input/output voltages. In this procedure the load value is changing and causes the power to change. According to this figure, the extracted efficiency is more than 90% at the reported output powers. It is notable that the extracted curve corresponds to high output voltage and low output current conditions. The reason upon the selection of such a condition lies in the application of this converter, which requires high voltage and low current. Moreover, the extracted results can be improved by utilization of high-quality and expensive components.

Fig. 28 presents the behavior of the output voltage according to the change in the load during a constant input voltage. According to this figure, during the load changing, the output voltage keeps its value and does not see any change. Such a result shows the accuracy of the designed controller in the small signal analysis. Consequently, the output voltage is robust according to the change in the load.

VIII. Conclusion

In this study, a non-isolated DC-DC converter was introduced. This topology provided a 26 times voltage gain with a 50 percent duty cycle by employing only one switch. This achievement showed the capability of the proposed topology in providing high voltage gain. Additionally, the benefits of traditional step-up converters were maintained while addressing their shortcomings. The high voltage gain and minimizing the voltage stress on the semiconductors, with the maximum voltage stress being one-third of the output voltage, were achieved. The experimental results were gathered and compared against design parameters, confirming the compatibility of all theoretical models and principles. The extracted compatibility between results and theoretical relations showed that the proposed topology can be employed with the mentioned application and achieves acceptable outcomes.

In order to reduce the EMI and electromagnetic compatibility (EMC), zero voltage switching (ZVS) and zero current switching (ZCS) techniques can be done. In the future study, the restructuring of the proposed topology with ZVC and ZCS will be considered. Moreover, the prototyping considerations such as Minimizing High di/dt Loops, Ground Plane Designing, putting noisy components (MOSFETs, diodes) away from sensitive analog circuits and placing ceramic capacitors close to switching devices to suppress high-frequency noise can be done. Furthermore, filtering techniques and shielding and grounding methods must be done with a detailed attention.

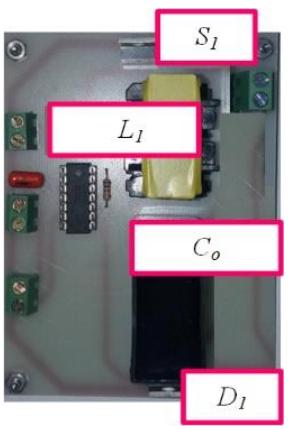

Fig. 24. Conventional boost converter.

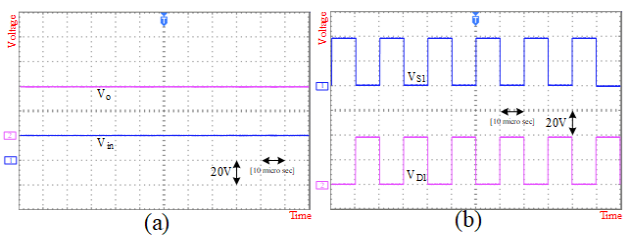

Fig. 25. Experimental results of the boost converter: (a) output voltage and input voltage, (b) Voltage waveforms of the semiconductors.

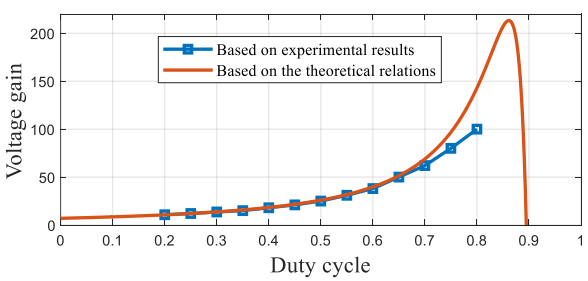

Fig. 26. Voltage gain of the converter according to the experimental results.

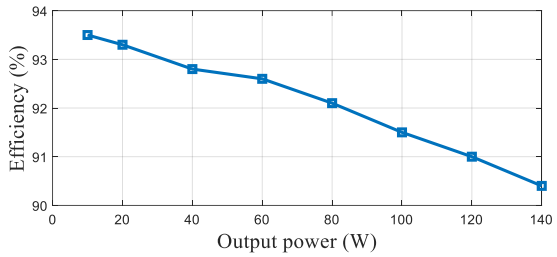

Fig. 27. Efficiency of the converter according to the experimental results.

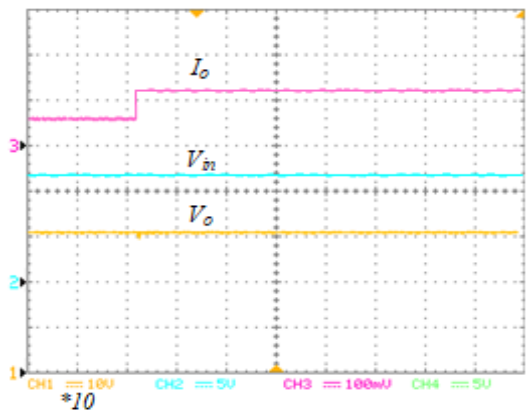

Fig. 28. Dynamic behavior of the proposed topology.

References

[1] H. Gholizadeh, M. Dehghan, R. S. Shahrivar, M. H. Samimi, and M. Ghassemi, "A Non-Isolated Quadratic DC-DC Converter Improved by Voltage-Lift Technique Suitable for High-Voltage Applications," in *IEEE Access*, vol. 12, pp.158292-158310, 2024, https://doi.org/10.1109/ACCESS.2024.3484667.

[2] H. Gholizadeh, S. A. Gorji, and D. Sera, "A Family of High-Gain Single-Switch DC-DC Converters for High-Intensity Discharge Lamps," in *IEEE Open Journal of Power Electronics*, vol. 5, pp. 1534-1561, 2024, https://doi.org/10.1109/OJPEL.2024.3462715.

[3] H. Gholizadeh, R. S. Shahrivar, S. Amini, and T. Rahimi," An Improved Cascaded Boost Converter with an Ultra-High Voltage Gain Suitable for Dielectric Quality Tests," *Energies* 2024, *17*, 3861. https://doi.org/10.3390/en17153861.

[4] S. A. Gorji and H. Gholizadeh, "A Modified Positive Output Super-Lift Luo DC-DC Converter with Improved Voltage Boost Ability," *2022 5th International Conference on Renewable Energy and Power Engineering (REPE)*, Beijing, China, 2022, pp. 282-286, https://doi.org/10.1109/REPE55559.2022.9949453.

[5] H. Gholizadeh, S. A. Gorji, and D. Sera, "A Quadratic Buck-Boost Converter With Continuous Input and Output Currents," in *IEEE Access*, vol. 11, pp. 22376-22393, 2023, https://doi.org/10.1109/ACCESS.2023.3253102.

[6] A. taheri, and N. Asgari, "Sliding Mode Control of LLC Resonant DC-DC Converter for Wide output voltage Range in Battery Charging Applications, " *International Journal of Industrial Electronics Control and Optimization*, (2019), 127-136. https://doi.org/10.22111/ieco.2018.27333.1096.

[7] S. Moosavi, " Efficiency improvement and inrush current reduction in a non-isolated DC-DC converter," *International Journal of Industrial Electronics Control and Optimization*, *2*(2), (2019), 137-144. https://doi.org/10.22111/ieco.2018.25890.1059.

[8] M. Elmi, M. R. Banaei, and H. Afsharirad, "Study on a Non-Isolated High Step-Up SEPIC-Based DC-DC Converter with Continuous Input Current for Photovoltaic Applications," *International Journal of Industrial Electronics Control and Optimization*, *8*(1), (2019), 95-104 https://doi.org/10.22111/ieco.2024.48587.1558.

[9] A. Sarikhani, B. Allahverdinejad and M. Hamzeh, "A Nonisolated Buck–Boost DC–DC Converter With Continuous Input Current for Photovoltaic Applications," in *IEEE Journal of Emerging and Selected Topics in Power Electronics*, vol. 9, no. 1, pp. 804-811, Feb. 2021. https://doi.org/10.1109/JESTPE.2020.2985844.

[10] H. Gholizadeh, R. S. Shahrivar, M. R. Hashemi, E. Afjei and S. A. Gorji, "Design and Implementation a Single-Switch Step-Up DC-DC Converter Based on Cascaded Boost and Luo Converters," *Energies* 2021, *14*, 3584. https://doi.org/10.3390/en14123584.

[11] S. Mahdizadeh, H. Gholizadeh, and S. A. Gorji, "A Power Converter Based on the Combination of Cuk and Positive Output Super Lift Lou Converters: Circuit Analysis, Simulation and Experimental Validation," *IEEE Access*, vol. 10, pp. 52899-52911, 2022. https://doi.org/10.1109/ACCESS.2022.3175892.

[12] S. V. K. Naresh, S. Peddapati, and M. L. Alghaythi, "Non-Isolated High Gain Quadratic Boost Converter Based on Inductor's Asymmetric Input Voltage," *IEEE Access*, vol. 9, pp. 162108-162121, 2021. https://doi.org/10.1109/ACCESS.2021.3133581.

[13] K. Varesi, N. Hassanpour, and S. Saeidabadi, "Novel high step-up DC–DC converter with increased voltage gain per devices and continuous input current suitable for DC microgrid applications," *Int J Circ Theor Appl*. 2020; 48: 18201837. https://doi.org/10.1002/cta.2804.

[14] A. Meftahpour, H. Ehssan, H. Gholizadeh and M. Samimi, "A Boost and Luo Based Non-isolated DC-DC Converter Suitable for DC Link of High Voltage Applications," *2024 32nd International Conference on Electrical Engineering (ICEE)*, Tehran, Iran, Islamic Republic of, 2024, pp. 1-6. https://doi.org/10.1109/ICEE63041.2024.10667738.

[15] S. Miao, F. Wang, and X. Ma, "A New Transformerless Buck–Boost Converter With Positive Output Voltage," in *IEEE Transactions on Industrial Electronics*, vol. 63, no. 5, pp. 2965-2975, May 2016. https://doi.org/10.1109/TIE.2016.2518118.

[16] S. Sadaf, N. Al-Emadi, P. K. Maroti, and A. Iqbal, "A New High Gain Active Switched Network-Based Boost Converter for DC Microgrid Application," in *IEEE Access*, vol. 9, pp. 68253-68265, 2021. https://doi.org/10.1109/ACCESS.2021.3077055.

[17] T. Rahimi, L. Ding, H. Gholizadeh, R. S. Shahrivar and R. Faraji, "An Ultra High Step-Up DC–DC Converter Based on the Boost, Luo and Voltage Doubler Structure: Mathematical Expression, Simulation, and Experimental," in *IEEE Access*, vol. 9, pp. 132011-132024, 2021. https://doi.org/10.1109/ACCESS.2021.3115259.

[18] H. Gholizadeh, and L. Ben-Brahim, "A New Non-Isolated High-Gain Single-Switch DC–DC Converter Topology with a Continuous Input Current," *Electronics* 2022, *11*, 2900. https://doi.org/10.3390/electronics11182900.

[19] S. Mahdizadeh, H. Gholizadeh, R. Shahrivar, E. Afjei, and A. Mosallanejad, "An ultra high step-up DC-DC converter based on VMC, POSLLC, and boost converter," *IET Power Electron*. vol. 15, pp. 901–918 (2022). https://doi.org/10.1049/pel2.12277.

[20] Y. Zhang, H. Liu, J. Li, M. Sumner and C. Xia, "DC–DC Boost Converter With a Wide Input Range and High Voltage Gain for Fuel Cell Vehicles," *IEEE Transactions on Power Electronics*, vol. 34, no. 5, pp. 4100-4111, May 2019, https://doi.org/10.1109/TPEL.2018.2858443.

[21] H. Gholizadeh, S. A. Gorji, A. Ektesabi and D. Sera, "A Family of Transformerless Step-Up DC-DC Converters: Analysis, Comparison and Experiment," *2024 IEEE Kansas Power and Energy Conference (KPEC)*, Manhattan, KS, USA, 2024, pp. 1-6, https://doi.org/10.1109/KPEC61529.2024.10676196.

[22] H. Gholizadeh, and S. Hasanpour, "A New Quadratic CUK-Based Step-Up DC/DC Converter Without Right Hand Plane Zero, " *International Journal of Industrial Electronics Control and Optimization*, 2024 https://doi.org/10.22111/ieco.2024.48683.1565.

Reza Hazratian received his B.S. and M.Sc. degrees in power electrical engineering from the Islamic Azad University of Tehran, Iran in 2010 and 2013, respectively. He is currently working toward obtaining Ph.D. degree at the faculty of electrical and electronics engineering at Shahid Beheshti University, Tehran, Iran. His main fields of interest include power electronics, predictive modeling, and deep learning.

Ebrahim S. Afjei received the B.S. and M.S. degrees in electrical engineering from The University of Texas at Austin, Austin, TX, USA, in 1984 and 1986, respectively, and the Ph.D. degree from New Mexico State University, Las Cruces, NM, USA, in 1991. He is currently Professor at the Department of Electrical Engineering, Shahid Beheshti University, Tehran, Iran. His current research interests include switched reluctance motor drives and power electronics.

IECO

This page intentionally left blank.

International Journal Of
Industrial Electronics Control and Optimization
Print ISSN: 3517-2645
Online ISSN: 3568-2645
Homepage: https://ieco.usb.ac.ir/

Approximate Optimal Control Governed by some Parabolic Equations via Laguerre Polynomials Collocation Approach

Yunes Mohamadi | Maryam Alipour | Akbar Hashemi Borzabadi

University of Sistan and Baluchestan, Zahedan, Iran.[1]
Faculty of Mathematics, University of Sistan and Baluchestan, Zahedan, Iran.[2]
Faculty of Applied Mathematics, University of Science and Technology of Mazandaran, Behshahr, Iran.[2]
Corresponding author's email: m.alipour@math.usb.ac.ir

Article Info

Article type:
Research Article

Article history:
Received: 21-February-2025
Received in revised form: 25-April-2025
Accepted: 10-May-2025
Published online: 21-March-2026

Keywords:
Collocation points,
Convergence analysis,
Laguerre polynomials,
Optimal control problems,
Spectral method,

ABSTRACT

The present paper proposes a novel numerical approach for approximating solutions to optimal control problems with parabolic constraints. Utilizing Laguerre polynomials as a novel basis set, a method was developed to address a class of this problem. The employment of these basis functions in conjunction with the collocation method facilitates the transformation of optimal control problems governed by parabolic constraints into a system of nonlinear algebraic equations. The present study proposes an efficient discretization and transformation of complex optimal control problems governed by parabolic equations into lower-dimensional algebraic systems by leveraging the unique properties of Laguerre polynomials. Convergence analysis has been demonstrated to ascertain the optimal value approximations of the proposed method. In order to provide a comprehensive illustration of the reliability and applicability of the proposed method, two illustrative examples are presented. The findings underscore the efficacy and precision of the implemented methodology. This work makes a significant contribution to the field by offering a robust framework for solving complex parabolic control problems, thereby demonstrating the potential of spectral methods in the context of optimal control theory.

I. Introduction

Recent advances in the theory and numerical analysis of optimal control problems governed by parabolic partial differential equations have significantly enhanced the capacity to model and solve complex systems in science and engineering. Parabolic partial differential equations, including the heat equation, are instrumental in the simulation of dynamic processes, such as the distribution of temperature, diffusion phenomena, and energy transport. The utilization of these equations is pervasive, encompassing diverse disciplines such as physics, biology, and engineering. Their application lies in the comprehension of imprecise dynamics, chaotic systems, and tangible phenomena in the real world, including fluid flow and chemical reactions [1, 8]. The optimal control of such systems entails the formulation of strategies that enhance performance while adhering to the constraints imposed by the governing equations and boundary conditions.

The study of optimal control problems for parabolic equations has introduced innovative approaches to addressing challenges related to the minimization or maximization of cost functionals. For instance, Casas [1] investigated semilinear parabolic equations with memory effects, deriving first and second order necessary optimality conditions and analyzing associated inverse systems. Similarly, Na [8] examined degenerate parabolic equations, highlighting their applications in economics and physical modeling. These studies emphasize theoretical advancements in understanding the behavior of parabolic systems within the framework of optimal control. Führer proposed a space-time least-squares finite element method for distributed optimal control problems [2]. In addition, in [12] employed algorithms based on the Pontryagin maximum principle for semilinear parabolic equations and demonstrated their convergence and efficiency in solving such problems. Other approaches, such as the Ritz method combined with Legendre polynomial bases, were presented

by Mamehrashi et al. in [6]. Similarly, Hosseini and co-authors utilized block-pulse Legendre functions to solve optimal control problems subject to parabolic differential equation constraints [4]. Latifi [5] applied the Jacobi-Gauss-Radau Lagrangian method, discretizing variables to create a parametric framework for solving parThe paucityabolic optimal control problems. In [9] modified variational iteration method (MVIM) to solve nonlinear optimal control problems more efficiently than the standard VIM by eliminating extra computations. The approach first transforms the optimal control problem into a two-point boundary value problem using Pontryagin's maximum principle and then applies MVIM with a Taylor series expansion for nonlinear terms. For additional numerical approaches see [10, 11].

The paucity of analytical solutions for optimal control problems with parabolic constraints (OCPPC) necessitates the development of robust numerical and approximate methods. This paper introduces a novel approach utilizing Laguerre polynomials, which represents a significant advancement in addressing these complex challenges. By leveraging a spectral method based on collocation points, this technique reduces computational complexity and enhances the accuracy of approximating solutions. Moreover, it has been demonstrated to expand analytical and practical capabilities, providing a comprehensive framework for tackling optimal control problems. The innovative application of Laguerre polynomials in this context signifies a pioneering effort within the field, addressing a critical gap in the extant literature and proposing novel avenues for research and application in optimal control theory. The objective of this work is to make a substantial contribution to the advancement of knowledge in the domain of parabolic optimal control problems, thereby laying the foundation for future progress in this field

The present study proposes an efficient discretization and transformation of complex optimal control problems governed by parabolic equations into lower-dimensional algebraic systems by leveraging the unique properties of Laguerre polynomials. This approach not only enhances the performance and accuracy of existing numerical methods but also opens promising avenues for future research in optimal control. The present study focuses on minimizing a cost functional that is dependent on the state variable $z(x,t)$, and the control input $u(x,t)$. These variables are governed by a partial differential equation (PDE) involving second-order spatial derivatives, as well as the direct influence of the control input. The cost functional, which has been defined, serves as a critical component in formulating the optimal control problem. This ensures that the proposed method effectively addresses the challenges posed by parabolic constraints. The following structure has been employed in the composition of the present manuscript: In Section II, the mathematical formulation and problem setup are presented. The Section III of this text is devoted to a discussion of the Laguerre polynomial approximation method and its application to optimal control. The convergence analysis is substantiated in Section IV. In Section V, the numerical implementation and experimental results are described, and a discussion of the results is provided. Finally, the conclusion is stated in Section VI.

II. Methodology

A. Problem Statement

We consider a class of optimal control problems governed by parabolic partial differential equations. The aim is to determine the state and control functions $z(x,t)$ and $u(x,t)$, respectively, that minimize the following quadratic cost functional [6]:

$$J(z,u) = \frac{1}{2}\int_0^1 \int_0^R x^k[Az^2(x,t) + Bu^2(x,t)]dx\,dt; \quad (1)$$

subject to the following dynamic constraints:

$$\frac{\partial z(x,t)}{\partial t} = \beta\left(\frac{\partial^2 z(x,t)}{\partial x^2} + \frac{k}{x}\frac{\partial z(x,t)}{\partial x}\right) + u(x,t); \quad (2)$$

and the initial and boundary condition:

$$z(x,0) = z_0(x), \quad 0 < x < R, \quad z(R,t) = 0, \quad t > 0. \quad (3)$$

That A and B are defined as two arbitrary functions, β is a positive constant representing the diffusivity coefficient, R is characterized as a positive real number, and k may assume the values of 1 or 2. Also the functions $z(x,t)$ and $u(x,t)$ are differentiable and exhibit smooth characteristics. The aim is to solve the above problem with the Laguerre polynomials, which is defined below.

B.Definition and Properties of 2D Laguerre Polynomials

The two-dimensional Laguerre polynomials $L_{m,n}(z,z')$, defined for two (generally independent) complex variables z and z', constitute a powerful basis for representing multivariate functions. These polynomials are employed for approximate solutions to a wide range of problems across various domains. The 2D Laguerre polynomials, are defined as follows [13, 14, 15, 16, 17]:

$$L_{m,n}(z,z') \equiv \exp\left(-\frac{\partial^2}{\partial z \partial z'}\right) z^m z'^n. \quad (4)$$

Expanding the exponential operator yields the explicit polynomial form:

$$L_{m,n}(z,z') = \sum_{j=0}^{\min\{m,n\}} \frac{(-1)^j m!n!}{j!(m-j)!(n-j)!} z^{m-j} z'^{n-j}. \quad (5)$$

The inverse of relation (4) is computed as follow

$$z^m z'^n = \exp\left(\frac{\partial^2}{\partial z \partial z'}\right) L_{m,n}(z,z')$$

$$= \sum_{j=0}^{\min\{m,n\}} \frac{m!n!}{j!(m-j)!(n-j)!} L_{m-j,n-j}(z,z'). \quad (6)$$

Remark 1. The following Laguerre polynomials are directly related to the inversion (6) [17].

$$\begin{aligned} L_{m,n}(z,0) &= \tfrac{(-1)^n m!}{(m-n)!} z^{m-n}; \\ L_{m,n}(0,z') &= \tfrac{(-1)^m n!}{(n-m)!} z'^{n-m}; \\ L_{m,n}(0,0) &= (-1)^n n!\, \delta_{m,n}; \\ L_{m,0}(z,z') &= z^m, \quad L_{0,n}(z,z') = z'^n, \quad L_{0,0}(z,z') = 1. \end{aligned}$$

Remark 2. We have the following relations for the partial derivatives of the Laguerre polynomials [17].

$$\begin{aligned} \frac{\partial}{\partial z} L_{m,n}(z,z') &= m L_{m-1,n}(z,z'); \\ \frac{\partial}{\partial z'} L_{m,n}(z,z') &= n L_{m,n-1}(z,z'). \end{aligned}$$

These relations are instrumental in deriving system dynamics and adjoint equations in the Laguerre spectral domain. They also satisfy the following recurrence identities [17]:

$$\begin{aligned} L_{m+1,n}(z,z') &= z L_{m,n}(z,z') - n L_{m,n-1}(z,z'); \\ L_{m,n+1}(z,z') &= z' L_{m,n}(z,z') - m L_{m-1,n}(z,z'). \end{aligned} \tag{7}$$

Since the problems considered in this manuscript are based on the real values x and t, all the relations stated in section 3 hold accordingly. In particular, the recurrence relation (7) takes the following form:

$$\begin{aligned} L_{m+1,n}(x,t) &= x L_{m,n}(x,t) - n L_{m,n-1}(x,t); \\ L_{m,n+1}(x,t) &= t L_{m,n}(x,t) - m L_{m-1,n}(x,t). \end{aligned} \tag{8}$$

III. Numerical solution method

In this section, we provide an approximate solution for problem (1)–(3). For this

$$\begin{cases} z(x,t) & \cong z_{M,N}(x,t) = \sum_{i=0}^{M} \sum_{j=0}^{N} c_{ij} L_{ij}(x,t); \\ u(x,t) & \cong u_{M,N}(x,t) = \sum_{i=0}^{M} \sum_{j=0}^{N} d_{ij} L_{ij}(x,t); \\ & 0 \le x \le x_f, \quad 0 \le t \le t_f. \end{cases} \tag{9}$$

We can rewrite the solution function (9) in the following matrix form

$$z_{M,N}(x,t) = \sum_{i=0}^{M} \sum_{j=0}^{N} c_{ij} L_{ij}(x,t) = \mathrm{C}^T \mathrm{L}(x,t); \tag{10}$$

that C is an $(M+1)\times(N+1)$ matrix whose entries are real-valued coefficients c_{ij}, where $i = 0,1,\dots,M$ and $j = 0,1,\dots,N$ and the matrix form are defined as follows:

$$\mathrm{C} = \begin{bmatrix} c_{0,0} & c_{0,1} & \dots & c_{0,N} \\ c_{1,0} & c_{1,1} & \dots & c_{1,N} \\ \vdots & \vdots & \ddots & \vdots \\ c_{M,0} & c_{M,1} & \dots & c_{M,N} \end{bmatrix},$$

c_{ij} denotes the unknown coefficients and will be determined during the solving process. L(x,t) represents a $(M+1)\times(N+1)$ matrix, whose elements are Laguerre polynomials $L_{ij}(x,t)$, where $i = 0,1,\dots,M$ and $j = 0,1,\dots,N$.

$$\mathrm{L}(x,t) = \begin{bmatrix} L_{0,0}(x,t) & L_{0,1}(x,t) & \dots & L_{0,N}(x,t) \\ L_{1,0}(x,t) & L_{1,1}(x,t) & \dots & L_{1,N}(x,t) \\ \vdots & \vdots & \ddots & \vdots \\ L_{M,0}(x,t) & L_{M,1}(x,t) & \dots & L_{M,N}(x,t) \end{bmatrix}.$$

The aforementioned 3×3 matrix form is as follows:

$$\mathrm{L}(x,t) = \begin{bmatrix} 1 & t & t^2 \\ x & -1+tx & -2t+t^2x \\ x^2 & -2x+tx^2 & 2-4tx+t^2x^2 \end{bmatrix}$$

A. Partial derivative with respect to $\boldsymbol{t}$ *and* $\boldsymbol{x}$*(First-Order)*

The first-order partial derivative with respect to t is given by:

$$\frac{\partial z(x,t)}{\partial t} = \mathrm{C}^T \frac{\partial \mathbf{L}(x,t)}{\partial t}. \tag{11}$$

Here

$$\frac{\partial \mathrm{L}(x,t)}{\partial t} = \begin{bmatrix} \frac{\partial L_{0,0}(x,t)}{\partial t} & \frac{\partial L_{0,1}(x,t)}{\partial t} & \dots & \frac{\partial L_{0,N}(x,t)}{\partial t} \\ \frac{\partial L_{1,0}(x,t)}{\partial t} & \frac{\partial L_{1,1}(x,t)}{\partial t} & \dots & \frac{\partial L_{1,N}(x,t)}{\partial t} \\ \vdots & \vdots & \ddots & \vdots \\ \frac{\partial L_{M,0}(x,t)}{\partial t} & \frac{\partial L_{M,1}(x,t)}{\partial t} & \dots & \frac{\partial L_{M,N}(x,t)}{\partial t} \end{bmatrix}.$$

where $\frac{\partial \mathrm{L}(x,t)}{\partial t}$ denotes a $(M+1)\times(N+1)$ matrix, whose elements are given by $\frac{\partial L_{ij}(x,t)}{\partial t}$, where $i = 0,1,\dots,M$ and $j = 0,1,\dots,N$. Using the properties of two-dimensional Laguerre polynomials

$$\frac{\partial}{\partial t} L_{m,n}(x,t) = n L_{m,n-1}(x,t).$$

Thus

$$\frac{\partial z(x,t)}{\partial t} = \mathrm{C}^T \mathrm{L}_t(x,t),$$

where

$$\mathrm{L}_t(x,t) = \left[n L_{m,n-1}(x,t) \right]_{m=0,\dots,M, n=1,\dots,N}.$$

The first-order partial derivative with respect to x is given by,

$$\frac{\partial z(x,t)}{\partial x} = \mathrm{C}^T \frac{\partial \mathrm{L}(x,t)}{\partial x}. \tag{12}$$

Here

$$\frac{\partial \mathrm{L}(x,t)}{\partial x} = \begin{bmatrix} \frac{\partial L_{0,0}(x,t)}{\partial x} & \frac{\partial L_{0,1}(x,t)}{\partial x} & \dots & \frac{\partial L_{0,N}(x,t)}{\partial x} \\ \frac{\partial L_{1,0}(x,t)}{\partial x} & \frac{\partial L_{1,1}(x,t)}{\partial x} & \dots & \frac{\partial L_{1,N}(x,t)}{\partial x} \\ \vdots & \vdots & \ddots & \vdots \\ \frac{\partial L_{M,0}(x,t)}{\partial x} & \frac{\partial L_{M,1}(x,t)}{\partial x} & \dots & \frac{\partial L_{M,N}(x,t)}{\partial x} \end{bmatrix}.$$

where $\frac{\partial \mathrm{L}(x,t)}{\partial x}$ denotes a $(M+1)\times(N+1)$ matrix, whose elements are given by $\frac{\partial L_{ij}(x,t)}{\partial x}$, where $i = 0,1,\dots,M$ and $j = 0,1,\dots,N$. Using the properties of two-dimensional Laguerre polynomials

$$\frac{\partial}{\partial x}L_{m,n}(x,t) = mL_{m-1,n}(x,t).$$

Thus

$$\frac{\partial z(x,t)}{\partial x} = \mathrm{C}^T\mathrm{L}_x(x,t);$$

where:

$$\mathrm{L}_x(x,t) = \left[mL_{m-1,n}(x,t)\right]_{m=1,\dots,M,n=0,\dots,N}.$$

B. Partial derivative with respect to $\boldsymbol{x}$ (Second-Order)

The second-order partial derivative with respect to x is given by

$$\frac{\partial^2 z(x,t)}{\partial x^2} = \mathrm{C}^T\frac{\partial^2 \mathrm{L}(x,t)}{\partial x^2}.$$

Here

$$\frac{\partial^2 \mathrm{L}(x,t)}{\partial x^2} = \begin{bmatrix} \frac{\partial^2 L_{0,0}(x,t)}{\partial x^2} & \frac{\partial^2 L_{0,1}(x,t)}{\partial x^2} & \dots & \frac{\partial^2 L_{0,N}(x,t)}{\partial x^2} \\ \frac{\partial^2 L_{1,0}(x,t)}{\partial x^2} & \frac{\partial^2 L_{1,1}(x,t)}{\partial x^2} & \dots & \frac{\partial^2 L_{1,N}(x,t)}{\partial x^2} \\ \vdots & \vdots & \ddots & \vdots \\ \frac{\partial^2 L_{M,0}(x,t)}{\partial x^2} & \frac{\partial^2 L_{M,1}(x,t)}{\partial x^2} & \dots & \frac{\partial^2 L_{M,N}(x,t)}{\partial x^2} \end{bmatrix}.$$

where $\frac{\partial^2 \mathbf{L}(x,t)}{\partial x^2}$ denotes a $(M+1)\times(N+1)$ matrix, whose elements are given by $\frac{\partial^2 L_{ij}(x,t)}{\partial x^2}$, where $i = 0,1,\dots,M$ and $j = 0,1,\dots,N$. Using the properties of two-dimensional Laguerre polynomials

$$\mathrm{L}_{xx}(x,t) = \frac{\partial^2}{\partial x^2}L_{m,n}(x,t) = m(m-1)L_{m-2,n}(x,t);$$

$$\text{if} \quad m \geq 2, \quad n \geq 0.$$

Thus

$$\frac{\partial^2 z(x,t)}{\partial x^2} = \mathrm{C}^T\mathrm{L}_{xx}(x,t).$$

Let us now assume that

$$u_{M,N}(x,t) = \sum_{i=0}^{M}\sum_{j=0}^{N} d_{ij}L_{ij}(x,t) = \mathrm{D}^T\mathrm{L}(x,t); \qquad (13)$$

that D is an $(M+1)\times(N+1)$ matrix whose entries are real-valued coefficients d_{ij}, where $i = 0,1,\dots,M$ and $j = 0,1,\dots,N$ and the matrix form are defined as follows:

$$\mathrm{D} = \begin{bmatrix} d_{0,0} & d_{0,1} & \dots & d_{0,N} \\ d_{1,0} & d_{1,1} & \dots & d_{1,N} \\ \vdots & \vdots & \ddots & \vdots \\ d_{M,0} & d_{M,1} & \dots & d_{M,N} \end{bmatrix}.$$

d_{ij} denotes the unknown coefficients and will be determined during the solving process. Taking into account for the dynamical system (2), we have

$$\mathrm{C}^T\mathrm{L}_t(x,t) - \beta(\mathrm{C}^T\mathrm{L}_{xx}(x,t) + \frac{k}{x}\mathrm{C}^T\mathrm{L}_x(x,t)) - \mathrm{D}^T\mathrm{L}(x,t) \simeq \hat{G}(x,t) \simeq 0. \qquad (14)$$

C. Selection of Collocation Points

This discretization transforms the differential equations into a system of algebraic equations. Furthermore, by taking the collocation points as

$$x_i = x_0 + \frac{x_f - x_0}{2(M+1)(N+1)-2}i; \quad i = 1,\dots,M,$$

$$t_j = t_0 + \frac{t_f - t_0}{2(M+1)(N+1)-2}j; \quad j = 1,\dots,N,$$

and substituting them into Eq. (14), it leads to the following system of algebraic equations

$$\Lambda_{ij} \cong \tilde{G}(x_i,t_j) = 0; \quad i = 1,\dots,M, \quad j = 1,\dots,N. \qquad (15)$$

The initial condition from Eq. (3) can be rewritten as:

$$\Lambda_{0,0} \cong C^T\mathrm{L}(x_0,0) - z_0(x) = 0. \qquad (16)$$

The cost function, as defined in Eq. (1), can be approximated as follows:

$$J(\mathrm{Z},\mathrm{U}) = \frac{1}{2}\int_0^1\int_0^R x^k[A(\mathrm{C}^T\mathrm{L}(x,t))^2 + B(\mathrm{D}^T\mathrm{L}(x,t))^2]\,dx\,dt.$$

To enforce the constraints and optimize the performance index, the Lagrange multipliers method is employed. The augmented functional is defined as

$$J^*(\mathrm{Z},\mathrm{U},\lambda) = J(\mathrm{Z},\mathrm{U}) + \sum_{i=0}^{M}\sum_{j=0}^{N}\lambda_{ij}\Lambda_{ij};$$

where λ_{ij} are the Lagrange multipliers corresponding to the residuals. The necessary conditions for optimality are

$$\frac{\partial J^*}{\partial \mathrm{Z}} = 0; \quad \frac{\partial J^*}{\partial \mathrm{U}} = 0; \quad \frac{\partial J^*}{\partial \lambda} = 0. \qquad (17)$$

To solve (17), various techniques have been developed for addressing nonlinear optimization problems. In this study, we have opted to utilize the techniques provided by the available software tools.

IV. Convergence Analysis

In this section, the convergence of the method presented in Section 4 is examined.

Theorem .١ For each $\Omega \in C^2([0,x_f]\times[0,t_f])$, there exists a sequence of polynomials $L_{ij}(x,t)\} \in \Omega$ that converges uniformly to $\hat{z}(x,t)$.

Proof. Refer to [3] for the proof.

Lemma 1. Let $\Omega \subset C^2([0,R]\times[0,1])$ denote the set of admissible pairs (z,u) satisfying the following parabolic partial

$$\frac{\partial z(x,t)}{\partial t} = \beta\left(\frac{\partial^2 z}{\partial x^2} + \frac{k}{x}\frac{\partial z}{\partial x}\right) + u(x,t);$$

with the initial and boundary conditions:

$$z(x,0) = z_0(x), \quad 0 < x < R,$$
$$z(R,t) = 0, \quad 0 < t < 1. \qquad (18)$$

The associated cost functional is defined by

$$J(z,u) = \frac{1}{2}\int_0^1\int_0^R x^k[Az^2(x,t) + Bu^2(x,t)]dx\,dt.$$

Let $\{\Omega_{MN}\}_{M,N=0}^{\infty}$ as a sequence of subspaces spanned by Laguerre polynomials of degree at most MN. Define the infimum of the cost functional J over each subspace as

$$\gamma_{MN} = \inf_{(z,u)\in\Omega_{MN}} J(z,u);$$

then,

$$\lim_{M,N\to\infty} \gamma_{MN} = \inf_{(z,u)\in\Omega} J(z,u).$$

Proof. Consider the cost functional $J: \Omega \to \mathbb{R}$ defined by

$$J(z,u) = \frac{1}{2}\int_0^1 \int_0^R x^k[Az^2(x,t) + Bu^2(x,t)]dx\,dt. \qquad (19)$$

where $(z,u) \in \Omega$ satisfy in (١٨) and (19). Let $\{L_{ij}(x,t)\}_{i,j=0}^{\infty}$ denote the Laguerre basis on $[0,R] \times [0,1]$. Define Ω_{MN} as the finite-dimensional subspace consisting of pairs (z_{MN}, u_{MN}) expressed as

$$z_{MN}(x,t) = \sum_{i=0}^{M}\sum_{j=0}^{N} c_{ij}L_{ij}(x,t); \qquad (20)$$

$$u_{MN}(x,t) = \sum_{i=0}^{M}\sum_{j=0}^{N} d_{ij}L_{ij}(x,t). \qquad (21)$$

where the coeffcients $\{c_{ij}, d_{ij}\}$ are unknown and will be determined during the solving process.

Define the infimum of the cost functional over each subspace Ω_{MN} as

$$\gamma_{MN} = \inf_{(z,u)\in\Omega_{MN}} J(z,u).$$

That the set Ω_{MN} is finite-dimensional and consists of continuous functions that meet theinitial and boundary conditions. Since J is continuous on Ω, we conclude that γ_{MN} is well-defined. Since every subspace of Laguerre polynomials of degree up to MN is contained within the subspace of Laguerre polynomials of degree up to $(M+1)(N+1)$, it follows that $\Omega_{MN} \subset \Omega_{(M+1)(N+1)}$.

Since J is defined as an infimum over each subspace Ω_{MN}, we have

$$\gamma_{(M+1)(N+1)} = \inf_{(z,u)\in\Omega_{(M+1)(N+1)}} J(z,u) \leq \inf_{(z,u)\in\Omega_{MN}} J(z,u) = \gamma_{MN}.$$

Consequently,

$$\gamma_{(M+1)(N+1)} \leq \gamma_{MN}.$$

Thus the sequence $\{\gamma_{MN}\}$ is monotonically decreasing

$$\gamma_{MN} \leq \gamma_{(M-1)(N-1)} \leq \cdots \leq \gamma_{11}.$$

Each subspace $\Omega_{MN} \subset \Omega$ consists of functions (z,u) that satisfy the same initial and boundary conditions as those in Ω. Consequently, the restriction of J to $\Omega_{N,M}$ is also bounded below by $\inf_{\Omega} J$. Specifically, we have

$$\gamma_{MN} \geq \inf_{\Omega}.$$

By the monotone convergence theorem, since $\{\gamma_{MN}\}$ is monotonically decreasing and bounded below, the limit exists. Define this limit as

$$\lim_{M,N\to\infty} \gamma_{MN} = L;$$

where $L \geq \inf_{\Omega} J$. To show that $L = \inf_{\Omega} J$, let $\epsilon > 0$ be arbitrary. By the definition of $\inf_{\Omega} J$, there exists a function $(z,u) \in \Omega$ such that

$$J(z,u) < \inf_{\Omega} J + \epsilon.$$

Since Laguerre polynomials are dense in $C^2([0,x_f] \times [0,t_f])$, we can approximate (z,u) by a sequence $(z_{MN}, u_{MN}) \in \Omega_{MN}$ that converges uniformly to (z,u). By continuity of J, we find

$$\lim_{M,N\to\infty} J(z_{MN}, u_{MN}) = J(z^*, u^*);$$

implying that

$$L < \inf_{\Omega} J + \epsilon.$$

Since ϵ is arbitrary, it follows that $L = \inf_{\Omega} J$.

Thus, we conclude that

$$\lim_{M,N\to\infty} \gamma_{MN} = \inf_{\Omega} J.$$

V. Numerical Implementation and Results

This section includes two numerical examples to demonstrate the effectiveness and computational efficiency of the proposed method. The findings substantiate the dependability and efficacy of the Laguerre-based methodology. The simulated results have been carried out using Mathematica 11 on a 2.53 MHz Alpha Machin with 8GB RAM.

Example 1. Consider the following OCPPC:

$$\min J(z,u) = \frac{1}{2}\int_0^1 \int_0^1 x[z^2(x,t) + u^2(x,t)]\,dx\,dt;$$

subject to the constraint

$$\frac{\partial z(x,t)}{\partial t} = \frac{\partial^2 z(x,t)}{\partial x^2} + \frac{1}{x}\frac{\partial z(x,t)}{\partial x} + u(x,t);$$

with the following initial and boundary conditions:

$$z(x,0) = 1 - x^2, \quad 0 < x < 1, \quad z(1,t) = 0; \quad t > 0. \quad (22)$$

This example is numerically solved by the proposed method for kind of iteration; $M = 2, N = 2$; $M = 2, N = 4$; $M = 3, N = 7$ and $M = 4, N = 4$. A comparison of the cost function values across different iterations for the proposed method and the methods presented in [4] and [6] is provided in Table 1. As shown in Table 1, for example, in iterations $M = 3, N = 7$, the cost functional value obtained by our method is 0.00292532, while for the method proposed in [6] is 0.013027. This demonstrates that our approach yields better results in comparable iterations. Furthermore, when examining the cost function values overall, our method provides superior results even in iterations $M = 2, N = 2$,

outperforming the methods proposed in [4] and [6]. Figure 1 shows the state function $z(x,t)$ over the space-time domain $[0,1]\times[0,1]$ for $M=2, N=2$. The plotted surface is smooth and continuous, clearly reflecting the system dynamics under the influence of optimal control. This observation indicates that the proposed method yields qualitatively accurate results even at a low order of approximation with $M=2$ and $N=2$. The corresponding optimal control function $u(x,t)$ is presented in Figure 2. The control surface is smooth and well-behaved, exhibiting no signs of numerical irregularities such as oscillations or instability. The relatively small magnitude of the control values suggests that the obtained solution is not only stable but also effective in minimizing the control effort, which is a fundamental goal in optimal control problems. The behavior of the state function $z(t)$ at a fixed spatial point $x=0.2$ for three different iterations designed in Figure 3 for $M=3, N=7$, $M=3, N=3$, and $M=4, N=6$. As depicted in the figure, the solution becomes progressively smoother and more accurate with increasing values of the approximation parameters M and N, demonstrating the convergence and improved performance of the proposed numerical method. Figure 4 shows the behavior of the control function $u(t)$ evaluated at $x=0.2$. As can be seen, the control profile $u_{46}(t)$ captures more precise variations compared to $u_{33}(t)$ and $u_{24}(t)$, indicating that higher-order approximations provide a more accurate representation of the control dynamics.

TABLE 1: $J^*(z,u)$ FOR EXAMPLE 1

Methods	J
Mamehrashi and Yousefi (2016)	
$m=1, n=4$	0.081044
$m=2, n=4$	0.028790
$m=2, n=7$	0.016484
$m=3, n=7$	0.013027
Hosseini (2022)	
$m=3, n=2$	0.029328
$m=3, n=3$	0.016930
$m=3, n=5$	0.0720
$m=4, n=5$	0.0665
Presented Method	
$M=2, N=2$	0.0104436
$M=2, N=4$	0.00359086
$M=3, N=7$	0.00292532
$M=4, N=4$	0.00190655

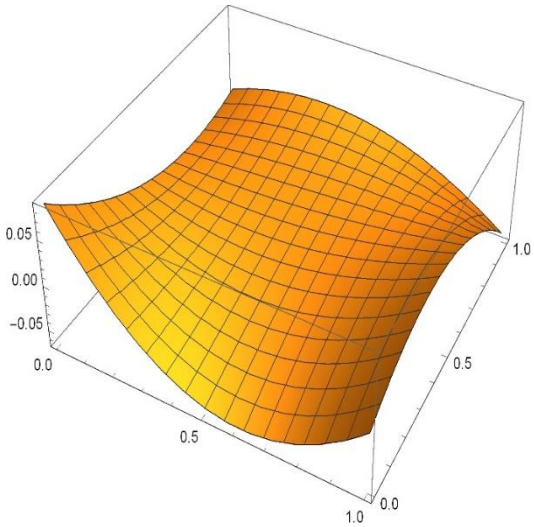

Figure 1: State function z(x,t) with N=2,M=2.

Example 2. Consider the following OCPPC:

$$\min J=\frac{1}{2}\int_0^1\int_0^1 x^2\left[z^2(x,t)+u^2(x,t)\right],dx,dt.$$

The dynamic constraint of the system is given by

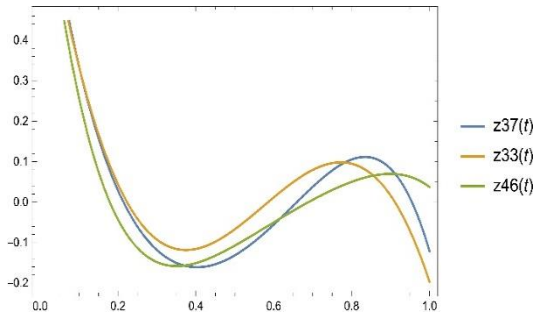

Figure 2: Control function $u(x,t)$ with $N=2, M=2$.

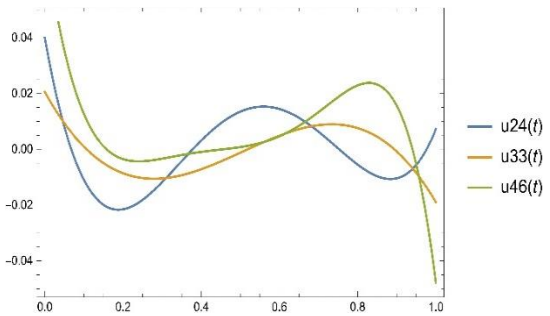

Figure 3: State function $z(t)$ with varying M and N.

$$\frac{\partial z(x,t)}{\partial t}=\frac{\partial^2 z(x,t)}{\partial x^2}+\frac{2}{x}\frac{\partial z(x,t)}{\partial x}+u(x,t), \qquad (19.4)$$

$$z(x,0)=\sin(2\pi x);\quad 0<x<1;$$

and the boundary condition

$z(1,t) = 0; \quad t > 0.$

Numericall results obtained by applying the proposed method for $J^*(z,u)$ are reported in the table 2. This table includes the computed values of $J(z,u)$ reported by Mamehrashi et al. [6] and Mohammadi et al. [7], as well as the results calculated in this study. As observed, the values of $J^*(z,u)$ obtained in this study demonstrate superior performance compared to those reported. For example, Table 2, in iterations $M = 2, N = 6$, the cost function value obtained by our method is 1.14694×10^{-9}, while for the method proposed in [6] is 0.018283. This shows that our approach yields better results in comparable iterations. Furthermore, when examining the cost function values overall, our method provides superior results in every iteration, outperforming the methods proposed in [6] and [7]. Figures 5 and 6 show the calculated state function $z(x,t)$ and control function $u(x,t)$ for the spectral approximation case with $N = 3$ and $M = 3$. In Figure 5, the surface plot of $z(x,t)$ demonstrates a smooth and continuous structure characterized by slight fluctuations on the order of 10^{-27}. The curvature of the surface indicates the nature of the dynamic response under the given approximation parameters. The nearly flat profile with minimal deviation suggests a system with negligible dynamics under the imposed control or a highly accurate balancing of the state trajectory within the constraints of the spectral method. In contrast, Figure 6 presents the control function $u(z,t)$, which exhibits more pronounced variations. Such

TABLE 2: $J^*(z,u)$ FOR EXAMPLE 2

Methods	J
Mamehrashi and Yousefi (2016)	
$m = 2, n = 4$	0.028790
$m = 2, n = 6$	0.018283
$m = 3, n = 7$	0.013027
$m = 3, n = 9$	0.010405
Mohammadi and Hassani (2018)	
$m_1 = m_2 = n_1 = n_2 = 2$	6.29×10^{-8}
$m_1 = 2, m_2 = 3, n_1 = n_2 = 3$	2.91×10^{-9}
$m_1 = m_2 = n_1 = n_2 = 3$	6.43×10^{-10}
$m_1 = m_2 = n_1 = n_2 = 7$	1.57×10^{-12}
Presented Method	
$M = 2, N = 6$	1.14694×10^{-9}
$M = 2, N = 7$	3.80595×10^{-15}
$M = 3, N = 5$	2.77562×10^{-14}
$M = 3, N = 7$	1.68474×10^{-18}

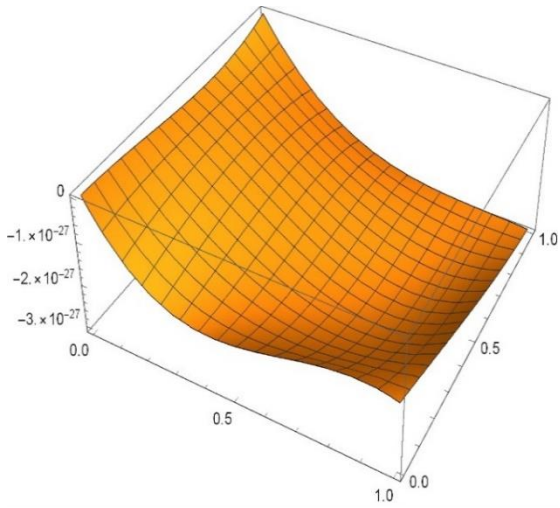

Figure 4: Control function $u(t)$ with varying M and N.

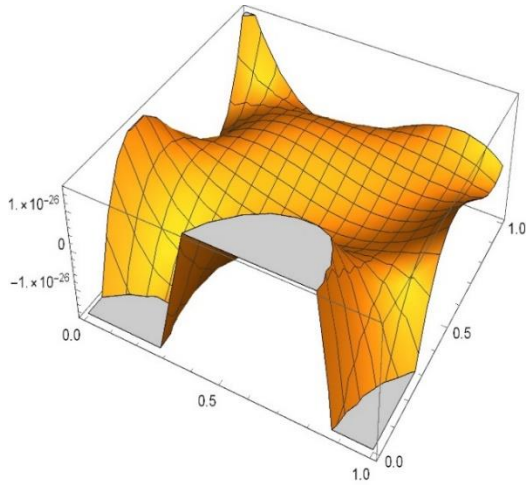

Figure 5: State function $x(t)$ with $N = 3, M = 3$.

behavior is indicative of low-order spectral approximations attempting to capture sharp control transitions or discontinuities in optimal solutions.

VI. Conclusion

This paper presented a novel approach to solving a class of parabolic optimal control problems. The proposed method utilizes a spectral collocation technique, underpinned by Laguerre polynomials, to facilitate the solution process. The proposed method involves expanding the state and control variables in terms of Laguerre basis functions. This transformation of the original optimal control problem into a finite-dimensional nonlinear system can be efficiently solved. The convergence of the proposed scheme was mathematically established, ensuring its theoretical validity. The efficacy of the method was confirmed through a series of numerical experiments, which demonstrated its accuracy, stability, and efficiency. The findings indicated that, even at low approximation orders, the method produces smooth and

physically meaningful solutions for both the state and control functions. Furthermore, a comparative analysis with previously published methods in [4] and [6] confirmed the superiority of the proposed approach. As demonstrated by the numerical results, the cost functional value obtained with iteration parameters $M = 3, N = 7$ was significantly lower than those reported in earlier works. The behavior of the state and control functions within their respective domains has been shown to exhibit improved accuracy and convergence with increasing approximation order. The findings indicate the robustness of the proposed technique and underscore its potential for broader applications, including future extensions to multidimensional or fractional-order optimal control problems.

REFERENCES

[1] E. Casas and J. Yong, "Optimal control of a parabolic equation with memory," *ESAIM: Control, Optimisation and Calculus of Variations*, vol. 29, pp. 23–40, Sep. 2023, doi:10.1051/cocv/2023013.

[2] T. Führer and M. Karkulik, "Space-time least-squares finite element methods for parabolic distributed optimal control problems," *Comput. Methods Appl. Math.,* Sep. 202۴; vol. 24, no. 3, pp. 673–691, doi:10.1515/cmam-2023-0087.

[3] R. Holmes, "An introduction to the approximation of functions (Theodore J. Rivlin)," *SIAM Review*, vol. 12, no. 2, pp. 311–312, Apr. 1970, doi:10.1137/1012069.

[4] S. M. Hosseini, F. Soltanian, and K. Mamehrashi, "Solution of two-dimensional optimal control problem using Legendre block-pulse polynomial basis," *Pure and Applied Mathematics Quarterly*, vol. 18, no. 3, pp. 1075–1094, Sep. 2022,doi:10.4310/PAMQ.2022.v18.n3.a7.

[5] S. Latifi, K. Parand, and M. Delkhosh, "Generalized Lagrange–Jacobi–Gauss–Radau collocation method for solving a nonlinear optimal control problem with the classical diffusion equation," *Eur. Phys. J. Plus*, vol. 135, no. 10, pp. 1–15, Oct. 2020, doi:10.1140/epjp/s13360-020-00847-1.

[6] K. Mamehrashi and S. Yousefi, "A numerical method for solving a nonlinear 2-D optimal control problem with the classical diffusion equation," *Int. J. Control*, vol. 90, no. 2, pp. 298–306, Feb. 2017, doi:10.1080/00207179.2016.1178807.

[7] F. Mohammadi and H. Hassani, "Numerical solution of two-dimensional variable-order fractional optimal control problem by generalized polynomial basis," *J. Optim. Theory Appl.*, vol. 180, no. 2, pp. 536–555, Aug. 2018, doi:10.1007/s10957-018-1389-z.

[8] Y. Na, T. Men, R. Du, and Y. Zhu, "Optimal control problems of a class of nonlinear degenerate parabolic equations," *Mathematics*, vol. 12, no. 14, p. 2181, Jul. 2024, doi:10.3390/math12142181.

[9] P. Omidiniya and M. Alipour, "A semi-analytic method for solving a class of non-linear optimal control problems," *Int. J. Ind. Electron. Control Optim.*, vol. 3, no. 4, pp. 407–414, Jul.–Aug. 2020,doi:10.22111/ieco.2020.32367.1225.

[10] S. M. Shafiof, J. A. Marnani, and M. Shamssolary, "Hybrid functions to solve fractional optimal control problems using the collocation method," *Int. J. Ind. Electron. Control Optim.*, vol. 4, no. 1, pp. 25–35, Feb. 2021, doi:10.22111/ieco.2021.37207.1334.

[11] F. Soufivand, F. Soltanian, and K. Mamehrashi, "An operational matrix method based on the Gegenbauer polynomials for solving a class of fractional optimal control problems," *Int. J. Ind. Electron. Control Optim.*, vol. 4, no. 1, pp. 29–40, Feb. 2021, doi:10.22111/ieco.2021.39546.1371.

[12] W. You and F. Zhang, "Pontryagin's principle based algorithms for optimal control problems of parabolic equation," *arXiv*, vol. 63, no. 2, pp. 995–1002, Feb. 2025, doi:10.48550/arxiv.2501.12745.

[13] A. Wünsche, "Laguerre 2D-functions and their application in quantum optics," *J. Phys. A: Math. Gen.*, vol. 31, no. 40, pp. 8267–8287, Oct. 1998, doi:10.1088/0305-4470/31/40/017.

[14] A. Wünsche, "Transformations of Laguerre 2D polynomials with applications to quasiprobabilities," *J. Phys. A: Math. Gen.*, vol. 32, no. 17, pp. 3179–3199, May 1999, doi:10.1088/0305-4470/32/17/309.

[15] A. Wünsche, "General Hermite and Laguerre two-dimensional polynomials," *J. Phys. A: Math. Gen.*, vol. 33, no. 8, pp. 1603–1629, Feb. 2000, doi:10.1088/0305-4470/33/8/307.

[16] A. Wünsche, "Hermite and Laguerre 2D polynomials," *J. Comput. Appl. Math.*, vol. 133, no. 1–2, pp. 665–678, Jan.–Feb. 2001, doi:10.1016/S0377-0427(00)00681-6.

[17] A. Wünsche, "Generating functions for products of special Laguerre 2D and Hermite 2D polynomials," *Applied Mathematics*, vol. 6, no. 12, pp. 2142–2168, Dec. 2015,doi:10.4236/am.2015.612188.

Yunes Mohamadi was born in Iranshahr, Sistan and Baluchestan. He received his M.Sc. degree in Mathematics from Islamic Azad University, Zahedan Branch, Zahedan, Sistan and Baluchestan, Iran, in 2011. He is currently a Ph.D. student in Applied Mathematics at the University of Sistan and Baluchestan, Iran. His current research interests include optimal control and iterative methods.

Maryam Alipour was born in Mazandaran, Iran. She received her M.Sc. degree in Applied Mathematics from the University of Mazandaran, Iran, in 2010. She earned her Ph.D. in Applied Mathematics from Shahid Bahonar University of Kerman, Iran in 2016. She is currently an Assistant Professor at the University of Sistan and Baluchestan, Zahedan, Iran. Her current research interests include numerical analysis, optimal control, and iterative methods

Akbar Hashemi Borzabadi was born in Mashhad, Iran, in 1974. He received his M.Sc. and Ph.D. degrees in Applied Mathematics from the Faculty of Mathematical Sciences, Ferdowsi University of Mashhad, Iran. In 1999, he joined Damghan University as a lecturer in the Department of Applied Mathematics, where he served as an Assistant Professor from 2005 to 2010 and as an Associate Professor from 2011 to 2016. Since 2016, he has been involved in teaching and research at the University of Science and Technology of Mazandaran, Behshahr, Iran, where he has held the position of Professor since 2023. His current research interests include optimization, optimal control, and numerical methods related to these fields.

IECO

This page intentionally left blank.

International Journal Of
Industrial Electronics Control and Optimization
Print ISSN: 3517-2645
Online ISSN: 3568-2645
Homepage: https://ieco.usb.ac.ir/

Artificial Intelligence for Assessing Composite Insulator Pollution Level: A Study on Partial Discharge Characteristics

Hamid Reza Sezavar | Saeed Hasanzadeh

Department of Electrical and Computer Engineering, Qom University of Technology, Qom, Iran.[1,2,3]
Corresponding author's email: hasanzadeh@qut.ac.ir

Article Info

Article type:
Research Article

Article history:
Received: 31-March-2025
Received in revised form: 11-May-2025
Accepted: 16-May-2025
Published online: 21-March-2026

Keywords:
Composite insulator,
Gradient boosting machines,
Leakage current,
Partial discharge,
Pollution flashover,
Wavelet transformation.

ABSTRACT

Insulator pollution levels are critical for ensuring the operational stability and safety of power transmission systems. Traditional methods for detecting pollution are often invasive, inaccurate, and time-consuming. To address these issues, this study investigates the application of Artificial Intelligence (AI), specifically Gradient Boosting Machines (GBM), to classify insulator pollution levels based on Partial Discharge (PD) characteristics. We utilize a combination of time-domain and frequency-domain features extracted from PD signals to train a predictive model. The results indicate that the proposed model achieves a high classification accuracy, averaging between 92% and 95% across various contamination levels. Furthermore, the study analyzes the model's sensitivity to environmental factors, including humidity and Hydrophobicity Class (HC), revealing important insights that could influence classification performance. By employing this AI-driven approach, we aim to significantly enhance the efficiency of power grid maintenance, ultimately contributing to the long-term stability and reliability of transmission systems. The findings from this research underscore the potential of AI in revolutionizing pollution assessment methods and optimizing maintenance practices in power infrastructure.

I. Introduction

Pollution is one of the factors affecting the failure of insulators in the power system. Insulators in power system equipment lose their insulating properties as they are exposed to pollution. The accumulation of pollution, along with the addition of moisture, causes the formation of a conductive layer on the insulator and causes leakage current (LC) to flow on its surface. These signals gradually cause the appearance of small discharges on the surface [1]. These discharges are not detectable at first and cause the insulator's ageing, the insulating surface's loss, and premature failure. Partial discharges (PDs) generally occur on the surface of all insulators. In polymer insulators, more attention has been paid to dry band discharges and flashover discharges, and less attention has been paid to the analysis of PDs.

The performance of insulators is susceptible to the level of contamination. For this reason, analyzing and examining the level of contamination can help prevent flashovers. Many studies have been conducted to introduce methods for analyzing the level of contamination on insulators. The LC value is an important signal for determining the contamination level. In [2], it is shown that with increasing contamination levels, the LC value of the insulator increases, and the insulation performance is impaired. However, the LC value may not increase much at low humidity levels. As a result, the system has difficulty predicting the level of contamination. As a result, the idea of frequency analysis of LC was expanded instead of analyzing its value. This analysis began with the Fast Fourier Transform (FFT) and was expanded with the Wavelet Transform (WT). Initially, it was shown that the FFT analysis was also effective in low humidity [3]. In [4], the odd harmonics of LC were considered an example of frequency analysis, and a simple technique without the need for complex calculations was presented. In [5], frequency analysis was performed in dry conditions of the insulator with a humidity of 5%, and the ratio of the fundamental to the fifth and third harmonics was

investigated. In this case, it was shown that the ratio of the fundamental to the fifth harmonic is very effective in dry conditions and to the third harmonic in wet conditions. In [6], soluble and insoluble contaminations are investigated using FFT analysis. The main idea was that the voltage distortion increases proportionally to the contamination level due to the dry band arc. Therefore, this distortion is considered as an indicator of the contamination level. In [7], it is shown that the third and fifth harmonics of the insulation voltage play a fundamental role in determining the contamination level. In [8], the' energy value of individual harmonics is discussed to analyses and investigate the contamination level of composite insulators.

With the development of frequency analysis studies, models gradually moved towards using WT analysis. Both low and high frequencies were investigated over time in these investigations. In [9], discrete WT on insulators was started to estimate the contamination level, and in [10], frequency analysis was extended to index the contamination level. In [11], the WT was investigated in insulators with salt fog conditions, and in [12], this topic was expanded to ceramic insulator. Along with WT, Artificial Intelligence (AI) has also been significantly developed in estimating pollution levels in recent studies. Recent advancements in AI provide opportunities to improve the accuracy and efficiency of insulator pollution level assessments. For example, Artificial Neural Networks (ANN) have been used in the analysis and investigation of insulator pollution conditions [13, 14], Support Vector Machines (SVM) [15, 16] in the assessment of pollution levels, and other methods related to AI to estimate pollution level density [17, 18] and fault diagnostic in transformers [19] have been significantly developed.

However, the most important gap in studies of pollution level determination is the lack of use of physics-based analyses of the problem. The physics of pollution on the insulator surface causes PD on the surface [20, 21], and therefore, this idea can be a starting point for determining the pollution level. In [22], it is mentioned that the intensity and power of PD can depend on the pollution level. Also, in [23, 24], it is shown that PD signals have significant changes in high frequencies with changing weather conditions. PDs, mainly in insulators, are the initiators of flashover and are often invisible and can only be calculated from the LC signal. Therefore, a suitable relationship between the physics at the contamination level and the initiation of PDs can be obtained.

This study explores the application of Gradient Boosting Machines (GBM), a powerful machine learning technique, to classify insulator pollution levels based on PD characteristics. These characteristics are extracted from both the time-domain and frequency-domain features of PD signals. The primary objective is to develop an AI model capable of assessing insulator pollution levels in a fast, non-invasive, and reliably. This AI model aims to bridge the gap between physics-based analysis and machine learning approaches by integrating the underlying physical principles governing PD and pollution effects on insulators. It has been shown that PDs have features in the range of 5 to 15 kHz that relate to pollution levels. By leveraging the characteristics of PD signals, the GBM will classify pollution levels more accurately, accounting for variations in environmental conditions, such as humidity and contamination types. Integrating GBM with physical insights into PD behavior significantly advances the assessment of insulator pollution levels. Furthermore, this study will incorporate a comprehensive dataset that includes various insulator types and environmental scenarios to ensure robust model training and validation. The findings are expected to provide a novel framework for real-time monitoring of insulator health, enhancing predictive maintenance strategies in power systems, and ultimately improving their reliability and performance.

II. Laboratory setup

The experiments were conducted in a cubic climate chamber measuring 2 meters. The power supply included a step-up transformer rated at 100 kV and a protective circuit. A capacitive voltage divider with a voltage ratio 10,000:1 was used to measure the applied voltage. The LC was also recorded through the voltage across a shunt resistor connected in series with the insulators. PD signals were gathered using LC peak detection and filtered to ensure accurate readings. Figure 1 illustrates the schematic of the testing circuit and the climate chamber.

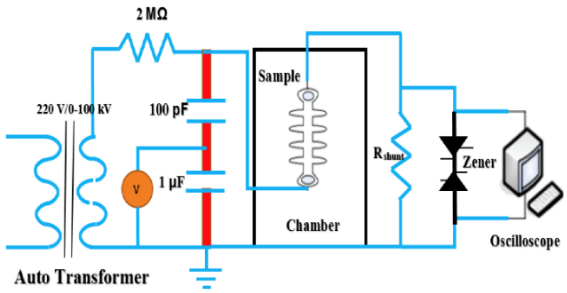

Fig. 1. Schematic view of the test setup.

TABLE I PARAMETERS OF THE SAMPLE TEST

Arcing Distance (cm).	Diameter of sheds (cm)	Num. of sheds	Creepage distance (cm)
33	10	6	85

All tests utilized 20 kV composite insulators from the same silicone rubber (SiR) material. The two types of pollution evaluated were equivalent salt deposit density (ESDD) and non-soluble deposit density (NSDD). The NSDD consisted of standard kaolin material. The ranges for ESDD and NSDD examined in this study were approximately 0 mg/cm² to 0.5 mg/cm² and from 0 mm to 5 mm in thickness, respectively, covering all levels of pollution classified as low, medium, high, and very high according to IEC 60815. The samples were contaminated by immersing them in a pre-prepared solution of distilled water mixed with kaolin to simulate NSDD. An average pollution ratio from top to bottom was calculated to be 0.96, indicating a relatively uniform distribution of the pollution layer. The specifications for the test insulator construction are detailed in Table 1 [25].

The input voltage was incrementally increased at a 1 kV/min rate throughout the testing phase, following IEC 60243-1, until dry-band arcing was noted. This protocol is used to achieve the PD signals because the PD signal typically appears before dry band arcing. During the experimentation, contaminants were sprayed into the chamber, maintaining a constant equivalent salt deposit density (ESDD) using a solution made of distilled water and sodium chloride (NaCl). During the test, PD activities were continuously monitored, and the signals were recorded to assess the insulation performance and detect any insulation degradation.

III. Methodology

A. PD Characteristics

The results in Figure 2 represent the four contamination levels according to the conditions described in section 2. The results are obtained based on low humidity and medium-class hydrophobicity. As Figure 2(b) shows, with increasing contamination levels, insulator LC, including peak signals, appears on the surface. Despite the difficulty of detecting PD, considering the changes in insulator LC with increasing contamination level in the insulator, signs of PD detection can be found. These changes can be a starting point for PD analysis and evaluating the insulator contamination level.

For a more detailed analysis, Figure 3a shows the relationship between the LC signal and its frequency analysis. The results of the Fourier transform analysis show that the frequency amplitude of the PD signal increases with the increase in the contamination level. However, a significant difference is observed in the 5 to 15 kHz range in figure 3b. With increasing contamination levels, the amplitude of the Fourier tidal signal in this range increases. This point is very valuable because it can be a relationship to evaluate the insulator contamination level based on the changes in the PD signal on the insulator surface. Further, based on the analysis of the frequency-time behavior in the stated range, features can be obtained to correctly assess the pollution level.

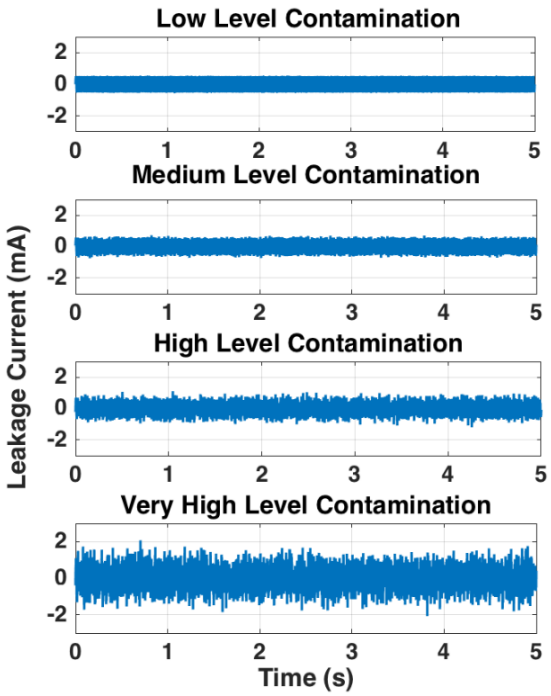

(a)

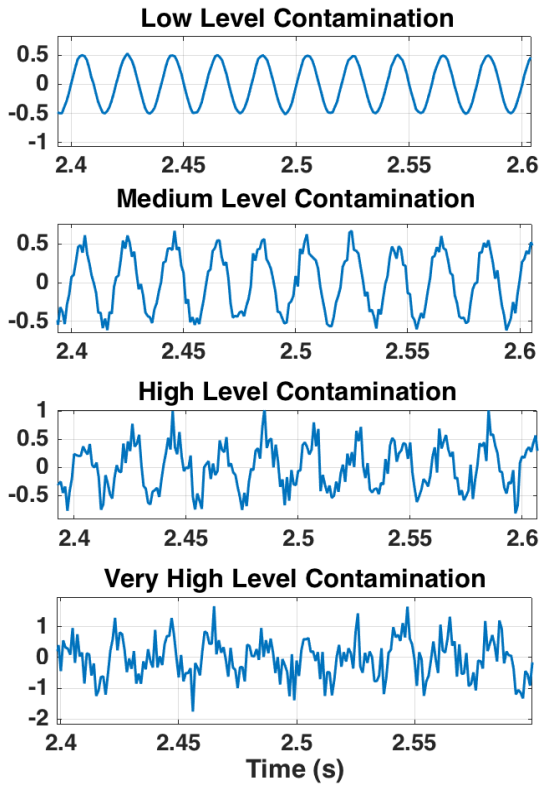

(b)

Fig. 2. (a) LC signals and (b) PD appearing, based on the four contamination levels.

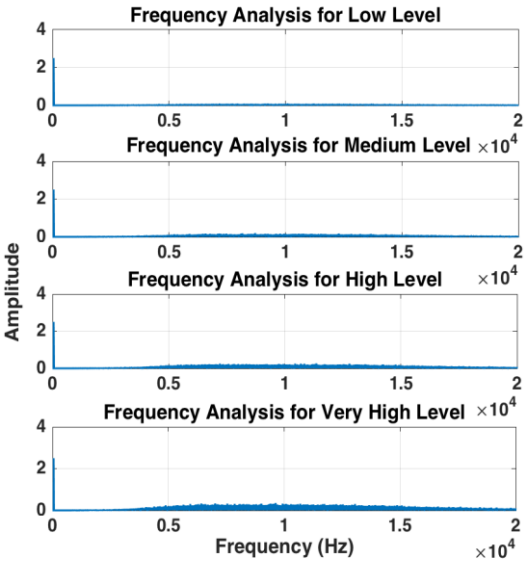

(a)

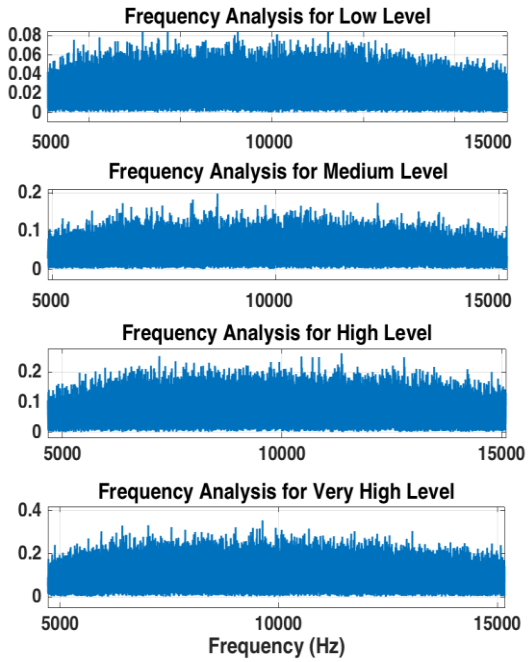

(b)

Fig. 3. a) Frequency analysis of LC signal. b) Amplitude of frequency analysis in 5000 to 15000 Hz

B. Feature Extractions

The current study employed Wavelet Packet Transform (WPT) for feature extraction, which serves as a broader representation of the wavelet transform. In each iteration, WPT executes a new decomposition based on coefficients obtained from its prior iterations. This implies that the final number of coefficients is contingent upon the number of decompositions conducted [26]. When applying a wavelet decomposition at the wavelet packet node level (WP), the segmentation of approximation coefficients results in a tree structure composed of two vectors: one representing the approximation coefficient vector and the other designated as the detailed vector. Information lost during the approximation process is encapsulated in the previously mentioned coefficients, forming a new vector. In this context, successive details are not reanalyzed [27].

The WP function can be expressed as:

$$W_{j,k}^{n}(t) = 2^{\frac{j}{2}}(2^{j}t - k) \tag{1}$$

where j is a scaling parameter, k denotes the translation operator, and n represents the oscillation parameter. The initial two WP functions for n=0, 1 are defined as follows:

$$W_{0,0}^{0}(t) = \emptyset(t) \tag{2}$$

$$W_{0,0}^{1}(t) = \psi(t) \tag{3}$$

The first function in Equation (2) is the scale function, while the second is the wavelet function [28]. Subsequent functions for n = 2, 3,…,N can be specified using these relationships:

$$W_{0,0}^{2n}(t) = \sqrt{2\sum_{k}\delta(k)W_{1,k}^{n}(2t-k)} \tag{4}$$

$$W_{0,0}^{2n+1}(t) = \sqrt{2\sum_{k}\xi(k)W_{1,k}^{n}(2t-k)} \tag{5}$$

where $\delta(k)$ refers to a low-pass filter and $\xi(k)$ denotes a high-pass filter, both associated with a predefined scaling function and the mother wavelet function. The coefficients $\Omega_j^n(t)$ can be derived by considering the product of the functions $x(t)$ and $W_{j,k}^{n}(t)$:

$$\Omega_j^n(t) = \int_{-\infty}^{+\infty} x(t)\, W_{j,k}^{n}(t)dt \tag{6}$$

Each coefficient WP corresponds to a specific frequency level. While the wavelet transform focuses on low-frequency components, WPT encompasses all elements. This results in low and high-frequency components, known as low and high approximations. In applying WPT, factors such as entropy, energy, and variation must be accounted for during the WP calculation process. Energy serves to characterize distinct classes and, in the proposed methodology, encapsulates failure indicators related to the condition of the insulator. Fluctuations in energy correspond to specific failure types similar to those outlined in [29]. The signal undergoes decomposition into j levels, which establishes orthogonal subspaces from where frequency components can be calculated using the following:

$$\mathrm{E}_j^n = \sum_{k}\left|\Omega_j^n(k)\right|^2 \tag{7}$$

For energy normalization within each frequency band, the distribution percentage for the energy component is expressed as:

$$\mathrm{e}_j^n = \frac{\mathrm{E}_j^n}{\sum_{n=1}^{2j}\mathrm{E}_j^n} \tag{8}$$

The relative energy of the vector illustrates temporal development considering low and high-frequency subspaces. Changes in this distribution pattern reflect energy flow and can reveal identifiable patterns. A binary optimal

value can be determined by the previously discussed tree structure formed by the segmentation of approximation coefficients. This creates new subdivisions (sub-trees) based on the entropy criterion. Depending on the application, these resulting sub-trees may be significantly smaller than the original. This method seeks to identify a minimum criterion to facilitate an efficient algorithm [28].

Figure 4 shows the energy results at four pollution levels at j=3, 4, 5, and 6 based on the presented wavelet model. According to the stated points, these four levels correspond to the energy received from the signal in the frequency range of 5 to 15 kHz. This interval is the same interval that was determined in the frequency analysis and can be effective in evaluating different pollution levels. However, considering the closeness of the results, a more appropriate model can be proposed. Entropy analysis is used considering the PD signal's random nature.

Considering the variability of PD based on the pollution level, the frequency-time analysis can be performed in the 5 to 15 kHz range. This analysis can be performed based on the wavelet transform model. According to [29], the wavelet packet is divided into low and high-frequency bands. In order to achieve a frequency of 5 to 15 kHz, the signal decomposition should be at levels 3, 4, 5, and 6, Considering that the LC signal acts sinusoidal, the mother function can be used based on the three-layer decomposition. In this situation, the uncertainty framework is adopted for probabilistic treatment and is defined as a logarithmic function $H(p_1, \dots, p_n)$, given by:

$$H(p_1, \dots, p_n) = -\sum_{i=1}^{n} p_i log p_i \quad (9)$$

where $p_i$denotes the probability of occurrence in an event i, the entropy reflects the probabilistic uncertainty in a probability distribution [30]. Figure 5 shows the entropy results based on the change in the pollution level. The results of the figure clearly show the change in the entropy level based on the change in the pollution level. This indicates the appropriate performance of the model in the analysis of PD based on the pollution level.

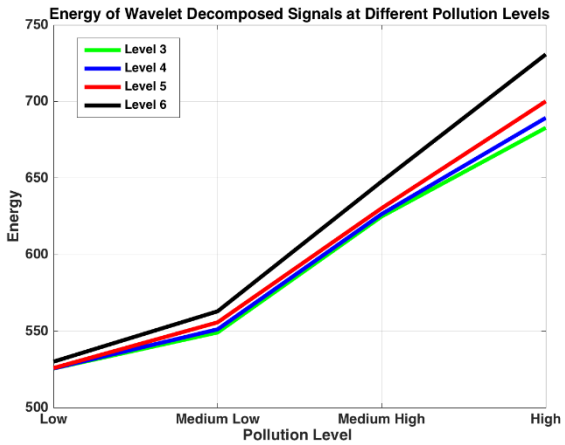

Fig. 4. Energy results at four pollution levels

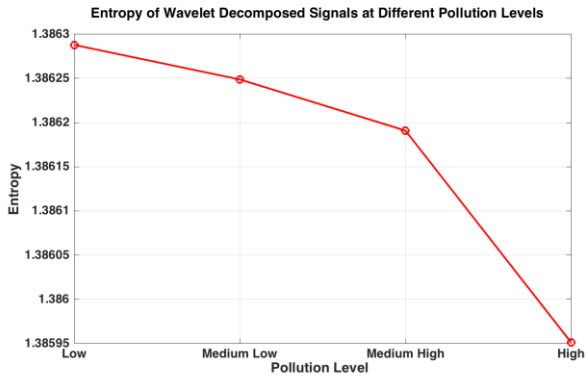

Fig. 5. Entropy results based on the change in the pollution level.

C. *Gradient Boosting Machine Model*

GBM is an advanced ensemble learning method that constructs a series of weak learners, typically decision trees, to create a strong predictive model. Rather than building a single complex model, GBM works by sequentially training multiple models, where each new model focuses on correcting the errors made by the previous ones. In each iteration, the model adjusts the weights assigned to the training samples; misclassified samples gain higher weights, while correctly classified samples are given lower weights. This iterative adjustment continues until a specified number of models have been trained or until the model's error minimizes to an acceptable level [31].

For this study, XGBoost, which stands for Extreme Gradient Boosting, is implemented. XGBoost is a highly optimized and efficient version of the traditional GBM, recognized for its exceptional speed and accuracy in making predictions. It includes numerous enhancements, such as parallel processing, tree pruning, and regularization techniques, contributing to its superior performance over standard GBM implementations. The model was trained using the extracted features derived from PD signals, where each feature vector encompasses specific signal characteristics, allowing the model to learn patterns indicative of varying pollution levels.

To ensure the best results, hyperparameters for XGBoost were meticulously tuned, focusing on critical parameters such as the learning rate, which controls the step size at each iteration; maximum depth, which dictates the complexity of the trees; and the number of estimators, which determines how many trees to build. This tuning process was conducted using cross-validation techniques, allowing us to evaluate the model's performance on unseen data and mitigate the risk of overfitting. By optimizing these hyperparameters, it is aimed to achieve a balance between model complexity and generalization, ultimately enhancing the model's predictive capability for assessing pollution levels in composite insulators through PD signal analysis. The neural network model employed in this study is a feedforward neural

network with five hidden layers containing 1000 neurons. The hidden layer uses ReLU activation, and the output layer employs a softmax activation for classification. The network was trained using a learning rate of 0.001 and the Adam optimiser, with early stopping to prevent overfitting. In comparison, the XGBoost model was implemented with hyperparameters optimised through grid search and cross-validation. The selected hyperparameters are: 100 estimators, maximum tree depth of 6, learning rate of 0.05, subsample ratio of 0.8, column sample by tree of 0.8, gamma of 0.1, and minimum child weight of 4. In gradient boosting, the key idea is to minimize the loss function *L(y,F(x))* using weak learners, each represented by a function $F(x)$. The updated model at iteration m can be expressed as: [31].

$$F_m(x) = F_{m-1}(x) + \nu h_m(x) \quad (10)$$

where $F_m(x)$ is the prediction from the model at the m_{th} iteration. $F_{m-1}(x)$ is the prediction from the previous iteration. ν is the learning rate, and $h_m(x)$ is the new a decision tree. The objective of gradient boosting is to minimize the loss function, which could be the mean squared error for regression tasks or log loss for binary classification tasks. For a regression problem, the loss function can be defined as:[31]

$$L(y, \hat{y}) = \frac{1}{N}\sum_{i=1}^{N}(y_i - \hat{y}_i)^2 \quad (11)$$

which y_i is the actual target value. $\hat{y}_i$ is the predicted value from the model.

The final prediction of the XGBoost model can be calculated as:

$$\hat{y} = F(x) = \sum_{m=1}^{M} h_m(x) \quad (12)$$

where M is the total number of trees. In the context of decision trees (which are the weak learners in GBM and XGBoost), entropy is used to measure the impurity of a node in the tree. The idea is to split the data based on features such that the entropy is minimized, leading to more homogeneous subsets. In XGBoost, while the primary objective function often utilizes squared loss for regression or log loss for classification, it can be uses entropy for classification tasks. The loss function can be expressed in terms of log loss and simulated using cross-entropy. For classification, the cross-entropy loss $L(y, \hat{y})$ can be defined as:

$$L(y, \hat{y}) = -[ylog(\hat{y}) + (1-y)\log(1-\hat{y})] \quad (13)$$

y is the true label (0 or 1) and $\hat{y}$ is the predicted probability. When combining the proposed model with the previous concepts, calculating gradients for XGBoost will involve the derivatives of the cross-entropy loss, effectively using entropy principles. The flowchart in Figure 6 is a representation of the proposed model.

Given the utilized XGBoost, it has leveraged the inherent feature importance scores provided by the algorithm. XGBoost computes feature importance based on how frequently a feature contributes to reducing the loss function across all trees (Tree-based Feature Importance). It selects features with high-importance scores as candidates for the optimal input set. Cross-validation techniques have been utilized to ensure the robustness of the feature selection. Training the model on different subsets of the data and validating it on complementary subsets has verified that the selected features consistently provided good predictive performance.

IV. Results and Discussion

In order to analyze the presented model, according to the flowchart of Figure 6, 400 test data samples from various contamination levels have been examined. One hundred data samples were examined at each contamination level. While The training dataset is derived from multiple tests, covering pollution levels ranging from 0 mg/cm² to 0.5 mg/cm² for ESDD and from 0 mm to 5 mm in thickness for NSDD, simulating low, medium, high, and very high pollution states as classified by IEC 60815. The signal data collected included Partial Discharge (PD) characteristics, which are processed to extract features. The testing dataset comprised additional measurements taken under the same experimental conditions but utilized different insulator samples to ensure the generalizability of the proposed model. Testing was conducted after training to evaluate the model's performance accurately. The training and testing data are 70% and 30% of all data, respectively.

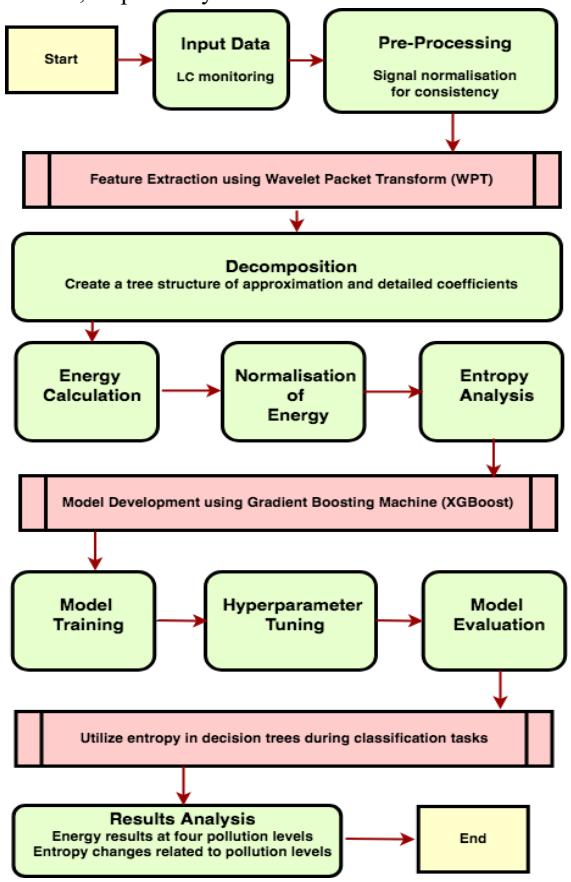

Fig. 6. Flowchart of the presented method

Figure 7 shows the trend of the loss function in the proposed method. The heat map matrix has been drawn as shown in Figure 8. The results of the figure show that the results match 93%, 95%, 92%, and 94% on average for low, medium, high, and very high contamination levels, respectively. The slight deviations from 95% accuracy can be attributed to inherent variability within the test data samples. Each contamination level may exhibit variations in characteristics that are less pronounced, making it challenging for the model to achieve uniform accuracy across all levels. The nature of insulator pollution can result in complex interactions that affect the partial discharge characteristics, which in turn impact the model's classification capabilities. These complexities are particularly evident at higher contamination levels where nuanced differences in the PD signals may influence the model's predictions. The model is trained to generalize across various contamination scenarios. While it performed well (as indicated by the accuracies), the less-than-perfect scores suggest room for improvement. This is typical in real-world scenarios where a model may not fully capture all the variations in the data. In order to comprehensively analysis the model, the precision ratio (Pr) has been examined as a suitable data evaluation model. The accuracy ratio is between the number of samples evaluated at each contamination level and the total number of data. Also, the ratios in Figure 8 are considered the recall rate (Rr). In order to obtain accurate information, the F-score index has been used. The formula of this index is as follows:

$$F - Score = 2 \times \frac{P_r \times R_r}{P_r + R_r} \tag{14}$$

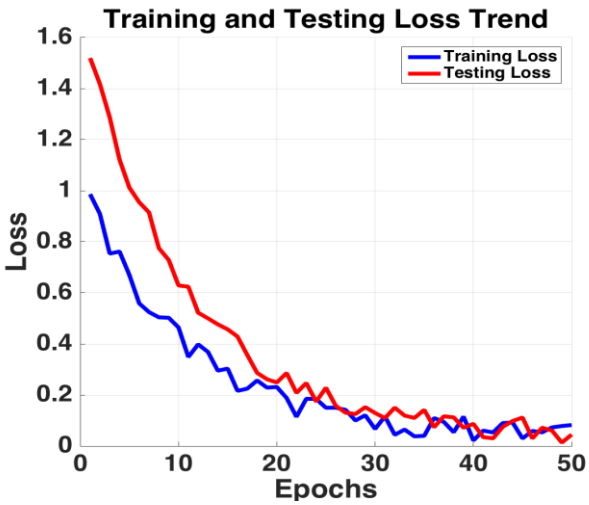

Fig. 7. The trend of the loss function in the proposed method in training and testing data

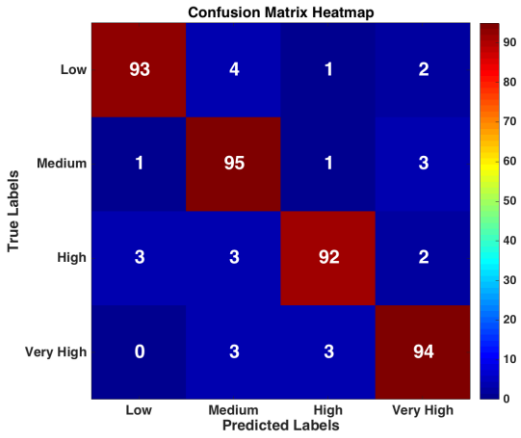

Fig. 8. The heat map matrix of the proposed method's results

A. Sensitivity analysis of pollution level

Table II presents the classification results of the predictive model used to assess pollution levels, revealing a strong overall performance characterized by high accuracy rates ranging from 92% to 95% across different pollution classifications (I to IV). The model demonstrates particularly robust performance for Pollution Level II with an accuracy of 95%. In comparison, high-level pollution (Pollution Level III) shows a slightly lower accuracy of 92%, indicating potential challenges in distinguishing this category. The average accuracy across all levels remains high, with values of 96%, 90%, 95%, and 93%, respectively, demonstrating the model's reliability. Furthermore, the F-scores, which range from 0.924 to 0.945 for the different pollution levels, emphasize a well-balanced approach in achieving both precision and recall rates, indicating that the model effectively minimizes false positives. Despite these commendable results, the assessment matrix reveals areas for improvement, particularly for high and very high-level (III and IV), where misclassifications occurred. Addressing these inaccuracies through model refinement and additional training data could enhance the model's effectiveness, ultimately leading to better classification of pollution levels and contributing to more informed environmental management strategies.

TABLE II ASSESSMENT RESULTS OF POLLUTION CLASS

Pollution Level		Assessment Levels				Total	Rr
		I	II	III	IV		
Actual	I	93	4	1	2	100	93%
	II	1	95	1	3	100	95%
	III	3	3	92	2	100	92%
	IV	0	3	3	94	100	94%
Total		97	105	97	101	-	-
Pr		96%	90%	95%	93%	-	-
F-Score		0.945	0.924	0.935	0.936	-	-

B. Sensitivity analysis of humidity

In order to verify the results, a humidity analysis was performed on the test insulator, revealing noteworthy insights into the model's sensitivity to varying humidity levels. As shown in Table III, the F-scores for pollution levels I to IV demonstrate a general trend of decreasing performance with increasing humidity; however, all F-score values remain above 90%, indicating robust model reliability. Specifically, for Pollution Level I, F-scores decreased from 94.5% at 60% humidity to 90.8% at 90% humidity, suggesting that higher humidity may complicate the classification of low pollution levels due to increased electrical discharges. Conversely, Pollution Level III exhibited a peak F-score of 95.3% at 70% humidity before declining at higher levels, indicating the model's adeptness at classifying moderate pollution under optimal conditions. The important point is the uniform trend in pollution levels III and IV in all humidity levels, which shows the model's reliability in high and very high pollution levels in different humidity. Despite the increased misclassifications at higher humidity, the model's ability to maintain strong performance metrics underscores its resilience.

C. Sensitivity analysis of HC level

In order to evaluate the model's performance concerning the age of the insulators, an HC analysis is conducted, as detailed in Table IV. The results demonstrate that the proposed model effectively detects older insulators, evidenced by consistently high F-scores across all pollution levels. Specifically, for Pollution Level I, the F-scores range from 90.1% for HC level 1 to 96.4% for HC levels 4 and 6, indicating that older insulators are more susceptible to partial discharges and, therefore, can be detected more readily by the model. In contrast, new insulators exhibit reduced F-scores, with the highest value at 95.7% for Pollution Level II at HC level 6, indicating their lower susceptibility to partial discharges and flashover events. While newer insulators tend to produce fewer misclassifications, which leads to lower F-scores, the model remains remarkably reliable when assessing older insulators. These findings underscore the model's potential for practical applications across varying contamination levels, conditions, and insulator ages.

TABLE III ASSESSMENT RESULTS OF HUMIDITY SENSITIVITY ANALYSIS

F-Score %		Humidity			
		60%	70%	80%	90%
Pollution Level	I	94.5	93.5	91.2	90.8
	II	92.4	92.7	91.1	90.2
	III	93.5	95.3	94.2	93.1
	IV	93.6	95.1	93.8	92.3

TABLE IV ASSESSMENT RESULTS OF HC SENSITIVITY ANALYSIS

F-Score %		HC			
		1	3	4	6
Pollution Level	I	90.1	94.5	96.4	96.4
	II	88.3	92.4	95.4	95.7
	III	89.2	93.5	94.3	94.8
	IV	85.4	93.6	93.2	94.4

D. Validation model

The comparative analysis of the proposed model, Support Vector Machine (SVM) [32], and Neural Network (NN) [33] reveals the strengths and weaknesses of each approach in classifying pollution levels based on synthetic data. The results indicate that the proposed model achieved the highest accuracy among the evaluated models, with performance reaching approximately 94.45%. The out-of-bag (OOB) error estimates provided during training further reinforce the model's reliability, indicating how well the model is likely to perform on unseen data.

In contrast, while generally regarded as a robust classification tool, the SVM model has a lower accuracy of around 91.13%. In addition, the use of the SVM method also has limitations. For example, there is complex, multi-dimensional data without carefully tuning hyperparameters and kernel functions. The ability of SVM to create decision boundaries is highly reliant on selecting these parameters, which may not always reflect the optimal separation for non-linear datasets. The Neural Network model, trained with a feedforward architecture containing ten hidden neurons, displayed comparable results to the SVM, achieving around 88.73% accuracy. However, its performance illustrates common challenges associated with neural networks, including the necessity for proper initialization, training time, and the risk of overfitting when working with synthetic data. While neural networks excel in capturing intricate relationships in larger datasets, their reliance on extensive tuning and the quality of training data can sometimes impede their efficiency in more straightforward tasks compared to ensemble methods.

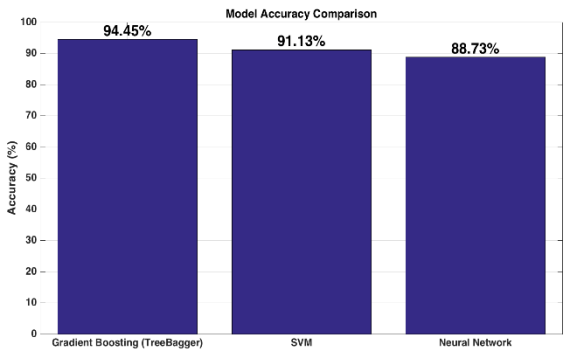

Fig. 9. The comparative analysis of the proposed model, Support Vector Machine, and Neural Network

The overall performance of the proposed model suggests its suitability for classification tasks in diverse contexts, including pollution monitoring, where adaptability to different conditions is vital. The model's resilience against overfitting and its ability to handle noisy data make it a powerful option for real-world applications. Given the nature of pollution data, which can be influenced by various environmental factors, a model that balances accuracy, interpretability, and computational efficiency is essential for effective management. While the Gradient Boosting Model stands out in this comparison, it is essential to recognize that no single model is universally superior. The choice of model ultimately depends on specific application requirements, computational resources, and the characteristics of the dataset being analyzed. Future work should explore enhancements to each model, such as fine-tuning hyperparameters for the SVM and NN or investigating more advanced ensemble methods to improve classification results even further.

The proposed model demonstrates robust performance in scenarios where multiple insulators operate in parallel, even in the presence of signal coupling and interactions. Advanced signal processing techniques have been integrated to enhance the model's capability for operating in coupled environments, allowing it to analyze mixed signals and identify individual partial discharge signatures effectively. Techniques such as time-frequency analysis aid in discerning the frequency components of PD signals over time, enabling the separation of signals from multiple insulators. Additionally, the model employs feature extraction methods to analyze key characteristics of PD signals—such as peak amplitudes, rise times, and energy levels—all of which support accurate pollution level classification even amidst coupling interference. Furthermore, using Gradient Boosting Machines (GBM) enhances the model's proficiency in managing complex datasets and interactions between input variables. This strategic design ensures that the proposed model maintains high classification accuracy and reliability across diverse operational conditions, effectively addressing the challenges of parallel insulator networks.

V. Conclusions

This study introduces a novel AI-driven approach for assessing insulator pollution levels using Gradient Boosting Machine (GBM) and Partial Discharge (PD) characteristics, demonstrating high accuracy across diverse pollution scenarios. The developed model offers a rapid, non-invasive, and reliable alternative to traditional inspection methods, which are often hindered by environmental conditions and physical contact limitations. Importantly, the computational efficiency and robustness of the model suggest strong potential for real-time, online condition monitoring in operational power systems. Implementing such an AI-based system could enable continuous health assessment of insulators, facilitating early detection of pollution-related issues and enabling proactive maintenance, ultimately reducing the risk of outages and enhancing system reliability. In order to prevent flashover in contaminated insulators, the proposed method, based on the detection of LC and PD characteristics, is capable of detecting the contamination level. In this case, the online monitoring system can predict a fault's occurrence before it occurs. Future advancements, including dataset expansion under various environmental conditions and the integration of the model into existing monitoring infrastructure, are essential steps toward realizing practical, real-time deployment in field conditions.

REFERENCES

[1] A. Ghaedi, R. Sedaghati, M. Mahmoudian, and S. Bazyari, “De-Noising of Partial Discharge Signals in HV XLPE Cables by Reference Noise based on the Wavelet Transform,” *International Journal of Industrial Electronics Control and Optimization,* vol. 6, no. 4, pp. 291-306, 2023, doi: 10.22111/ieco.2023.46346.1498

[2] T. Kim and J. Yi, “Application of hydrophobic coating to reduce leakage current through surface energy control of high voltage insulator,” *Applied Surface Science,* vol. 578, p. 151820, 2022, doi: 10.1016/j.apsusc.2021.151820

[3] S. N. Razavinia *et al.*, “Numerical Simulation of Electron Cyclotron Resonance Discharge Generated by Permanent Magnets,” *Power, Control, and Data Processing Systems,* vol. 2, no. 1, 2025, doi: 10.30511/pcdp.2025.718447

[4] M. E. Ibrahim and A. M. Abd-Elhady, “Rogowski coil transducer-based condition monitoring of high voltage insulators,” *IEEE Sensors Journal,* vol. 20, no. 22, pp. 13694-13703, 2020, doi: 10.1109/jsen.2020.3005223

[5] S. Deb, R. Ghosh, S. Dutta, S. Dalai, and B. Chatterjee, “Effect of humidity on leakage current of a contaminated 11 kV Porcelain Pin Insulator,” in *2017 6th International Conference on Computer Applications In Electrical Engineering-Recent Advances (CERA)*, 2017, pp. 215-219: IEEE, doi: 10.1109/CERA.2017.8343329

[6] L. Jin, Z. Xu and S. Zhang, “A pre-warning method of contamination flashover based on the leakage current of insulators in dry condition,” *2017 International Symposium on Electrical Insulating Materials (ISEIM)*, Toyohashi, Japan, 2017, pp. 757-760, doi: 10.23919/ISEIM.2017.8166599.

[7] U. Benisheikh, Z. Abdul-Malek, and A. Sahito, “Classification of leakage current odd harmonic component of aged insulator surface condition under different relative humidity using crest factor,” *Archives of Electrical Engineering,* pp. 1069-1085, 2024, doi:10.24425/aee.2024.152111

[8] L. Zhengfa *et al*., “Study on leakage current characteristics and influence factors of 110kV polluted composite insulators,” *2018 12th International Conference on the Properties and Applications of Dielectric Materials (ICPADM)*, Xi'an, China, 2018, pp. 896-900, doi: 10.1109/ICPADM.2018.8401173.

[9] M. A. Amini and A. R. Sedighi, “A new procedure for determination of insulators contamination in electrical distribution networks,” *International Journal of Electrical Power & Energy Systems,* vol. 61, pp. 380-385, 2014, doi: 10.1016/j.ijepes.2014.03.034.

[10] M. Amini, A. S. Anaraki and M. Sadeghi, "High frequency components of feeder current as diagnostic tool to study contamination conditions of outdoor insulators in power distribution networks," *2013 21st Iranian Conference on Electrical Engineering (ICEE)*, Mashhad, Iran, 2013, pp. 1-6, doi: 10.1109/IranianCEE.2013.6599890.

[11] S. Ahmad, R. Ahmed, R. Abd Rahman, A. Ullah, A. Jamal, and R. Akram, "A comprehensive study of nano/micro fillers on silicone rubber insulators: Electrical, mechanical, and thermal characterization," *Results in Engineering,* vol. 25, p. 103654, 2025, doi: 10.1016/j.rineng.2024.103654.

[12] B. Cao, Y. Liu, Z. Li, S. Shen, L. Wang and Z. Wang, "Assessment of Insulator Pollution Degree Based on Contamination Moisture With Temperature Change," in *IEEE Sensors Journal*, vol. 22, no. 21, pp. 21172-21178, 1 Nov.1, 2022, doi: 10.1109/JSEN.2022.3206215.

[13] Y.-T. Lin and C.-C. Kuo, "Real-time salt contamination monitoring system and method for transmission line insulator based on artificial intelligence," *Applied Sciences,* vol. 14, no. 4, p. 1506, 2024, doi: 10.3390/app14041506.

[14] S. Gao *et al*., "Prediction method of leakage current of insulators on the transmission line based on BP neural network," *2018 IEEE 2nd International Electrical and Energy Conference (CIEEC)*, Beijing, China, 2018, pp. 569-572, doi: 10.1109/CIEEC.2018.8745839.

[15] Z. Fei, Y. Li, and S. Yang, "Partial Discharge Pattern Recognition Based on an Ensembled Simple Convolutional Neural Network and a Quadratic Support Vector Machine," *Energies,* vol. 17, no. 11, p. 2443, 2024, doi: 10.3390/en17112443

[16] Q. Zhu *et al.*, "Research on partial discharge pattern recognition of transformer based on KPCA and JS-SVM algorithm," in *Journal of Physics: Conference Series*, 2025, vol. 2963, no. 1, p. 012013: IOP Publishing, doi: 10.1088/1742-6596/2963/1/012013

[17] H. Jung, Y.-T. Kim, S.-K. Lee, and J.-h. Ahn, "Study on Deep-Learning Model for Phase Resolved Partial Discharge Pattern Classification Based on Convolutional Neural Network Algorithm," *Journal of Electrical Engineering & Technology,* vol. 20, no. 1, pp. 873-878, 2025, doi: 10.1007/s42835-024-01967-9

[18] C. W. Priananda, H. A. Illias, W. J. K. Raymond and I. M. Y. Negara, "Hybrid Deep Learning Models for Enhanced Classification of Phase-Resolved Partial Discharge Patterns from High-Voltage Rotating Machine Insulation," in *IEEE Transactions on Dielectrics and Electrical Insulation*, doi: 10.1109/TDEI.2025.3542343.

[19] H. Shadfar and H. R. Izadfar, "Frequency Response Analysis: An Overview of the Measurement Process and Interpretation of Results for Fault Diagnosis and Location in Power Transformers," *International Journal of Industrial Electronics Control and Optimization,* vol. 8, no. 2, pp. 149-163, 2025, doi: 10.22111/ieco.2024.49470.1603

[20] M. M. Mohsenzadeh, S. Hasanzadeh, H. R. Sezavar, and M. H. Samimi, "Flashover voltage and time prediction of polluted silicone rubber insulator based on artificial neural networks," *Electric Power Systems Research,* vol. 221, p. 109456, 2023, doi: 10.1016/j.epsr.2023.109456

[21] H. Sezavar, N. Fahimi, S. Hasanzadeh, and A. S. Akmal, "Risk assessment of contaminated composite insulators in pre-flashover conditions," *Electric Power Systems Research,* vol. 230, p. 110256, 2024, doi: 10.1016/j.epsr.2024.110256

[22] A. H. Alshalawi and F. S. Al-Ismail, "Partial Discharge Detection Based on Ultrasound Using Optimized Deep Learning Approach," in *IEEE Access*, vol. 12, pp. 5151-5162, 2024, doi: 10.1109/ACCESS.2024.3350555.

[23] S. Li *et al.*, "Partial Discharge Data Enhancement and Pattern Recognition Method Based on a CAE-ACGAN and ResNet," *Symmetry,* vol. 17, no. 1, p. 55, 2024, doi: 10.3390/sym17010055.

[24] M. Messaoudi, S. M. Kameli, S. S. Refaat, H. Abu-Rub and M. Trabelsi, "Deep Learning Based Corona Discharge Severity Classification for High Voltage Equipment," *IECON 2024 - 50th Annual Conference of the IEEE Industrial Electronics Society*, Chicago, IL, USA, 2024, pp. 1-5, doi: 10.1109/IECON55916.2024.10905579.

[25] H. R. Sezavar, N. Fahimi and A. A. Shayegani-Akmal, "An Improved Dynamic Multi-Arcs Modeling Approach for Pollution Flashover of Silicone Rubber Insulator," in *IEEE Transactions on Dielectrics and Electrical Insulation*, vol. 29, no. 1, pp. 77-85, Feb. 2022, doi: 10.1109/TDEI.2022.3146531.

[26] H. R. Sezavar and S. Hasanzadeh, "Integrating Weibull analysis and KAN-ODEs for enhanced flashover prediction in contaminated composite insulators," *Electric Power Systems Research,* vol. 244, p. 111584, 2025, doi: 10.1016/j.epsr.2025.111584

[27] S. F. Stefenon *et al.*, "Wavelet group method of data handling for fault prediction in electrical power insulators," *International Journal of Electrical Power & Energy Systems,* vol. 123, p. 106269, 2020, doi: 10.1016/j.ijepes.2020.106269.

[28] Z. Zhang, F. Yang, H. Zhang, C. Zhou, Y. Li, and H. Liu, "A probabilistic neural network assessment method for insulator pollution level based on discharge noise," *Measurement,* vol. 242, p. 115869, 2025, doi: 10.1016/j.measurement.2024.115869.

[29] Y. I. Jang, J. Y. Sim, J.-R. Yang, and N. K. Kwon, "The optimal selection of mother wavelet function and decomposition level for denoising of DCG signal," *Sensors,* vol. 21, no. 5, p. 1851, 2021, doi:10.3390/s21051851.

[30] H. Farajpanah, A. Adib, M. Lotfirad, H. Esmaeili-Gisavandani, M. M. Riyahi, and A. Zaerpour, "A novel application of waveform matching algorithm for improving monthly runoff forecasting using wavelet–ML models," *Journal of Hydroinformatics,* vol. 26, no. 7, pp. 1771-1789, 2024, doi: 10.2166/hydro.2024.128

[31] C. Bentéjac, A. Csörgő, and G. Martínez-Muñoz, "A comparative analysis of gradient boosting algorithms," *Artificial Intelligence Review,* vol. 54, pp. 1937-1967, 2021, doi: 10.1007/s10462-020-09896-5.

[32] A. A. Salem *et al.*, "Classification of RTV-coated porcelain insulator condition under different profiles and levels of pollution," *Scientific Reports,* vol. 14, no. 1, p. 22759, 2024, doi: 10.1038/s41598-024-73520-7

[33] N. Fahimi, H. R. Sezavar and A. A. Shayegani-Akmal, "Flashover Prediction of Polymer Insulators Based on Dynamic Modeling of Pollution Layer Resistance Using ANN," in *IEEE Transactions on Dielectrics and Electrical Insulation*, vol. 30, no. 1, pp. 122-130, Feb. 2023, doi: 10.1109/TDEI.2022.3207452.

Hamid Reza Sezavar was born in Qom, Iran, in 1991. He received a B.Sc. degree from the Sharif University of Technology, Tehran, Iran, in 2013 and a M.Sc. in electrical engineering from the University of Tehran, Tehran, Iran, in 2015. He then received his PhD in High Voltage from the University of Tehran, Tehran, Iran, in 2022. He is currently working toward an assistant professor position at Qom University of Technology. His principal research interests are High voltage engineering, outdoor insulators, Electrical discharge, and AI algorithms.

Saeed Hasanzadeh was born in Shirvan, Iran, in 1981. He earned his B.Sc. in electrical engineering from Shahroud University of Technology in 2003, followed by his MSc. and Ph.D. from the University of Tehran in 2006 and 2012, respectively. His MSc. thesis focused on High Voltage Engineering, while his Ph.D. dissertation explored Wireless Power Transfer (WPT). In 2013, he joined Qom University of Technology as an Assistant Professor in the Department of Electrical and Computer Engineering, rising to Associate Professor in 2022. He served as the department's Dean from 2018 to 2023. Dr. Hasanzadeh is an editorial board member of the Power Electronics Society of Iran (PELSI), a Technical Program Committee member of the IEEE PEDSTC Conference, and the Scientific Chair of ICREDG2025. He received Qom University of Technology's Top Research Prize in 2019 and 2023 and was recognized as an Outstanding Lecturer in 2020 and 2022. In 2023, he was named Qom province's top innovator for developing two innovative products in partial discharge detection. His research interests include power electronics, electrical machines, wireless power transfer, and high voltage engineering.

IECO

This page intentionally left blank.

International Journal Of
Industrial Electronics Control and Optimization
Print ISSN: 3517-2645
Online ISSN: 3568-2645
Homepage: https://ieco.usb.ac.ir/

Controlling and Estimating the Speed of Shaking Table by Fusing Camera, Encoder and Accelerometer using AUKF and Fuzzy Sliding Mode Controller

Nima Rajabi Namini[1] | Ramazan Havangi[2] | Amir Hossein Abolmasoumi[3]

Faculty of Electrical Engineering and Computer, University of Birjand, Iran.[1,2]
Electrical Engineering department, Arak University, Arak, Iran Iran.[3]
Corresponding author's email: Havangi@Birjand.ac.ir

Article Info

Article type:
Research Article

Article history:
Received: 08-March-2025
Received in revised form: 05-May-2025
Accepted: 26-May-2025
Published online:21-March-2026

Keywords:
Earthquake Simulator,
Multi-Sensor Data Fusion,
Fuzzy,
Sliding Mode Control.

ABSTRACT

An earthquake is a sudden and destructive natural disaster that often results in unpredictable damage to human life and property. Investigating the effects of earthquakes on buildings and enhancing the seismic performance of structures is a crucial approach to mitigating severe damage during such events. One effective tool in testing the resistance of structures against earthquakes is the use of shaking tables. In this paper, the stabilization and control of an earthquake simulator using a fuzzy sliding mode controller (FSMC), an adaptive unscented Kalman filter (AUKF), and an adaptive extended Kalman filter (AEKF) are presented. These filters employ a recursive technique to effectively adjust the noise covariance by utilizing an adaptation method known as the steepest descent. In the proposed approach, the shaking table states are estimated using an accelerometer, encoder, and camera. These estimated states are then utilized by the AEKF/AUKF to stabilize and control the closed-loop system. A fuzzy sliding mode controller is designed to track the reference input and eliminate external disturbances and noise. In sliding mode control, the occurrence of chattering in the control input is unavoidable. To mitigate this undesired chattering phenomenon, a fuzzy inference mechanism has been employed. The image processing approach has been utilized to measure the displacement online using the camera. The advantages of using the camera include not requiring direct contact with the table, as well as offering a low cost and good accuracy. The performance of the proposed method has been examined using the shaking table at the Research Center of Arak University. The obtained results indicate that the suggested method exhibits a high level of efficiency.

NOMENCLATURE

F	Linear force	β	Viscous damping coefficient
p	Number of pole pairs	T_e	Electromagnetic torque
i_d , i_q	Currents on the d and q axes	u_{eq}	Equivalent control input
v_d , v_q	Voltages on the d and q axes	u_{sw}	Switching control input
T	Torque of motor	T_l	Load torque
L_d,L_q	Inductances on d- and q-axes	λ	Flux amplitude
R	Motor winding resistance	η	Ball-screw efficiency
Ω	Angular velocity of the rotor	h	Lead of the ball screw
Θ	Angular displacement of the motor shaft	M	Total mass of the stage
J	Moment of inertia	φ	Boundary layer thickness in FSMC
ξ	Ball-screw efficiency	s	Sliding surface variable
$\tilde{x}$	Tracking error	$\dot{\omega}_{des}$	Desired acceleration signal
		I	Image matrix

I. Introduction

Seismic shake tables serve as indispensable tools for studying the dynamic response of structures subjected to earthquake-like excitations [1–2]. Depending on the application scale and power requirements, these systems typically employ hydraulic or electric actuation[3-4]. Hydraulic mechanisms, characterized by high power density and large stroke capability, are favored for large-scale shaking tables, while electric actuation is generally restricted to smaller laboratory setups [5-6].

Despite substantial advancements in actuation technology and control system design, accurately reproducing complex seismic excitations, particularly acceleration profiles, remains a formidable challenge [7–9]. Small displacement tracking errors can magnify through differentiation, leading to significant inaccuracies in acceleration reproduction. Furthermore, factors such as mechanical backlash, environmental disturbances, system nonlinearities, and sensor imperfections exacerbate this difficulty [10-12].

Previous studies have attempted to improve shaking table performance through various control strategies, including feedforward compensation [13], iterative learning control (ILC) [14], and adaptive control techniques such as minimal control synthesis and model reference adaptive control [15–18]. Additionally, robust controllers like sliding mode control (SMC) have been explored to address system uncertainties and disturbances [19–20]. Despite the success of these methods, they often face limitations: conventional Kalman filtering approaches assume fixed noise statistics, making them vulnerable to model mismatches and variations in measurement noise. While SMC approaches offer robustness, they suffer from undesirable chattering phenomena, which can compromise actuator lifespan and energy efficiency [21-23]. Furthermore, traditional sensor setups that rely heavily on encoders are prone to mechanical degradation, high costs, and installation complexity. Thus, a critical research gap exists: the lack of an integrated approach that simultaneously addresses sensor noise, dynamic system uncertainties, and controller chattering in a practical, cost-effective manner. This study proposes a novel solution by combining adaptive sensor fusion techniques with an intelligent robust control strategy to achieve superior tracking performance [24-26].

In recent years, artificial intelligence (AI)-based control strategies—such as fuzzy logic, neural networks, and adaptive neuro-fuzzy inference systems have attracted considerable interest in the field of seismic control of shaking tables due to their ability to manage nonlinear dynamics and model uncertainties effectively [27, 28]. These methods provide adaptive learning mechanisms that can enhance robustness and suppress undesirable chattering phenomena typically observed in classical sliding mode controllers [29]. Despite these advantages, AI-based control approaches are not without limitations. They often require large datasets for training, exhibit sensitivity to sensor noise, and can encounter challenges in real-time applications due to their computational demands. Moreover, their performance is highly dependent on appropriate design choices, such as the tuning of membership functions in fuzzy systems or the architecture of neural networks. Additionally, unlike conventional model-based techniques, providing formal stability guarantees for AI-based controllers remains an ongoing challenge [30]. Recent advancements, particularly in deep learning, have further expanded the potential of AI in control applications. Methods such as deep reinforcement learning and neural adaptive controllers have demonstrated superior performance in managing highly nonlinear and time-varying systems, particularly in high-uncertainty environments [31–33]. Nevertheless, the application of these advanced techniques to shake table control is still in its early stages and presents a promising direction for future research [34].

Motivated by the aforementioned challenges, This paper presents the design and implementation of a fuzzy sliding mode controller integrated with adaptive estimation filters—namely the AEKF and AUKF—for a laboratory-scale seismic shake table system. The primary objective is to develop an efficient control strategy capable of accurately tracking scaled earthquake excitations, even in the presence of parameter uncertainties and unmodeled dynamics. Particular emphasis is placed on acceleration tracking performance throughout the study. The proposed control framework integrates measurements from encoder sensors, a vision-based camera system, and an accelerometer using the AEKF/AUKF to estimate the system states. These estimated states are then used within the FSMC to ensure precise trajectory tracking. The authors believe that the full integration of the AEKF/AUKF measurement fusion filter and FSMC, along with the corresponding hardware and software implementation, constitutes an innovative and cost-effective solution. This framework holds significant potential for future deployment in commercial shake tables used in earthquake engineering applications. The main contributions of this paper are summarized as follows:

Adaptive Sensor Fusion: Development of a multi-sensor fusion system combining MEMS accelerometers, encoders, and vision-based displacement measurements, with online adaptation of Kalman filter noise covariances for improved state estimation under nonlinear and noisy conditions.

Chattering-Reduced Robust Control: Design of a fuzzy sliding mode control strategy that dynamically regulates the switching surface boundary, reducing chattering effects without compromising robustness.

Practical Implementation: Realization and experimental validation of the proposed approach on a power screw-driven

seismic simulator, demonstrating superior tracking accuracy, disturbance rejection, and robustness compared to conventional control techniques.

The remainder of the paper is organized as follows: Section 2 describes the system modeling and problem formulation. Section 3 presents the sensor fusion design using adaptive Kalman filters. Section 4 details the proposed fuzzy sliding mode controller. Section 5 discusses experimental validation and performance analysis. Finally, Section 6 concludes the paper and outlines directions for future research.

II. Dynamic Model of the System

To derive the system dynamics and facilitate the subsequent control design, the following assumptions are adopted. Sensor noise and drift are bounded and mitigated using adaptive Kalman filtering. Actuator dynamics are considered sufficiently fast relative to the system dynamics, allowing actuator lag to be neglected. External disturbances and modeling uncertainties are assumed to be bounded and modeled as additive terms. The shake table operates within its linear elastic range, and the initial system states are assumed to be measurable or reasonably estimable through multi-sensor fusion. These assumptions are standard and ensure the robustness and practical applicability of the proposed method. The d and q coordinate systems serve as mathematical converters for analysing and modelling three-phase circuits[27].

$$\begin{aligned}\frac{di_d}{dt} &= \frac{v_d}{L_d} - \frac{Ri_d}{L_d} + \frac{L_q}{L_d} p\omega i_q \\ \frac{di_q}{dt} &= \frac{v_q}{L_q} - \frac{Ri_q}{L_q} + \frac{L_d}{L_q} p\omega i_d - \frac{\lambda p\omega}{L_d} \\ T_e &= \frac{3}{2}((L_d - L_q) i_q i_d + \lambda i_q) p\end{aligned} \quad (1)$$

where i_d and i_q are the currents on the d and q axes, espectively. Similarly, for the inductances on these axes, we use the symbols L_d and L_q. The voltages on the d and q axes, we denote them as v_d and v_q respectively. The symbol ω represents the angular velocity of the rotor. λ Signifies the flux amplitude. Furthermore, we introduce two more variables: p denotes the number of pole pairs, while T_e represents the electromagnetic torque. The dynamic equations that describe the motion of a motor shaft can be stated as follows:

$$\frac{d}{dt}\omega = \frac{1}{J}(T_e - \beta\omega - T_l) \quad (2)$$

$$\frac{d\theta}{dt} = \omega \quad (3)$$

where β denotes the viscous damping coefficient associated with the motor bearings, θ is the angular displacement of the shaft, and T_l signifies the load torque acting on the motor shaft[3]. Then, the mechanism of the ball screw is also represented in the following manner.

$$T = \frac{FL}{\xi} \quad (4)$$

where T is the torque generated by the motor, F is linear force, ξ is ball-screw efficiency, and L stands for the lead of the ball screw. For a normal screw wing, the efficiency is approximately 90% [27]. Equation (5) establishes a relationship between the driving force and the rotational acceleration of the ball-screw. By substituting Equation (6) into Equation (2), the fundamental dynamic equation governing the motion of the electric motor shaft can be reformulated, resulting in Equation (7).

$$F = ML\ddot{\theta} \quad (5)$$

$$T_l = \frac{ML^2\ddot{\theta}}{\xi} \quad (6)$$

$$j\frac{d\omega}{dt} = T_e - \beta\omega - \frac{ML^2\ddot{\theta}}{\xi} \quad (7)$$

The term $\ddot{\theta}$ denotes the rotational acceleration of the motor shaft. Additionally, M signifies the combined mass of the stage. This relationship is expressed in (8),

$$M = m + m_1 \quad (8)$$

By rearranging equations (7) and (8):

$$\left(j + \frac{ML^2}{\xi}\right)\frac{d\omega}{dt} = T_e - \beta\omega \quad (9)$$

$$\frac{d\omega}{dt} = \frac{1}{J}(T_e - \beta\omega) \quad (10)$$

$$J = j + \frac{mL^2}{\xi} \quad (11)$$

FSMC for trajectory tracking of shake table with adaptive filtering

Figure 1 shows the schematic diagram of the PMSM/Shake Table system. Data fusion is essential for accurately estimating the system's displacement, velocity, and acceleration by integrating measurements from a MEMS accelerometer, encoder, and camera. Image processing provides advantages over traditional encoders and cameras in displacement measurement for shaking tables, such as non-contact operation, high spatial resolution, adaptability, robustness, and the ability to capture contextual information.

Accelerometers perform well at higher frequencies but lose accuracy at lower frequencies due to sensitivity to low-frequency noise and reduced signal resolution. These low-frequency errors can significantly impact the stability of closed-loop systems, as they are amplified when differentiated to calculate velocity and displacement. This leads to challenges in tracking low-frequency seismic components, causing potential instability or performance degradation.

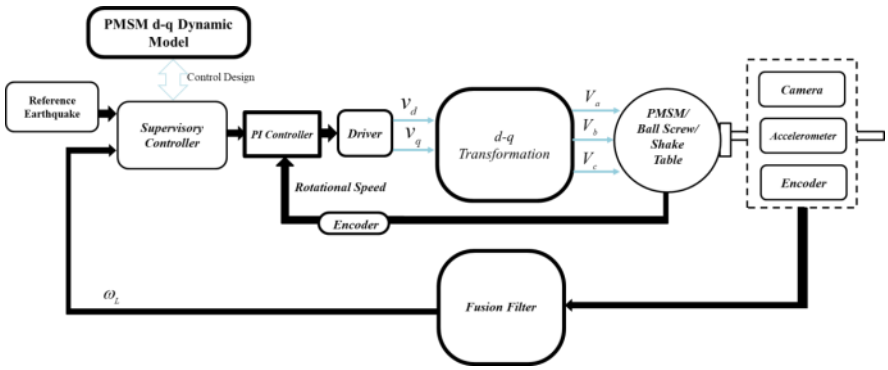

Fig.1. Communication diagram of components and supervisor controller

Accelerometers perform well at higher frequencies but lose accuracy at lower frequencies due to sensitivity to low-frequency noise and reduced signal resolution. These low-frequency errors can significantly impact the stability of closed-loop systems, as they are amplified when differentiated to calculate velocity and displacement. This leads to challenges in tracking low-frequency seismic components, causing potential instability or performance degradation.

To address these issues, adaptive filtering and multi-sensor fusion with systems like encoders and cameras are crucial for improving control system reliability and stability. The data fusion process in AEKF and AUKF follows a recursive procedure. Initially, sensor data—displacement from the encoder, acceleration from the accelerometer, and visual data from the camera—are inputs. In the prediction step, AEKF and AUKF algorithms forecast the next system state using a dynamic model. The update step incorporates actual sensor measurements to refine the predicted states.

In AEKF, the correction is based on a linearized model using Jacobian matrices to approximate the system's nonlinear dynamics. Conversely, AUKF uses the unscented transformation to directly propagate the mean and covariance through nonlinear functions, avoiding linearization. This enables AUKF to better handle nonlinearities in sensor data. Both AEKF and AUKF adaptively update noise covariance matrices, a critical feature given the variability in measurement noise caused by environmental conditions or sensor performance. A recursive adaptation rule adjusts the noise covariance matrices dynamically, ensuring filter robustness and enhancing state estimation accuracy over time.

A. Fuzzy-Sliding-Mode Supervisory Controller

Developing an effective controller to accurately follow the desired acceleration trajectory of a shake table involves numerous challenges, mainly due to system nonlinearities and environmental uncertainties. The presence of friction, actuator saturation, and nonlinear electrical or hydraulic dynamics complicates modeling and control design.

Remark 1 : Nonlinearities such as actuator saturation and friction introduce unpredictable behavior that cannot be fully captured by linear models, necessitating adaptive and robust control approaches like FSMC.

Moreover, acceleration, being the second derivative of displacement, amplifies any noise or error present in displacement or velocity measurements. Low-frequency noise and sensor limitations further degrade feedback quality, making precise trajectory tracking difficult. External disturbances such as temperature variations and varying payloads also affect system dynamics.

Remark 2. Errors in displacement or velocity are magnified in acceleration, particularly at low frequencies—making noise rejection and real-time adaptability essential for accurate tracking.

To overcome these challenges, this study integratesFSMC with AUKF. The combined scheme aims to achieve robust tracking of earthquake-like signals under two key uncertainties:

Model uncertainties, arising from unaccounted system dynamics.

Payload inconsistencies, caused by the installation of various structures on the shake table during experiments.

The shake table control system consists of two loops. The first loop uses a proportional-integral (PI) controller to track the control input. The second loop is a supervisory controller that monitors the overall system performance. Since the motor controller operates with a PI configuration, the supervisory FSMC ensures robust system behavior. By integrating AEKF/AUKF techniques into closed-loop velocity control, the system achieves precise control over velocity and acceleration.

The FSMC is specifically designed to regulate the shake table's velocity, with the sliding surface defined as detailed in [29]. This approach effectively handles dynamic system behavior and ensures accurate trajectory tracking, even under varying experimental conditions. The sliding surface s is selected based on the system's states, as defined below:

$$s(x,t) = \left(\frac{d}{dt} + \alpha\right)^{n-1} \tilde{x} \tag{12}$$

Here, $\tilde{x}$ is the tracking error between the reference trajectory and the actual state of the system, the parameter n represents the order of the governing dynamic equations, α denotes a constant that is strictly positive.The choice of the sliding surface (S) is determined by the system states, with $s(x,t)=\tilde{x}$ [30]. Employing equation (1), the time derivative for s is as:

$$\dot{s}(t)=\frac{1}{J}(T_e-\beta\omega-T_l)-\dot{\omega}_{des} \quad (13)$$

The desired acceleration signal, denoted as $\dot{\omega}_{des}$, is bounded, meaning there exists a positive constant L such that: $|\dot{\omega}_{des}(t)|\le L$, $\forall t\ge 0$.The control input is also defined as (14) where u_{eq} is the equivalent control and is obtained from (15).

$$u=u_{eq}-u_{reach} \quad (14)$$

To obtain the equivalent control law necessary for the electric torque here, we derive the following relationship by setting equation (13) equal to zero.

$$u_{eq}=\hat{\beta}\omega+T_l+\hat{J}\dot{\omega}_{des} \quad (15)$$

where $\hat{\beta}$, and $\hat{J}$ are estimated values of β, and J parameters, respectively. To ensure the stability of the sliding surface using the Lyapunov stability theory, we initially consider the selected Lyapunov function as follows:

$$V(s)=\frac{1}{2}S^2 \quad (16)$$

which is a positive definite function.

$$\dot{V}(s)=\frac{1d}{2dt}S^2\le-\eta|S|,\eta\ge 0 \quad (17)$$

where η is a positive non-Fer constant, when inequality (17) is achieved, it indicates that the system is both stable and well-regulated. u_{reach} is also calculated as (18) satisfying the sliding condition.

$$u_{reach}=ksgn(S) \quad (18)$$

To achieve the intended sliding behaviour, it is necessary to select the controller output is as:

$$u=\hat{\beta}\omega+T_l+\hat{J}\dot{\omega}_{des}-ksgn(S) \quad (19)$$

To reduce the chattering caused by control command, we propose the implementation of a boundary layer with a thickness φ . Consequently, Equation (19) is reformulated as follows:

$$u=\hat{\beta}\omega+T_l+\hat{J}\dot{\omega}_{des}-ksat\left(\frac{s}{\varphi}\right) \quad (20)$$

The sgn(·) function represents the standard sign function, while the sat(·) function refers to the standard saturation function, which limits the output within the range [−1,1]. discontinuous switching of the control input as the system state approaches the sliding surface. This high-frequency oscillation can lead to actuator wear, system instability, and degraded control performance. In precision applications like shake tables, where accurate tracking of displacement, velocity, and acceleration is critical, chattering can significantly reduce control accuracy and system lifespan.

To address this problem, a fuzzy inference mechanism was incorporated into the sliding mode control design, resulting in FSMC. FSMC mitigates chattering by dynamically adjusting the boundary layer thickness through fuzzy logic. In traditional SMC, discontinuous control actions produce high-frequency oscillations that adversely affect performance. In contrast, the fuzzy system adaptively fine-tunes the boundary layer thickness based on real-time system states, such as velocity and acceleration errors.

TABLE 1FUZZY RULES RELATED TO FUZZY SLIDING MODE CONTROLLER WITH SPEED AND ACCELERATION ERRORS

		Acceleration Error				
		nb	nm	Ze	pe	**pb**
Velocity Error	nb	nb	nb	Nm	nm	**ze**
	nm	nb	nm	Nm	ze	**pm**
	ze	nm	nm	Ze	pm	**pm**
	pm	nm	ze	Pm	pm	**pb**
	pb	ze	pm	Pm	pb	**pb**

This adaptive adjustment ensures a smoother transition between control states, minimizing abrupt changes in the control signal. Fuzzy rules dynamically modify the saturation function within the control law, preserving robust performance while effectively reducing chattering. Consequently, FSMC enhances both control precision and system stability, even under varying conditions and external disturbances, as validated through experimental results.

TABLE 2 THE VALUES OF THE DESIGNED CONTROLLER

Parameter	**Value**
β_{min}	**18**
β_{max}	**22**
$\hat{\beta}$	**19.9**
J_{min}	**0.000577** kgm^2
J_{max}	**0.001421** kgm^2
$\hat{J}$	**.00090596** kgm^2
k	**0.88**
φ	**0.01**

Table 1 presents the fuzzy controller's rule base, where each input variable is divided into five membership functions: negative big (nb), negative medium (nm), zero (ze), positive medium (pm), and positive big (pb). A schematic diagram of the proposed supervisory controller based on the fuzzy sliding mode methodology is shown in

Fig.1.To ensure the reproducibility of our results, detailed information regarding the tuning of FSMC is provided. The membership functions were designed as triangular shapes with 50% overlap, and the fuzzy rule base was determined through expert knowledge and iterative optimization based on minimizing the root mean square error (RMSE) of the control output. The sliding surface parameters λ and η were initially selected based on system dynamics and then fine-tuned through grid search within predefined stability margins. The gains of the equivalent control law and switching control components were adjusted using trial-and-error guided by Lyapunov stability criteria. Table 2 summarizes all final parameter values used in the experiments, providing a complete reference for replicating the controller design and validation process. Design of adaptive filters (AEKF and AUKF)

The integration of the MEMS accelerometer, encoder, and camera sensor is performed through a data fusion process, where each sensor contributes complementary information to estimate the shake table's displacement, velocity, and acceleration. To optimally combine these measurements, Extended Kalman Filter (EKF) and Unscented Kalman Filter (UKF) techniques are employed.

The Kalman filter is a recursive algorithm that estimates the state of a dynamic system by processing noisy measurements in real-time, without the need to store previous data. It achieves this by fusing model-based predictions with actual observations [31]. However, due to the high nonlinearity of the system analyzed in this study, the conventional Kalman filter is inadequate. Therefore, the EKF and UKF are adopted to address the nonlinearities. The UKF, leveraging the unscented transformation, directly propagates the mean and covariance through nonlinear dynamics, offering a more accurate state estimation compared to linearization-based approaches. Although slightly more computationally demanding than the EKF, the UKF's enhanced capability in handling nonlinear systems makes it particularly suitable for high-precision applications such as seismic tracking in shake tables.

Remark 3: Compared to the linearization-based EKF, the UKF improves estimation accuracy in highly nonlinear systems by eliminating the need for Jacobians and instead applying the unscented transformation on sigma points.

Adaptive filtering techniques dynamically adjust the process and measurement noise covariance matrices, Q and R, which are critical to filter performance. This study focuses on the adaptive estimation of these covariances. Two primary objectives are pursued: (1) implementing AEKF and AUKF algorithms to accurately estimate the table's state variables, and (2) analyzing and comparing the performance of AEKF and AUKF to highlight their respective strengths and limitations.

Since the shake table dynamics are modeled in continuous time, while the adaptive filters are formulated in discrete time, the fourth-order Runge-Kutta method is employed to discretize the system. This method numerically approximates the solutions of the ordinary differential equations governing the shake table, enabling the application of the discrete-time filtering algorithms.

$$y_k = \begin{bmatrix} y_{Encoder} + r_{Encoder} \\ y_{camera} + r_{camera} \\ y_{Acceleration} + r_{Acceleration} \end{bmatrix} \tag{21}$$

where $\left(r_{Encoder}, r_{camera}, r_{Acceleration}\right)$ are measurement noises. The measurement and process noise covariance terms are uncorrelated, possessing white noise characteristics and following a Gaussian distribution with a mean of zero. These noise terms have known covariance matrices R and Q, respectively.

How to measure displacement using image processing technique is explained. The purpose of image processing in this research is to measure the displacement response of the moving plate of the shaking table. For this purpose, a screen with a white background, in the middle of which a rectangular sign in black colour with specific dimensions is installed on the table as the desired target for tracking. A 30-frame camera is also placed at a certain distance from the target screen. The image matrix is formed by the following relation:

$$I(x,y) = I(x+u, y+v) \tag{22}$$

where I is the image matrix, u and v are the pixel displacement descriptors. The image processing algorithm looks for pixels in each column that have values lower than the threshold value. The threshold value is the value that separates the black rectangle from the image background. Any column in which the number of pixels with a value less than the threshold is close to the number of pixels of the width of the black rectangle is averaged from the spatial coordinates of those pixels, and vertical calculations end in that column. The number obtained from this average is the coordinate of the center of the black mark in the vertical direction. The same method is used to obtain the horizontal center of the mark. Hence, by procuring the precise coordinates of the mark's center within each frame, one can ascertain the displacement of the table. Equation (23) shows this process.

$$y = \frac{\sum i \in [0,R]^{i}[I(i,yn) < T]}{\sum i \in [0,R]^{1}[I(i,yn) < T]} \tag{23}$$

where y is the coordinate of the center of the target in the vertical direction. R is the number of pixels in a column and T is the threshold value and yn is the columns to be processed and is obtained from equation (24). The center of the target in the horizontal direction is obtained in the same way.

$$yn = \sum_{j=1}^{n} \frac{c \times j}{n} \quad (24)$$

Here, according to the dimensions of the image and the black rectangle, the image is divided into 8 parts. In equation (24), n is equal to 8. C is the number of pixels in a row or the same number of columns. By having the coordinates of the center of the mark in each frame of the image, the displacement of the table is obtained in terms of the number of pixels, but the goal is to calculate the displacement of the meter in millimeters. Therefore, the dimensions of each pixel should be obtained in millimeters. For this, first, according to the dimensions of the black mark and the number of pixels it occupies in the image, the dimensions of each pixel can be obtained in millimeters. A simple camera is used in this research. In summary, the discrete nonlinear system is as:

$$\begin{aligned} x_k &= f(x_{k-1}) + u_{k-1} + w_{k-1} \\ y_k &= h(x_k) + v_k \end{aligned} \quad (25)$$

Is the process noise, the function f represents a dynamic model, which may be nonlinear. Similarly, the function h represents a measurement model, which may also be nonlinear[31]. Furthermore, the covariance of process noise $Q_k = E[w_k {w_k}^T]$is as:

$$Q_k = diag[q_k^1 \quad q_k^2 \quad q_k^3 \quad q_k^4 \quad q_k^5], q_k^n \rangle 0 \quad (26)$$

Ultimately, the $v_k \sim N(0, R_k)$ represents a measurement noise characterized by a Gaussian distribution with a mean of zero. This noise is referred to as white noise due to its constant power across all frequencies. The covariance of this noise, denoted by $R_k = E[v_k {v_k}^T]$, can be represented in the following mathematical expression.

$$R_k = diag[r_k^1 \quad r_k^2 \quad r_k^3] \quad r_k^m \rangle 0, \quad m = 1,2,3 \quad (27)$$

3-2-1-Estimation of Table Parameters using EKF

The Extended Kalman filter algorithm has two steps of prediction and updating as below [32].

• Prediction

$$\hat{x}_{k|k-1} = F_k \hat{x}_{k-1} + u_{k-1} \quad (28)$$

$$P_{k|k-1} = F_k P_{k-1} F_k^T + Q_{k-1} \quad (29)$$

• Update

$$S_{k|k-1} = H_k P_{k|k-1} H_k^T + R_k \quad (30)$$

$$K_k = F_k P_{k|k-1} H_k \left(S_{k|k-1}\right)^{-1} \quad (31)$$

$$\hat{Z}_{k|k-1} = h\left(\hat{x}_{k|k-1}\right) \quad (32)$$

$$\hat{x}_k = \hat{x}_{k|k-1} + K_k\left(y_k - \hat{y}_{k|k-1}\right) \quad (33)$$

$$P_{k-1} = (I - K_k H_k) P_{k|k-1} \quad (34)$$

$$F_k = \frac{\partial f}{\partial x} | x = \hat{x}_{k-1} \quad (35)$$

$$H_k = \frac{\partial h}{\partial x} | x = \hat{x}_{k-1} \quad (36)$$

Estimation of Table Parameters using UKF

The EKF is widely utilized for estimating the states of nonlinear continuous-time systems by combining model-based predictions with real-time measurements. However, EKF requires linearization of the nonlinear system dynamics around the current estimated state at each time step. In complex systems such as the PMSM, this linearization process must be repeated continuously and can result in substantial computational complexity. Furthermore, the resulting linearized equations may become increasingly intricate, thereby adding to the processing burden.

In contrast, the UKF serves as a highly effective alternative to the EKF. Rather than linearizing the differential equations, the UKF utilizes the unscented transformation (UT) to directly propagate the mean and covariance of the state distribution through the nonlinear functions [33]. The UT provides a more accurate representation of the nonlinear transformations by capturing higher-order moments, which leads to improved estimation performance, especially in systems characterized by significant nonlinearities and model uncertainties.

This advantage is clearly reflected in the shake table experiments conducted in this study, where the UKF demonstrated superior accuracy and robustness compared to the EKF. The estimation process using UKF is described as follows:

• Initialization:

$$\begin{aligned} \hat{x}_0 &= E(x_0) \\ P_0 &= E((x_0 - \hat{x}_0)(x_0 - \hat{x}_0)^T) \\ W_0^m &= \frac{\lambda}{L + \lambda} \\ W_0^c &= \frac{\lambda}{L + \lambda} + (n - \alpha^2 + \beta) \\ W_i^m &= W_i^c = \frac{1}{2(\lambda + L)}, i = 1, \ldots, 2L \\ \lambda &= \alpha^2 (L + \kappa) - L \end{aligned} \quad (37)$$

where λ represents a scaling parameter, which is determined by the constant parameters $0 \le \alpha \le 1$ and $\boldsymbol{K}$ [34]. L denotes the dimensions of the state vector. Additionally, β is a non-negative parameter . When dealing with a Gaussian prior, the optimal value for β is considered to be 2 [34].

• Sigma Points Calculation and Time Update:

A set of weighted sigma points x_{k-1} is generated by

$$\begin{aligned} x_{k-1} &= \\ &\left[\hat{x}_{k-1} \quad \hat{x}_{k-1} + \sqrt{L + \lambda}(\sqrt{P_{k-1}})_i \quad \hat{x}_{k-1} - \sqrt{L + \lambda}\right(\\ &i = 1, \ldots, n \end{aligned} \quad (38)$$

Cholesky decomposition is used to calculate$\sqrt{P_{k-1}}$, and the subscript i represents the column of the matrix.

$$\begin{aligned} P_{k|k-1} &= \sum_{i=0}^{2L} W_i^c \left(x_{i,k|k-1} - \hat{x}_{k|k-1}\right)\left(x_{i,k|k-1} - \hat{x}_{k|k-1}\right)^T \\ &\quad + Q_k \\ y_{i,k|k-1} &= h(x_{i,k|k-1}) \\ \hat{y}_{k|k-1} &= \textstyle\sum_{i=0}^{2L} W_i^m y_{i,k|k-1} \end{aligned} \quad (39)$$

During the forecasting stage, the model information serves as a vital factor, whereas the measurement data is incorporated into the estimates in the data assimilation stage.

• **Measurement Update:**

$$P_k^{\hat{y}\hat{y}} = \sum_{i=0}^{2L} W_i^m [y_{i,k|k-1} - \hat{y}_{k|k-1}][y_{i,k|k-1} - \hat{y}_{k|k-1}]^T + R_k$$

$$P_k^{\hat{x}\hat{y}} = \sum_{i=0}^{2L} W_i^c [x_{i,k|k-1} - \hat{x}_{k|k-1}][y_{i,k|k-1} - \hat{y}_{k|k-1}]^T \quad (40)$$

$$K_k = P_k^{\hat{x}\hat{y}} P_k^{\hat{y}\hat{y}}$$

$$\hat{x}_k = \hat{x}_{k|k-1} + K_k[y_k - \hat{y}_{k|k-1}]$$

$$P_k = P_{k|k-1} - K_k P_k^{\hat{y}\hat{y}} K_k^T$$

Innovative Adaptive Algorithm Utilizing the Steepest Descent Method

In adaptive filtering algorithms, the process and measurement noise covariance matrices, denoted as Q and R respectively, serve as critical parameters that directly influence the performance and robustness of the estimator [35], [36]. In traditional Kalman filtering frameworks, these matrices are typically assumed to be known a priori and remain fixed throughout the estimation process. However, in many real-world applications, particularly in dynamic and uncertain environments, the statistical properties of noise may evolve over time due to changing operational conditions, sensor degradation, or environmental disturbances. As a consequence, maintaining static covariance assumptions can severely impair filter performance, leading to biased estimates and loss of optimality. To overcome these limitations, this study introduces a recursive covariance adaptation mechanism based on the steepest descent method. The steepest descent technique is a classical yet powerful optimization approach widely employed in adaptive filtering, offering an efficient means of iteratively minimizing cost functions associated with estimation errors. By leveraging the steepest descent principle, the proposed adaptation algorithm updates Q and R in real time, thereby enabling the filter to remain responsive to nonstationary noise characteristics.

The core idea behind the proposed adaptation strategy is to minimize the discrepancy between the empirical innovation covariance, derived from actual measurement residuals, and the theoretical innovation covariance predicted by the Kalman filter. Specifically, a cost function is formulated based on the norm of the difference between these two covariance matrices. The steepest descent method is then applied to adjust Q and R iteratively in the direction that reduces this cost, thereby ensuring that the filter maintains consistency and optimality even under time-varying noise conditions. This dynamic adjustment mechanism not only enhances the adaptability of the Kalman filter but also improves its robustness against modeling inaccuracies and external perturbations, making it particularly suitable for practical applications where noise environments are unpredictable and rapidly changing. In order to accomplish this objective, the initial step involves defining the disparity between the measurements in the following manner:

$$e_k = y_k - \hat{y}_{k|k-1} \quad (41)$$

Here, Z_k and $\hat{Z}_{k|k-1}$ are the real measurement and its estimated value, respectively. The remaining actual covariance of the above relationship is estimated by averaging this sequence according to the following relationship.

$$\hat{C}_{ek} = \frac{1}{M} \sum_{j=k-M+1}^{k} e_j \, e_j^T \quad (42)$$

The size of the estimation window is denoted by M. Deterministic and stochastic methods are employed to select the optimal size of the moving window. In the realm of deterministic techniques, an optimization problem is typically characterized by the deliberate selection of a suitable objective function, while taking into account the constraints imposed by limited memory[37]. Now, having the actual covariance $\hat{C}_{ek}$ and the theoretical covariance $S_{k|k-1}$ of the system, the cost function is defined as follows [38]:

$$J_k = \frac{1}{2} tr\{(S_{k|k-1} - \hat{C}_{ek})(S_{k|k-1} - \hat{C}_{ek})^T\} \quad (43)$$

The objective of employing sequence-based strategies for innovation is to minimize $S_{k|k-1} - \hat{C}_{ek}$ by altering R and Q. Hence, to minimize the cost function, it is crucial to ensure that the actual and theoretical covariance are identical. If there is a difference between the process and measurement noise covariance's from their actual values, it leads to a difference between these two covariance. The adaptive algorithm for process and measurement noise covariances is as follows:

$$q_k^n = |\lambda_{q,k}^n q_{k-1}^n + \mu_{q,k}^n| \quad n = 1,2,3,4,5 \quad (44)$$

$$r_{k+1}^m = |\lambda_{r,k+1}^m r_k^m + \mu_{r,k+1}^m| \quad m = 1,2,3 \quad (45)$$

where q_k^n and r_{k+1}^m, representing the Q_k and R_k matrices respectively. The primary objective is to refine the values of $\lambda_{r,k+1}^m$, $\mu_{r,k+1}^m$, $\lambda_{q,k}^n$ and $\mu_{q,k}^n$ using the steepest descent technique. This technique aims to minimize the value of J_k as much as possible.

$$\lambda_{r,k+1}^m = \lambda_{r,k}^m - \eta_k^R \frac{\partial J_k}{\partial \lambda_{r,k}^m} = \lambda_{r,k}^m - \eta_k^R \frac{\partial J_k}{\partial r_k^m} \frac{\partial r_k^m}{\partial \lambda_{r,k}^m} \quad (46)$$

$$\mu_{r,k+1}^m = \mu_{r,k}^m - \eta_k^R \frac{\partial J_k}{\partial \mu_{r,k}^m} = \mu_{r,k}^m - \eta_k^R \frac{\partial J_k}{\partial r_k^m} \frac{\partial r_k^m}{\partial \mu_{r,k}^m} \quad (47)$$

$$\lambda_{q,k}^{n} = \lambda_{q,k-1}^{n} - \eta_k^{Q} \frac{\partial J_k}{\partial \lambda_{q,k-1}^{n}} = \lambda_{q,k-1}^{n} - \eta_k^{R} \frac{\partial J_k}{\partial q_{k-1}^{m}} \frac{\partial q_{k-1}^{m}}{\partial \lambda_{q,k-1}^{n}} \quad (48)$$

$$\mu_{q,k}^{n} = \mu_{q,k-1}^{n} - \eta_k^{Q} \frac{\partial J_k}{\partial q_{q,k-1}^{n}} = \mu_{q,k-1}^{n} - \eta_k^{Q} \frac{\partial J_k}{\partial q_{k-1}^{n}} \frac{\partial q_{k-1}^{n}}{\partial q_{q,k-1}^{n}} \quad (49)$$

The training parameters η_k^{R} and η_k^{Q} are selected based on empirical evidence. For relations (46), (47), (48) and (49), the following equalities hold:

$$\frac{\partial r_k^m}{\partial \lambda_{r,k}^m} = r_{k-1}^m . sgn\left(\lambda_{r,k}^m r_{k-1}^m + \mu_{r,k}^m\right) \quad (50)$$

$$\frac{\partial r_k^m}{\partial \mu_{r,k}^m} = sgn\left(\lambda_{r,k}^m r_{k-1}^m + \mu_{r,k}^m\right) \quad (51)$$

$$\frac{\partial q_{k-1}^m}{\partial \lambda_{q,k-1}^n} = q_{k-2}^n . sgn\left(\lambda_{q,k-1}^n q_{k-2}^n + \mu_{q,k-1}^n\right) \quad (52)$$

$$\frac{\partial q_{k-1}^n}{\partial q_{q,k-1}^n} = sgn\left(\lambda_{q,k-1}^n q_{k-2}^n + \mu_{q,k-1}^n\right) \quad (53)$$

The provided equations employ the notation sgn to represent the sign function. Furthermore, to calculate $\frac{\partial J_k}{\partial r_k^m}$ and $\frac{\partial J_k}{\partial q_{k-1}^m}$, the following relationship is used.

$$\frac{\partial J_k}{\partial r_k^m} = \frac{1}{2} tr\left(\frac{\partial (S_{k|k-1} - \hat{C}_{ek})^2}{\partial r_k^m}\right) = tr\left(\left(\frac{\partial S_{k|k-1}}{\partial r_k^m} - \frac{\partial \hat{C}_{ek}}{\partial r_k^m}\right)(S_{k|k-1} - \hat{C}_{ek})\right) \quad (54)$$

By utilizing Equations (28) and (40), we can derive the following result.

$$\frac{\partial \hat{C}_{ek}}{\partial r_k^m} = 0 \quad (55)$$

$$\frac{\partial S_{k|k-1}}{\partial r_k^m} = \frac{\partial R_k}{\partial r_k^m} \quad (56)$$

where $\frac{\partial R_k}{\partial r_k^m}$ is a square matrix with dimension m. Similarly, $\frac{\partial J_k}{\partial q_{k-1}^n}$ for q_{k-1}^n is expressed as

$$\frac{\partial J_k}{\partial q_{k-1}^n} = \frac{1}{2} tr\left(\frac{\partial (S_{k|k-1} - \hat{C}_{ek})^2}{\partial q_{k-1}^n}\right) = tr\left(\left(\frac{\partial S_{k|k-1}}{\partial q_{k-1}^n} - \frac{\partial \hat{C}_{ek}}{\partial q_{k-1}^n}\right)(S_{k|k-1} - \hat{C}_{ek})\right) \quad (57)$$

$$\frac{\partial \hat{C}_{ek}}{\partial q_{k-1}^n} = 0 \quad (58)$$

$$\frac{\partial S_{k|k-1}}{\partial q_{k-1}^n} = H_k \frac{\partial Q_k}{\partial q_{k-1}^n} H_k^T \quad (59)$$

where $\frac{\partial Q_k}{\partial q_{k-1}^n}$ is a square matrix with dimension n. Finally, we can express the laws for adapting coefficients as follows:

$$\lambda_{r,k+1}^m = \lambda_{r,k}^m - \eta_k^R . r_{k-1}^m . sgn\left(\lambda_{r,k}^m r_{k-1}^m + \mu_{r,k}^m\right) tr\left(\left(\frac{\partial R_k}{\partial r_k^m}\right)\left(S_{k|k-1} - \hat{C}_{ek}\right)\right) \quad (60)$$

$$\mu_{r,k+1}^m = \mu_{r,k}^m - \eta_k^R . sgn\left(\lambda_{r,k}^m r_{k-1}^m + \mu_{r,k}^m\right) tr\left(\left(\frac{\partial R_k}{\partial r_k^m}\right)\left(S_{k|k-1} - \hat{C}_{ek}\right)\right) \quad (61)$$

$$\lambda_{q,k}^n = \lambda_{q,k-1}^n - \eta_k^Q . q_{k-2}^n . sgn\left(\lambda_{q,k-1}^n q_{k-2}^n + \mu_{q,k-1}^n\right) tr\left(\left(H_k \frac{\partial Q_{k-1}}{\partial q_{k-1}^n} H_k^T\right)\left(S_{k|k-1} - \hat{C}_{ek}\right)\right) \quad (62)$$

$$\mu_{q,k}^n = \mu_{q,k-1}^n - \eta_k^Q . sgn\left(\lambda_{q,k-1}^n q_{k-2}^n + \mu_{q,k-1}^n\right) tr\left(\left(H_k \frac{\partial Q_{k-1}}{\partial q_{k-1}^n} H_k^T\right)\left(S_{k|k-1} - \hat{C}_{ek}\right)\right) \quad (63)$$

TABLE 3 PARAMETERS OF THE BALL-SCREW-DRIVEN SERVOMECHANISM

Parameter	Value	Units
L_d	0.00525	H
L_q	0.00525	H
R	0.9585	Ohm
p	8	_
β	0.0003035	Nm/rad/s
λ	0.1827	v/rad/s
η	%90	_
j	0.00805512	Kgm²
h	20	Mm
m	16.75	Kg
m_1	10	Kg

Figure 2 illustrates the block diagram of the proposed adaptive filter. As shown, measurements from three linear encoders, a camera, and an accelerometer are fed into the AEKF/AUKF to estimate all relevant system states. The estimated linear velocity is processed by the feedback filter, which subtracts it from the reference input representing the desired earthquake ground motion. The resulting velocity error is then passed to the FSMC to generate appropriate control signals. The proposed method, combining FSMC with AEKF/AUKF for shake table control, significantly enhances the accuracy and robustness of seismic simulations. Its ability to handle system nonlinearities, sensor noise, and payload variations improves the reliability of shake table tests, thereby contributing to the development of safer and more resilient structures.

III. Results of Experimental Setup Testing

To evaluate the proposed control strategy for regulating displacement, velocity, and acceleration, an experimental study was conducted at Arak University [26] using a uniaxial

earthquake simulator, as shown in Fig. 2. The shake table is driven by a PMSM coupled to a ball-screw mechanism, capable of achieving a maximum velocity of 100 mm/s and an acceleration of 2g, suitable for replicating moderate seismic events. The control system includes a servo drive, a Windows-based host PC, an ATMega32 microcontroller, an Advantech PCI-1716 DAQ card, a SCXI-1000 signal conditioner, and analog input modules. A linear encoder with 5 µm resolution measures the stage displacement, while a shaft encoder operating at 2500 pulses per revolution monitors the motor shaft angle. An ADXL203 analog accelerometer captures horizontal acceleration, and a camera operating at 30 fps provides additional displacement measurements. The sampling period for model discretization and controller implementation is set to 1 ms. Sensor data from the linear encoder are transmitted to the microcontroller for real-time processing. The parameters of the ball-screw-driven servomechanism are summarized in Table 3.

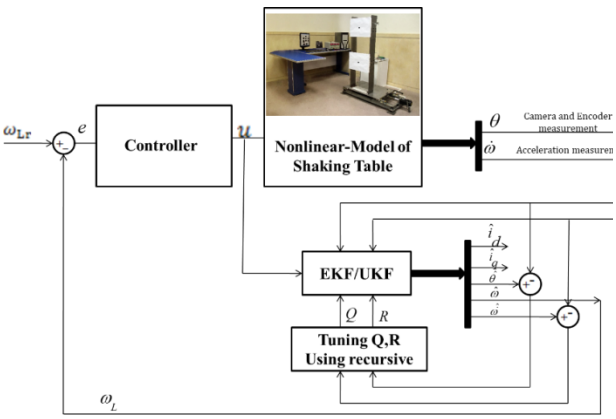

Fig.2.The uniaxial earthquake simulator at Arak University

The microcontroller calculates the position of the shake table and sends it to the DAQ card as a 16-bit word. The camera also sends data to the computer via the USB port. Acceleration data are also acquired by the DAQ card connected to the PC where the control program is implemented in MATLAB software. Furthermore, for safety reasons two infrared CNY70 limit switches are used to shut down the system in case the stage travel exceeds the predefined ±90-mm stroke range.

As calibration is a critical step in ensuring the accuracy and reliability of the measurement system. The linear encoder, MEMS accelerometer, and camera system is all calibrated prior to the experiments. The linear encoder was calibrated by comparing its displacement measurements to a high-precision micrometer. The MEMS accelerometer was calibrated using a vibration table with known acceleration profiles. For the camera system, calibration involved determining the pixel-to-millimeter conversion factor by measuring a target of known dimensions at various distances. This process was crucial for minimizing

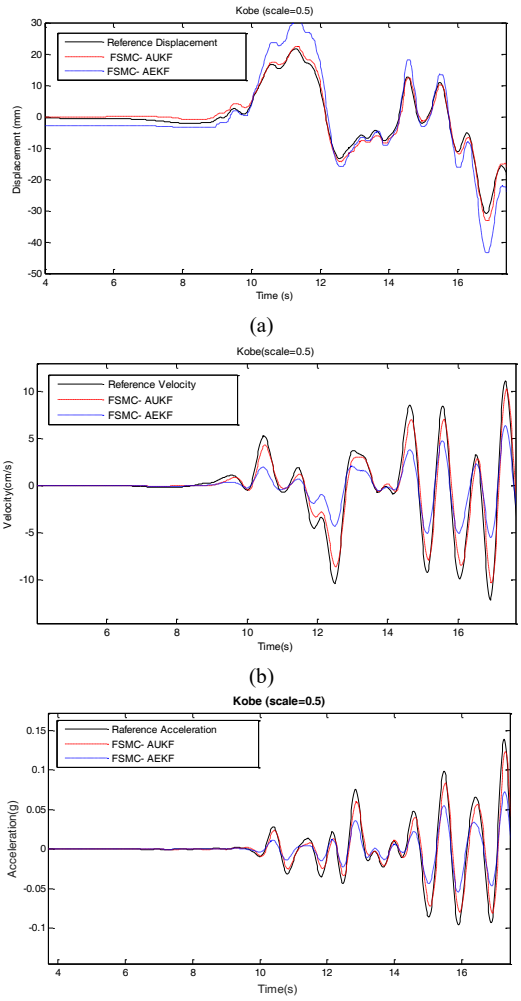

Fig.3. a Comparison between Reference Displacement (a), Velocity (b), and Acceleration (c), for Kobe Earthquake and Laboratory Test Results without structure installed on the shake table

profiles. For the camera system, calibration involved determining the pixel-to-millimeter conversion factor by measuring a target of known dimensions at various distances. This process was crucial for minimizing measurement errors and ensuring the data fusion algorithms provided accurate state estimates, enhancing the overall methodology. Environmental disturbances such as EMI, vibrations, temperature variations, and dust significantly affect the performance of measurement sensors within control systems. While these challenges cannot be entirely eliminated, the integration of noise filtering, sensor shielding, and multi-sensor fusion techniques effectively mitigates their impact. This study highlights the importance of designing resilient control systems to address these issues, ensuring reliable operation and high precision in dynamic testing environments. The proposed control framework has been successfully implemented on the shake table using MATLAB. For evaluation, scaled versions of two significant seismic events—namely the Kobe and Chalfant

earthquakes—were employed as reference inputs for displacement tracking and dynamic response analysis.

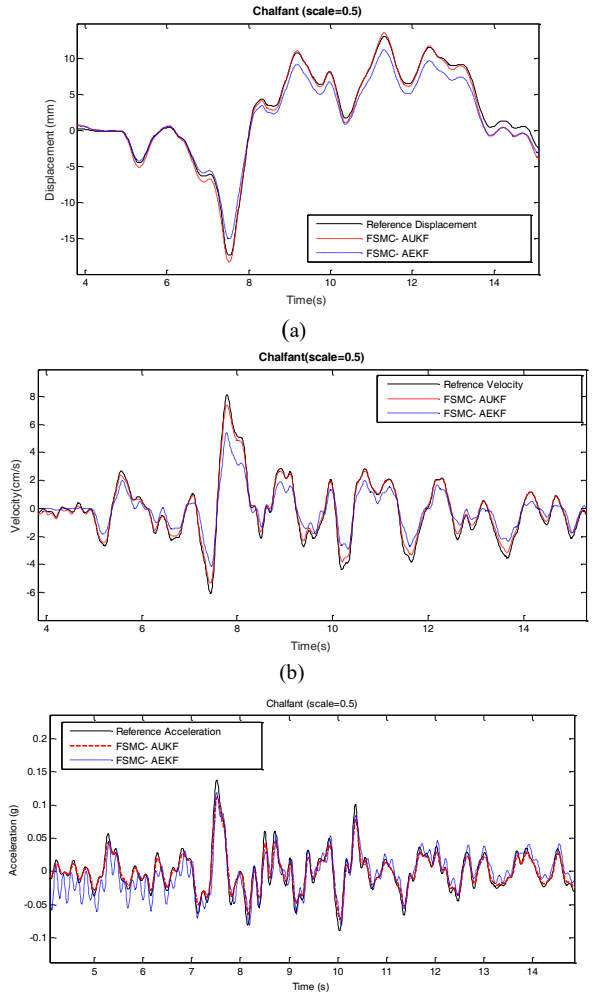

Fig .4. A Comparison between Reference Displacement (a), Velocity (b), and Acceleration (c), for Chalfant Earthquake and Laboratory Test Results without structure installed on the shake table

Figures 3(a)–(c) present a comparative assessment of tracking performance for different controller configurations, particularly the supervisory control scheme that integrates AEKF/AUKF-based sensor fusion with FSMC. As shown in Figure 3(A), the control system incorporating AEKF fails to track the displacement trajectory with sufficient precision. In contrast, the control system based on AUKF in conjunction with FSMC achieves a significant reduction in displacement tracking error. Similar performance enhancements are evident in velocity and acceleration tracking, as depicted in Figures 3(B) and 3(C), respectively. These outcomes highlight the superior estimation and control capabilities of the proposed AUKF-based FSMC framework, demonstrating its effectiveness in accurately reproducing complex earthquake motion profiles. When executing the adaptive algorithm, the initial values for the parameters $\lambda_{r,1}$, $\mu_{r,1}$, $\lambda_{q,0}$, and $\mu_{q,0}$ are established. These parameters should not be chosen too small, because of the effect of these parameters on R and Q. At the beginning of the process, R should not be smaller than its real value and Q should not be bigger than its real value. Based on the effect that η_k^R and η_k^Q have on R and Q respectively, η_k^R is chosen around 0.1 and η_k^Q can be chosen larger or smaller than this value.

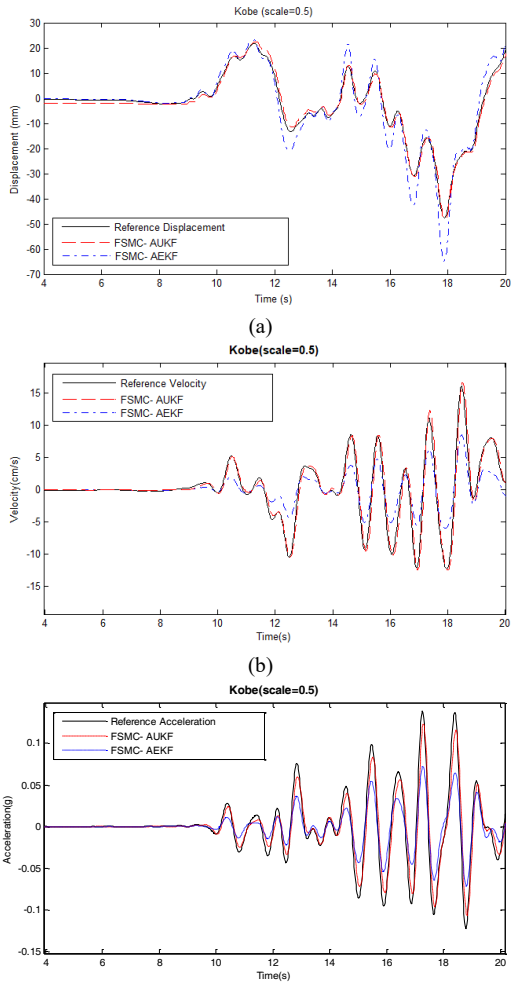

Fig.5. (a), Comparison between Reference Displacement, Velocity (b), and Acceleration (c) for Kobe Earthquake and Laboratory Test Results with structure installed on the shake table

Figures 4 (a)–(c) illustrate the trajectory tracking performance of the proposed control framework during the Chalfant earthquake scenario. The evaluation focuses on displacement, velocity, and acceleration responses over a representative short time window. Experimental results were obtained using real seismic data to assess the method's effectiveness in capturing acceleration dynamics. The figures compare the system's response under AUKF- and AEKF-based control strategies against the reference Chalfant earthquake records. In all three cases, the AUKF-based approach consistently outperforms its AEKF counterpart, achieving more accurate tracking of the target

trajectories. These comprehensive experimental findings reinforce the effectiveness of integrating AUKF with FSMC, confirming its superior capability in accurately tracking displacement, velocity, and acceleration under realistic earthquake conditions.

According to the findings provided, the incorporation of the FSMC and the AUKF-based technique on the shake table yielded a notable decrease in errors related to the tracking of displacement, velocity, and acceleration. To evaluate the resilience of the proposed controller, supplementary shake table experiments were performed using a mounted structure weighing 11.9 kilograms. Figure 2 depicts the shake table along with the structure securely mounted on its surface.

Tables 4 and 5 provide the root mean square error (RMSE) values. These results pertain to designs utilizing both AUKF and AEKF in conjunction with FSMC strategy, analyzed within the time domain. The tracking errors presented as follows:

$$Err_{RMS} = \left[\frac{1}{N}\sum_{i=0}^{N}\left(x[i] - x_{ref}[i]\right)^2\right]^{\frac{1}{2}}$$

The variable x_{ref} is utilized to represent the signal of interest that is to be tracked, which may include parameters such as displacement, velocity, or acceleration. Additionally, we generate a simulated signal that corresponds to the reference signal. The variable N indicates the quantity of data points measured in each experiment.

TABLE 4RMSE WITHOUT STRUCTURE INSTALLED ON THE SHAKE TABLE FOR THE KOBE AND CHALFANT SAMPLE EARTHQUAKE

Earthquake	Controller and Estimator	Tracking Error		
		Displacement	Velocity	**Acceleration**
Kobe	PID	9.12	1.122	**1.235**
	FSMC+EKF	0.598	0.831	**0.932**
	FSMC+UKF	0.471	0.567	**0.673**
	FSMC+AEKF	0.417	0.499	**0.892**
	FSMC+AUKF	0.294	0.311	**0.434**
Chalfant	PID	9.198	1.108	**1.198**
	FSMC+EKF	0.489	0.606	**0.787**
	FSMC+UKF	0.301	0501	**0.690**
	FSMC+AEKF	0.312	0.475	**0.553**
	FSMC+AUKF	0.0923	0.399	**0.484**

Figures 5(a)–(c) display the system's performance in tracking displacement, velocity, and acceleration under conditions involving parametric uncertainty. The combination of FSMC and the AUKF-based estimation approach exhibited a strong degree of robustness, successfully tracking the reference trajectories across all dynamic variables.

TABLE 5 RMSE WITH THE STRUCTURE INSTALLED ON THE SHAKE TABLE FOR THE KOBE AND CHALFANT SAMPLE EARTHQUAKE

Earthquake	Controller and Estimator	Tracking Error		
		Displacement	Velocity	**Acceleration**
Kobe	PID	9.122	1.245	**1.465**
	FSMC+EKF	0.632	0.912	**1.003**
	FSMC+UKF	0.512	0.611	**0.765**
	FSMC+AEKF	0.499	0.832	**0962**
	FSMC+AUKF	0.386	0.457	**0.603**
Chalfant	PID	9.987	1.199	**1.532**
	FSMC+EKF	0.622	0.901	**0.991**
	FSMC+UKF	0.403	0.609	**0.821**
	FSMC+AEKF	0.5199	0.8013	**0.9154**
	FSMC+AUKF	0.296	0.5142	**0.7021**

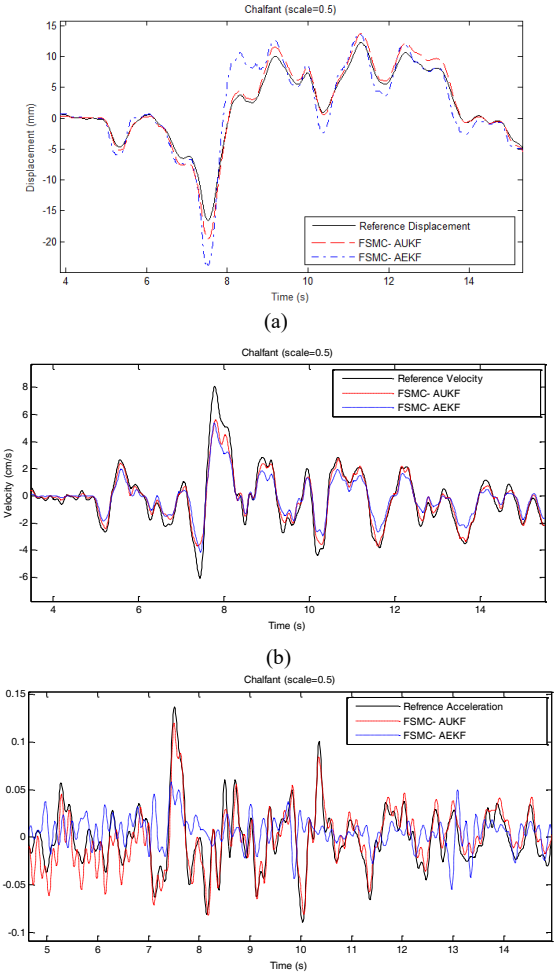

Fig.6. (a), Comparison between Reference Displacement, Velocity (b), and Acceleration (c), for Chalfant Earthquake and Laboratory Test Results with structure

In contrast, the AEKF-based control strategy failed to maintain acceptable tracking accuracy, particularly in the presence of model uncertainties. Further insights are

provided in Figures 6(a)–(c), which compare the tracking performance of the supervisory controllers—specifically the integration of FSMC with either AEKF or AUKF—during the Chalfant earthquake scenario under uncertainty. The results clearly indicate that the FSMC+AUKF configuration achieves significantly lower errors across displacement, velocity, and acceleration trajectories. This underscores the advantage of the proposed adaptive filtering and control scheme in uncertain and nonlinear dynamic environments. The AUKF-based control consistently outperforms the AEKF-based control in trajectory tracking across all scenarios, as evidenced by the RMSE in the time domain. Extensive experimental results clearly demonstrate that combining the AUKF and FSMC techniques with reference velocity records yields superior control performance for tracking displacement, velocity, and acceleration trajectories. In summary, the integration of AEKF/AUKF with FSMC significantly enhances the controller's adaptability, accuracy, and overall controllability, offering a robust control strategy well-suited for earthquake simulator applications. Furthermore, the experimental findings highlight the AUKF's notable superiority over the AEKF in trajectory tracking, achieving consistently lower RMSE values for displacement, velocity, and acceleration. Specifically, during the tracking of seismic profiles such as the Kobe and Chalfant earthquakes, the AUKF-based system demonstrated superior accuracy and stability, even under varying conditions and in the presence of parameter uncertainties.

TABLE 6 COMPARISON OF CONTROL INPUT CHATTERING

Control Method	RMS Voltage(V)	Relative Reduction
Standard SMS	12.45	20%
Proposed FSMC	4.08	67%

To rigorously validate the proposed FSMC-AUKF framework, its performance was compared against PID and FSMC-EKF/UKF based controllers under identical experimental conditions. As shown in Table 4 and 5, the proposed method reduced displacement, velocity, and acceleration RMSE by 45–60% compared to PID and 32–52% compared to FSMC-EKF/UKF. The adaptive noise covariance in AUKF outperformed conventional EKF/UKF by 18–28%, particularly under payload uncertainties. These results confirm that the synergy of fuzzy boundary layer adaptation and adaptive filtering uniquely addresses the limitations of existing methods in high-precision seismic tracking. Also, to quantify the chattering suppression, the RMS values of the control input voltage were computed for both the standard SMC and FSMC during the high-frequency phase of the Kobe earthquake simulation (10–15 seconds). As demonstrated in Table 6, the FSMC reduces the RMS voltage from 12.45 V (SMC) to 4.08 V, achieving a 67% reduction in chattering.

Table 7 presents a comparative analysis of the computational cost associated with the implemented algorithms (PID, FSMC+EKF, FSMC+UKF, FSMC-AEKF, and FSMC-AUKF). All methods were executed on identical hardware specifications (Intel Core i7-9700K CPU, 16 GB RAM) to ensure a fair comparison. Among the evaluated approaches, FSMC-AUKF exhibits a higher computational burden compared to the conventional PID controller, primarily due to the incorporation of adaptive filtering mechanisms and fuzzy inference systems. Nonetheless, this increased computational demand is justified by the significantly enhanced tracking performance offered by the FSMC-AUKF method.

TABLE 7 COMPARISONS OF COMPUTATIONAL COST

Controller and Estimator	Computational Cost
PID	**0.12**
FSMC+EKF	**0.15**
FSMC+UKF	**0.17**
FSMC+AEKF	**0.165**
FSMC+AUKF	**0.19**

IV. Conclusion

This paper presented the development and application of a novel supervisory controller combining FSMC with AEKF and AUKF techniques for precise motion control of a laboratory-scale shake table. A structure was employed to mitigate chattering in the sliding mode control input, thereby improving the operational lifespan of the electric motors. An adaptive recursive method for noise covariance estimation was proposed, offering low computational complexity while ensuring the non-negativity of covariance matrix elements. Optimal state estimation was achieved through sensor fusion, integrating encoder, accelerometer, and camera data using Kalman filtering techniques. This fusion effectively compensated for sensor faults, maintaining system performance even under partial sensor failure. The image processing approach also demonstrated strong performance at a low cost. Through the proposed methodology, accurate estimation of the table velocity, previously unmeasurable, was accomplished using AEKF and AUKF. Two experimental setups were designed: one integrating FSMC with AUKF, and the other with AEKF. Results demonstrated that the proposed controller successfully suppressed excessive vibrations caused by the system's inherent flexibility. Furthermore, AUKF consistently achieved higher estimation accuracy compared to AEKF, despite similar computational complexity. Experimental validation using the Chalfant and Kobe earthquake records confirmed the controller's robustness in both stability and performance. While the experimental results are promising, several limitations must be acknowledged. The experiments were conducted on a laboratory-scale shake table with specific configurations. Broader validation across diverse payloads, actuator types, and environmental conditions is necessary for

generalization. Moreover, challenges such as latency, hardware constraints, and unmodeled dynamics, typical in industrial applications, were not fully addressed. Future work will focus on extending validation to large-scale shake tables, integrating deep learning-based adaptive control methods, and optimizing computational efficiency for real-time embedded system implementation. These efforts aim to bridge the gap between laboratory research and industrial application.

References

[1] S. Bianchi et al., "Shake-table tests of innovative drift sensitive nonstructural elements in a low-damage structural system," Earthquake Engineering & Structural Dynamics, vol. 50, no. 9, pp. 2398-2420, 2021, doi: https://doi.org/10.1002/eqe.3452.

[2] S. Chen, H. Zhuang, D. Quan, J. Yuan, K. Zhao, and B. Ruan, "Shaking table test on the seismic response of large-scale subway station in a loess site: A case study," Soil Dynamics and Earthquake Engineering, vol. 123, pp. 173-184, 2019.

[3] H. Yang, D. Cong, Z. Yang, and J. Han, "A Practical Adaptive Sinusoidal Vibration Control Strategy for Electro-Hydraulic Shake Table," Journal of Vibration Engineering & Technologies, vol. 11, pp. 1725–1739, 2023

[4] S. Pampanin et al., "Triaxial shake table testing of an integrated low-damage building system," Earthquake Engineering & Structural Dynamics, 2023.

[5] M. Flah, M. Ragab, M. Lazhari, and M. Nehdi, "Localization and classification of structural damage using deep learning single-channel signal-based measurement," Automation in Construction, vol. 139, p. 104271, 2022.

[6] M. Diaz, P.-É. Charbonnel, and L. Chamoin, "A new Kalman filter approach for structural parameter tracking: application to the monitoring of damaging structures tested on shaking-tables," Mechanical Systems and Signal Processing, vol. 182, p. 109529, 2023.

[7] M. A. Kuddus, J. Li, H. Hao, C. Li, and K. Bi, "Target-free vision-based technique for vibration measurements of structures subjected to out-of-plane movements," Engineering Structures, vol. 190, pp. 210-222, 2019.

[8] J. Wen, C. Zhao, and Z. Shi, "LSTM-based adaptive robust nonlinear controller design of a single-axis hydraulic shaking table," IET Control Theory & Applications, vol. 17, no. 7, pp. 825-836, 2023.

[9] A. Najafi and B. F. Spencer Jr, "Modified model-based control of shake tables for online acceleration tracking," Earthquake Engineering & Structural Dynamics, vol. 49, no. 15, pp. 1721-1737, 2020.

[10] J. Yao et al., "Sinusoidal acceleration harmonic estimation using the extended Kalman filter for an electro-hydraulic servo shaking table," Journal of Vibration and Control, vol. 21, no. 8, pp. 1566-1579, 2015.

[11] J. Yao, D. Di, G. Jiang, S. Gao, and H. Yan, "Real-time acceleration harmonics estimation for an electro-hydraulic servo shaking table using Kalman filter with a linear model," IEEE Transactions on Control Systems Technology, vol. 22, no. 2, pp. 794-800, 2013.

[12] Z. Lu, Z. Wang, Y. Zhou, and X. Lu, "Nonlinear dissipative devices in structural vibration control: A review," Journal of Sound and Vibration, vol. 423, pp. 18-49, 2018.

[13] J. Lu, H. Xie, L. Hu, H. Yang, and Y. Chen, "Variable-parameter feedforward control for centrifuge shaking table based on nonlinear frequency characteristic model," Mechanical Systems and Signal Processing, vol. 161, p. 108011, 2021.

[14] Y. Tang, G. Shen, Z.-C. Zhu, X. Li, and C.-F. Yang, "Time waveform replication for electro-hydraulic shaking table incorporating off-line iterative learning control and modified internal model control," Proceedings of the Institution of Mechanical Engineers, Part I: Journal of Systems and Control Engineering, vol. 228, no. 9, pp. 722-733, 2014, doi: 10.1177/0959651814536553.

[15] S. Welikala, H. Lin, and P. Antsaklis, "A Decentralized Analysis and Control Synthesis Approach for Networked Systems with Arbitrary Interconnections," arXiv preprint arXiv:2204.09756, 2022.

[16] F. Beltran-Carbajal and G. Silva-Navarro, "Output feedback dynamic control for trajectory tracking and vibration suppression," Applied Mathematical Modelling, vol. 79, pp. 793-808, 2020.

[17] G. Shen, G.-M. Lv, Z.-M. Ye, D.-C. Cong, and J.-W. Han, "Implementation of electrohydraulic shaking table controllers with a combined adaptive inverse control and minimal control synthesis algorithm," Iet control theory & applications, vol. 5, no. 13, pp. 1471-1483, 2011.

[18] T. B. Ma and F. Du, "Minimal control synthesis algorithm for panel vibration control," Advanced Materials Research, vol. 804, pp. 269-274, 2013.

[19] C.-h. Gao and X.-b. Yuan, "Development of the shaking table and array system technology in China," Advances in Civil Engineering, vol. 2019, 2019.

[20] O. A. Al-Fahdawi and L. R. Barroso, "Adaptive neuro-fuzzy and simple adaptive control methods for full three-dimensional coupled buildings subjected to bi-directional seismic excitations," Engineering Structures, vol. 232, p. 111798, 2021.

[21] A. S. Sayed, A. T. Azar, Z. F. Ibrahim, H. A. Ibrahim, N. A. Mohamed, and H. H. Ammar, "Deep learning based kinematic modeling of 3-rrr parallel manipulator," in Proceedings of the International Conference on Artificial Intelligence and Computer Vision (AICV2020), 2020: Springer, pp. 308-321.

[22] E. W. Suseno and A. Ma'arif, "Tuning of PID controller parameters with genetic algorithm method on DC motor," International Journal of Robotics and Control Systems, vol. 1, no. 1, pp. 41-53, 2021.

[23] H. Zhang, L. Wang, and W. Shi, "Seismic control of adaptive variable stiffness intelligent structures using fuzzy control strategy combined with LSTM," Journal of Building Engineering, vol. 78, p. 107549, 2023.

[24] K. Seki, M. Iwasaki, M. Kawafuku, H. Hirai, and K. Yasuda, "Adaptive compensation for reaction force with frequency variation in shaking table systems," IEEE Transactions on Industrial Electronics, vol. 56, no. 10, pp. 3864-3871, 2009.

[25] S. Strano and M. Terzo, "A non-linear robust control of a multi-purpose earthquake simulator," in Proceedings of the World Congress on Engineering, 2013, vol. 3.

[26] M. Soleymani, A. Khalatabari-S, and B. Ghanbari-S, "Fuzzy-sliding-mode supervisory control of a seismic shake table with variable payload for robust and precise acceleration tracking," Journal of earthquake Engineering, vol. 23, no. 4, pp. 539-556, 2019.

[27] M. Tárník and J. Murgaš, "Model reference adaptive

control of permanent magnet synchronous motor," Journal of Electrical Engineering, vol. 62, no. 3, pp. 117-125, 2011.
[28] C. J. O'Rourke, M. M. Qasim, M. R. Overlin, and J. L. Kirtley, "A geometric interpretation of reference frames and transformations: dq0, clarke, and park," IEEE Transactions on Energy Conversion, vol. 34, no. 4, pp. 2070-2083, 2019.
[29] X. Li and G. Gong, "Objective-oriented genetic algorithm based dynamical sliding mode control for slurry level and air pressure in shield tunneling," Automation in Construction, vol. 109, p. 102987, 2020.
[30] H. Komurcugil, S. Biricik, S. Bayhan, and Z. Zhang, "Sliding mode control: Overview of its applications in power converters," IEEE Industrial Electronics Magazine, vol. 15, no. 1, pp. 40-49, 2020.
[31] X. Cheng, X. Liu, X. Li, and Q. Yu, "An intelligent fusion estimation method for state of charge estimation of lithium-ion batteries," Energy, vol. 286, p. 129462, 2024.
[32] N. Kayhani, W. Zhao, B. McCabe, and A. P. Schoellig, "Tag-based visual-inertial localization of unmanned aerial vehicles in indoor construction environments using an on-manifold extended Kalman filter," Automation in Construction, vol. 135, p. 104112, 2022.
[33] H. Tang et al., "Feature extraction of multi-sensors for early bearing fault diagnosis using deep learning based on minimum unscented kalman filter," Engineering Applications of Artificial Intelligence, vol. 127, p. 107138, 2024.
[34] I. Ullah, Y. Shen, X. Su, C. Esposito, and C. Choi, "A localization based on unscented Kalman filter and particle filter localization algorithms," IEEE Access, vol. 8, pp. 2233-2246, 2019.
[35] Y. Zhang, M. Li, Y. Zhang, Z. Hu, Q. Sun, and B. Lu, "An enhanced adaptive unscented kalman filter for vehicle state estimation," IEEE Transactions on Instrumentation and Measurement, vol. 71, pp. 1-12, 2022.
[36] D. Lee, G. Vukovich, and R. Lee, "Robust unscented Kalman filter for nanosat attitude estimation," International Journal of Control, Automation and Systems, vol. 15, pp. 2161-2173, 2017.
[37] J. H. Yoon, D. Y. Kim, and V. Shin, "Window length selection in linear receding horizon filtering," in 2008 International Conference on Control, Automation and Systems, 2008: IEEE, pp. 2463-2467.
[38] R.Havangi,F.Karimi, "Improvement of The Battery State of Charge Estimation Using Recursive Least Square Based Adaptive Extended Kalman Filter "International Journal of Industrial Electronics, Control and Optimization ,vol.7,no.2,pp.141-151,2024.

Nima Rajabi Namin i received the M.S. degree in Electrical Engineering from Arak University, Arak, Iran, in 2015, the Ph.D. degree in Control Engineering from the University of Birjand, Birjand, Iran, in 2024. His research interests include Control, Nonlinear Dynamic Systems, Robust Control, State Estimation and Filtering, evolutionary filtering, Multi-Sensor Data Fusion.

Ramazan Havangi received his M.S. and Ph.D. degrees from the K.N. Toosi University of Technology, Tehran, Iran, in 2003 and 2012, respectively. He is currently an Associate Professor of control systems with the Department of Electrical and Computer Engineering, University of Birjand, Birjand, Iran. His main research interests are inertial navigation, integrated navigation, estimation and filtering, evolutionary filtering, simultaneous localization and mapping, fuzzy, neural network, and soft computing.

Amir Hossein Abolmasoum i received the B.S. degree in Electrical Engineering from University of Tehran in 2004, the M. Sc. degree from Tarbiat Modares University in 2007 and his PhD in control engineering department, Tarbiat Modares University, Tehran, Iran. He is currently with the Electrical Engineering department of Arak University. His research interests include stochastic switching systems, delayed dynamical systems and congestion control in communication networks.

IECO

This page intentionally left blank.

International Journal Of
Industrial Electronics Control and Optimization
Print ISSN: 3517-2645
Online ISSN: 3568-2645
Homepage: https://ieco.usb.ac.ir/

Enhancing Small-Signal Stability of Multi-Machine Power Systems Using PMU Data

Zivar Rigi | Mahdi Hassanniakheibari

Department of Electrical Engineering, ZAH.C., Islamic Azad University, Zahedan, Iran.[1,2]
Corresponding author's email: mahdi.hassannia@iau.ac.ir

Article Info

Article type:
Research Article

Article history:
Received: 07-August-2025
Received in revised form: 26—October-2025
Accepted: 06-November-2025
Published online: 21-March-2026

Keywords:
PMU data,
PSD and CSD methods,
Small signal,
Stability analysis,
14-bus IEEE system.

ABSTRACT

As power systems rapidly expand and the demand for uninterrupted power supply to network loads increases, ensuring the safe and stable operation of these systems has become crucially important. However, conducting dynamic stability assessments with detailed dynamic models is nearly impossible in today's complex power networks. The introduction of Phasor Measurement Units (PMUs) has paved the way for new stability evaluation techniques that rely on real-time measurement data. A common limitation of most measurement-based techniques is their vulnerability to noise in the data. While some newer methods offer improved noise resistance, they are often hindered by high computational demands and slow processing times, limiting their practical use. This paper developed a measurement-based method that uses power spectral density (PSD) and cross-spectral density (CSD) to achieve a more precise estimation of low-frequency oscillations in power systems. Simulation results on the IEEE 14-bus and 39-bus test systems, tested under both noisy and noise-free conditions, show that the proposed method yields more accurate frequency and oscillation shape estimates, even when measurement noise is present. Additionally, the Prony algorithm, a well-known measurement-based method, is also implemented, and its high sensitivity to noisy data is demonstrated.

NOMENCLATURE

H	Inertia constant of the generator-turbine system	K_S	Synchronizing coefficient
ω	Rotor speed	K_D	Damping coefficient
ω_o	Synchronous electrical speed	A	State matrix
$\Delta\omega_r$	Rotor speed deviation (per unit)	B	Input matrix
δ	Rotor angle	$x(t)$	State vector
$\Delta\delta$	Rotor angle deviation	$u(t)$	Input vector
P_{mech}	Mechanical power input	$z_i(t)$	Modal state of the i-th mode
P_e	Electrical power output	λ_i	Eigenvalue of the i-th mode
T_D	Damping torque	R_i, L_i	Right and left eigenvectors corresponding to λ_i
P_D	Damping power	$S_{kk}(\omega)$	Power Spectral Density (PSD) of signal y_k
X_T	Total reactance (machine + line)	$S_{kl}(\omega)$	Cross Spectral Density (CSD) between signals y_k and y_l
X_D'	Transient reactance of the generator	$Y_k(\omega)$	Fourier transform of signal $y_k(t)$
X_E	Line reactance	$Z_i(\omega)$	Frequency domain representation of modal response
$\acute{E}$	Internal transient voltage	$S_x^{\omega}(\omega_k)$	Welch's averaged periodogram estimate
E_B	Infinite bus voltage		

I. Introduction

Recent operational experience with multi-machine power systems has revealed that power oscillations, especially during heavy loading of transmission lines, are common occurrences. When these oscillations persist or intensify, they pose a significant risk to the overall stability of the system [1–8]. Under such conditions, the rotors of synchronous generators begin to oscillate, which in the worst case can lead to a total loss of synchronism within the whole

network [9]. The large-scale blackout in the Western Electricity Coordinating Council (WECC) region in 1996 highlighted to operators and power system engineers the vital need for effective monitoring and control of low-frequency oscillations [10].

Consequently, precise and real-time detection of low-frequency oscillations within today's complex multi-machine power networks is crucial for preserving system synchronism and averting large-scale blackouts. Current research on identifying these oscillatory modes generally falls into two primary approaches:

- Model-based analytical methods that utilize dynamic system representations,
- Measurement-based techniques grounded in signal processing.

Traditional model-based approaches, such as modal analysis, require linearizing the system around a stable operating point, and the identification of oscillatory modes depends heavily on having detailed knowledge of the system's dynamic model [11]. However, obtaining accurate models of large-scale, interconnected power networks is highly challenging and frequently unreliable. Moreover, even assuming full model availability, developing a real-time control system capable of rapidly and precisely responding to system oscillations remains practically unfeasible.

Conversely, the advent of Phasor Measurement Units (PMUs) and the implementation of Wide Area Measurement Systems (WAMS) have facilitated the provision of high-resolution, time-synchronized data to control centers [12]. This technological progress has enabled the application of a variety of signal processing techniques for oscillation analysis, such as Fast Fourier Transform (FFT) [13], wavelet transform [14], Prony analysis [15], Stochastic Subspace Identification (SSI) [16], Auto-Regressive Moving Average (ARMA) modeling [17], and Hilbert-Huang Transform (HHT) [18]. While these methods facilitate faster detection of oscillatory phenomena, they also present inherent limitations. For instance, the Fast Fourier Transform (FFT) estimates only the dominant frequency and cannot track instantaneous damping, rendering it ineffective for analyzing nonlinear or non-stationary signals. The Wavelet Transform utilizes localized wavelets with finite duration and zero mean [19]. Despite its strength in capturing time-frequency characteristics, it encounters challenges such as frequency overlap and difficulties in selecting appropriate wavelet bases.

Prony analysis, as a well-known measurement-based method, can rapidly extract dominant oscillatory modes but is highly sensitive to noise and becomes unreliable when multiple signal components coexist [20]. Comparative studies with FFT and eigenvalue analysis [21], [22] have demonstrated Prony's superiority in extracting oscillatory features. A modified Prony technique incorporating signal subspace theory was proposed in [23] to mitigate noise sensitivity; however, it still exhibits some vulnerability to noise. Another approach based on noise subspace decomposition, introduced in [24], identifies low-frequency modes by applying a median filter to reduce variability in mode estimation. Comparative analyses indicate this method surpasses conventional Prony analysis in terms of frequency standard deviation and damping accuracy [25], [26].

Several investigations [27–30] have employed subspace estimation methods, such as Principal Component Analysis (PCA) and Stochastic Subspace Identification (SSI), for low-frequency oscillation parameter identification. These methods generally outperform Prony analysis in parameter estimation. Nevertheless, both Prony and SSI techniques face challenges in accurately estimating model order under high-noise conditions, often leading to misidentification of oscillatory modes.

Despite the relative promise of these recent methods, their accuracy remains compromised in noisy signal environments. In response, this paper developed a spectral analysis approach based on PMU measurement data, utilizing Power Spectral Density (PSD) and Cross-Spectral Density (CSD) functions. This method aims to reduce noise sensitivity while enabling more accurate detection of low-frequency oscillations.

The remainder of this paper is organized as follows: Section 2 outlines the theoretical background of small-signal stability in power systems. Section 3 details the PSD and CSD methodologies. Section 4 introduces the IEEE 14-bus and 39-bus test systems and describes the simulation scenarios. Section 5 presents and discusses the simulation results. Finally, Section 6 offers conclusions and suggestions for future research.

II. Small-Signal Stability Fundamentals

In multi-machine power systems, small-signal stability is commonly defined as follows [2]:

"Small-signal stability refers to the ability of a power system to return to a steady operating condition following a small physical disturbance."

A fundamental assumption in this definition is that the system maintains coherence and that the oscillations remain limited in magnitude following a disturbance. Consequently, this form of stability is commonly known as small-signal stability.

A. Rotor Angle Stability

When a disturbance takes place in the system, the rotors of synchronous generators experience acceleration, resulting in variations in rotor angle and speed. In extreme cases, these deviations may lead to a loss of synchronism among generators. This behavior is typically represented by the swing equation. To facilitate stability analysis in multi-machine systems, the classical Single-Machine Infinite Bus (SMIB) model is often employed as a simplification. Figure

1 illustrates the simplified representation of an SMIB system.

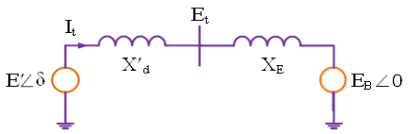

Fig. 1. Simplified SMIB System Model [5]

For an n-machine system, the motion equation of the i[th] machine is given by:

$$\frac{d\omega_i}{dt} = \frac{\omega_i}{2H_i}(P_{mech_i} - P_{e_i} - P_{D_i}) \quad (1)$$

Here, H_i is the inertia constant, ω_i is the rotor speed, P_{mech_i} and P_{e_i} are the mechanical and electrical powers, and P_{D_i} represents the damping power (a non-physical term used to model system damping).

According to Figure 1, the system current and apparent power can be defined as:

$$I_t = \frac{E'\angle\delta - E_B\angle 0}{jX_T} \;.\; X_T = X'_d + X_E \quad (2)$$

$$S' = P + jQ' = E'I_t^* = \frac{E'E_B \sin\delta}{X_T} + j\frac{E'(E' - E_B\cos\delta)}{X_T} \quad (3)$$

where:

E_B: Infinite bus voltage

E': Internal transient voltage

X_T: Total reactance (machine + line)

δ: Rotor angle (the angular difference between E' and E_B)

In the per-unit system and under small deviation assumptions, the electrical torque equals the electrical power. Hence:

$$P_e(\delta) = T_e(\delta) = \frac{E'E_B \sin\delta}{X_T} \quad (4)$$

As illustrated in Figure 2, rotor angle oscillations correspond directly to variations in power. This relationship forms the basis for measurement-based techniques used to evaluate small-signal stability.

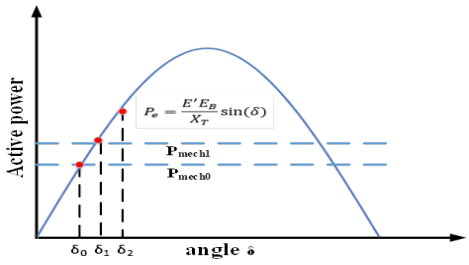

Fig. 2. Rotor Angle vs. Power Curve

Electromechanical oscillations naturally exist in power systems and depend on the slope of the $P-\delta$ curve. A steeper slope corresponds to a smaller $\Delta\delta$ for the same ΔP, implying a higher oscillation frequency [5].

From equation (4), the derivative of the electrical torque with respect to δ is:

$$\Delta T_e(\delta) = \frac{\partial T_e}{\partial\delta}\Delta\delta\frac{E'E_B\cos\delta_0}{X_T}\Delta\delta = K_S\Delta\delta \quad (5)$$

Here, K_S is the synchronizing coefficient. The linearized swing equation can be expressed as:

$$\frac{d}{dt}\Delta\omega_r = \frac{1}{2H}(T_m - T_e - K_D\Delta\omega_r) \quad (6)$$

$$\frac{d}{dt}\Delta\delta = \omega_0\Delta\omega_r \quad (7)$$

where:

$\Delta\omega_r$: Rotor speed deviation

δ: Rotor angle

ω_0: Base electrical speed

K_D: Damping coefficient

In state-space form:

$$\frac{d}{dt}\begin{bmatrix}\Delta\omega_r\\ \Delta\delta\end{bmatrix} = \begin{bmatrix}\frac{-K_D}{2H} & \frac{-K_S}{2H}\\ \omega_0 & 0\end{bmatrix}\begin{bmatrix}\Delta\omega_r\\ \Delta\delta\end{bmatrix} + \begin{bmatrix}\frac{1}{2H}\\ 0\end{bmatrix}\Delta T_m \quad (8)$$

Or more compactly:

$$\Delta\dot{X} = A\Delta X + BU \quad (9)$$

Here, A is the system state matrix. The eigenvalues of A determine system stability and form the foundation of model-based techniques such as modal analysis. Obtaining this matrix, however, requires precise knowledge of network dynamic parameters and accurate modeling of all dynamic elements.

III. Developed method

In future power systems, the use of signal processing techniques will become indispensable. The introduction of Phasor Measurement Units (PMUs) and the advancement of Wide-Area Monitoring Systems (WAMS) have made high-resolution, time-synchronized measurement data readily available to control centers. Within this framework, and assuming full system observability, spectral analysis methods such as Power Spectral Density (PSD) and Cross-Spectral Density (CSD) are developed as effective tools for assessing small-signal stability using PMU data.

B. Mathematical Frameworks

Assuming small disturbances in a multi-machine power system, the linearized differential equations around a stable operating point can be expressed as follows [2–5]:

$$\dot{\underline{x}}(t) = A\underline{x}(t) + B\underline{u}(t) \quad (10)$$

In typical multi-machine power systems, the input vector $\underline{u}(t)$ is modeled as a random disturbance caused by stochastic load switching events. Using eigenvalue decomposition, the system equations in (10) can be diagonalized. The eigenvalues and corresponding eigenvectors are defined as:

$$|\lambda_i I - A| = 0 \quad (11)$$

$$AR_i = \lambda_i R_i \quad (12)$$

$$L_i A = \lambda_i L_i \quad (13)$$

where λ_i is the i-th eigenvalue, and R_i and L_i are the corresponding right and left eigenvectors, respectively. The identity matrix I is of size $n \times n$. These eigenvectors can be organized into matrices:

$$R = [R_1 \dots R_n] \quad (14)$$

$$L = \begin{bmatrix} L_1 \\ \vdots \\ L_n \end{bmatrix}$$

These matrices satisfy the biorthogonality condition:

$$R \times L = I \tag{15}$$

A linear transformation is applied as:

$$z_i(t) = \underline{l}_i \, \underline{x}(t) \tag{16}$$

This leads to the diagonalized system:

$$L \times A \times R = \mathrm{diag}(\lambda_i) \tag{17}$$

Thus, the system dynamics are transformed into modal coordinates:

$$\dot{z}_i(t) = \lambda_i z_i(t) + \underline{l}_i B \underline{u}(t) \tag{18}$$

Here, $z_i(t)$ represents the response of the i-th mode to the input $\underline{u}(t)$. Each state can then be reconstructed using the right eigenvectors:

$$\underline{x}(t) = \sum_{i=1}^{n} z_i(t) \underline{r}_i \tag{19}$$

To analyze modal contributions in the frequency domain, we define the spectral functions [31]:

$$S_{kl}(\omega) = \lim_{T\to\infty} \frac{1}{T} E\{Y_k^*(\omega) Y_l(\omega)\} \tag{20}$$

$$S_{kk}(\omega) = \lim_{T\to\infty} \frac{1}{T} E\{Y_k^*(\omega) Y_k(\omega)\} \tag{21}$$

Here, $S_{kl}(\omega)$ is the cross-spectral density (CSD) between two signals y_k and y_l, and $S_{kk}(\omega)$ is the power spectral density (PSD) of signal y_k. The terms $Y_k(\omega)$and $Y_l(\omega)$ are Fourier transforms of the respective time-domain signals, and $E\{\bullet\}$ is the expectation operator.

$$S_{kl}(\omega) = \lim_{T\to\infty} \frac{1}{T} E\{(\sum_{r=1}^{n} Z_r(\omega) R_{r,k})^* (\sum_{p=1}^{n} Z_p(\omega) R_{p,l})\} \tag{22}$$

By applying the Fourier transform to equation (18):

$$Z_i(\omega) = \frac{L_i B U(\omega)}{j\omega - \lambda_i} \tag{23}$$

Assuming λ_i is a lightly damped mode

$$\lambda_i = \alpha_i + j\omega_i \tag{24}$$

where $\alpha_i \ll \omega_i$, and substituting $\omega = \omega_i$ into the spectral expression, we approximate:

$$S_{kl}(\omega_i) \cong \lim_{T\to\infty} \frac{1}{T} E\{(Z_i(\omega_i) R_{i.k})^* (Z_i(\omega_i) R_{i.l})\} \tag{25}$$

Since $R_{i.k}$ and $R_{i.l}$ are constants:

$$S_{kl}(\omega_i) \cong R_{i.k}{}^* R_{i.l} \left[\lim_{T\to\infty} \frac{1}{T} E\{|Z_i(\omega_i)|^2\} \right] \tag{26}$$

Due to the stochastic nature of disturbances, this expectation term converges to a fundamental constant representing the variance at the mode frequency. Thus, the CSD angle can be approximated as:

$$\angle S_{kl}(\omega_i) \cong \angle R_{i.l} - \angle R_{i.k} \tag{27}$$

If $k = 1$, the PSD of the signal becomes:

$$S_{kk}(\omega_i) \cong |R_{i.k}|^2 \left[\lim_{T\to\infty} \frac{1}{T} E\{|Z_i(\omega_i)|^2\} \right] \tag{28}$$

Equations (27) and (28) are used to estimate the oscillation mode shape. Accurate PSD and CSD estimation requires synchronized measurements over a sufficiently long time interval. In this paper, Welch's method is employed for estimating the PSD and CSD from PMU data.

Using Welch averaging:

$$S_x^W(\omega_k) \triangleq \frac{1}{K} \sum_{m=0}^{K-1} P_{x_{m.M}}(\omega_k) \tag{29}$$

For a rectangular window ω_n, the periodograms are computed from non-overlapping data blocks. With other windows, overlapping frames are typically used.

IV. Case Study

To assess the effectiveness of the proposed PSD and CSD methods in estimating local and inter-area oscillatory modes within multi-machine power systems, simulations are performed on two standard IEEE test systems—the 14-bus and 39-bus networks. The simulations consider both ideal (noise-free) and noisy measurement conditions. Furthermore, the results are compared against those obtained from modal analysis, a model-based approach, as well as Prony analysis, a measurement-based (model-free) technique.

Dynamic simulations and modal analysis are performed using DIgSILENT PowerFactory 15.1, which includes predefined 14-bus and 39-bus standard systems. In order to implement the Prony method, the Signal Processing Toolbox in MATLAB R2022a is utilized.

C. 14-Bus and 39-Bus Description

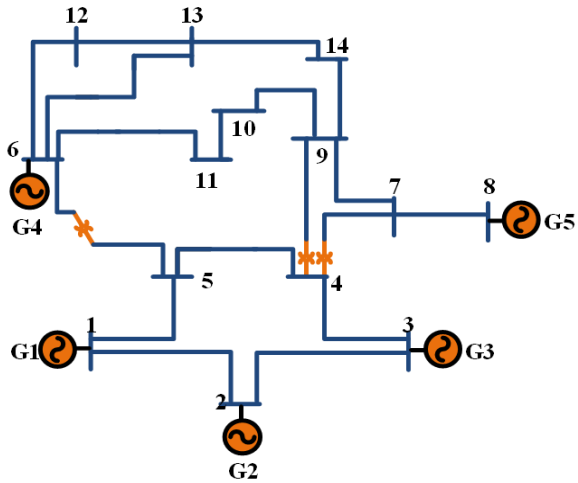

Fig. 3. IEEE 14-Bus Single-Line Diagram

The IEEE 14-bus system includes:

- 14 buses
- 5 generator units
- 11 loads
- 20 transmission lines
- 3 transformers connecting different voltage levels

Nominal voltage levels:

- Buses 1 to 5: 132 kV

- Buses 6, 9 to 14: 33 kV
- Bus 7: 1 kV
- Bus 8: 11 kV

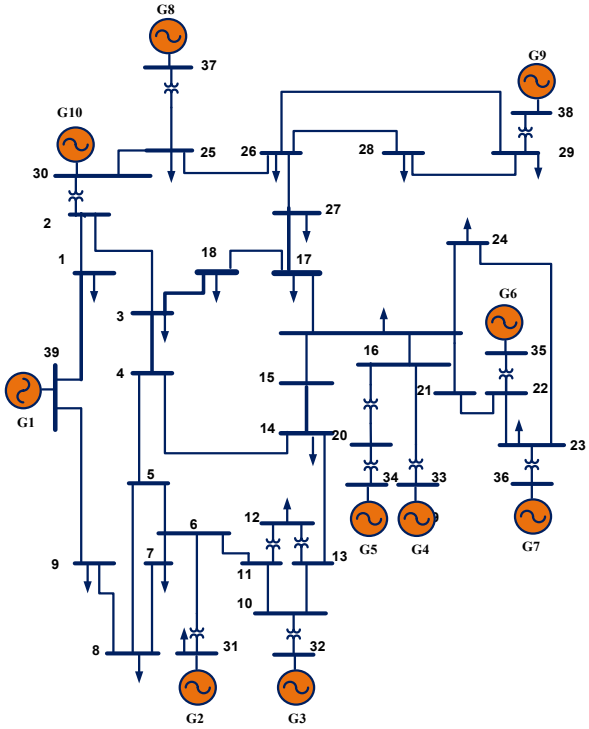

Fig. 4. IEEE 39-Bus Single-Line Diagram

All data are obtained from [32], representing a standard benchmark for power system stability analysis.

The IEEE 39-bus system is well known as a 10-machine New-England power system, where Generator 1 represents the aggregation of a large number of generators. The system includes [33]:

- 39 buses
- 10 generator units
- 18 loads
- 46 transmission lines
- 12 transformers connecting different voltage levels

D. Simulation Scenarios

To evaluate the proposed method, two simulation scenarios are considered for both the 14-bus and 39-bus test systems. In each system, after dynamic simulations, modal analysis, a developed method, and the Prony algorithm are implemented to compare their effectiveness.

- **Ideal Case**:

In this scenario, the measured signal is analyzed directly. For instance, variations of active power flow or bus frequency are recorded immediately following a small-signal disturbance. These measurements are captured directly from signal recordings in DIgSILENT and are used as inputs for comparison of different approaches.

- **Noisy Case**:

To emulate the uncertainties present in actual measurement conditions, Gaussian white noise is added to the recorded signals. This simulates real-world PMU data that may be affected by noise. After the disturbance, a white Gaussian noise with zero mean is added to the measured signals, which are then used as inputs for comparison of different approaches.

E. Modal Analysis

Before applying measurement-based methods, oscillatory modes of 14-bus and 39-bus systems are calculated using modal eigenvalue analysis to serve as the basis for comparisons. It should be noted that modal analysis is done using predefined models of DIgSILENT Power Factory, where the eigenvalues are calculated using the QR method through system reduction. The obtained eigenvalue plots, indicating oscillatory modes of 14-bus and 39-bus systems, are shown in Figure 5 and Figure 6, respectively.

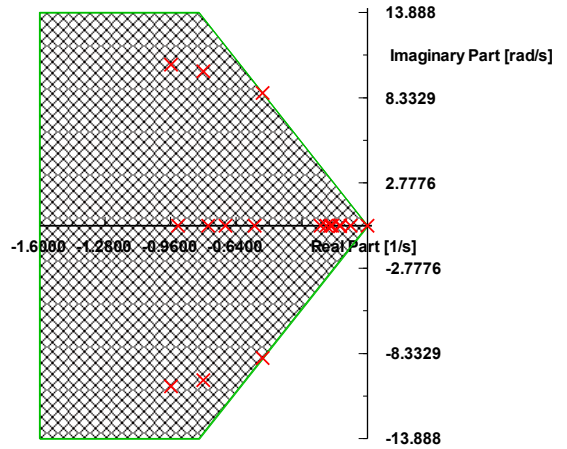

Fig. 5. Eigenvalue plot of 14-bus system

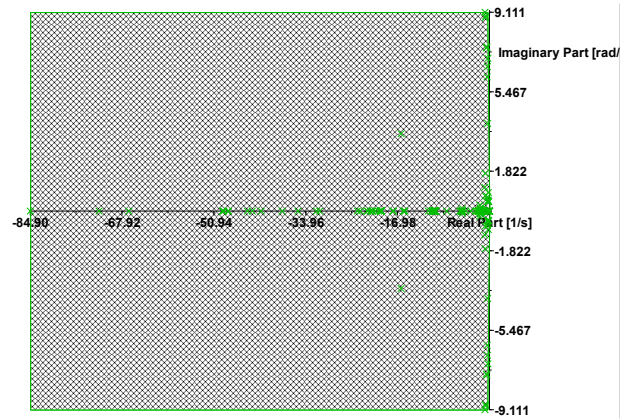

Fig. 6. Eigenvalue plot of 39-bus system

As observed in Figure 5 and Figure 6, there are four dominant oscillatory modes in the 14-bus and nine oscillatory modes in the 39-bus systems, whose specifications are listed in the following tables, respectively.

TABLE I OSCILLATORY MODES OF THE 14-BUS SYSTEM

Mode No.	Frequency (Hz)	Damping (1/s)	Mode Shape
1	1.36	0.51	G_1, G_2 vs. G_5
2	1.60	0.80	G_1 vs. G_3
3	1.66	0.96	G_3 vs. G_2
4	2.21	1.56	G_1 vs. G_2

TABLE II OSCILLATORY MODES OF THE 39-BUS SYSTEM

Mode No.	Frequency (Hz)	Damping (1/s)	Mode Shape
1	1.32	1.51	G_8 vs. G_{10}
2	1.13	1.08	G_9 vs. G_8, G_{10}
3	1.30	0.99	G_5 vs. G_4, G_6, G_7
4	1.30	1.01	G_5 vs. G_4, G_6
5	1.07	0.85	G_5, G_4 vs. G_7, G_6
6	1.08	0.61	G_3 vs. G_2
7	0.87	0.54	G_9 vs. G_2, G_3
8	0.94	0.52	G_4-G_7 vs. G_2, G_3
9	0.66	0.37	G_1 vs. grid

F. Developed Method Simulations

To evaluate the effectiveness of the developed methods, simulations are carried out under two scenarios: Ideal and Noisy conditions, and the obtained results are compared with those from modal analysis.

Ideal Case Simulation:

In this case, simulations are conducted on both 14-bus and 39-bus systems. In each system, the oscillatory modes are identified using a developed method and the Prony algorithm as measurement-based methods. In addition, the results are verified compared to a realistic modal specification that has been obtained via modal analysis as a model-based method.

IEEE 14-bus test system

In the 14-bus system, a three-phase-to-ground fault is simulated on the transmission line, connecting bus2-bus4, at second 2 for a duration of 200ms. The fault is cleared at 2.2 s, occurring at the midpoint of the 132 kV transmission line. In practice, synchronized rotor angle and rotor speed signals are not directly measurable, although they contain detailed modal information. Thus, the evaluation is performed using PMU-accessible signals such as active power.

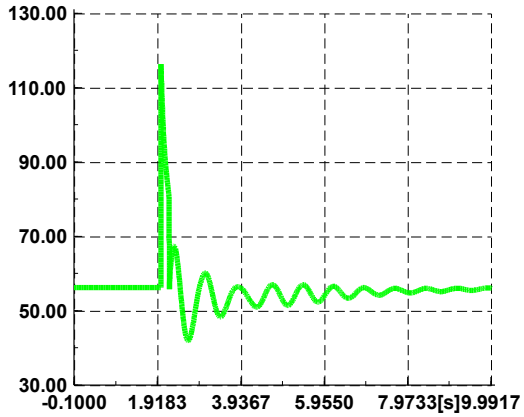

Fig. 7. Active power variation on Line$_{2-4}$ under 200-ms fault in 14-bus system

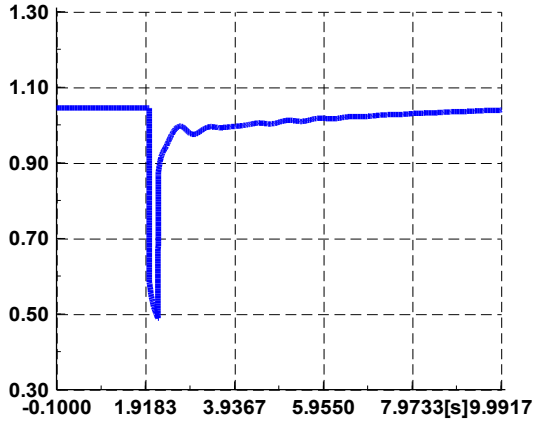

Fig. 8. Voltage variation at Bus 2 under 200-ms fault in 14-bus system

Since PMUs can capture time-synchronized power and voltage data, these are used in the analysis. As shown in Figure 7, the power flow initially measures 56.17 MW, and after the disturbance, the system stabilizes, and the power flow returns to its original level. Similarly, the per-unit voltage at Bus 2, shown in Figure 8, also returns to pre-fault levels. The PSD method is then applied to the active power signal of Line$_{2-4}$. From Figure 9, two dominant oscillation frequencies—1.66 Hz and 1.36 Hz—are identified, corresponding to Modes 1 and 3 in Table 1. This confirms that the PSD method can accurately estimate modal frequencies without requiring the system model. From repeated simulations, the following key insights were obtained:

- Oscillatory modes are more evident in line power flow signals than in bus voltage signals.
- Other oscillatory modes can also be identified in different line power signals. For better reliability, it is recommended to use multiple signals for robust mode estimation.
- The time window for PSD input must start a few milliseconds after fault clearance (e.g., ~100 ms) and end before the oscillations have fully decayed.

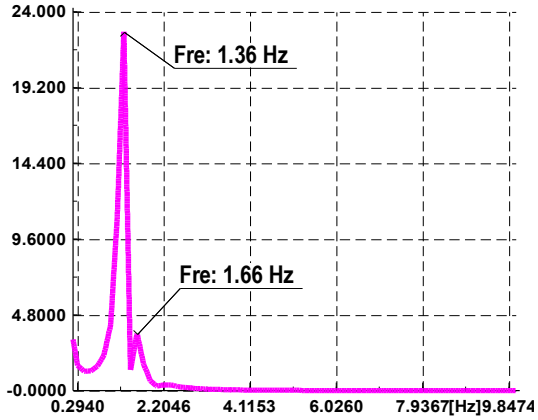

Fig. 9. PSD result for Line$_{2-4}$ power signal in 14-bus system

To compute the CSD, the voltage angle of one generator bus must be used as a reference. In the IEEE 14-bus system, Generator 1 (with 1.06pu and 0° angle) is chosen as the reference. Then, CSD is applied to the generator's bus frequency signals. The variation of generator buses' frequency during the fault occurrence and after its clearance is shown in Figure 10.

Corresponding CSD to Figure 10 is illustrated in Figure 11. As can be seen in Figure 11, at 1.36 Hz, Buses 1, 2, and 3 oscillate against Buses 6 and 8. At 1.66 Hz, Buses 3 and 6 oscillate against Buses 1 and 8. These coherent groupings confirm the effectiveness of the CSD method in identifying mode shapes.

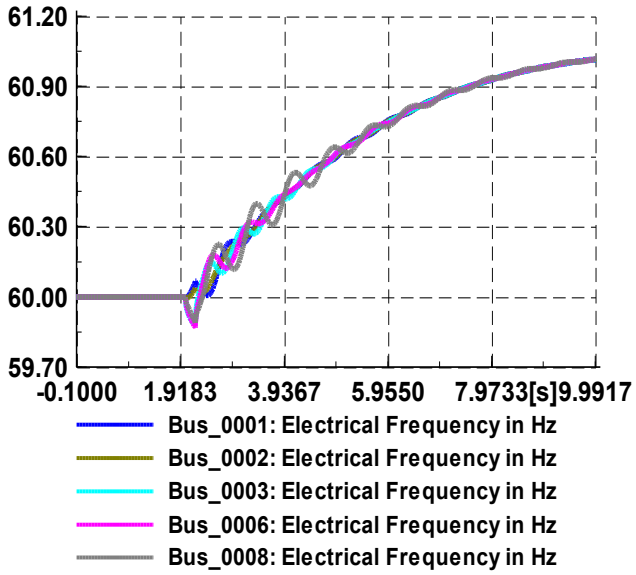

Fig. 10. Generator bus frequency variations during the 200-ms fault in 14-bus system

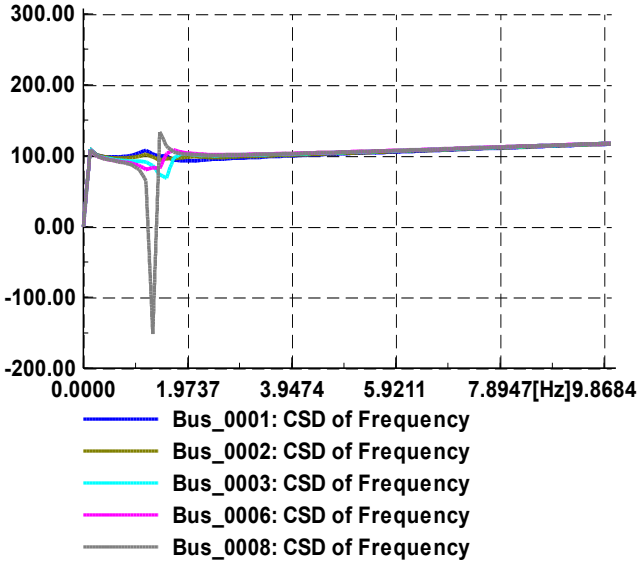

Fig. 11. CSD phase analysis of generator bus frequencies in 14-bus system

IEEE 39-bus test system

In the 14-bus system, a three-phase-to-ground fault is simulated on the transmission line, connecting bus14-bus4, at second 2 for a duration of 200[ms]. The fault is cleared at 2.2 s, occurring at the midpoint of the transmission line. In practice, synchronized rotor angle and rotor speed signals are not directly measurable, although they contain detailed modal information. Thus, the evaluation is performed using PMU-accessible signals such as active power and bus voltage. The variation of the total active power of line 14-4 is indicated in Figure 12. Same as previous simulations, the PSD is applied to the active power signal captured from PMU data. The corresponding PSD to Figure 12 is illustrated in Figure 13.

As can be observed in Figure 13, the dominant oscillation frequency of 0.66 Hz is well identified, corresponding to Mode 9 in Table II. This confirms that the PSD method can accurately estimate modal frequencies without requiring the system model. It should be noted that other modes could be obtained by applying PSD to different power signal variations. The power variation of Line14-4 provides the exact information of the ninth mode.

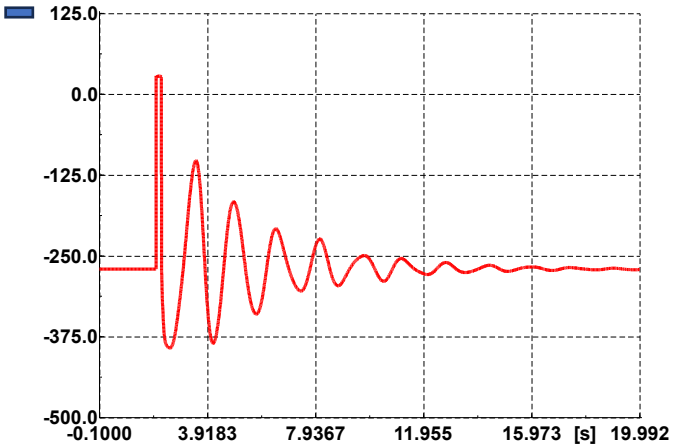

Fig. 12. Active power variation on Line$_{14\text{-}4}$ under 200-ms fault in 39-bus system

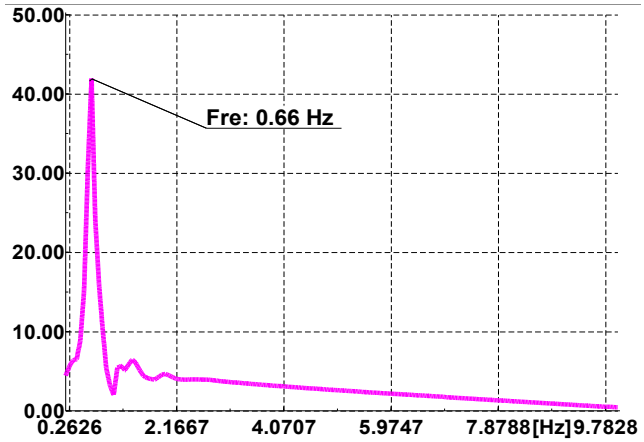

Fig. 13. PSD result for Line$_{14\text{-}4}$ power signal in 39-bus system

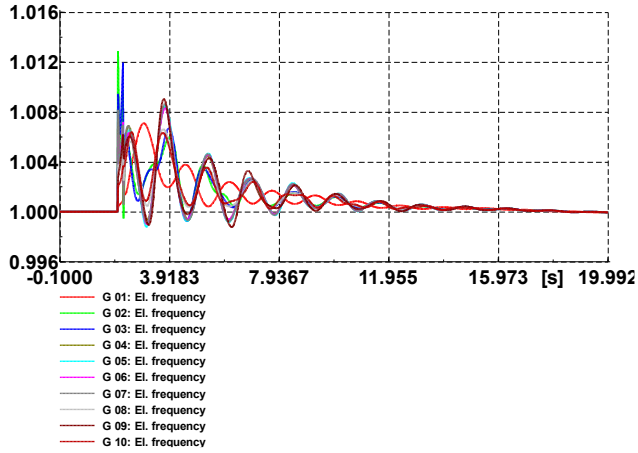

Fig. 14. Generator bus frequency variations during the 200-ms fault in 39-bus system

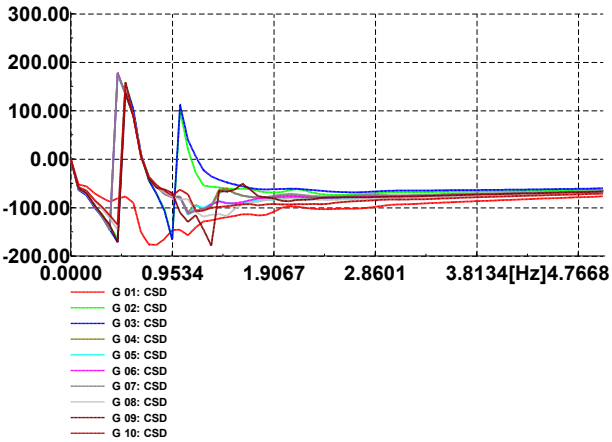

Fig. 15. CSD phase analysis of generator bus frequencies in 39-bus system

To calculate the Cross-Spectral Density (CSD), the voltage angle of a generator bus must be considered as a reference. In the 39-bus system, Generator 1—which represents an aggregation of multiple generators—is selected as this reference. The frequency variations of all ten generator buses following the three-phase fault are depicted in Figure 14. Subsequently, CSD is applied to the frequency signals of the generator buses, with the results shown in Figure 15. As illustrated, at approximately 0.66 Hz, Generator 1 (red line) oscillates against the other generators. Figure 15 provides additional detailed information regarding the oscillatory interactions among generators across the grid, which correspond directly to the mode shapes of various oscillatory modes. While multiple details can be extracted, the primary focus here is the generator's behavior at the 0.66 Hz frequency. These coherent groupings validate the effectiveness of the CSD method in accurately identifying mode shapes.

G. Simulation under Noisy Conditions (SNR = 30)

In this section, all simulations are repeated under the noisy conditions.

IEEE 14-bus test system

In this scenario, white Gaussian noise with an SNR of 30 is added to the active power flow signal of $Line_{2-4}$ in the 14-bus system. The results of the PSD analysis are presented in Figure 16. As shown, the two dominant frequencies—1.66 Hz and 1.36 Hz—are still clearly identifiable, while the peak magnitudes are a little bit lower in comparison to ideal conditions. After identifying the modal frequencies, the CSD function is applied to the noisy generator bus frequency signals (Figure 17).

The results indicate that the oscillatory behavior of the generators remains consistent with the ideal case. Despite the added noise, the CSD outputs are not significantly degraded, confirming the noise immunity of the proposed methods.

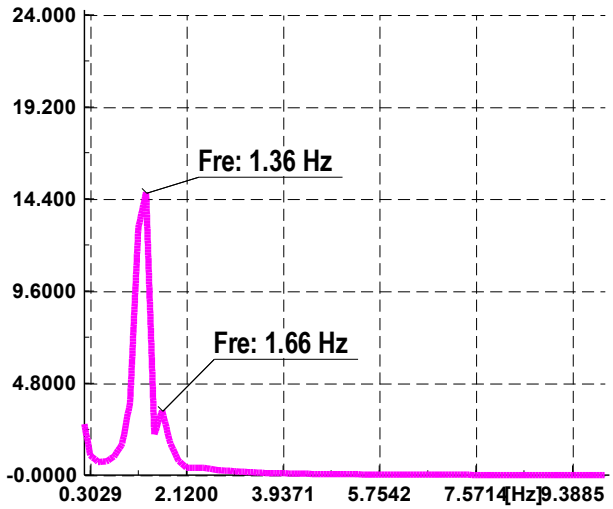

Fig. 16. PSD result for $Line_{2-4}$ with SNR = 30 in 14-bus system

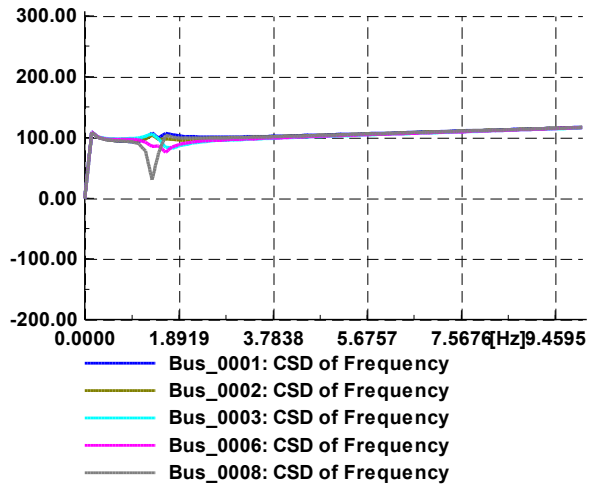

Fig. 17. Corresponding CSD to generator frequencies with SNR = 30 in 14-bus system

IEEE 39-bus test system

All the simulations are repeated for the 39-bus system under noisy conditions. The PSD corresponding to the active power flow signal of Line14-4 in the 39-bus system is indicated in Figure 18. As can be seen, the dominant frequency 0.66 Hz is still clearly identifiable, while the peak

magnitudes are a little bit lower in comparison to ideal conditions. After identifying the modal frequencies, the CSD function is applied to the noisy generator bus frequency signals. Corresponding CSD results are shown in Figure 19.

As can be seen, the oscillatory behavior of the generators remains consistent with the ideal case. Despite the added noise, the CSD outputs are not significantly degraded, confirming the noise immunity of the developed methods.

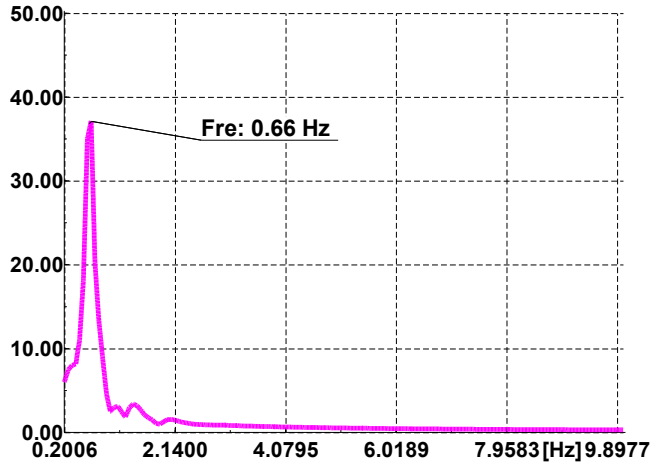

Fig. 18. PSD result for Line$_{14-4}$ with SNR = 30 in 39-bus system

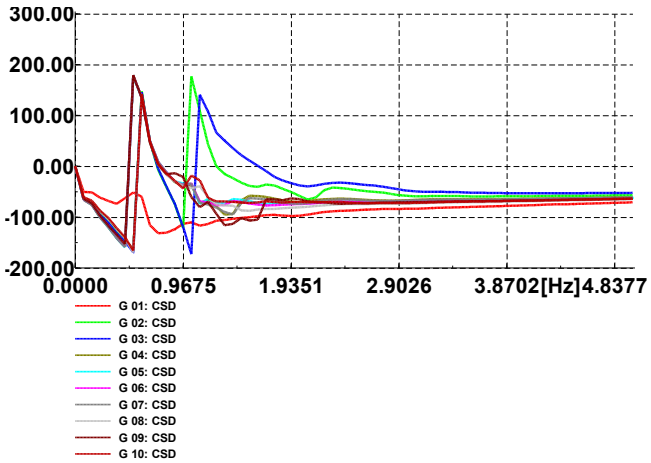

Fig. 19. Corresponding CSD to generator frequencies with SNR = 30 in 39-bus system

H. Prony Algorithm

In order to prove the robustness of the developed method, the results are compared with the Prony algorithm as a measurement-based method under ideal and noisy conditions. The comparison is done for the 39-bus case study. The same input data that has been used for PSD calculation is set as the Prony algorithm input.

It should be noted that the raw data obtained from the dynamic simulation is exported from DIgSILENT Power Factory version 15.1.7 and then imported to MATLAB R2022a, where the Prony algorithm is applied via Signal Processing Toolbox. Simulation results for the ideal case and

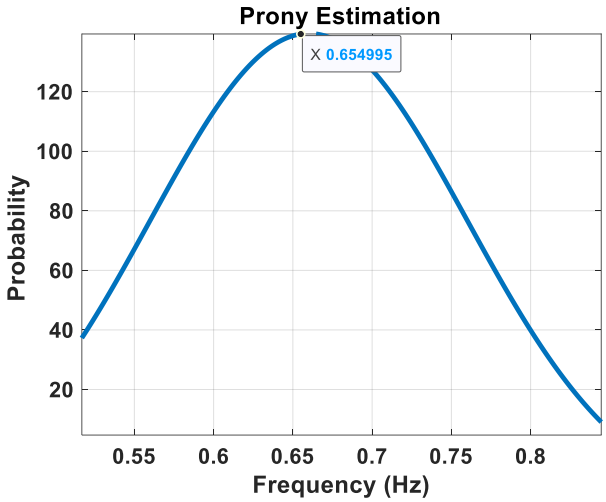

Fig. 20. Prony algorithm in ideal case in 39-bus system

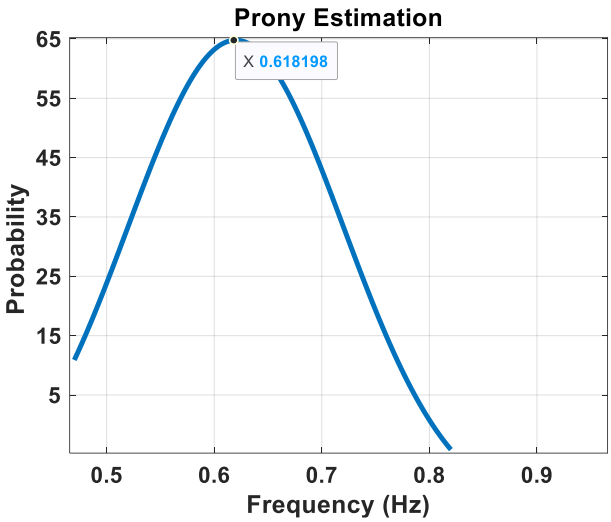

Fig. 21. Prony algorithm in noisy case in 39-bus system

It should be noted that the raw data obtained from the dynamic simulation is exported from DIgSILENT Power Factory version 15.1.7 and then imported to MATLAB R2022a, where the Prony algorithm is applied via Signal Processing Toolbox. Simulation results for the ideal case and noisy case are shown in Figure 20 and Figure 21, respectively.

As can be seen, in the ideal condition without considering noise, the Prony algorithm estimates the frequency near its real value, 0.66 Hz, with the minimum error. However, the probability plot in Figure 21 proves the Prony inefficiency under noisy conditions exactly as other papers in the literature review. Therefore, the Prony algorithm accuracy is highly degraded under noisy conditions.

I. Interpretation of Results

The comparative evaluation of model-based (modal analysis) and measurement-based (developed method and Prony algorithm) methods yields the following key findings:

- Model-based techniques, such as modal analysis, require accurate dynamic modeling of all system components, particularly synchronous generators. While this is feasible for small benchmark systems, such as the IEEE 14-bus, it becomes impractical for large interconnected power networks due to the lack of complete and precise dynamic data.
- A significant outcome of this study is that measurement-based methods can reveal oscillatory modes in various system signals. For PSD, long transmission line power signals are most suitable, while for CSD, bus frequencies are the best input signals.
- The timing of the analysis window is critical for measurement-based methods. The time window should begin a few milliseconds (approximately 100ms) after fault clearance and end before the oscillations fully decay. Early signal portions only reflect transient dynamics and do not accurately contain modal information.
- The estimated frequencies from the developed method closely match the results from modal analysis. For instance, modal analysis detects modes at 1.36 Hz and 1.60 Hz, while the developed method estimates them as 1.359 Hz and 1.659 Hz. Even under noisy conditions (SNR = 30), estimated values remain highly accurate.
- Whether in ideal or noisy environments, the CSD method correctly identifies oscillatory relationships among generators. Given its speed and accuracy, it can be used for preventive control and mitigation of wide-area blackouts.
- An important operational insight is that long inter-area transmission lines are particularly prone to initiating system-wide instability, especially when heavily loaded. Monitoring power flow across these lines can help detect early signs of oscillations and prevent system collapse.
- Comparison between the developed method and the Prony algorithm, as a measurement-based method, shows that the Prony algorithm accuracy is highly prone to noisy data. However, in the ideal condition, the Prony algorithm estimates the frequency very accurately.

V. Conclusion and Future Work

According to the literature, power oscillations—particularly under high loading conditions—can lead to the loss of synchronism in power systems. Therefore, accurately detecting and responding to these oscillations in real time is critical for ensuring the stability of modern multi-machine power systems and preventing blackouts. Model-based methods are often unsuitable for large-scale networks due to their reliance on complete and accurate dynamic models. With the emergence of PMUs, measurement-based approaches have become essential. While several measurement-based methods have been proposed, many suffer from noise sensitivity or computational inefficiency.

In this paper, PSD and CSD techniques are developed as efficient tools for small-signal stability assessment using only synchronized PMU data. In addition, the Prony algorithm accuracy degradation as a measurement-based method under noisy data has been proven.

Simulation results on the IEEE 14-bus and 39-bus systems demonstrate that the developed method can accurately estimate oscillatory modes—even in the presence of measurement noise—without requiring knowledge of system model order or the entire network. The results are also validated against modal eigenvalue analysis from DIgSILENT, confirming their high accuracy.

J. Recommendations for Future Work:

- The developed methods should be applied to larger benchmark systems, such as the IEEE 118-bus system, to thoroughly evaluate their scalability and overall performance.
- This study focused exclusively on white Gaussian noise; however, real-world systems often experience colored noise, which incorporates system dynamics and can affect accuracy. Future research should investigate the effects of different noise types on results.
- The selection of signals plays a critical role in the accuracy of measurement-based approaches. Even the most advanced identification techniques may fail if the input signals do not contain pertinent dynamic information. Therefore, it is vital to choose signals that capture steady-state modal behavior rather than transient responses.

REFERENCES

[1] Phadke, Arun G. "Synchronized phasor measurements-a historical overview." In IEEE/PES transmission and distribution conference and exhibition, vol. 1, pp. 476–479. IEEE, 2002.

[2] Kundur, Prabha. "Power system stability." Power system stability and control 10 (2007): 7–1.

[3] Maleki Rizi, Masoud, Saeed Abazari, and Nima Mahdian. "Dynamic Stability Improvement of Power System with Simultaneous and Coordinated Control of DFIG and UPFC using LMI." International Journal of Industrial Electronics Control and Optimization 4, no. 3 (2021): 341-353.

[4] Kundur, Prabha, John Paserba, Venkat Ajjarapu, Göran Andersson, Anjan Bose, Claudio Canizares, Nikos Hatziargyriou et al. "Definition and classification of power system stability IEEE/CIGRE joint task force on stability terms and definitions." Power Systems, IEEE Transactions on 19, no. 3 (2004): 1387-1401

[5] Farmer, Richard G. "Power system dynamics and stability." The Electric Power Engineering Handbook Series, CRC Press LLC, 2001.

[6] Babaali, AmirHossein, and Mohammad Taghi Ameli. "Multi-class short-term voltage stability assessment considering the missing data."

International Journal of Industrial Electronics Control and Optimization (2025).

[7] IEEE Working Group. "IEEE Guide for Identification, Testing and Evaluation of the Dynamic Performance of Excitation Control Systems." 421–2.

[8] Pourbeik, Pouyan, Prabha S. Kundur, and Carson W. Taylor. "The anatomy of a power grid blackout-root: causes and dynamics of recent major blackouts." IEEE Power and Energy Magazine 4, no. 5 (2006): 22–29.

[9] Han, Lei, Yibing Wang, Yu Zhang, Cheng Lu, Chengwei Fei, and Yongjun Zhao. "Competitive cracking behavior and microscopic mechanism of Ni-based superalloy blade respecting accelerated CCF failure." International Journal of Fatigue 150 (2021): 106306.

[10] Yu, Yiping, Yaling Shen, Xiang Zhang, Jiyun Zhu, and Jiajia Du. "The load oscillation energy and its effect on low-frequency oscillation in power systems." In 2015, the 5th International Conference on Electric Utility Deregulation and Restructuring and Power Technologies (DRPT), pp. 1336–1341. IEEE, 2015.

[11] Jami, Mehran. "Virtual inertia control and small-signal stability analysis of electric vehicle." International Journal of Industrial Electronics Control and Optimization 6, no. 4 (2023): 261-270.

[12] Cai, Guowei, Deyou Yang, Ying Jiao, and Chunyu Shao. "Power system oscillation mode analysis and parameter determination of PSS based on stochastic subspace identification." In 2009 Asia-Pacific Power and Energy Engineering Conference, pp. 1–6. IEEE, 2009.

[13] Suzuki, Naoto, Takashi Hiyama, and Takahiko Funakoshi. "Real time FFT based on-line identification of power system oscillation modes." IEEJ Transactions on Power and Energy 120, no. 2 (2000): 134–140.

[14] Rueda, José L., Carlos A. Juárez, and István Erlich. "Wavelet-based analysis of power system low-frequency electromechanical oscillations." IEEE Transactions on Power Systems 26, no. 3 (2011): 1733–1743.

[15] Hauer, J. F. "Application of Prony analysis to the determination of modal content and equivalent models for measured power system response." IEEE Transactions on Power Systems 6, no. 3 (1991): 1062–1068.

[16] Teshnehlab, Mohamad, and Mehdi Aliyari-shoredeli. "Fault detection and identification of high dimension system by GLOLIMOT." International Journal of Industrial Electronics Control and Optimization 2, no. 4 (2019): 331-342.

[17] Wies, Richard W., John W. Pierre, and Daniel J. Trudnowski. "Use of ARMA block processing for estimating stationary low-frequency electromechanical modes of power systems." IEEE Transactions on Power Systems 18, no. 1 (2003): 167-173.

[18] M. A. Heydari , M. HassanniaKheibari and G. Sadeghi, "Control of a shunt Active Power Filter with Voltage Source Model to Improve the Power Quality Performance," International Journal of Industrial Electronics Control and Optimization, 7 3 (2024): 247-255, doi: 10.22111/ieco.2024.48277.1547.

[19] Poisson, Olivier, Pascal Rioual, and Michel Meunier. "Detection and measurement of power quality disturbances using wavelet transform." IEEE Transactions on Power Delivery 15, no. 3 (2000): 1039–1044.

[20] Trudnowski, Daniel J., J. M. Johnson, and John F. Hauer. "Making Prony analysis more accurate using multiple signals." IEEE Transactions on Power Systems 14, no. 1 (1999): 226-231.

[21] Qi, Li, Lewei Qian, Stephen Woodruff, and David Cartes. "Prony analysis for power system transient harmonics." EURASIP Journal on Applied Signal Processing 2007, no. 1 (2007): 170–170.

[22] Grund, C. E., J. J. Paserba, J. F. Hauer, and S. L. Nilsson. "Comparison of Prony and eigenanalysis for power system control design." Power Systems, IEEE Transactions on 8, no. 3 (1993): 964–971.

[23] Xiao, Jinyu, Xiaorong Xie, Yingduo Han, and Jingtao Wu. "Dynamic tracking of low-frequency oscillations with improved Prony method in wide-area measurement system." In the Power Engineering Society General Meeting, 2018. IEEE, pp. 1104-1109. IEEE.

[24] Tripathy, P., S. C. Srivastava, and S. N. Singh. "A noise space decomposition based method for identifying low frequency oscillations using synchro-phasor measurements." In the 2010 IEEE Power and Energy Society General Meeting, pp. 1–6. IEEE, 2010.

[25] Ye, Hua, Yutian Liu, and Xinsheng Niu. "Low frequency oscillation analysis and damping based on Prony method and sparse eigenvalue technique." In Networking, Sensing and Control, 2006. ICNSC'06. Proceedings of the 2006 IEEE International Conference on, pp. 1006–1010. IEEE, 2006.

[26] Tripath, P., S. C. Srivastava, and S. N. Singh. "An improved Prony method for identifying low frequency oscillations using synchro-phasor measurements." InPower Systems, 2009. ICPS'09. International Conference on, pp. 1–5. IEEE, 2009.

[27] Zhao, Yishu, Yang Gao, Zhijian Hu, Yongjun Yang, Jie Zhan, and Yan Zhang. "A new method of identifying the low frequency oscillations of power systems." In Energy and Environment Technology, 2009. ICEET'09. International Conference on, vol. 2, pp. 19-22. IEEE, 2009.

[28] Tripathy, P., S. C. Srivastava, and S. N. Singh. "A noise space decomposition based method for identifying low frequency oscillations using synchro-phasor measurements." In the 2010 IEEE Power and Energy Society General Meeting, pp. 1–6. IEEE, 2010.

[29] Fangzong, Wang, and Li Chengcheng. "Online Identification of Low-Frequency Oscillation Based on Principal Component Analysis Subspace Tracking Algorithm." In Power and Energy Engineering Conference (APPEEC), 2010 Asia-Pacific, pp. 1–4. IEEE, 2010.

[30] Yang, Jann N., Ying Lei, Shuwen Pan, and Norden Huang. "System identification of linear structures based on Hilbert–Huang spectral analysis. Part 1: normal modes." Earthquake engineering & structural dynamics 32, no. 9 (2003): 1443-1467.

[31] Osipov, Denis, Stavros Konstantinopoulos, and Joe H. Chow. "A cross-power spectral density method for locating oscillation sources using synchrophasor measurements." IEEE Transactions on Power Systems 2022.
[32] L. L. Freris, A. M. Sasson: “Investigation of the load-flow problem”, PROC. IEEE, Vol. 115, No. 10, October 1968, pp. 1459–1470.
[33] DIgSILENT GmbH, PowerFactory User Manual, Version 15.1, 2022. (Reference for the software tool containing the IEEE 39-bus system).

Zivar Rigi received her B.Sc degree in Electrical engineering from the Islamic Azad Zahedan Univercity,Iran in 2012. Now she is pursuing M.Sc degree in Power Electrical at the Islamic Azad Zahedan Univercity, Iran. Her research interests include power systems, distribution networks and demand response.

Mahdi Hassanniakheibari was born in Gonabad, Iran, in 1987. He received his PhD in Power Electrical Engineering from the Islamic Azad University, Science and Research Branch, Tehran, Iran, in 2020. He is an Assistant Professor at the Islamic Azad University, Zahedan Branch. His research interests include power systems, distribution networks, demand response, and power electronic converters.

International Journal Of
Industrial Electronics Control and Optimization
Print ISSN: 3517-2645
Online ISSN: 3568-2645
Homepage: https://ieco.usb.ac.ir/

Compact Ultra-Wideband Arch-Shaped Wide-Slot Antenna with High Fidelity Factor and Bandwidth Enhancement for Microwave Imaging of Breast Cancer

Motahareh Arezoomandan[1] | Shahram Mohanna[2] | Ahmad Bakhtiari Shahri[3]

Faculty of Electrical and Computer Engineering, University of Sistan and Baluchestan, Zahedan, Iran.[1,2,3]
Corresponding author's email: mohana@ece.usb.ac.ir

Article Info

Article type:
Research Article

Article history:
Received: 02-August-2024
Received in revised form: 15-October-2024
Accepted: 09-December-2024
Published online: 21-March-2026

Keywords:
Ultra-wideband antenna,
Microwave imaging,
Arch shaped,
Wide-slot,
Fidelity factor.

ABSTRACT

A new compact Ultra-Wide Band (UWB) arch-shaped wide-slot antenna was implemented for Microwave Imaging (MI) of breast cancer. It is composed of a fork-shaped strip and an arched slot ground, with a compact size of 16×20 mm and a height of 1 mm. The arched slot in the ground plate enhances the impedance bandwidth and the gain of the antenna. It has a bandwidth of 3.7 GHz to 18 GHz, covers WLAN (5.4 GHz), X band (8-12 GHz), and Ku band (12-18 GHz), and has a gain of 2.7 dBi to 6.3 dBi in the frequency ranges. The fidelity factor was computed for both E-plane and H-plane scenarios, indicating a range of 0.922 - 0.975 for the E-plane across all angles. It has a small size, a simple design, less signal distortion, a high gain of 6.3 dBi, a fractional bandwidth percentage of 131%, and an efficiency of 93.7% at 6 GHz. It exhibited reliable performance in terms of the fidelity factor at all angles compared to the most recent works. An MI simulation for breast tumor detection was performed to detect changes in the backscattering signal in the presence or absence of a tumor with a high dielectric inclusion. S11 is quite high when measured in front of a breast model. There is a noticeable difference in S21 between the scenarios with and without a tumor in the breast model. There are significant variations in the transmission parameter across the entire frequency range between the scenarios with and without a tumor.

I. Introduction

Microwave Imaging (MI) has the potential for early detection and localization of malignant tissues in the human body [1]. As a non-invasive medical imaging technique, it can be employed to detect breast and brain tumors, image bones, diagnose localized anemia in various parts of the human body, and monitor thermal ablation of liver tumors. Breast cancer is globally recognized as a leading cause of mortality among women [2]. Current imaging techniques for breast cancer detection include X-ray mammography, ultrasound, Magnetic Resonance Imaging (MRI), and combined techniques. Early detection plays a crucial role in successful cancer treatment. The maximum accuracy achieved among these techniques is almost 75.6 percent [3].

MI for breast cancer diagnosis works based on the changes in electrical properties of healthy tissues and tumors. MI is a non-ionizing radiation technique, with proper tissue penetration and low power transmission with fewer health risks [4].

Antennas are essential components of any MI system. Basically, in Ultra-Wide Band (UWB) radar imaging systems, the transmitting antennas emit short UWB pulses and then process the back-scattered signals from the tissue received by the receiving antennas, where significant scattering signatures can be identified and localized. Increasing the bandwidth of these pulses has advantages, including deep tissue penetration at lower frequencies and improved range resolution at higher frequencies. Therefore, the antenna element should possess a

wide bandwidth to transmit such pulses with minimal signal distortion to achieve a high-resolution image of the human body (tissues) [5].

In the microwave radar imaging context, the literature highlights the requirements of using directive antennas with a compact size, very wide frequency bandwidth, high gain and improved efficiency. Specifically for MI of human tissues, it is essential to design antennas that have high-fidelity factors in the time domain [3, 6-9]. Furthermore, the time-domain performance of the antenna must be high to ensure successful penetration through human tissues without significant distortion. Two important distortion characteristics of an antenna are the fidelity factor, which refers to distortion in the time domain, and the group delay, which refers to distortion in the frequency domain [10]. Considering these criteria, UWB antennas are well-suited for MI systems.

Various UWB antennas have been proposed for MI and radar systems, including Vivaldi antennas [11-15], spiral antennas [16], planar monopole antennas [8, 17-19], planar slot antennas [20-22], bowtie antennas, and horn antennas. A comprehensive review of these antennas and their characteristics can be found in [5]. Monopole and wide slot planar antennas are commonly used in antenna arrays for microwave breast imaging systems. These antennas offer advantages such as simple design, small axial length, wide frequency range, and convenient fabrication process. Additionally, designing compact antennas enables more antenna elements to be positioned around the tissue, improving signal utilization and overall resolution [23].

An eagle-shaped UWB patch antenna has also been designed for MI, emphasizing its innovative shape for achieving directional radiation [25]. In comparison with other methods, this work utilizes a simple and effective approach to achieve a bi-directional radiation pattern. In another wide-slot antenna, the radiating element is modified by cutting slots in both patches and the ground plane, enhancing the electrical length to achieve an omnidirectional radiation pattern with a high gain. This method increases the resonance frequency, gain, and efficiency of the antenna without changing its dimensions [20].

In another study [34], the antenna described in [20] has been modified by adding a reflector to create a more directive high-gain antenna. Although this design enhances gain, directivity, and the correlation factor, the large profile of the antenna (29.4 × 32.2 × 25 mm^3) challenges the benefits of compactness and simplicity. In [35], a metamaterial-layer-based lens and an Artificial Magnetic Conductor (AMC) have been utilized to enhance field performance (gain, radiation patterns). Despite achieving high gain, this structure has a larger size (50 × 50 mm^2) and limited impedance matching (2-5 GHz) compared to other designs intended for breast tissue imaging.

Most communication systems prefer to utilize a single radiating element that supports multiple bands and functions, resulting in reduced size and weight [36]. However, for MI, antennas with multi-purpose operation and broader frequency coverage are required. Thus, this project aims to implement an antenna optimized for MI systems. The design of the antenna in this project is based on the structure in [24] exhibiting significant modifications and optimizations to achieve efficient performance in the UWB frequency range.

This project implements a new compact antenna with a high-fidelity factor, which is suitable for MI applications. The antenna has a uniform radiation pattern and notable gain and is efficient in the frequency range, making it suitable for microwave breast imaging applications. The analysis is performed in the time domain, as well as a frequency domain, employing CST Microwave Studio.

II. The Project Overview

The new antenna is composed of a fork-shaped strip, an arched ground slot, and a meander line embedded into the ground plain of the slot. The application of an arched slot in the ground effectively improves both the impedance bandwidth and the gain of the antenna. As a result, the new radiation design provides a wide fractional bandwidth exceeding 131% across its operational range of 3.7–18 GHz. The implementation of novel techniques in designing the antenna's radiation components has led to the attainment of various characteristic parameters, including a maximum simulated gain of 6.3 dBi for the compact antenna. Compared to several documented UWB-based antennas in the literature, the suggested antenna exhibits greater compactness and a wider bandwidth. Moreover, the proposed antenna was analyzed in the time domain was, resulting in a fidelity factor of 0.975 within the frequency range of 3-13 GHz in a face-to-face scenario. This proves a remarkable reduction in signal distortion of the antenna.

An MI simulation for breast tumor detection was performed to detect changes in the backscattering signal in the presence or absence of a tumor with a high dielectric inclusion.

III. Antenna Design

The new wide-slot antenna consists of an arched-shaped slot with meandered arms in a ground plane on one side of an FR4 substrate (with $\varepsilon r = 4.3$ and $\tan \delta = 0.025$). A forked microstrip feed is located on the opposite side of the substrate, as depicted in Fig. 1. The proposed antenna has dimensions of L×W×hs, and a 50Ω coaxial transmission line is used for antenna feeding.

As shown in Figure 2(a), the primary structure has a rectangular slot on its ground plane. In the subsequent stage, an arched-shaped aperture is implemented on the ground plane of the antenna, as depicted in Figure 2(b). This alteration is intended to generate extra resonant frequencies and enhance the return loss. The last step involves using the meandering technique to decrease the lowest operating frequency of the

antenna. Through the implementation of meandering, the current path is extended, resulting in antenna miniaturization and improved matching (lower S11) within the 6-13 GHz range. The proposed antenna is displayed in Fig. 2(c). The parameters for the final antenna configuration, leading to a reflection coefficient (S11) below -10 dB across the frequency range of 3.6-18.5 GHz, can be found in Table I. Figures 3 and 4 show the simulated return loss performance, gain, and efficiency of the designed structure throughout the evolution process.

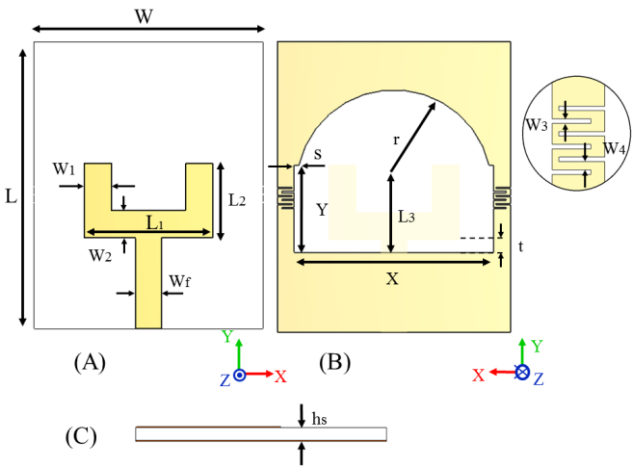

Fig. 1. The geometry of the proposed wide-slot antenna: A) top view, B) bottom view, and C) side view.

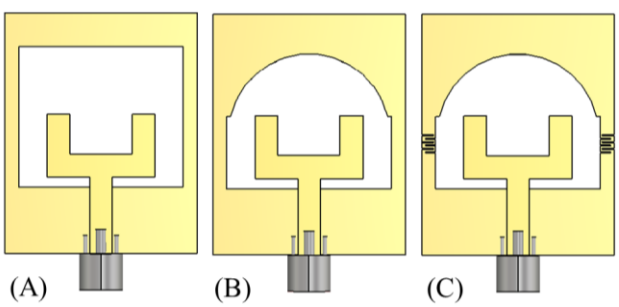

Fig. 2. The structure of the various antennas: A) basic structure, B) basic structure with an arched shape slot, and C) basic structure with arched shape slot and meandered arms (the proposed antenna).

Figure 5 demonstrates the impact of design parameters t, L1, L2, and W3 on S11 by varying one parameter at a time, while keeping all other parameters fixed at the values specified in Table I. This parametric study aimed to investigate the impact of specific antenna design parameters on overall performance. The plot illustrates the relationship between the antenna's reflection coefficient (S11) and each of the four parameters.

Optimal values for these parameters were determined based on achieving the widest bandwidth for S11 below -10 dB (indicated by the black solid line). The substantial influence of all the parameters on the antenna's return loss

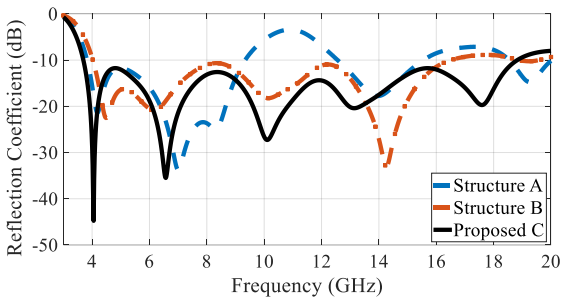

Fig. 3. Simulated reflection coefficient characteristics for various wide-slot antenna structures, as illustrated in Figure 2.

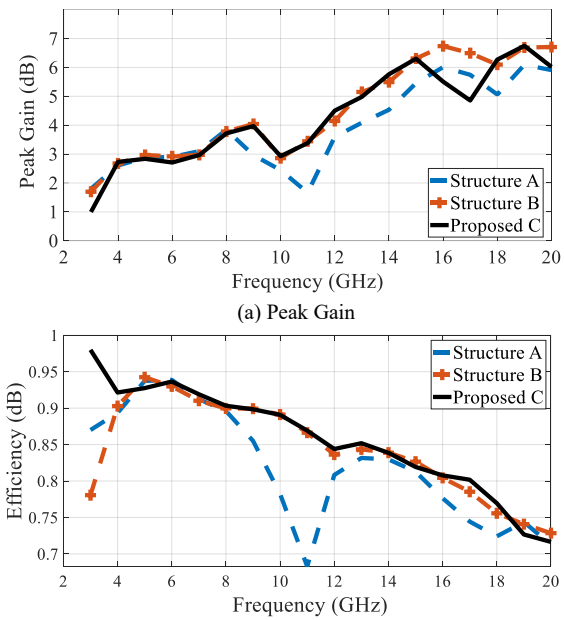

Fig. 4. Simulated (a) gain and (b) efficiency for various wide-slot antenna structures.

is observed through the plots. Changing the distance of t has a significant effect on S11 performance, and when t = 0, the return loss performance deteriorates. As shown in Figure 5(b), the upper frequency of the bandwidth decreases as L1 increases. Additionally, changing the width of W3 can affect both the lower and upper frequencies of the bandwidth.

IV. Frequency Domain Analysis

The fabricated images of the designed wide-slot antenna, including both the front and back views, are illustrated in Figure 6(a). To validate the performance of the antenna, the measured results are compared with the simulated results.

The return loss results obtained from the measurements and simulations in free space demonstrate a satisfactory agreement, as depicted in Figure 6(b). The wide-slot antenna exhibits a measured bandwidth of 10 dB return loss, ranging from 3.7 to 18 GHz.

Figures 7(a) to (c) display the measured and simulated far-field radiation patterns of the wide-slot antenna at frequencies

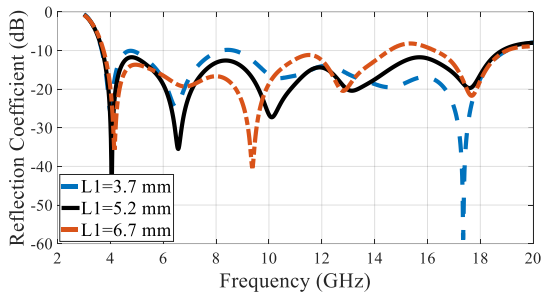

(a) L1

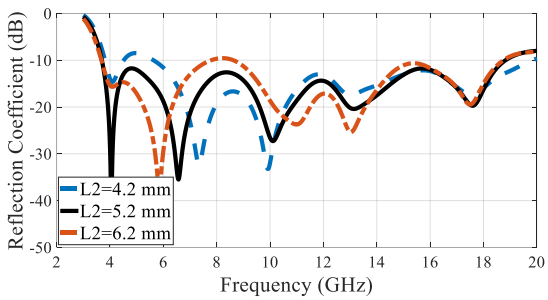

(b) L2

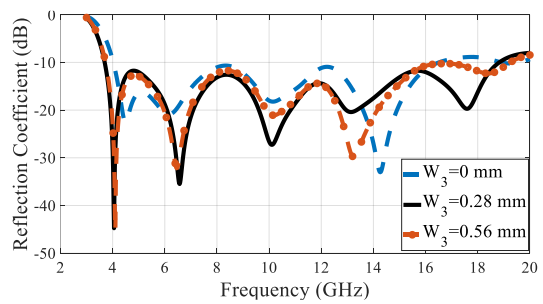

(c) W3

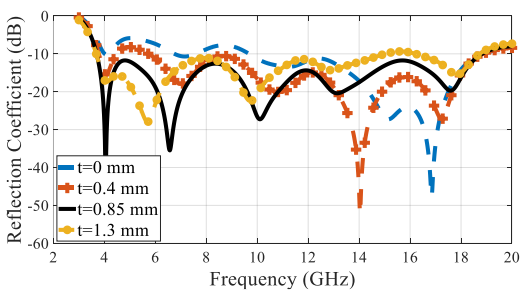

(d) t

Fig. 5. The impact of design parameters t, L1, L2 and W3 on S11 by varying one parameter at a time, with respect to (a) distance t, (b) forked width L1, (c) forked length L2, and (d) meandering width W3. The finalized parameters correspond to the (black) solid line in all plots.

of 4, 8, and 12 GHz. The radiation patterns for the E-plane (y-z plane) and H-plane (x-z plane) are presented, showing a satisfactory alignment between the measured and simulated patterns. This agreement indicates a strong correlation between the predicted and observed radiation characteristics of the antenna.

TABLE 1 PARAMETERS OF THE ANTENNA SHOWN IN FIG.1

Parameter	Value	Parameter	Value
L	20mm	W2	1.9mm
W	16mm	W3	0.1mm
X	13.7mm	W4	0.2mm
Y	6mm	Wf	1.83mm
L1	5.2mm	R	6.7mm
L2	5.2mm	S	0.32mm
L3	4.5mm	T	0.28mm
W1	1.9mm	Hs	1mm

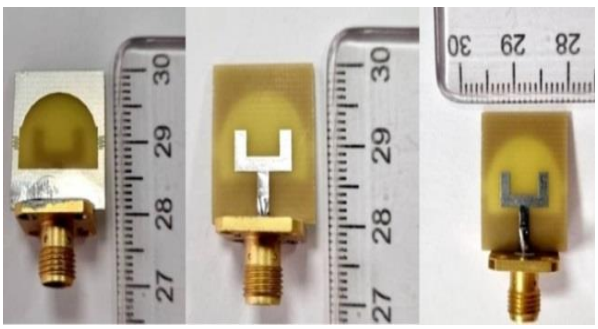

(a) Fabricated Antenna

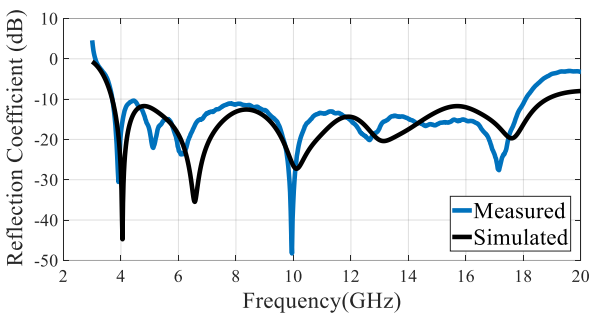

(b) Reflection coefficient

Fig. 6. (a) Photo of fabricated UWB scheme in the front and back view. (b) Measured and Simulated curve of Reflection Coefficient

Figure 8 compares the measured and simulated changes in gain for the proposed antenna. At a frequency of 15 GHz, the simulated and measured gain for the proposed antenna reaches its highest values of 6.3 dBi and 8.6 dBi.

V. Time Domain Analysis

MI systems utilize UWB antennas to transmit data using short pulses across a wide frequency range. However, these narrow pulses are susceptible to dispersion, resulting in distortion upon reception. Nevertheless, the receiver is still capable of recognizing and interpreting the incoming pulse. To mitigate this issue, a time domain analysis of the transmitted pulse is conducted to anticipate and compensate for the system-induced distortion. So, the antenna must have high time-domain performance to effectively penetrate pulses in human tissues and minimize waveform distortions. The fidelity factor is employed to quantify the distortion in the time domain.

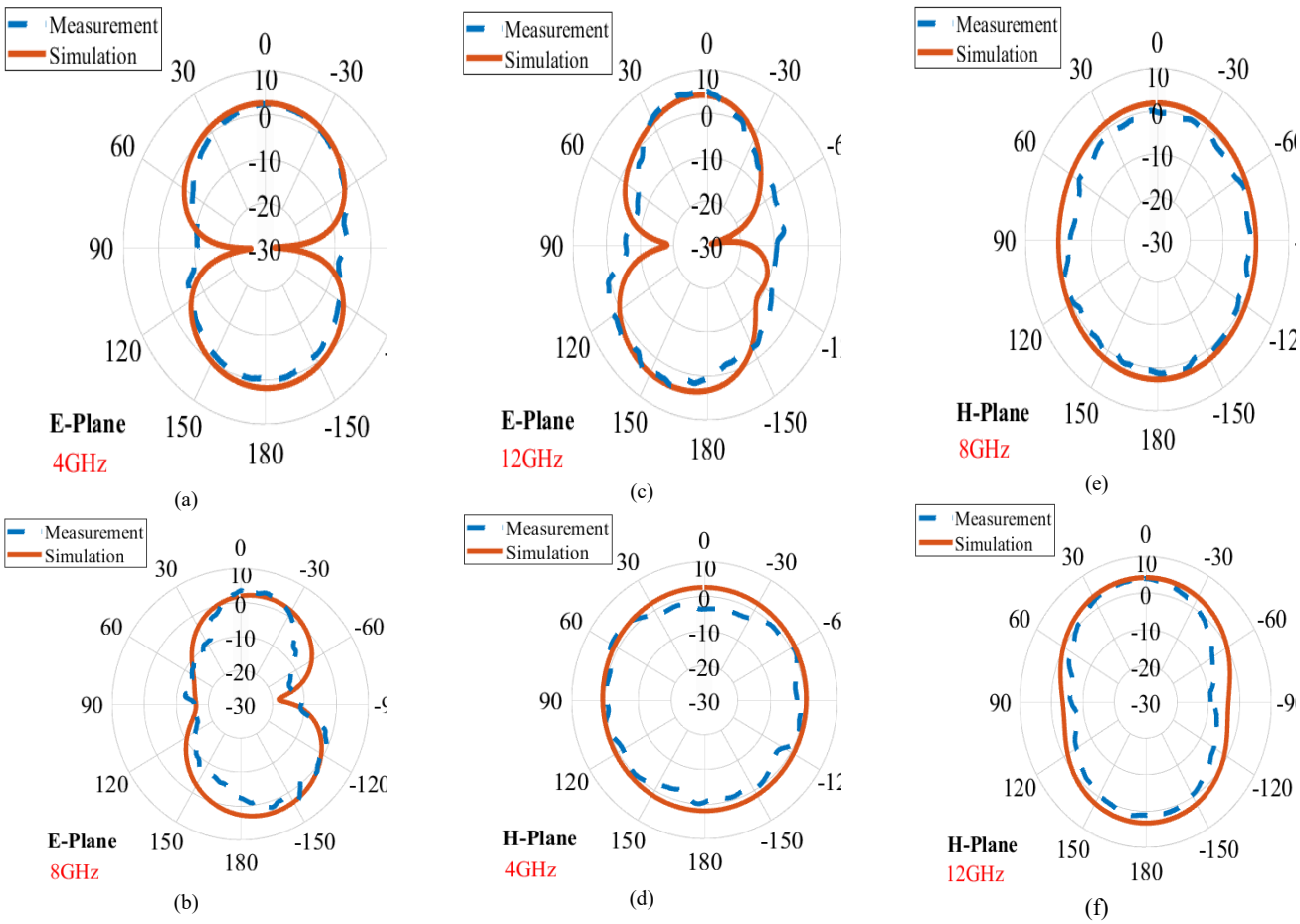

Fig. 7. The simulated and measured radiation patterns at 4 GHz, 8 GHz and 12 GHz. (a-c) E-Plane, (d-f) H-plane.

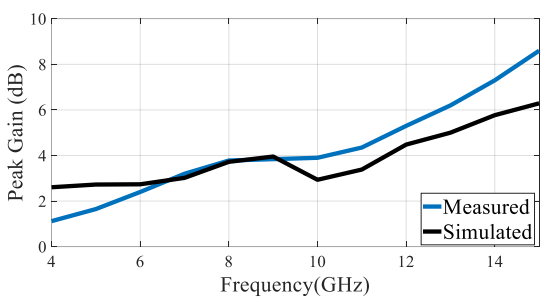

Fig. 8. The simulated and measured gain.

It utilizes the frequency domain transmission coefficient (S21) to compute the correlation between the received and transmitted signals. The fidelity factor depends on various parameters, including the incident signal waveform, gain, and return loss [8]. The calculation of the fidelity factor involves determining the maximum amplitude of the cross-correlation between the received and transmitted signals.

The fidelity factor (FF) is given by:

$$FF = \max_{\tau} \int_{-\infty}^{+\infty} \hat{T}(t)\hat{R}(t+\tau) \quad (1)$$

where $\hat{T}(t)$ and $\hat{R}(t)$ are the normalized transmitted and received signals. To obtain the received signal in the time domain, the following relation can be used:

$$R(\omega) = FFT\big(T(t)\big)H(\omega) \quad (2)$$

$$R(t) = IFFT(R(\omega)) \quad (3)$$

where H(ω) is the system transfer function and is also equivalent to S21, based on the above relationship. To minimize distortion in the received signal in the time domain, the antenna transfer function should possess a flat magnitude.

Group delay is a significant parameter that describes the response of UWB antennas in the frequency domain. It is defined as the derivative of the phase response ∠H(ω) [10].

To ensure minimal signal distortion during pulse transmission, it is necessary for the group delay of the antenna to be constant or have a deviation of less than 1 ns within its operating frequency band. The formula for calculating group delay is:

$$\tau = -\frac{d\phi(\omega)}{d(\omega)} \quad (4)$$

where ϕ represents the phase of the transfer function and ω represents the angular frequency.

Consistency in the magnitude of the antenna transfer function across the operating bandwidth is essential to minimize fluctuations in group delay [8]. This, in turn, is crucial for ensuring limited signal distortion and maintaining a high-fidelity factor in the time domain. Therefore, there is an interconnection between the group delay in the frequency domain and the fidelity factor in the time domain.

To demonstrate it, we positioned two antennas facing each other spaced by 240 mm and calculated the amplitude and phase of S21 and the group delay of the antenna. As shown in Fig.9 the variation of the group delay in this interval is lower than 0.4ns. Additionally, the amplitude of S21 remains approximately constant, and the phase of S21 is linear in the frequency range. Furthermore, side-by-side and face-to-face configuration scenarios were investigated and compared. As depicted in Fig.8, the group delay remains constant from 3 to 14 GHz in the side-by-side scenario, while the phase of S21 exhibits distortion specifically at the frequency of 14 GHz. Additionally, the amplitude of S21 experiences a decrease at this frequency.

To assess the performance of the antenna, two distinct signals are utilized as inputs. The first signal is a default Gaussian pulse generated within the CST software, spanning the frequency range specified by the UWB standard, which is between 3.1 GHz and 10.6 GHz (Signal I). The second signal is a sine-modulated Gaussian pulse with specific parameters, including a central frequency (Fc) of 7 GHz and a pulse width (b) of 220 ps (Signal II) [8, 25]. Figure 10(b) provides a visual representation of the normalized input signals. Then, the fidelity factor for both the E-plane and H-plane, based on the angle, is calculated. In the far-field region of the transmitting antenna, a total of 19 virtual probes are strategically positioned in both planes. These probes are evenly spaced at 10-degree intervals, ranging from -90 to 90 degrees along a circular trajectory centered at the antenna's midpoint (Figure 10).

Figure 10 illustrates a high-fidelity factor achieved in the E-plane, ranging from 0.922 to 0.975 for signal I. Furthermore, a fidelity factor between 0.831 and 0.975 was obtained for signal I in the H-plane. The fidelity factor for signal II exhibited slightly better performance, as it ranged from 0.979 to 0.990 across angles from -80 to 80 degrees in both the H-plane and E-plane.

Figure 11 illustrates examples of the normalized radiated signals in both the E-plane and H-plane at various angles along the specified arcs. The signals depicted in Figure 11 demonstrate the antenna's capability to transmit short pulses with minimal signal distortion.

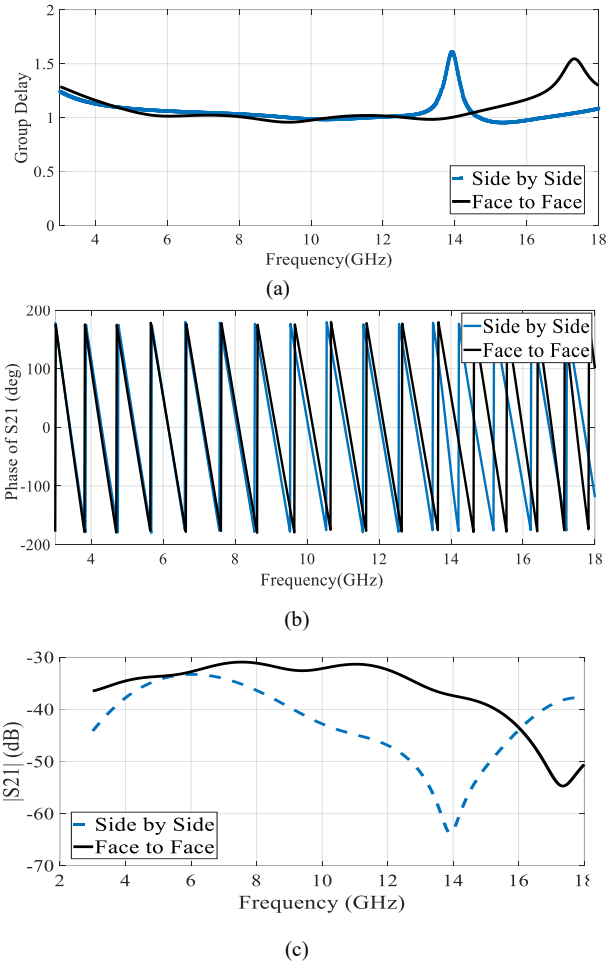

Fig. 9. (a) Group delay, (b) phase of S21, and (c) amplitude of S21 of the simulated antennas in the face-to-face and side-by-side scenario

VI Imaging Result

The system configuration for breast tumor detection is depicted in Figure 12. The primary goal is to detect changes in the backscattering signal in the presence or absence of a tumor with a high dielectric inclusion. The breast model used in this setup comprises two layers: the breast tissue layer and the skin layer. A tumor is situated 6 mm underneath the skin layer.

The performance evaluation of the proposed system involved examining the S21 parameter for different configurations: free space, the breast model with a tumor, and the breast model without a tumor. To obtain the S-parameters, two antennas were positioned in a face-to-face configuration around the breast model, maintaining a separation distance of 12 mm from the skin layer. Also, the S11 parameter was derived by positioning the antenna in front of the breast model. It was

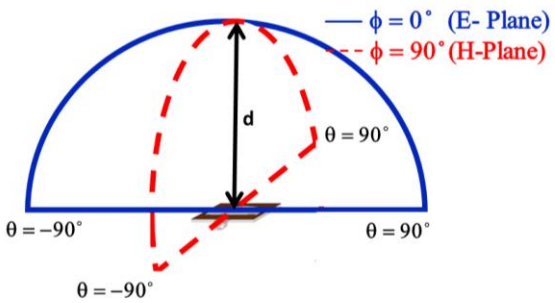

(a)

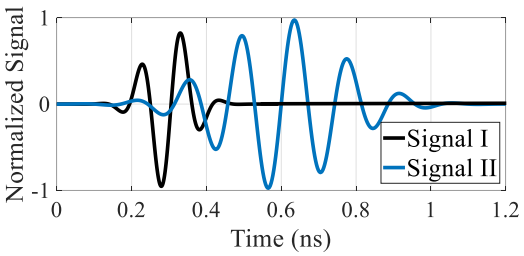

(b)

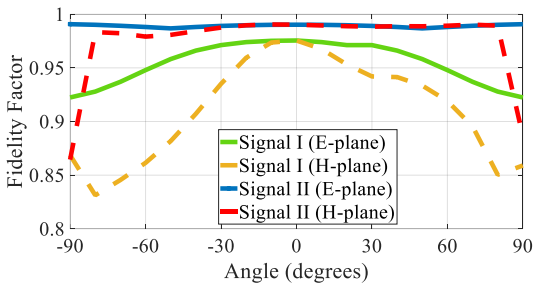

(c)

Fig. 10. (a) The far-field radiation performance evaluation of the antenna along arcs with a radius of 240 mm, (b) the waveform of input signals, and (c) the calculated fidelity factor of the wide-slot antenna, in the E-plane and H-plane.

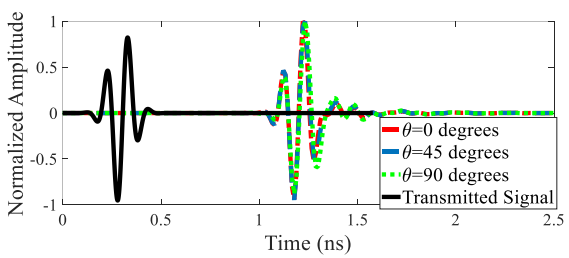

(a)

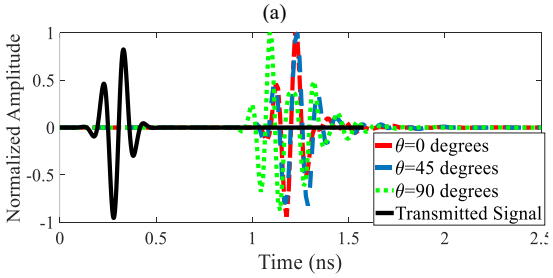

(b)

Fig. 11. Examples of the normalized radiated signals at (a) E-plane and (b) H-plane.

TABLE 2 FIDELITY FACTOR COMPARISON OF THE UWB ANTENNA WITH OTHER LITERATURE

Ref.	Bandwidth	Dimensions(mm)^3	Fidelity Factor	
[25]	3.5-11	39×36.6 (Signal II)	(Phi=0°, Theta=0°)= 0.9131 (Phi=0°, Theta=90°)=0.9002	
[26]	1.6-7.1	51.6×51.6 (Sine-Gaussian)	0.65-0.95	
[27]	2.8-11.5	29×24 (Signal I)	**E-plane** FtF=0.9091 SbS=0.8283	**H-plane** SbS=0.8270
[28]	4-11	20×19 (Signal I)	**E-plane** FtF=0.906 SbS=0.8524	
[32]	3.8-10.1	29×26.6 (Signal I)	**E-plane** FtF=0.916 SbS=0.912	
[34]	3.02-12	29.2×32.2 (Gaussian)	**E-plane** FtF=0.8633 SbS=0.9486	
Our work	3 -13	16×20 (Signal I) (Signal II)	**E-plane** 0.922 - 0.975 0.986 - 0.990	**H-plane** 0.831-0.975 0.864-0.990

Table 3 presents detailed information about the properties of the breast components at a frequency of 3 GHz [20, 28].

TABLE 3 GEOMETRICAL PARAMETERS AND ELECTRICAL PROPERTIES OF THE BREAST MODEL

Tissue	Conductivity (S/m)	Permittivity	Thickness (mm)
Skin	1.8	38	2.5
Tumor	3.1	67	10
Fat	0.1	5	87.5

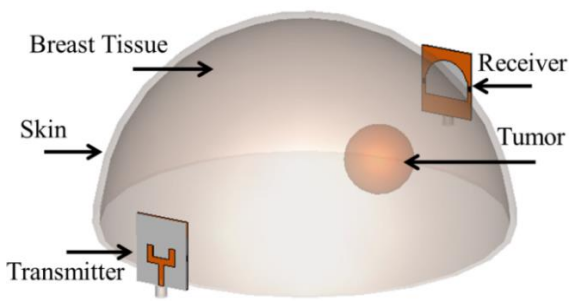

Fig. 12. Breast phantom model and simulation setup for microwave imaging

found that minimal variations were detected when compared to the configuration where the antenna was situated in free space.

The initial section of Figure 13 effectively showcases the strong performance of S11 when measured in front of the breast model. It demonstrates a noticeable difference in S21 between the scenarios with and without a tumor in the breast model. This contrast highlights the impact of tumors on the transmission characteristics. Furthermore, a significant variation in the transmission parameter can be observed across

the entire frequency range, the scenarios with and without the presence of the tumor.

Figures 14 and 15 present the assessment of Power Loss Density (PLD) and Specific Absorption Rate (SAR) for tissues with and without a tumor at 9.1 GHz. In healthy tissues, a uniform distribution of electrical energy is observed. However, the presence of a tumor disrupts this uniformity, leading to variations in the power distribution. The tumor absorbs some energy, resulting in deflections and changes in the power distribution pattern. The color density is noticeably higher in cancerous breasts than in healthy breasts. This difference in color density is attributed to the diverse dielectric properties present within the breast phantom models. These findings demonstrate the impact of tumors on the power distribution and highlight the variations in PLD between healthy and cancerous tissues. Also, we investigated the SAR for a sample weighing 0.01 g at a frequency of 9.1 GHz. This choice of sample size allows for quicker calculation of the SAR results. For both a healthy breast and a breast with a tumor, a maximum SAR of 5.56 W/kg was considered.

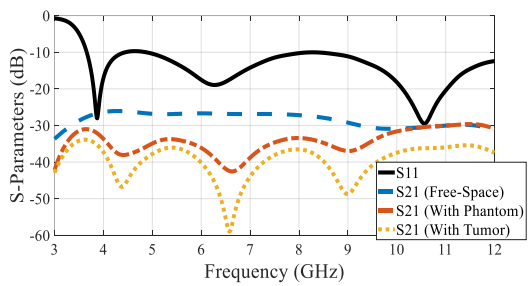

Fig. 13. S-parameters of the imaging setup

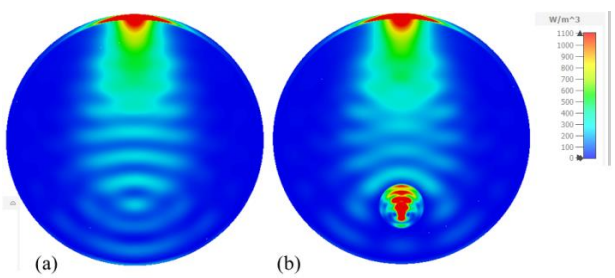

Fig. 14. Power loss density for normal and cancerous Breast

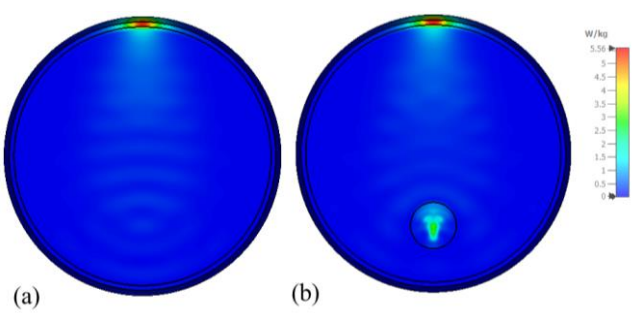

Fig. 15. Specific absorption rate for normal and cancerous Breast

VII Comparison

The fidelity (correlation) factor of antennas is an important criterion for tumor detection in microwave imaging applications. Table 2 compares the fidelity factor of the new design, and some structures addressed in recent literature on microwave imaging. As can be seen, the antenna in this project demonstrates reliable performance in terms of the fidelity factor at all angles compared to the most recent works.

Also, the innovative UWB antenna proposed in this study is compared to previously published UWB antennas for tumor detection, as presented in Table 4. Compared to previously published UWB antennas for Microwave Imaging, the proposed UWB antenna showcases notable features: its compact size and wide frequency range, as demonstrated by the comparative table. This smaller form factor contributes to its uniqueness and sets it apart from the previously mentioned antennas. The proposed antenna, despite its small size and without the use of a reflector or additional structural elements, offers an acceptable gain compared to other antennas.

TABLE 4 COMPARISON OF THE PROPOSED UWB ANTENNA WITH OTHER LITERATURE

Ref.	Dimensions(λ)^3	Operational Range[GHz]	Bandwidth (%)	Gain (dB))	Application
[29]	0.23×0.27×0.016	3.1-16	135	5	Microwave Imaging
[30]	0.4×0.4×0.0.015	2.79-8.93	104.8	4.03	Microwave Imaging
[31]	0.32×0.3×0.018	3.58-14	119	4.7	Energy harvesting
[32]	0.37×0.34×0.02	3.8-10.1	90.6	6.8	Microwave Imaging
[33]	0.24×0.20×0.015	2.79-18	146	5.74	Microwave Imaging
[34]	0.29×0.32×0.25	3.02-12	119	7.3	Microwave Imaging
[35]	0.33×0.33×0.09	2-5	85	8.47	Microwave Imaging
Pro.	0.20×0.25×0.012	3.7-18	131	6.3	Microwave Imaging

VIII Conclusions

The performance characteristics of an antenna were analyzed, studied, and optimized using the 3D simulator CST Microwave Studio 2018. Additionally, the proposed antenna was experimentally verified, demonstrating a satisfactory agreement between the simulation and measurement results. The fidelity factor was examined for both E-plane and H-plane scenarios, indicating a good range of 0.922 - 0.975 for the E-plane across all angles. With its smaller size, simple design, less signal distortion, and commendable performance, the proposed antenna is an excellent choice for implementing breast tumor imaging applications. Finally, a simulation model was suggested including a breast phantom with a tumor, along with transceiver. The performance of the antennas on the breast phantom was validated by studying parameters such as isolation and SAR. The proposed UWB antenna exhibited excellent characteristics, including a high gain of 6.3 dBi and

a fractional bandwidth percentage of 131%. Moreover, it achieved a remarkable efficiency of over 93.7% at the operational frequency of 6 GHz within the specified range. The antenna's fidelity factor was evaluated to assess distortion level in various scenarios. The maximum fidelity factor of 0.975 was achieved for the E-plane.

To show the effectiveness of using the new antenna, an MI simulation for breast tumor detection was performed to detect changes in the backscattering signal in the presence or absence of a tumor with a high dielectric inclusion. It was shown that S11 was quite high when measured in front of the breast model. Additionally, there was a noticeable difference in S21 between the scenarios with and without a tumor in the breast model. This contrast highlights the impact of tumors on the transmission characteristics. Furthermore, a significant variation was observed in the transmission parameter across the entire frequency range, the scenarios with and without the presence of the tumor.

ACKNOWLEDGMENTS

The authors would like to thank the Antenna Laboratory of K. N. Toosi University of Technology for measuring the antenna parameters.

REFERENCES

[1] E. C. Fear, S. C. Hagness, P. M. Meaney, M. Okoniewski, and M. A. Stuchly, "Enhancing breast tumor detection with near-field imaging," *IEEE Microwave magazine,* vol. 3, no. 1, pp. 48-56, 2002.

[2] Kahar, A. Ray, D. Sarkar, and P. Sarkar, "An UWB microstrip monopole antenna for breast tumor detection," *Microwave and Optical Technology Letters,* vol. 57, no. 1, pp. 49-54, 2015.

[3] M. Z. Mahmud, M. T. Islam, N. Misran, S. Kibria, and M. Samsuzzaman, "Microwave imaging for breast tumor detection using uniplanar AMC based CPW-fed microstrip antenna," *IEEE Access,* vol. 6, pp. 44763-44775, 2018.

[4] V. De Santis, J. M. Sill, J. Bourqui, and E. C. Fear, "Safety assessment of ultra-wideband antennas for microwave breast imaging," *Bioelectromagnetics,* vol. 33, no. 3, pp. 215-225, 2012.

[5] U. Rafique, S. Pisa, R. Cicchetti, O. Testa, and M. Cavagnaro, "Ultra-Wideband Antennas for Biomedical Imaging Applications: A Survey," *Sensors,* vol. 22, no. 9, p. 3230, 2022.

[6] M. Jalilvand, X. Li, L. Zwirello, and T. Zwick, "Ultra wideband compact near-field imaging system for breast cancer detection," *IET Microwaves, Antennas & Propagation,* vol. 9, no. 10, pp. 1009-1014, 2015.

[7] S. M. Aguilar, M. A. Al-Joumayly, M. J. Burfeindt, N. Behdad, and S. C. Hagness, "Multiband miniaturized patch antennas for a compact, shielded microwave breast imaging array," *IEEE transactions on antennas and propagation,* vol. 62, no. 3, pp. 1221-1231, 2013.

[8] Z. Lasemi and Z. Atlasbaf, "Impact of fidelity factor on breast cancer detection," *IEEE Antennas and Wireless Propagation Letters,* vol. 19, no. 10, pp. 1649-1653, 2020.

[9] F.-E. Zerrad *et al.*, "Multilayered metamaterials array antenna based on artificial magnetic conductor's structure for the application diagnostic breast cancer detection with microwave imaging," *Medical Engineering & Physic,* vol. 99, p. 103737, 2022.

[10] G. Quintero, J.-F. Zurcher, and A. K. Skrivervik, "System fidelity factor: A new method for comparing UWB antennas," *IEEE Transactions on Antennas and Propagation,* vol. 59, no. 7, pp. 2502-2512, 2011.

[11] R. Cicchetti, V. Cicchetti, A. Faraone, L. Foged, and O. Testa, "A compact high-gain wideband lens Vivaldi antenna for wireless communications and through-the-wall imaging," *IEEE transactions on antennas and propagation,* vol. 69, no. 6, pp. 3177-3192, 2020.

[12] N. Sharma and S. S. Bhatia, "Performance enhancement of hexagonal ring-shaped compact multiband integrated wideband fractal antennas for wireless applications," *International Journal of RF and Microwave Computer-Aided Engineering,* vol. 30, no. 3, p. e22079, 2020.

[13] S. Guruswamy, R. Chinniah, and K. Thangavelu, "A printed compact UWB Vivaldi antenna with hemi cylindrical slots and directors for microwave imaging applications. AEU—Int," *J. Electron. Commun,* vol. 110, p. 152870, 2019.

[14] C. Zhao, X. Li, M. Yang, and C. Sun, "Resistance-loaded miniaturized dual-layer Vivaldi antenna for plasma reflection diagnosis," *Microwave and Optical Technology Letters,* vol. 63, no. 1, pp. 205-210, 2021.

[15] N. Nurhayati, A. M. De Oliveira, J. F. Justo, E. Setijadi, B. E. Sukoco, and E. Endryansyah, "Palm tree coplanar Vivaldi antenna for near field radar application," *Microwave and Optical Technology Letters,* vol. 62, no. 2, pp. 964-974, 2020.

[16] M. Yousefnia, A. Ebrahimzadeh, M. Dehmollaian, and A. Madannejad, "A time-reversal imaging system for breast screening: Theory and initial phantom results," *IEEE Transactions on Biomedical Engineering,* vol. 65, no. 11, pp. 2542-2551, 2018.

[17] I. M. Danjuma, M. O. Akinsolu, C. H. See, R. A. Abd-Alhameed, and B. Liu, "Design and optimization of a slotted monopole antenna for ultra-wide band body centric imaging applications," *IEEE Journal of Electromagnetics, RF and Microwaves in Medicine and Biology,* vol. 4, no. 2, pp. 140-147, 2020.

[18] S. N. Mahmood *et al.*, "Full ground ultra-wideband wearable textile antenna for breast cancer and wireless body area network applications," *Micromachines,* vol. 12, no. 3, p. 322, 2021.

[19] Z. Lasemiimeni, Z. Atlasbaf, and N. Karbaschi, "Dual-functional ultrawideband antenna with high fidelity factor for body area networks and microwave imaging systems," *IEEE Access,* vol. 9, pp. 112930-112941, 2021.

[20] M. T. Islam, M. Samsuzzaman, M. Rahman, and M. Islam, "A compact slotted patch antenna for breast tumor detection," *Microwave and Optical Technology Letters,* vol. 60, no. 7, pp. 1600-1608, 2018.

[21] M. Mehranpour, S. Jarchi, A. Keshtkar, A. Ghorbani, A. Araghi, and M. Khalily, "Low-profile aperture stacked patch antenna for early-stage breast cancer detection applications," *International Journal of RF and Microwave Computer-Aided Engineering,* vol. 31, no. 3, p. e22531, 2021.

[22] M. T. Islam, M. Samsuzzaman, M. Faruque, M. J. Singh, and M. Islam, "Microwave imaging based breast tumor detection using compact wide slotted UWB patch antenna," *Optoelectron. Adv. Mater. Rapid Commun,* vol. 13, pp. 448-457, 2019.

[23] H. Bahramiabarghouei, E. Porter, A. Santorelli, B. Gosselin, M. Popović, and L. A. Rusch, "Flexible 16 antenna array for microwave breast cancer detection," *IEEE Transactions on Biomedical Engineering,* vol. 62, no. 10, pp. 2516-2525, 2015.
[24] D. Gibbins, M. Klemm, I. J. Craddock, J. A. Leendertz, A. Preece, and R. Benjamin, "A comparison of a wide-slot and a stacked patch antenna for the purpose of breast cancer detection," *IEEE transactions on antennas and propagation,* vol. 58, no. 3, pp. 665-674, 2009.
[25] B. Yeboah-Akowuah, P. Kosmas, and Y. Chen, "A Q-slot monopole for UWB body-centric wireless communications," *IEEE Transactions on Antennas and Propagation,* vol. 65, no. 10, pp. 5069-5075, 2017.
[26] A. Akbarpour, and S. Chamaani. "Ultrawideband circularly polarized antenna for near-field SAR imaging applications," *IEEE transactions on antennas and propagation ,* vol. 68, no. 6, pp. 4218-4228, 2020.
[27] A. Hossain, *et al*. "An octagonal ring-shaped parasitic resonator based compact ultrawideband antenna for microwave imaging applications," *Sensors* 20(5): 1354. vol. 20, no. 5, p. 1354, 2020.
[28] F.-E. Zerrad *et al.*, "Novel measurement technique to detect breast tumor based on the smallest form factor of UWB patch antenna," *International Journal of Microwave and Wireless Technologies,* vol. 15, no. 2, pp. 227-235, 2023.
[29] Z. Khan, A. Razzaq, J. Iqbal, A. Qamar, and M. Zubair, "Double circular ring compact antenna for ultra-wideband applications," *IET Microwaves, Antennas & Propagation,* vol. 12, no. 13, pp. 2094-2097, 2018.
[30] H. Jumaat, K. H. Ping, N. H. Abd Rahman, H. Yon, and F. N. M. Redzwan, "A compact modified wideband antenna with CBCPW, stubline and notch-staircase for breast cancer microwave imaging application," *AEU-International Journal of Electronics and Communications,* vol. 129, p. 153492, 2021.
[31] M. S. Jameel, Y. S. Mezaal, and D. C. Atilla, "Miniaturized coplanar waveguide-fed UWB Antenna for wireless applications," *Symmetry,* vol. 15, no. 3, p. 633, 2023.
[32] F.-e. Zerrad *et al.*, "Microwave Imaging Approach for Breast Cancer Detection Using a Tapered Slot Antenna Loaded with Parasitic Components," *Materials,* vol. 16, no. 4, p. 1496, 2023.
[33] H. T. Sediq, "Tumor detection concepts using eagle-shaped UWB antenna signals for medical purposes," *Sensors and Actuators A: Physical,* vol. 362, p. 114653, 2023.
[34] D.Awan, S. Bashir, S. Khan, S.S. Al-Bawri, and M. Dalarsson, "UWB Antenna with Enhanced Directivity for Applications in Microwave Medical Imaging," *Sensors*, vol. 24, no.4, p.1315, 2024.
[35] M.N. Hamza, S. Koziel, and A. Pietrenko-Dabrowska, "Design and experimental validation of a metamaterial-based sensor for microwave imaging in breast, lung, and brain cancer detection,".*Scientific Reports*, vol. 24, no.1, p.16177, 2024.
[36] F.Kazemi, "A Compact Antenna with Dual Polarization for Mobile and Wireless Communication," *International Journal of Industrial Electronics Control and Optimization*, vol. 6, no.1, pp.73-82. 2023.

MS Motahareh Arezoomandan is currently working toward the doctoral degree with the Faculty of Electrical and Electronics Engineering at the University of Sistan and Baluchestan, Zahedan, Iran. She received the M.Sc. degree in Telecommunication Engineering from the University of Semnan, Semnan, Iran, in 2014, and the B.Sc. degree in Electrical and Electronics Engineering from the University of Birjand, Birjand, Iran, in 2011. Her current research interests include microwave imaging, antenna propagation, and antenna design for mobile and wireless communication systems.

Dr. Shahram Mohanna received a Ph.D. degree in electronics engineering from the University of Manchester in July 2006 and a M.Sc. in Telecommunications Engineering from University of Shiraz, Iran. He worked as a research assistant in the Sensing, Imaging and Signal Processing (SISP) Research Centre at the University of Manchester from 2002 to 2006. During 2012 and 2016, he joined the University of Nottingham Malaysia (UNM) as an associate professor until September 2016 then moved to the University of Sistan and Baluchestan, Zahedan, Iran, as an associate professor. As a multidisciplinary researcher, skillful in microwave imaging, electromagnetic tomography, ultrasonic and wireless sensors, and related physics and mathematics, he has contributed to the discipline by delivering 18 articles in international conferences and publishing 31 papers in indexed journals.

Dr. Ahmad Bakhtiyari Shahri received the B.Sc. degree in electrical and electronic engineering from the University of Sistan and Baluchestan (USB), Zahedan, Iran, in 1999, and the M.Sc. degrees in Telecommunications Engineering in 2006 and a PhD degree in Computer Science from the University of Malaya, Malaysia in 2015. He is currently an assistant professor and director of Education Services in USB. He is expert in Internet of Things (IoT) and IoT security and delivered 8 articles to international conferences and has published 10 journals papers.

International Journal Of
Industrial Electronics Control and Optimization
Print ISSN: 3517-2645
Online ISSN: 3568-2645
Homepage: https://ieco.usb.ac.ir/

Design a High-Efficiency Rectifier Circuit Using Various Couplers for Microwave Power Transmission

Mohammad M. Fakharian

Faculty of Engineering, University of Garmsar, Garmsar, Iran
Corresponding author's email: fakharian@fmgarmsar.ac.ir

Article Info

Article type:
Research Article

Article history:
Received: 08-February-2025
Received in revised form: 09-April-2025
Accepted: 05-June-2025
Published online: 21-March-2026

Keywords:
Rectifier circuit,
RF-DC efficiency,
Microwave coupler,
Wide range of input power.

ABSTRACT

This paper presents an optimized microwave rectifier circuit that integrates various couplers to enhance RF-to-DC conversion efficiency. A comprehensive theoretical analysis and performance evaluation of different microwave couplers are conducted to determine their impact on power distribution and impedance matching. The study demonstrates that incorporating couplers into the rectifier circuit effectively reduces reflected power over a broad input power range. Among the evaluated configurations, the rectifier incorporating a branch-line coupler (BLC) exhibits superior RF-to-DC efficiency over a wide range of operating frequencies, input power levels, and output loads, ensuring broad impedance matching. To validate the proposed design, a rectifier circuit based on the BLC is implemented and fabricated at 2.45 GHz. The prototype consists of two identical sub-rectifying networks connected to the two output ports of the coupler, with the isolated port grounded. Experimental results indicate that the rectifier consistently achieves efficiency levels exceeding 50% for input power levels ranging from 0 to 12.5 dBm. Additionally, the design maintains high efficiency across a frequency range of 2.16 to 2.96 GHz. These findings underscore the potential of BLC-based rectifiers for high-efficiency microwave power transmission systems, offering enhanced energy harvesting capabilities and improved system performance.

I. Introduction

Recently, microwave power transmission (MPT) has been a topic of research interest for a variety of applications in near-field and far-field categories, such as radio frequency (RF) identification, energy harvesting, and wireless sensor networks [1-5]. In MPT systems, rectennas play a significant role, and their efficiencies primarily depend on rectifier circuits. Therefore, the design of high-efficiency rectifying circuits is crucial for MPT systems. As a key component of MPT systems, rectifiers are used to convert RF power into direct current (DC) power. The rectifying circuit performance is typically verified by its RF-DC conversion efficiency.

So far, to enhance and optimize the efficiency of the rectifiers, many studies in analytical models and different types of structures have been presented [7-12]. To improve efficiency, Class-F rectifiers [7] were introduced by suppressing the power of harmonic components. In [8], a technique of harmonic recycling was employed, while in [9], a terminated diode with harmonic behavior was applied for this purpose. In [10], a high-efficiency rectifier with a load of Class-F, using a charge pump circuit, was designed. In [11], a computationally efficient iterative method with fast convergence for rectifier modification was introduced. A C-band rectifier utilizing a single silicon-based Schottky diode is proposed in [12]. In [13], a high-input power (>30 dBm) rectifier circuit for 2.45 GHz was presented, using a rectifier circuit based on a GaAs FET and a Schottky diode together as the rectification components. These designed rectifiers are typically improved for single working frequency, fixed output load, and narrow input power level, especially when the rectifier is integrated with a narrow-band antenna. On the other hand, the available RF energy is usually not continuous, causing variations in operating conditions that lead to input impedance changes and reduced efficiency due to the nonlinear characteristics of rectification. To enhance rectifier performance under various operating conditions, several structures and techniques have been developed to broaden bandwidth [14-19], extend the load range [20], improve the operating power range [21-26], or achieve a

combination of these improvements [27-30]. In [31-34], rectifiers were designed by incorporating multiple sub-rectifiers optimized in parallel to accommodate a wide range of input power. As well as, GaAs pHEMT [35] and Varactor diodes [23] have been employed to enhance and extend the maximum breakdown power and the matching performance. Moreover, based on previous works [26, 27], and [28], a rectifier circuit integrated with a suitable coupler can simultaneously operate under varying input power and output load conditions by recycling the reflected power from a sub-rectifier that is not perfectly matched. For example, in [27], the rectifier contains two sub-rectifier networks and a branch-line coupler (BLCoupler) with a grounded isolation port to enhance efficiency. Nevertheless, other couplers such as tee power divider (TCoupler), Wilkinson divider (WDCoupler), rat-race coupler (RRCoupler), coupled-line coupler (CLCoupler), and lange coupler (LCoupler), can also be used for rectifiers, and then the efficiency comparisons between them with the different couplers can also be verified and studied. Recently, a dual-channel RF-DC rectifier circuit is presented at 2.45 Ghz with a 2:1 power distribution ratio in a Wilkinson power splitter in [36], however, in this work as well, no comparison has been made with other coupler structures.

In this paper, various couplers are analyzed and compared for developing and designing a high-efficiency rectifying circuit. In these designs, the two output ports of the coupler are connected to two identical sub-rectifying networks, while the isolated port is grounded. This rectifier configuration maintains high RF-DC efficiency over a broad range of operating frequencies, input power levels, and output loads, resulting in improved impedance matching [37]. Section II presents the topology and theoretical analysis of couplers. Section III discusses rectifier designs and evaluates their RF-DC efficiency with and without different couplers. For validation, Section IV describes the implementation and fabrication of a prototype rectifier circuit based on a BLCoupler at 2.45 GHz. Finally, the conclusions are summarized in Section V.

II. Topology and Theoretical Analysis of Couplers

According to [27], the topology of the rectifier circuit based on two branches with a coupler is shown in Fig. 1. For each branch, it comprises a matching network (MN), a sub-rectifier, and a DC-pass block to weaken the rectified voltage harmonics and output a smooth voltage on the resistances R_{L1-2}. Two identical sub-rectifiers using Schottky diodes HSMS2850 from Avago [38] are linked to the output ports of the MN. This diode is a good choice for designing a rectifier circuit, due to its electrical characteristics, such as low forward voltage, fast switching, low reverse leakage current, high-frequency suitability, and compact size. The input impedances Zin1 and Zin2 of the sub-rectifiers vary when the input operating frequency, input power, and output load change, resulting in an impedance mismatch. The designed topology can enhance matching performance, increase RF-DC efficiency, and reduce the power loss caused by impedance mismatch.

To study the operating principle of the designed rectifier with the different couplers or power dividers, it should first discuss the properties of the common types of couplers and power dividers.

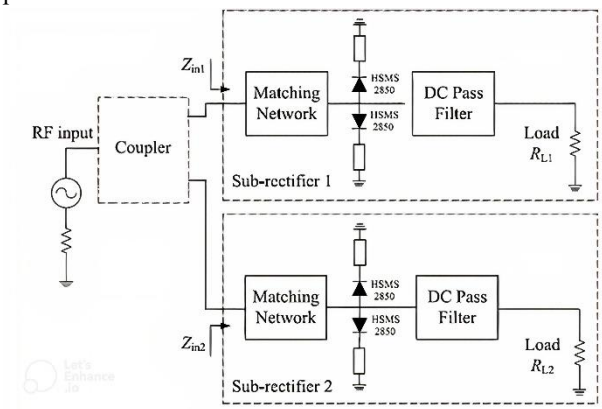

Fig. 1. Block diagram of the rectifier with coupler.

A. TCoupler and WDCoupler

The T-junction power divider (TCoupler) and Wilkinson power divider (WDCoupler) are three-port networks that can be used for power combining or division, as well as automatic impedance transformation in the rectifying circuit [28]. In this regard, a symmetric 3-dB lossless TCoupler and a symmetric two-way WDCoupler with an isolation resistor of 2Rs are used, as shown in Fig. 2(a) and 2(b), respectively. In the WDCoupler, if a mismatch occurs, the reflected power is dissipated through the isolation resistor. Compared with [28], the two symmetric branches each have an electrical length of 90°, a1 is the input wave to the couplers, ZL1 and ZL2 represent the input impedances of the two sub-rectifying networks, and Rs is set to 50 Ω. According to [28] and [39], output waves d1 and d2 can be described as follows:

$$d_1 = d_2 = -j\frac{a_1}{\sqrt{2}}. \quad (1)$$

Since the output load ZL1-2 changes and mismatching are produced, the reflected waves ar1 and ar2 are

$$a_{r1} = a_{r2} = -j\frac{a_1}{\sqrt{2}}\Gamma \quad (2)$$

The waves ar1 and ar2 are transmitted to the TCoupler or WDCoupler and then delivered to port 1; consequently, the power loss of the couplers can be determined as

$$P_{lossT} = \frac{1}{2}|a_{r1}|^2 + \frac{1}{2}|a_{r2}|^2 = \frac{1}{2}|\Gamma|^2|a_1|^2, \quad (3)$$

$$P_{lossWD} = \frac{1}{2}|a_{r1}|^2 + \frac{1}{2}|a_{r2}|^2 + P_{2Rs} = \frac{1}{2}|\Gamma|^2|a_1|^2 + P_{2Rs}. \quad (4)$$

In equation (4), Since the output load ZL1-2 is variable, the isolation resistor is not equivalent to being open in an ideal case, and it is considered in the losses. In the following,

as illustrated in Fig. 2, in the rectifier with the TCoupler, the reflected power is $P_{lossT} = P_{ref} = |\Gamma|^2 P_{inc}$, while with the WDCoupler is $P_{lossWD} = P_{ref} = |\Gamma|^2 P_{inc} + P_{2Rs}$, the power injected to the subrectifiers Pin is equal to $(1 - |\Gamma|^2) \times P_{inc}$ for TCoupler and $(1 - |\Gamma|^2) \times P_{inc} - P_{2Rs}$ for WDCoupler, while the incident power is equal to $\frac{|a_1|^2}{2}$.

The DC output power of the rectifier circuit with the couplers is (Pin ×ηPin), where ηPin presents the RF-DC efficiency of the sub-rectifying networks at the inserted power Pin. Thus, the efficiency ηPinc at the incident power of Pinc can be obtained by

$$\text{for TCoupler: } \eta_{P_{inc}} = \frac{P_{in} \times \eta_{P_{in}}}{P_{inc}} = (1 - |\Gamma|^2) \times \eta_{P_{in}} \quad (5)$$

$$\text{for WDCoupler: } \eta_{P_{inc}} = \frac{P_{in} \times \eta_{P_{in}}}{P_{inc}} = (1 - |\Gamma|^2) \times \eta_{P_{in}} - P_{2Rs} \times \eta_{P_{in}} \quad (6)$$

Thus, after the sub-rectifiers are specified, the RF-DC efficiency ηPinc depends on reflection coefficients Γ of the sub-rectifiers and the efficiency ηPin. Moreover, it is proved that the efficiency of the TCoupler is higher than the WDCoupler for variable loads; this is a common problem in sensor applications.

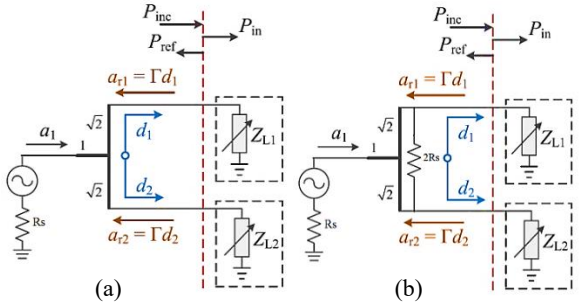

Fig. 2. The rectifier based on the symmetric a) TCoupler and b) WDCoupler.

B. RRCoupler

In this section, the rat-race coupler (RRCoupler), which is well known as a network with four ports and a phase shift of 180° between the two output ports, is verified. It can also be worked as in the in-phase outputs. The rectifiers based on the RRCoupler with the grounded isolation port are shown in Fig. 3(a) and Fig. 3(b) as an in-phase and a 180-degree hybrid. According to [39], for the ideal 3-dB 180° hybrids, the scattering matrix has the following definition:

$$[S] = \frac{-j}{\sqrt{2}} \begin{bmatrix} 0 & 1 & 1 & 0 \\ 1 & 0 & 0 & -1 \\ 1 & 0 & 0 & 1 \\ 0 & -1 & 1 & 0 \end{bmatrix}. \quad (7)$$

First, consider a wave incident with unit amplitude (a1) at port 1 (the sum port) of the RRCoupler. At the ring junction, the a1 will be distributed into two ports, which arrive at ports 2 and 3 in-phase, and Port 4 is isolated from port 1. Similar to previous couplers, we can prove the following equation:

$$\text{for in} - \text{phase:} \quad P_{lossRR} = \frac{1}{2}|\Gamma|^2 |a_1|^2. \quad (8)$$

Now, if the signal is driven into port 2, the incident power is distributed between ports 1 and 4, although port 3 is isolated. The signals at ports 1 and 4 have 180° phase shift, and therefore, this coupler is stated as a 180-degree hybrid, and we have the following equation:

$$\text{for } 180 - \text{degree hybrid:} \quad P_{lossRR} = \frac{1}{2}|\Gamma|^2 |a_2|^2, \quad (9)$$

that in equations 1 and 2, $|a_1| = |a_2|$. Similar to the previous section, it can be concluded that the efficiency ηPinc in the incident power of Pinc is as follows: for RRCoupler:

$$\eta_{P_{inc}} = \frac{P_{in} \times \eta_{P_{in}}}{P_{inc}} = (1 - |\Gamma|^2) \times \eta_{P_{in}} \quad (10)$$

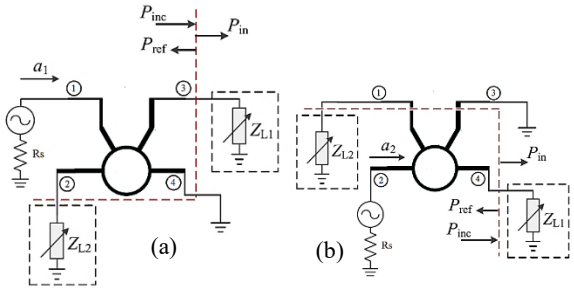

Fig. 3. The rectifier based on the RRCoupler as a) an in-phase and b) a 180-degree hybrid with grounded isolation port.

C. BLCoupler

Branch-line coupler (BLCoupler) is a 3-dB directional coupler that produces a 90° phase difference between the outputs of the coupler and through the arms. This type of coupler has already been studied in [27]. As shown in Fig. 4, the rectifier consists of two sub-rectifying circuits and a BLCoupler with a grounded isolation port. In the analysis, the sub-rectifiers are assumed to be identical, and the loss of the BLCoupler is ignored. Based on [27] and [39], the scattering matrix of the BLCoupler is given by the following form:

$$[S] = \frac{-1}{\sqrt{2}} \begin{bmatrix} 0 & j & 1 & 0 \\ j & 0 & 0 & 1 \\ 1 & 0 & 0 & j \\ 0 & 1 & j & 0 \end{bmatrix}. \quad (11)$$

It can be proved that the power loss of the rectifier circuit with the BLCoupler is as follows:

$$P_{lossBL} = \frac{1}{2}|\Gamma|^2 |\Gamma'|^2 |a_1|^2, \quad (12)$$

where Γ and Γ′ are the reflection coefficients at the corresponding power, and a1 is the input wave to the coupler. Therefore, it can be concluded that the efficiency ηPinc at the incident power of Pinc is as follows:

$$\text{for BLCoupler:} \quad \eta_{P_{inc}} = \frac{P_{in} \times \eta_{P_{in}}}{P_{inc}} = (1 - |\Gamma'|^2 |\Gamma|^2) \times \eta_{P_{in}}, \quad (13)$$

since $0 < |\Gamma| < 1$ and $0 < |\Gamma'| < 1$, it is indicated that the RF-DC conversion efficiency can be enhanced by applying the BLCoupler configuration than TCoupler and WDCoupler.

D. CLCoupler and LCoupler

When two transmission lines are adjacent to each other, electromagnetic field interactions can cause power to couple from one line to another. Such lines are referred to as

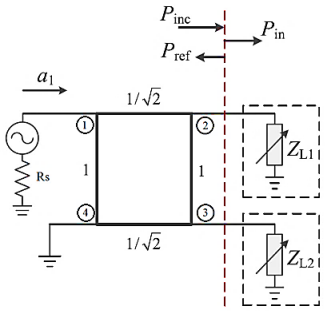

Fig. 4. The rectifier based on the BLCoupler with grounded isolation port.

coupled-line couplers (CLCouplers). The CLCouplers are usually symmetric, meaning that the two conductive strips have the same position and width relative to the ground. This symmetric layout simplifies the analysis of their characteristics. However, the coupling of a CLCoupler is too loose. A Lange coupler (LCoupler) is a practical implementation that achieves high coupling between edge-coupled lines by using multiple parallel lines [39]. The rectifiers based on the CLCoupler and LCoupler with the grounded isolation port are shown in Fig. 5(a) and 5(b). According to [39], the scattering matrix of the quadrature CLCoupler and LCoupler is:

$$[S] = \begin{bmatrix} 0 & j\sqrt{1-c^2} & c & 0 \\ -j\sqrt{1-c^2} & 0 & 0 & c \\ c & 0 & 0 & -j\sqrt{1-c^2} \\ 0 & c & -j\sqrt{1-c^2} & 0 \end{bmatrix}. \quad (14)$$

where c is the voltage coupling coefficient, for example, between ports 3 and 1.

For an analysis of the couplers, at first, the input wave a1 transmits to ports 2 and 3, and then from these ports will be returned to other ports. Similar to the BLCoupler, we can prove the following equations:

$$P_{lossCL} \;\&\; P_{lossL} = \frac{1}{2}[(2c^2|a_1||\Gamma| - 1)^2] + \frac{1}{2}[16c^4(1-c^2)^2|\Gamma|^2|\Gamma'|^2]|a_1|^2 \quad (15)$$

if $0.7 < c < 1$, the second term in the above equation is ten times larger than the first term, so we have approximately efficient:

$$\text{for CLCoupler \& LCoupler: } \eta_{P_{inc}} = \frac{P_{in} \times \eta_{P_{in}}}{P_{inc}} \cong (1 - 16c^4(1-c^2)^2|\Gamma|^2|\Gamma'|^2) \times \eta_{P_{in}}. \quad (16)$$

Since $16C^4(1-C^2)^2 < 1$, the improved efficiency by the CLCoupler and LCoupler in the incident power of Pinc can be obtained than mentiond previous couplers. Of course, it is expected to have a higher efficiency in LCoupler than CLCoupler because of the higher voltage coupling coefficient. On the other hand, the design methods of a coupler are presented in [39] based on the characteristic impedance (Z0), even- (Z0e) and odd- (Z0o) mode impedances of coupled adjacent lines in terms of the strip width and the gap between strips. The voltage coupling coefficient based on this theory can be determined by the following equations:

$$Z_0^2 = Z_{0e}Z_{0o} \;.\; c = \frac{Z_{0e}-Z_{0o}}{Z_{0e}+Z_{0o}}. \quad (17)$$

since, the odd and even mode impedance depends on the physical structure of the coupled lines, the LCoupler may be driving lower impedances than the CLCoupler and so more power transfer as possible.

For $0 < c < 0.7$, the input wave of a1 directly affects the efficiency, and it is not suitable for low input power. Thus, the CLCoupler is most suitable for high voltage coupling factors or high input power.

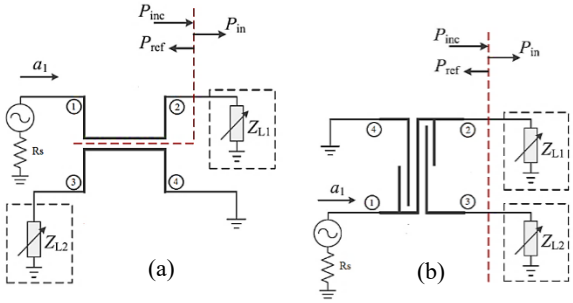

Fig. 5. The rectifier based on a) the CLCoupler and b) LCoupler with grounded isolation port.

III. Rectifier Design and Performance Comparison of Couplers

A. Rectifier Design

To confirm the mentioned theoretical analysis, the designed layout in Fig. 1 has used the various couplers in the rectifier circuit design with the following methodology.

Step 1: According to [20] and [27], a modified single rectifier is designed and developed for maximum efficiency at 2.45 GHz. The level of power is improved between -5 dBm and +5 dBm for medium-power applications, and the designed system can also be used for low and high-power applications, by selecting suitable rectifying diodes. The configuration of the adapted rectifying structure is shown in Fig. 6 (a). It is composed of an MN, rectifying Schottky diodes, and a DC-pass filter. Proper Schottky diodes HSMS2850 are chosen for the rectifying circuit because of the reversed input impedance trend. Note that when the level of input power is more than the finest power of the rectifier, the most power is consumed by the Schottky diodes due to the diode breakdown. The MN converts the complex impedance to 50-Ω, and the DC-pass filter with harmonic rejection is designed using harmonic termination. The DC-pass filter is realized with two fan-shaped branches with different radius, followed by a resistive load (R_L) to excerpt the DC power.

Step 2: According to the analysis in Section II, an appropriate coupler is designed and optimized to operate at

the operating frequency. Actually, the couplers are designed based on quarter-wavelength impedance matching principles. Key design considerations include operating frequency, impedance matching, insertion loss, power division, isolation, and bandwidth. Optimization is achieved using advance design system (ADS) as an electromagnetic simulation software, ensuring high performance in practical applications. It is expected that the rectifier performance is affected by the coupler. The various couplers are applied in the proposed design, with the structures shown from Fig. 6 (b) to Fig. 6 (f) with the optimized physical dimensions. It is worth noting that the optimal dimensions of each coupler are obtained based on a separate design. Their combination with the rectifier is re-optimized to achieve optimal performance. Therefore, the output of their results with the rectifier combination is more important than their individual output.

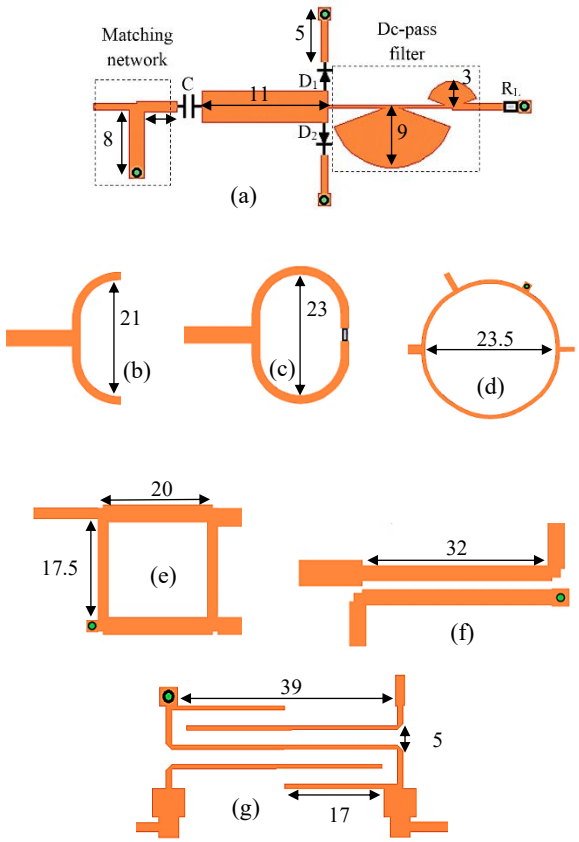

Fig. 6. Geometry of the designs in the proposed circuit with the optimized physical dimensions. (a) Single rectifier; (b) TCoupler; (c) WDCoupler. (d) RRCoupler; (e) BLCoupler; (f) CLCoupler; (g) LCoupler with grounded isolation port. Dimensions are in mm.

Step 3: Two identical single rectifiers are adjoined to the coupler output ports in order to the reflected power can be recycled and the conversion efficiency can be improved in different operating frequencies, input powers, and loads.

In the presented design, the substrate is Rogers-4003, with a thickness of 0.8 mm, a dielectric constant of 3.55, and a loss tangent of 0.0027. It should be illustrated that in the simulation model, the losses of the microstrip line and diodes are considered, and the capacitor models are from MURATA.

B. Simulated Results and Comparison

At first, in order to verify the rectifier circuit performance based on the different couplers, the reflection coefficient |S11| versus operating frequency is shown and compared with Fig. 7. It can be seen that a single rectifier without the coupler (SRWC) is also designed for comparison. It is clear that the rectifier with the various couplers has a smaller reflection coefficient than SRWC. Therefore, the loss of power due to impedance mismatch is decreased by applying the coupler, as indicated in Section II. As shown in Fig. 7, bandwidth for |S11| < -10 dB is increased from 0.05 GHz to 0.23 GHz by applying the proposed technique with the CLCouple, LCoupler, and RRcoupler. Furthermore, the frequency bandwidth can be more extended to 0.3 GHz by using the BLcoupler and Toupler than the other one.

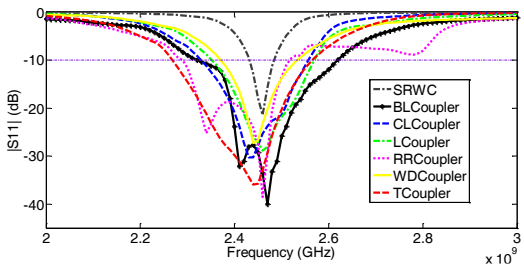

Fig. 7. The |S11| of the rectifiers in terms of operating frequency with the various couplers.

Fig. 8 demonstrates the RF-DC efficiency comparison between the rectifiers based on the different couplers regarding operating frequency, output load, and input power. The losses of the different couplers, such as mismatch loss, isolation loss, dissipative loss, cascade loss, and transmission loss, are taken into the simulation. As illustrated in Fig. 8(a), the conversion efficiency is significantly affected by using the different couplers, so that the efficiency of the rectifier with the BLCoupler is higher than other designs when the input power level is very low or around 0 dBm and more so for maximum efficiency. Nevertheless, from -15 dBm to -5 dBm, the efficiency of the rectifier with the LCoupler is more than other couplers, and then the CLCoupler is better. It should be mentioned that this research on the condition of operating in which the breakdown voltage is not reached, has been focused. Therefore, as shown in Fig. 8(a), the loss of power in the breakdown diodes is highly increased. The TCoupler, RRCouple, and WDCoupler have relatively similar performance in the efficiency of input power, while they have lower efficiency in the performance area compared with previous couplers. The diode breakdown voltage happens later because of lower power loss in these couplers.

The rectifiers using TCoupler, RRCoupler, and WDCoupler work at a higher power level; therefore these rectifiers achieve higher maximum efficiency at the higher power levels, although the focus of this article is on low-level powers. The input power range for over 60% efficiency of the rectifier with TCoupler is from 5.4 dBm to 14.6 dBm, while with the BLCoupler is from 3.8 dBm to 10.2 dBm. The difference in the efficiency of the rectifier with various couplers is primarily because of the rectifier matching in terms of the reflection coefficient and the re-used power. As illustrated in Fig. 8(b), the rectifier with BLCoupler exhibits a higher efficiency (over 60%) in a wide range of load than the other couplers when the output load changes from 210 Ω to 1190 Ω. While, within the output load range of 170 Ω to 490 Ω, the rectifier with the CLCoupler has a higher efficiency in a lower range of output load. As shown in Fig. 8(c), the rectifier based on the BLCoupler has the broadest frequency bandwidth from 2.05 GHz to 2.89 GHz (over 60% efficiency) as compared with the others, while the rectifier based on the CLCoupler has the lowest frequency bandwidth. For better comparison, Table 1 shows the important rectifier parameters based on different coupler structures for efficiency over 60%. Therefore, it can be seen in Table 1 that the rectifier based on the BLCoupler can work in the broader ranges of operating frequency and output load, while it is more sensitive to lower input power level (3.8 dBm) in comparison with the other couplers. Obviously, if input power range was the criterion for superiority, TCoupler is superior to the others with a range of more than 9 dBm.

V. Prototype of Rectifier Based on Blcoupler

For validation, a rectifier circuit with the BLCoupler is designed, optimized, and then fabricated, as shown in Fig. 9. The dimensions of the design are shown in same Fig. 9. The

The fabricated rectifier is characterized and compared with simulation as a function of RF-DC conversion efficiency in terms of output load, operating frequency, and input power. Fig. 10 shows the experimental measurement setup, in which the measurement is extracted by a multi-meter. The measured conversion efficiency can be obtained by:

$$\eta(\%) = \frac{P_{out1}+P_{out2}}{P_{in}}. \quad (18)$$

Pout1 and Pout2 are the output power of the two sub-rectifying networks, and Pin is the input power delivered by a signal generator and a power amplifier. The output powers can be obtained by:

$$P_{out1} = \frac{P_{out1}+P_{out2}}{P_{in}}. \quad (19)$$

$$P_{out1} = \frac{V_{dc1}^2}{R_L}. P_{out2} = \frac{V_{dc2}^2}{R_L}. \quad (20)$$

The 330 pF capacitor (C) and the 360 Ω output load (R_L) are used in the proposed design.

Vdc1 and Vdc2 are the DC output voltage on the loads R_L of the two sub-rectifiers. Note that the two output ports can

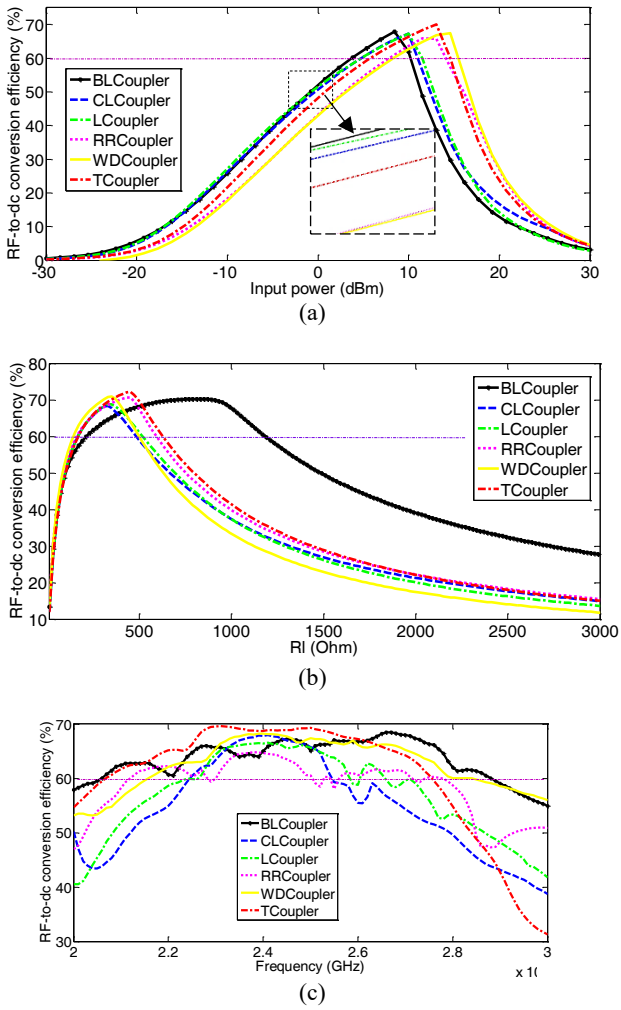

Fig. 8. The RF-DC efficiency of the rectifiers with the various couplers in terms of (a) input power, (b) output load, and (c) operating frequency.

TABLE. I COMPARISON AMONG RECTIFIER WITH VARIOUS COUPLERS FOR EFFICIENCY OVER 60%.

Type of coupler	Input power (dBm)	Output load (Ω)	Operating frequency (GHz)
BLCoupler	3.8-10.2	210-1190	2.05-2.89
CLCoupler	4.5-10.9	170-490	2.24-2.55
LCoupler	4.5-11.5	170-530	2.24-2.66
RRCoupler	8.2-14.3	150-590	2.12-2.78
WDCoupler	8.3-15.3	130-510	2.15-2.86
TCoupler	5.4-14.6	170-630	2.07-2.76

also be linked together with a DC-DC converter in series or parallel.

The simulated and measured results of conversion efficiencies of the rectifier circuit versus operation frequency, input power level, and output load are shown in Fig. 11. As depicted, the simulated results agree with the measured results, which validate the rectifier circuit design. The minor variance is due to the diode model inaccuracy and the fabrication tolerance. As observed in Fig. 11(a), the

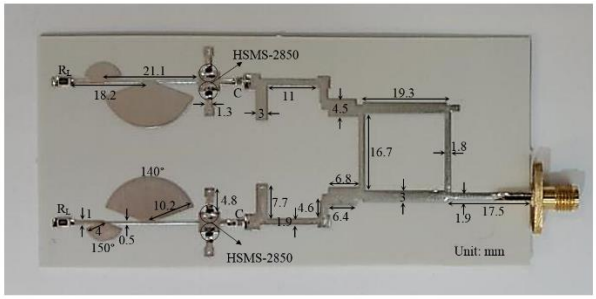

Fig. 9. Layout of the rectifier circuit based on the BLCoupler.

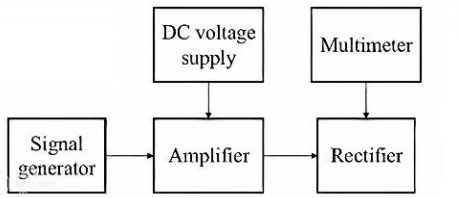

Fig. 10. Schematic of the measurement setup of the rectifier.

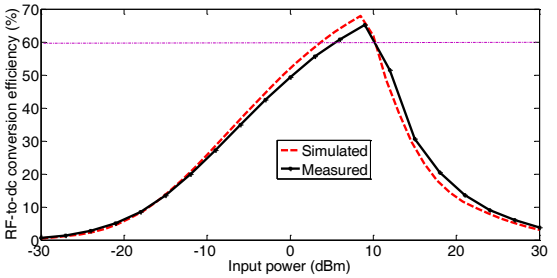

(a)

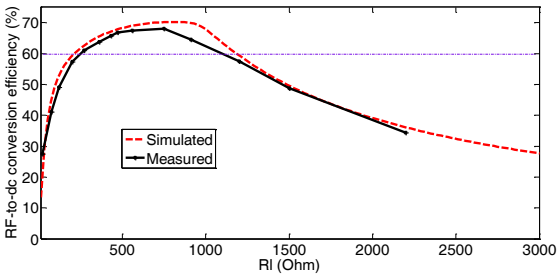

(b)

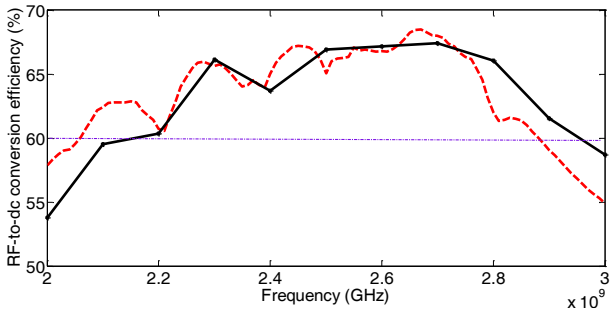

(c)

Fig. 11. Measurement and simulation efficiencies of the rectifier with the BLCoupler in terms of a) input power, b) versus output load for Pin = 9 dBm, and c) operating frequency for Pin = 8 dBm.

rectifier remains above 60% measured RF-DC efficiency from 5.3 to 10.6 dBm, containing a 5.3 dB range of input power for over 60% efficiency with a peak efficiency of 66% at 9 dBm. Moreover, the measurement and simulation efficiencies in term of output load are shown in Fig. 11(b). The rectifier can keep high RF-DC efficiency (over 60%) for a broader range of output load from 200 Ω to 1130 Ω. It can also be observed from Fig. 11(c), that the more than 60% measurement RF-dc efficiency of the rectifier circuit can be obtained in a wideband range from 2.16 GHz to 2.96 GHz (32% fractional bandwidth). These results indicate better performance of the rectifier.

In Table 2, a comparison between the proposed rectifier based on BLCoupler and recent prior works is shown. The proposed circuit has been compared for RF-dc conversion efficiency more than 60%. The proposed work can realize wide input power range, output load range, operating frequency bandwidth with relatively high rectifying efficiency at the same time, while previous works only focus on extending the operating input power range or frequency bandwidth of the rectifiers. Although the efficiency is not the highest one, but it is sensitive at a lower power level, which is an advantage.

TABLE. II PERFORMANCE COMPARISON WITH RELATED RECTIFIERS IN RECENT LITERATURE.

Ref.	[12]	[13]	[36]	This work
Diode model	HSMS282B	HSMS2820 + NE3210S01	HSMS2820 + HSMS2860	HSMS2850
Substrate	RO4003C	RT_Duroid5880	(ε_r=2.65) N.S*	Rogers-4003
Operating frequency for efficiency over 60% (GHz)	4.8-6.2	2.45	2.45	2.16-2.96
Output load for efficiency over 60% (Ω)	160-800	80-520	N.S	200-1130
Input power for efficiency over 60% (dBm)	15-27.5	18.5-33	12-25	5.3-10.6
Maximum efficiency @ Input power	74.1% @ 23dBm	74.4% @ 30dBm	75.5% @ 13dBm	66% @ 9dBm

*Not Stated

IV. Implementing the Rectifier Circuit in MPT Systems

The practical implementation of a rectifier circuit in MPT systems necessitates addressing multiple engineering and operational challenges to optimize performance and reliability. By incorporating advanced design techniques and adhering to established standards, rectifier circuits can facilitate the reliable deployment of MPT systems for

various applications. Some of the important implementation challenges are as follows:

Efficiency Optimization: the rectification process should maximize the conversion efficiency to ensure minimal energy loss. Diode selection, matching networks, and load optimization are key factors influence efficiency [40].

Power Handling and Thermal Management: MPT systems often operate at high power levels, making thermal management a crucial design consideration. The rectifier circuit should incorporate heat sinks or advanced cooling techniques to prevent thermal degradation [41]. Moreovere, the nonlinear characteristics of diodes may cause efficiency degradation at high power levels, necessitating careful circuit design [42].

Harmonic Suppression and Electromagnetic Interference (EMI) Mitigation: Harmonics generated during rectification can interfere with nearby communication systems and reduce rectifier efficiency. Filtering, shielding, and grounding techniques can significantly suppress unwanted frequencies and improve system stability [43].

Environmental Robustness: The rectifier circuit should be designed to withstand external environmental factors, such as resistance in temperature and humidity, and mechanical reliability [44].

Antenna Integration and Beam Alignment: The rectifier's integration with the receiving antenna affects overall system performance. Misalignment can reduce power reception efficiency, requiring adaptive control mechanisms [42].

V. Conclusion

This article has presented and introduced a study on various couplers in the rectifier circuit topology to design optimized high-efficiency rectifier circuits with an extended range of frequency bandwidth, output load, and input power. The design principles of different couplers have been analyzed, and closed-form design formulas have been derived. Furthermore, the mechanism and design procedure of the rectifier with and without coupler have been presented and compared. Among the various couplers, the rectifier based on the BL Coupler demonstrates superior RF-DC conversion efficiency across a wider frequency band and output load range. Therefore, to validate the approach, the designed rectifier operating at 2.33–2.63 GHz, based on the BL Coupler, was implemented and fabricated. The rectifier achieves over 60% efficiency within the 2.16–2.96 GHz range, with an input power range of 5.3 dBm to 10.6 dBm. The measurement results confirm the effectiveness of the proposed method for designing rectifiers. Additionally, this approach can be applied to other scenarios.

REFERENCES

[1] F. Geran, N. Mirzababaee, and S. Mohanna, "RF power harvester using a broadband monopole antenna and a quad-band rectifier," *International Journal of Industrial Electronics Control and Optimization*, vol. 4, no. 1, pp. 59-65, 2021.

[2] H. Xiong, Q. Yang, Y.-Z. Huang, X. Wang, Z. Yi, and H.-Q. Zhang, "A high-efficiency hybrid microwave power receiving metasurface array with dual matching of surface impedance and phase gradient," *Applied Physics Letters*, vol. 125, no. 4, 2024.

[3] M. M. Fakharian, "A dual circular and linear polarized rectenna for RF energy harvesting at 0.9 and 1.8 GHz GSM bands," *Electromagnetics*, vol. 41, no. 8, pp. 545-556, 2021.

[4] M. M. Fakharian, "A wideband rectenna using high gain fractal planar monopole antenna array for RF energy scavenging," *International Journal of Antennas and Propagation*, vol. 2020, pp. 1-10, 2020.

[5] M. M. Fakharian, "A wideband fractal planar monopole antenna with a thin slot on radiating stub for radio frequency energy harvesting applications," *International Journal of Engineering*, vol. 33, no. 11, pp. 2181-2187, 2020.

[6] J. Alirio and B. C. Nuno, "A batteryless RFID remote control system," *IEEE Transactions on Microwave Theory and Techniques*, vol. 61, no. 7, pp. 2727-2736, 2013.

[7] J. Guo, H. Zhang, and X. Zhu, "Theoretical analysis of RF-DC conversion efficiency for class-F rectifiers," *IEEE Transactions on Microwave Theory and Techniques*, vol. 62, no. 4, pp. 977-985, 2014.

[8] S. Ladan and K. Wu, "Nonlinear modeling and harmonic recycling of millimeter-wave rectifier circuit," *IEEE Transactions on Microwave Theory and Techniques*, vol. 63, no. 3, pp. 937-944, 2015.

[9] M. Roberg, T. Reveyrand, I. Ramos, E.A. Falkenstein, and Z. Popović, "High-efficiency harmonically terminated diode and transistor rectifiers," *IEE IEEE Transactions on Microwave Theory and Techniques*, vol. 60, no. 12, pp. 4043-4052, 2012.

[10] C. Wang, N. Shinohara, and T. Mitani, "Study on 5.8-GHz single-stage charge pump rectifier for internal wireless system of satellite," *IEEE Transactions on Microwave Theory and Techniques*, vol. 65, no. 4, pp. 1058-1065, 2017.

[11] Q. Zhang, J-H. Ou, Z. Wu, and H-Z. Tan, "Novel microwave rectifier optimizing method and its application in rectenna designs," *IEEE Access*, vol. 6, pp. 53557-53565, 2018.

[12] H. Zeng, Y. Tang, and Y. Liu, "Compact high-efficiency c-band rectifier with high input power for microwave power transmission," *Electronics Letters*, vol. 59. e12776, 2023.

[13] H. Xiao, H. Zhang, W. Song, J. Wang, W. Chen, and M. Lu, "A High-Input Power Rectifier Circuit for 2.45-GHz Microwave Wireless Power Transmission," *IEEE Transactions on Industrial Electronics*, vol. 69, no. 3, pp. 2896-2903, March 2022.

[14] J. Kimionis, A. Collado, M.M. Tentzeris, and A. Georgiadis, "Octave and decade printed UWB rectifiers based on nonuniform transmission lines for energy harvesting," *IEEE Transactions on Microwave Theory and Techniques*, vol. 65, no. 11, pp. 4326-4334, 2017.

[15] M. Mansour, X.L. Polozec, and H. Kanaya, "Enhanced broadband RF differential rectifier integrated with archimedean spiral antenna for wireless energy harvesting applications," *Sensors*, vol. 19, no. 3, pp. 1-13, 2019.

[16] M. Nariman, F. Shirinfar, S. Pamarti, A. Rofougaran, and F.D. Flaviis, "High-efficiency millimeter-wave energy-harvesting systems with milliwatt-level output power,"

IEEE Transactions on Circuits and Systems II, vol. 64, no. 6, pp. 605-609, 2017.
[17] Y. L. Lin, X. Y. Zhang, Z.-X. Du, and Q. W. Lin, "High-efficiency microwave rectifier with extended operating bandwidth," *IEEE Transactions on Circuits and Systems II*, vol. 65, no. 7, pp. 819-823, 2017.
[18] J. Liu, X. Y. Zhang, and C. L. Yang, "Analysis and design of dual-band rectifier using novel matching network," *IEEE Transactions on Circuits and Systems II,* vol. 65, no. 2, pp. 431-435, 2018.
[19] M. M. Fakharian, "A compact UWB antenna with dynamically switchable band-notched characteristic using broadband rectenna and DC-DC booster," *International Journal of Microwave and Wireless Technologies*, vol. 13, no. 10, pp. 1086-1095, 2021.
[20] Y. Huang, N. Shinohara, and T. Mitani, "A constant efficiency of rectifying circuit in an extremely wide load range," *IEEE Transactions on Microwave Theory and Techniques* vol. 62, no. 4, pp. 986-993, 2014.
[21] Y. Lu, H. J. Dai, M. Huang, M.-K. Law, S.-W. Sin, S.-P. U, and R.P. Martins, "A wide input range dual-path CMOS rectifier for RF energy harvesting," *IEEE Transactions on Circuits and Systems II*, vol. 64, no. 2, pp. 166-170, 2017.
[22] T. W. Barton, J. Gordonson, and D. J. Perreault, "Transmission line resistance compression networks and applications to wireless power transfer," *IEEE Journal of Emerging and Selected Topics in Power Electronics, v*ol. 3, no. 1, pp. 252-260, 2015.
[23] S. H. Abdelhalem, P.S. Gudem, and L.E. Larson, "An RF-dc converter with wide-dynamic-range input matching for power recovery applications," *IEEE Transactions on Circuits and Systems II, Express. Briefs*, vol. 60, no. 6, pp. 336-340. 2013.
[24] X. Y. Zhang and Q.-W. Lin, "High-efficiency rectifier with extended input power range based on two parallel sub-rectifying circuits," *IEEE International Wireless Symposium*, Shenzhen, China, Match 2015, pp. 1-4.
[25] Z.-X. Du and X. Y. Zhang, "High-efficiency microwave rectifier with less sensitivity to input power variation," *IEEE Microwave and Wireless Components Letters*, vol. 27, no. 11, pp. 1001-1003, 2017.
[26] Y. Y. Xiao, Z.-X. Du, and X. Y. Zhang, "High-efficiency rectifier with wide input power range based on power recycling," *IEEE Transactions on Circuits and Systems II: Express. Briefs,* vol. 65, no. 6, pp. 744-748, 2018.
[27] X. Y. Zhang, Z.-X. Du, and Q. Xue, "High-efficiency broadband rectifier with wide ranges of input power and output load based on branch-line coupler," *IEEE Transactions on Circuits and Systems I: Reg. Papers*, vol. 64, no. 3, pp. 731-739, 2016.
[28] M. Huang, Y. L. Lin, J.-H. Ou, X. Y. Zhang, Q. W. Lin, W. Che, and Q. Xue, "Single- and dual-band RF rectifiers with extended input power range using automatic impedance transforming," *IEEE Transactions on Microwave Theory and Techniques*, vol. 67, no. 5, pp. 1974-1984, 2019.
[29] K. Niotaki, A. Georgiadis, A. Collado, and J. S. Vardakas, "Dual-band resistance compression networks for improved rectifier performance," *IEEE Transactions on Microwave Theory and Techniques*, vol. 62, no. 12, pp. 3512-3521, 2014.
[30] M. M. Fakharian, "A high gain wideband circularly polarized rectenna with wide ranges of input power and output load," *International Journal of Electronics,* vol. 109, no. 1, pp. 83-99, 2021.
[31] V. Marian, C. Vollaire, J. Verdier, and B. Allard, "Potentials of an adaptive rectenna circuit," *IEEE Antennas and Wireless Propagation Letters*, vol. 10, pp. 1393-1396, 2011.
[32] C. J. Li and T. C. Lee, "2.4-GHz high-efficiency adaptive power harvester," *IEEE Transactions on Very Large Scale Integration Systems,* vol. 22, no. 2, pp. 434-438, 2014.
[33] Z. Liu, Z. Zhong, and Y.-X. Guo, "Enhanced dual-band ambient RF energy harvesting with ultra-wide power range," *IEEE Microwave and Wireless Components Letters*, vol. 25, no. 9, pp. 630-632, 2015.
[34] Z. Du, S. F. Bo, Y. F. Cao, J. Ou, and X. Y. Zhang, "Broadband circularly polarized rectenna with wide dynamic-power-range for efficient wireless power transfer," *IEEE Access*, vol. 8, pp. 80561-80571, 2020.
[35] M. M. Fakharian, "RF energy harvesting using high impedance asymmetric antenna array without impedance matching network," *Radio Science*, vol. 56, no. 3, pp. 1-10, 2021.
[36] C. Peng, Z. Ye, J. Wu, C. Chen, and Z. Wang, "Design of a wide-dynamic RF-DC Rectifier circuit based on an unequal wilkinson power divider," *Electronics*, vol. 10, p. 2815, 2021
[37] V. Marian, B. Allard, C. Vollaire, and J. Verdier, "Strategy for microwave energy harvesting from ambient field or a feeding source," *IEEE Transactions on Power Electronics, vol. 27, n*o. 11, pp. 4481-4491, 2012.
[38] Non RF applications for surface mount schottky diode pairs HSMS2850, Datasheet, Avago Technol., San Jose, CA, USA, May 2010.
[39] D. M. Pozar, Microwave engineering, 4th edition. New York, NY, USA: Wiley, 2012.
[40] J. Huang, Y. Zhou, Z. Ning, and H. Gharavi, "Wireless Power transfer and energy harvesting: current status and future prospects," *IEEE Wireless Communications*; vol. 26, no. 4, pp. 1-7, 2019.
[41] X. Zhu, K. Jin, Q. Hui, W. Gong, and D. Mao, "Long-range wireless microwave power transmission: a review of recent progress," *IEEE Journal of Emerging and Selected Topics in Power Electronics*, vol. 9, no. 4, pp. 4932-4946, 2021.
[42] N. Shinohara, Wireless power transfer via radiowaves. John Wiley & Sons, 2014.
[43] D. Kobuchi, G. E. Moore, Y. Narusue and J. R. Smith, "Suppression of receiver harmonic currents in wireless power transfer systems," *IEEE Wireless Power Technology Conference and Expo*, San Diego, USA, 2023, pp. 1-5.
[44] P. Lazzeroni, V. Cirimele, and A. Canova, "Economic and environmental sustainability of Dynamic Wireless Power Transfer for electric vehicles supporting reduction of local air pollutant emissions," *Renewable and Sustainable Energy Reviews*, vol. 138, pp. 1-15, March 2021.

Mohammad M. Fakharian was born in Tehran, Iran, in 1987. He received the B.S., M.S., and Ph.D. degrees in Electrical Engineering from Semnan University, Semnan, Iran, in 2009, 2012, and 2016, respectively. Currently, he is an associate professor at the University of Garmsar, Garmsar, Iran. His research interests include low-profile printed and patch antennas for wireless communication, fractal, miniature, and multiband antennas, meta-materials and EBG structures interaction with antennas and RF passive components, reconfigurable antennas, RF energy harvesting, and electromagnetic theory: numerical methods and optimization techniques.

IECO

This page intentionally left blank.

International Journal Of
Industrial Electronics Control and Optimization
Print ISSN: 3517-2645
Online ISSN: 3568-2645
Homepage: https://ieco.usb.ac.ir/

Analysis of the Squirrel Cage Induction Motor in the Broken Rotor Bar Condition Based on the Calculation of the Rotor Bar Current

Hamed Shadfar, Hamid Reza Izadfar*

Faculty of Electrical and Computer Engineering Department, Semnan University, Semnan, Iran
Corresponding author's email: hrizadfar@semnan.ac.ir

Article Info

Article type:
Research Article

Article history:
Received: 25-May-2025
Received in revised form: 28-August-2025
Accepted: 01-September-2025
Published online: 21-March-2026

Keywords:
Broken rotor bar fault,
Multiple coupled circuit,
Rotor bar current,
Squirrel cage Induction motor.

ABSTRACT

Calculating the current of the rotor bars in a squirrel cage induction motor (SCIM) using stator data is difficult, but it is very useful. With the calculation of the rotor bars' current, analysis and investigation of various parameters of the motor can be conducted precisely. One of the faults faced by SCIM is the broken rotor bar (BRB) fault. The breakage of one or more bars causes a change in the current of the healthy bars, as well as in the behavior and parameters of the motor. In this paper, the method of calculating the rotor bars' current in the SCIM in both healthy and defective states (breakage of one bar and two adjacent bars) is introduced using the multiple coupled circuit (MCC) model. In addition to currents, some important parameters, such as speed and magnetic field, will also be calculated. For validation of results, a two-pole SCIM with a nominal specification of 1.1 kW, 220/380 V, and 50 Hz is subjected to experimental testing. The results are confirmed by practical tests and simulations using the Ansys Maxwell software.

I. Introduction

Squirrel cage induction motors (SCIMs) are widely used in industrial applications due to their simplicity, low cost, easy maintenance, high efficiency, and reliability [1-2]. IM failures lead to significant process delays, increased maintenance costs, and lost revenue. Therefore, implementing predictive maintenance is crucial for identifying the root causes of these failures [3]. Types of faults in induction motors (IMs) include faults related to the stator winding, faults related to bearings, faults related to the rotor, and finally, faults related to external devices. These faults result in unexpected motor failures and substantial costs for the production department [4-6]. Consequently, it is crucial to regularly monitor the condition of IMs. Understanding a machine's electrical, magnetic, and mechanical behavior is essential for reliable condition monitoring [7]. Mathematical models are required for accurate motor performance prediction, computer simulation, and fault signature identification [8-10]. Non-destructive testing is vital for investigating faulty motors in both healthy and faulty conditions, and motor performance models are effective tools for this purpose [11]. As shown in Figure 1, the modeling of IMs can be categorized into three main groups: 1. circuit models, such as multiple-coupled circuits [12] and magnetic equivalent circuit models [13]; 2. state space models, including modified d-q models [14]; and 3. finite element method models, which include full FEM and FEM-SS methods [15]. To obtain a complete solution, full FEM solutions require the utilization of a FEM solver for all solution stages. On the other hand, FEM-SS involves using FEM modeling to estimate parameters for a separate simulator. Table I compares these methods. By examining the characteristics of each of these methods, it can be said that the use of MMC modeling for circuit analysis has proven to be highly effective and versatile, capable of accurately modeling a variety of stator and rotor faults, such as BRB, end ring faults, open circuit and short circuit in the stator winding, static and dynamic eccentricity, and even corrosion [16]. Parameterization of an MCC model for IM requires either detailed knowledge of the internal structure and materials of an IM or sophisticated measurement and testing methods. In [17], the modeling parameters are automatically determined and optimized using measurement data from standard operation with a differential evolution algorithm.

The method is primarily oriented toward practical suitability for industrial applications. The multilevel approach allows for the simulation of the dynamic behavior of unknown IMs. The parametric modeling can then be used to diagnose and identify fault cases. [18] presents a method for coupled electromagnetic and dynamic modeling of an IM with a BRB. It involves creating an MCC model of the IM, a dynamic model of the rotor, and addressing the interaction between these two models. Dynamic simulations and analyses are conducted to investigate the effects of the BRB fault on both the electromagnetic and dynamic characteristics of the IM. [19] presents a model of an SCIM with BRB, utilizing MCC. This analytical model encompasses all spatial harmonic components of the air-gap magnetic force, allowing for an examination of the machine's transient behavior. Equivalent circuits (EC) compatible with both healthy and faulty squirrel-cage rotor topologies are developed. In the EC for a healthy rotor, placing an independent current source in the bar that breaks in the

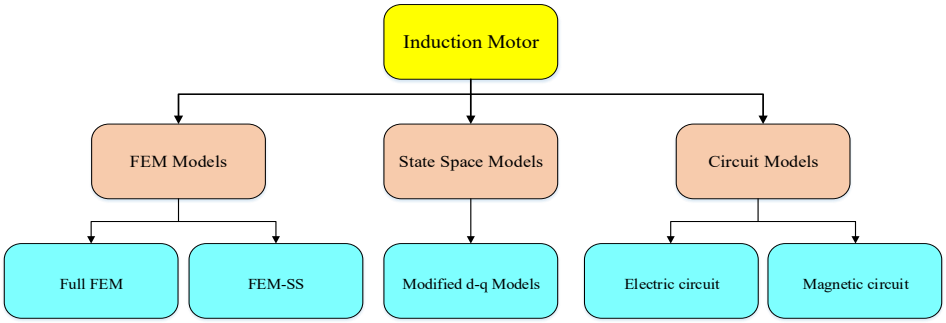

Fig. 1. Types of IM modeling methods

TABLE I COMPARISON OF COMMON IM MODELING METHODS

Method	Advantage	Disadvantage
Multiple coupled circuit (MCC)	• Non-uniform air gap • Practical winding functions • Saturation can be defined in analytical terms. • Different types of faults can be simulated. • The computation time is significantly lower Compared to the FEM. • It strikes a great balance between complexity and accuracy.	• Some geometric constraints, such as those for cooling ducts in the stator or rotor, are difficult to manage.
d-q modeling	• Simple • Comprehensive • Provides good equations for parameter estimation • Good for control and drives	• Negligible saturation • Uniform air gap • Sinusoidal stator winding • No inter-bar currents • No spatial harmonics • No eccentricity faults • No skin effects • Dealing with asymmetries, which are inevitable when a fault occurs, can be quite challenging.
Magnetic equivalent circuit (MEC)	• Spatial dependencies can be included. • Computationally less intense than FEM but more than MCC • It can include geometry, material parameters, and winding distribution	• As all slots must be modeled and the faulty machine is no longer symmetrical, the model becomes quite complex.
Finite element method (FEM)	• Complex geometries can be considered • Non-linearity, such as saturation, skinning effect, and non-idealities can be considered • All types of faults can be simulated; combining FEM with analytical modeling is a good approach.	• The computational complexity is the main issue, particularly in fault diagnostics where symmetry is absent. This problem worsens with 3D analysis and makes it unsuitable for hardware-in-the-loop environments and inverse problem theory.

damaged rotor—whose current is the negative of the current through the same bar—and replacing all voltage sources in the remaining bars with short circuits results in an EC that can be used to resolve the deviations in the rotor mesh currents caused by the bar breakage. Depending on the type of fault, the model parameters can be adjusted to match the machine's behavior. This allows the fault severity to be estimated from the model parameters. Classical models based on the Clark transform are unable to reproduce asymmetric fault conditions. For this purpose, models based on modified WFT and MCC are used. These models allow flexible emulation of many different fault conditions and match the machine's behavior over a wide operating range, even in the faulted condition. The developed model has been evaluated using steady-state measurements on a 5.5 kW inverter-fed induction machine [20]. [21] presents an

approach for detecting BRB in an IM based on an MCC. All self-inductances and mutual inductances of the model are calculated based on the WFT. By employing a genetic algorithm (GA), optimized parameters are obtained by minimizing the errors between the experimental results and the simulation results. The comparison of speed and current shows good agreement between the model and the experimental data under healthy conditions. Because faults related to the rotor account for about 20% of all IM faults [22], and given the importance of monitoring the condition of the motor to prevent unexpected failure, the purpose of this paper is to estimate the rotor bars' current in the SCIM under healthy operating conditions and with a BRB fault using WFT and the MCC model. In other words, we intend to measure the impact of BRB on the main parameters of the SCIM, including the current of other rotor bars. For this purpose, a 2-pole SCIM with nominal specifications of 1.1 kW, 220/380 V, and 50 Hz is subjected to experimental testing and 2D FEM analysis. This motor is tested and analyzed under healthy and defective conditions (breakage of one and two adjacent bars). Under these conditions, the current of the rotor bars is calculated.

The rest of the paper is as follows. In section II, the SCIM modeling based on the MCC model is presented. In section III, the modeling of the BRB fault is described. In section IV, the proposed method for calculating the RBC is shown as a flowchart. In section V, the experimental results are examined and compared with the simulation results. In section VI, losses are evaluated in the BRB fault, and finally, in section VII, the conclusion is presented.

II. IM modelling based on the MCC model

The MCC model was initially introduced in [16] to analyze concentrated winding IMs. This model formulates multiple induction circuits by coupling the stator and rotor of an SCIM. Consider an SCIM having m stator circuits and n rotor bars. The rotor cage is assumed to have n equal loops that are equally spaced, each comprising two rotor bars and the connecting parts of the end rings between them. This configuration is illustrated in Figure 2. In the circuit shown in this figure, we use an RL model. Since we focus on low frequencies, we can ignore the capacitance between turns and windings. Once we have the values for the parameters, we can calculate the loop currents using standard circuit analysis techniques [23].

Therefore, the equations of the IM can be written as a vector matrix in equations (1) to (4).

$$V_S = R_S I_S + \frac{d\Lambda_s}{dt} \quad (1)$$

$$V_r = R_r I_r + \frac{d\Lambda_r}{dt} \quad (2)$$

$$\Lambda_s = L_{ss} I_s + L_{sr} I_r \quad (3)$$

$$\Lambda_r = L_{sr}^T I_s + L_{rr} I_r \quad (4)$$

The L_{sr}^T matrix is the transpose of the L_{sr} matrix. Also:

$$I_s = [i_{s1}\ i_{s2} \dots\ i_{sm}]^T \quad (5)$$

$$I_r = [i_{r1}\ i_{r2} \dots\ i_{rn}]^T \quad (6)$$

$$V_s = [v_{s1}\ v_{s2} \dots\ v_{sm}]^T \quad (7)$$

$$[R_s] = \begin{bmatrix} R_s & 0 & \cdots & 0 & 0 \\ 0 & R_s & \vdots & 0 & 0 \\ \vdots & \vdots & \ddots & \vdots & \vdots \\ 0 & 0 & 0 & R_s & 0 \\ 0 & 0 & \cdots & 0 & R_s \end{bmatrix}_{m\times m} \quad (8)$$

$$[R_r] = \begin{bmatrix} 2(r_b+r_e) & -r_b & 0 & \dots & -r_b \\ -r_b & 2(r_b+r_e) & -r_b & \dots & 0 \\ 0 & -r_b & 2(r_b+r_e) & \dots & \vdots \\ \vdots & \vdots & \vdots & \dots & \vdots \\ -r_b & 0 & \dots & & 2(r_b+r_e) \end{bmatrix}_{n\times n} \quad (9)$$

In the case of the squirrel cage rotor, V_r = [O]. To clarify, it should be noted that the currents in the stator and rotor circuits are assumed to be independent. These circuits can then be connected in any way to create the phases of the stator windings, and the configuration of the rotor bars and end rings can be considered. The torque and mechanical equations of the machine are:

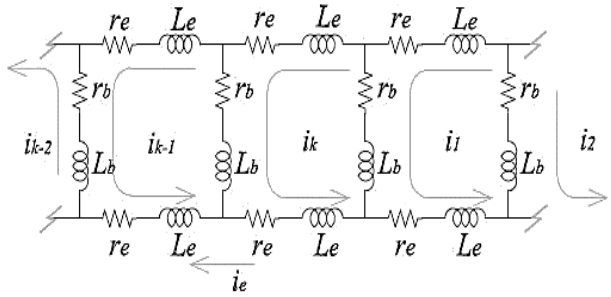

Fig. 2. MCC topology

$$\frac{d\theta}{dt} = \omega \quad (10)$$

$$\frac{d\omega}{dt} = \frac{1}{J}(T_e - T_L) \quad (11)$$

$$T_e = \frac{1}{2} I_s^T \frac{\partial L_{ss}}{\partial \theta_r} I_s + \frac{1}{2} I_s^T \frac{\partial L_{sr}}{\partial \theta_r} I_r + \frac{1}{2} I_r^T \frac{\partial L_{rs}}{\partial \theta_r} I_s + \frac{1}{2} I_r^T \frac{\partial L_{rr}}{\partial \theta_r} I_r \quad (12)$$

where θ is the mechanical angle, ω is the mechanical speed, T_L is the load torque, and J is the rotor inertia.

The calculation of all machine inductances, as indicated by the inductance matrices in the above relations, is the key to a successful simulation of an IM. These inductances are easily calculated using WFT. This method does not assume any symmetry in placing each coil in the slots. According to WFT, the mutual inductance between windings i and j in any electric machine can be calculated using (13) (assuming the permanence of iron is infinite):

$$L_{ij}(\varphi) = \mu_0 r l \int_0^{2\pi} g^{-1}(\varphi.\theta) N_i(\varphi.\theta) N_j(\varphi.\theta) d\theta \quad (13)$$

Where φ is the angular position of the rotor relative to the stator reference, θ is a specific angular position along the inner surface of the stator, $g^{-1}(\varphi.\theta)$ is called the inverse of the distance function, which becomes l/g assuming the air gap is uniform. l is the stack length and r is the average radius

of the air gap. $N_i(\varphi.\theta)$ is called the winding function. Therefore, it is possible to calculate the RBC using these equations.

The key challenge in the analytical approach of SCIM lies in accurately determining the induced current in the rotor bars of the squirrel cage. This requires a precise estimation of the magnetic flux passing through the rotor surfaces. Moreover, it necessitates the use of a highly precise electrical equivalent circuit, whose elements must be correctly identified and determined [16].

III. BRB modeling

The rotor bars of the SCIM are short-circuited by end rings on both sides. This can be modeled as several resistors of equal size (each bar) in parallel with each other. Therefore, when the BRB occurs, it leads to a sudden increase in the resistance of the rotor to a certain extent. There are different methods to identify the resistance of the BRB. One method of measuring the amount of rotor resistance change with the broken bars is expressed as (14). According to (14), the amount of rotor resistance change depends on the number of BRBs [24-25].

$$\Delta R = \frac{n_b}{\frac{N}{3}-n_b} R_r \tag{14}$$

where R_r is the resistance of the healthy rotor, N is the total number of rotor bars, and n_b is the number of BRB.

As mentioned, the method based on MCC and WFT can be used to model SCIM. Using this model, it is possible to successfully simulate the IM under different conditions without changing the model. Therefore, by ignoring the saturation effect, it is possible to simulate the BRB fault by increasing the resistance of the broken bar. The greater the resistance, the greater the severity of the fault. It is sufficient to increase the resistance of the bar to several times its initial value to model the BRB fault [26]. [27] To model an initial fault (a partial BRB), the resistance of the defective bar has been increased. A 10-fold increase in the resistance of the bar creates a similar effect to that of a complete BRB. A 3.5-fold increase is used to simulate a partial BRB fault.

IV. Proposed method for calculating the RBC

The IM's dynamic simulation involves solving the differential equations (1), (2), (10), and (11) together. Various methods can be employed for this purpose. This section describes a relatively simple method. Assuming that the simulation time step (Δt) is chosen to be small enough, these equations can be well approximated in the form of differential equations as follows:

$$[\Lambda_s]_i = \{[V_S]_i - [R_S][I_S]_{i-1}\}\Delta t + [\Lambda_s]_{i-1} \tag{15}$$

$$[\Lambda_r]_i = -[R_S][I_S]_{i-1}\Delta t + [\Lambda_r]_{i-1} \tag{16}$$

$$\omega_i = \frac{1}{J}(\mathrm{T}_{e.i-1} - \mathrm{T}_{L.i})\Delta t + \omega_{i-1} \tag{17}$$

$$\theta_{r.i} = \omega_i \Delta t + \theta_{r.i-1} \tag{18}$$

Also, (3) and (4) can be expressed in terms of the current vectors as follows:

$$[\mathrm{I}_r]_i = ([\mathrm{L}_{rr}]_i - [\mathrm{L}_{sr}]_i{}^T[\mathrm{L}_{ss}]_i{}^{-1}[\mathrm{L}_{sr}]_i)^{-1} \times ([\Lambda_r]_i - [\mathrm{L}_{sr}]_i{}^T[\mathrm{L}_{ss}]_i{}^{-1}[\Lambda_s]_i) \tag{19}$$

$$[\mathrm{I}_s]_i = [\mathrm{L}_{ss}]_i{}^{-1}[\Lambda_s]_i - [\mathrm{L}_{ss}]_i{}^{-1}[\mathrm{L}_{sr}]_i[\mathrm{I}_r]_i \tag{20}$$

The simulation process depicted in Figure 3 begins with the initial step, followed by a loop of simulation stages. During each stage, the parameters and variables of the IM are calculated using the given equations. This loop repeats until the end of the simulation time. The simulation method described here is similar to the numerical solution of state equations and can be accomplished by using software codes such as MATLAB. The proposed method, utilizing numerical and iteration-based techniques with stator data and motor nominal specifications, has a higher convergence speed and accuracy than the conventional MCC method. This is confirmed by the results of Maxwell software simulations based on the FEM method. In the governing equations of the proposed model, considering that the motor power is low and the saturation effect is insignificant, the saturation effect has been ignored to reduce computational load and increase the convergence speed of the proposed model. The advantages and disadvantages of the proposed method are presented in Table II.

The proposed model has the potential to be used in industrial motors and is not limited to a specific power range; in this respect, it is completely scalable.

In this model, given that it focuses more on modeling steady-state conditions of the motor to increase the accuracy of calculations and to consider the effect of increasing motor temperature in steady-state, based on (21) and motor temperature changes in these conditions, this effect has been applied as a coefficient to the constant values of the resistors [28].

$$R_{new} = R_0(1 + \alpha\Delta\theta) \tag{21}$$

where, α is the temperature coefficient of copper or aluminum, Δθ is the temperature change.

Also, in order to consider the effect of skewed rotors in the proposed model, the skew factor approach has been used. In this method, a skew factor is applied to the mutual inductance. This factor is given by (22) [29].

$$K_{skew} = \frac{\sin(\alpha_{skew}/2)}{\alpha_{skew}/2} \tag{22}$$

$$L_{sr.eff} = K_{skew} L_{sr0} \tag{23}$$

V. Simulation results

A SCIM, whose parameters are given in Table III, is investigated in this paper. The stator winding connection is Y. The simulation results are obtained using a balanced three-phase power supply of 380 V, 50 Hz, and under a load of 3.5 Nm (full load). It should be noted that the calculations

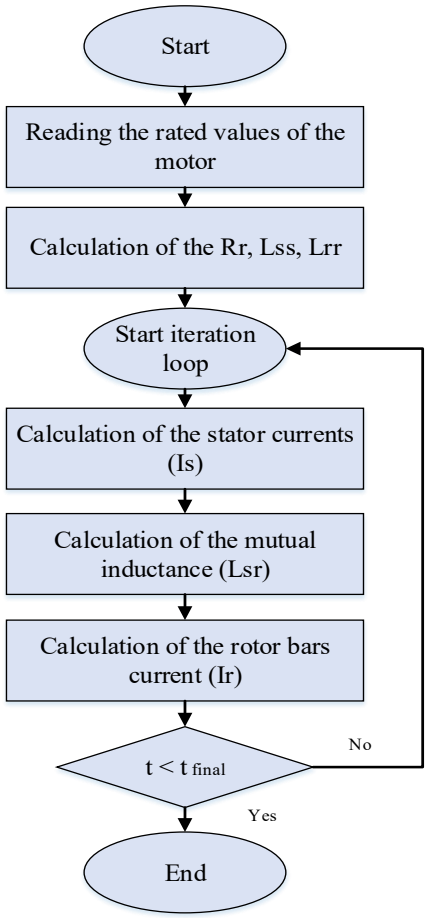

Fig. 3. Flowchart of the calculation process of rotor bars' current

TABLE II ADVANTAGES AND DISADVANTAGES OF THE PROPOSED METHOD

Advantages	Disadvantages
It is Suitable for real-time calculation of the RBC as well as online fault diagnosis	Noise or sensor inaccuracies effect on the RBC calculation.
It is easily implemented on DSPs because they are based on differential equations.	Ignoring the skin effect, hysteresis losses and eddy current at high frequencies
It is straightforward and directly provides information about the IM under different operating conditions.	High sensitivity to changes in motor parameters, including changes in resistances due to temperature changes, changes in inductances due to magnetic saturation.
It uses a smaller number of sensors and only standard variables (voltage, current, and speed).	
It is capable of operating under various loading conditions.	
It can be used for industrial motors with different rated power or number of poles.	
It can model any type of stator and rotor winding structure.	

of the proposed model focus more on the steady-state conditions of the motor and do not examine the start-up transient conditions. Therefore, the results presented in this section are the results of the steady state of the motor. This model performs under different loading conditions, and there are no limitations in this regard. In this section, as an example, the results of the proposed model under nominal load (3.5 N·m) are presented. As shown in Figure 4, this motor is evaluated and tested under both healthy and faulty conditions with a BRB fault (one and two adjacent bars). Figure 5 shows a picture of the laboratory setup. Additionally, to confirm the experimental results, the simulation results of this motor have been obtained using Ansys Maxwell software based on FEM.

A) Matrices of Self and Mutual Inductance

After calculating the inductance matrices based on a method involving repetition by solving the dynamic equations, the stator winding current, the mutual inductance of the stator windings and the rotor bars (L_{sr}), and finally the RBC are calculated.

TABLE III CHARACTERISTICS OF THE STUDIED SCIM

Parameter	Specifications
Power (kW)	1.1
Voltage (V)	380
Frequency (Hz)	50
Speed (RPM)	2850
Nominal Current (A)	2.46
Pole number	2
Number of stator slot	18
Number of rotor bars	16
Air gap length (mm)	1
The inner diameter of the stator core (mm)	67
The outer diameter of the stator core (mm)	121
Number of conductors per stator slot	85
Stator core length (mm)	76
Skew angle of rotor bars (degrees)	5

(a) (b) (c)

Fig. 4. Squirrel cage rotor: (a) healthy (b) 1 broken bar (c) 2 broken bars

According to the proposed method (Figure 4) to calculate the RBC at full load (3.5 Nm) under different conditions, the matrices of self-inductances include the inductance of the stator windings (L_s) and the inductance of the rotor bars (L_r). Additionally, the mutual inductance matrices of the stator windings and the rotor bars have been calculated in the BRB condition, with one BRB (bar number 1) and two BRBs (bars

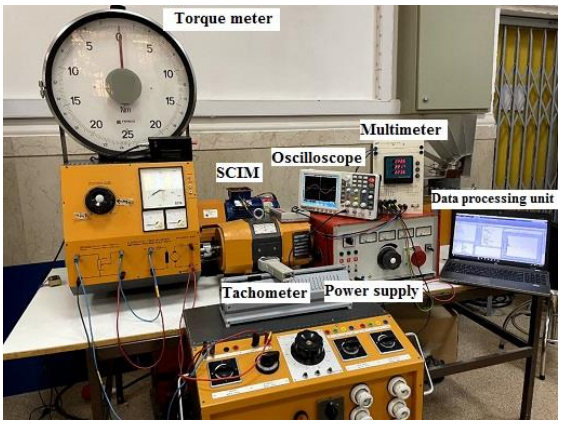

Fig. 5. Laboratory set to calculate the rotor bars' current

number 1 and 2). To validate the experimental results, the results of Ansys Maxwell software have been used.

B) Stator Winding Current

The results of calculating the stator current (Phase A) in a healthy condition, with one BRB (bar number 1), and with two BRBs (bars number 1 and 2) under nominal voltage and full load (3.5 Nm) are shown in Figure 6. The results of the laboratory test measurement of the stator current under the above conditions are equal to 3.5, 4, and 1.4 amps, respectively.

C) Rotor Bars Current

After calculating the matrices of inductance and stator current, the magnitude of RBC under different conditions at time t = 180 ms is presented in Figure 7. As an illustration, Figure 8 displays the current curve for rotor bar number 8. When a BRB fault arises in a rotor, the resistance of the damaged bars increases significantly compared to the resistance of the healthy bars. Figure 7 illustrates that when there are broken bars, some rotor currents flow into the adjacent bars instead of the broken bars due to high resistance, causing an uneven distribution of rotor currents. When a rotor experiences a broken bar, the current in the adjacent bars increases. However, the total current in the rotor is less than what flows through an undamaged rotor. The high current density in the affected bars leads to overheating, which can cause a number of issues, including fluctuations in torque and speed, increased noise, unstable stator currents, and reduced average torque [30].

The sensitivity of the proposed model to changes in the resistance value of the rotor bars is notable. In this model, a 5-fold increase in the bar resistance produces a similar effect to complete BRB, and a 2-fold increase in the bar resistance produces a similar effect to partial BRB. As an example, the current of one of the rotor bars (bar number 8) for a 5-fold increase (complete BRB), a 2-fold increase (partial BRB), and a 10-fold increase at full load (3.5 Nm) is shown in Figure 9.

D) Evaluation of Other Characteristics of the Motor

When the BRB fault occurs, it causes a significant imbalance in the magnetic field within the air gap. As a result, rotating flux harmonics are generated, which consume a considerable amount of reactive power. This reactive power can be greater than the active power, thereby reducing the motor's torque. Rotor faults in IMs generally originate from a minor break in the rotor bar or a point of high resistance. Once such a fault spreads, the magnetic field becomes increasingly asymmetric because of the lack of induced current in the broken bars. This can lead to uneven magnetic distribution and saturation in the stator and rotor teeth near the broken bars, resulting in high harmonic components that can cause electromagnetic issues such as reverse magnetic field generation, torque ripples, and unbalanced magnetization. In Figure 10, you can see the curve of the magnetic flux density in the air gap, which was obtained from the motor models in both healthy and faulty conditions. Figure 11 compares the harmonic components of the magnetic flux density in the air gap. When the rotor is in a healthy state, the THD is equal to 17%, while that of the rotor with one broken bar and two broken bars is equal to 25% and 28%, respectively.

The electromagnetic force is calculated by averaging torque in the simulation. The radial electromagnetic forces (F_r) are computed using Maxwell's stress tensor in (27).

$$F_r = \frac{1}{2\mu_0}(B_n^2 - B_t^2) \quad (27)$$

where B_n and B_t represent the radial and tangential components of the magnetic flux density, μ_0 is vacuum magnetic permeability. The electromagnetic torque is determined by integrating T over the stator and rotor surfaces [31]. Radial electromagnetic forces are shown in Figure 12. The results show that under defective conditions, the level of these forces increases greatly compared to healthy conditions. While the average of these forces is in a healthy state, the rotor with 1 broken bar and the rotor with 2 broken bars have values equal to 0.5, 67, and 152 newtons, respectively. This condition indicates that the areas of the broken bars are subjected to more force, which raises the likelihood of their breakage. If the level of these forces increases, it will result in more electromagnetic noise in the motor.

The speed and torque curves for different motor conditions are shown in Figures 13 and 14, respectively. It can be seen from the comparison of the speed curves that the speed in defective conditions decreases with the increase in the number of BRBs. Also, the speed of the motor in its steady state in healthy and faulty conditions was measured by the tachometer, yielding values of 2791, 2740, and 2720 rpm, respectively. Furthermore, in the torque curves, it can be observed that the torque obtained from the motor with 1 broken bar and 2 broken bars results in a decrease of 10% and 17%, respectively, compared to the healthy motor. Therefore, it can be concluded that with the increase in the

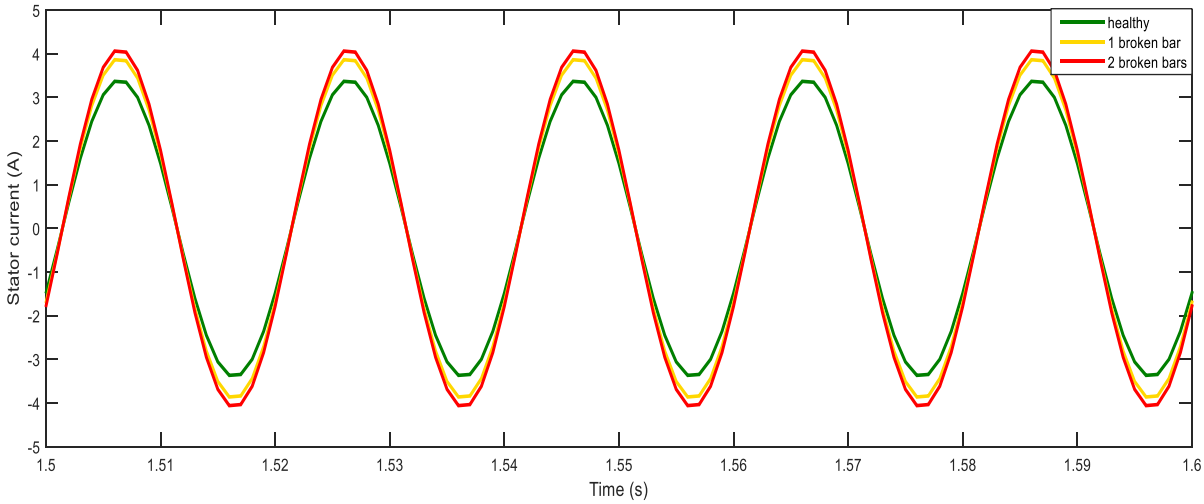

Fig. 6. Stator current (phase A) in different operating conditions

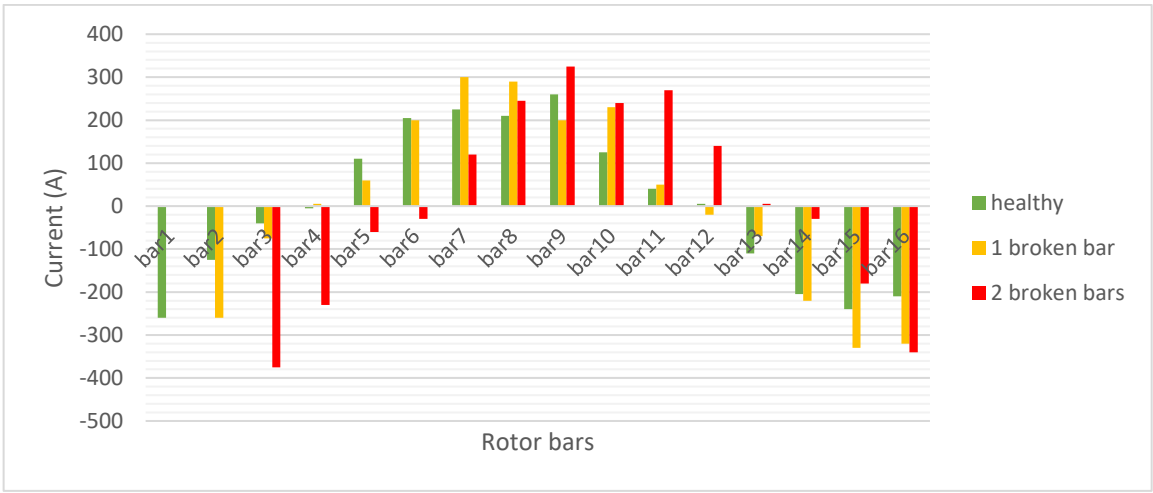

Fig. 7. Magnitude of rotor bars current in healthy and faulty conditions

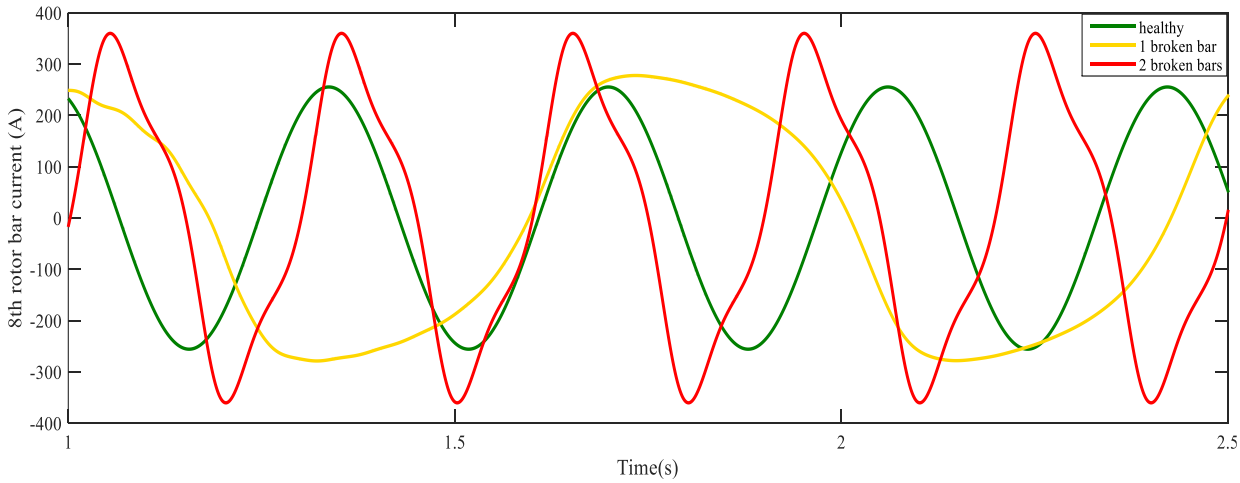

Fig. 8. The current of rotor bar number 8 in healthy and faulty conditions

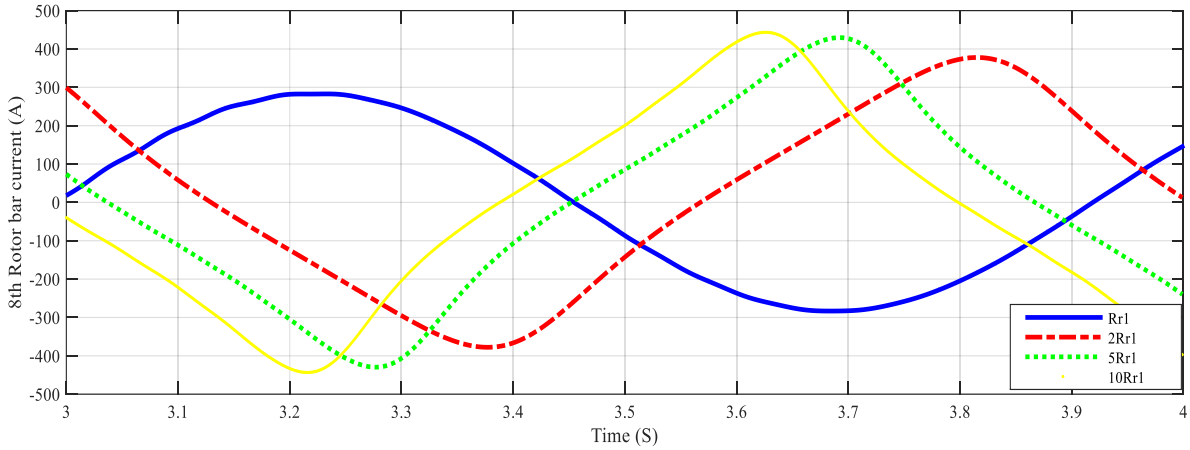

Fig. 9. The current of rotor bar number 8 under conditions of increasing the resistance of rotor bar number 1 by 2, 5 and 10 fold.

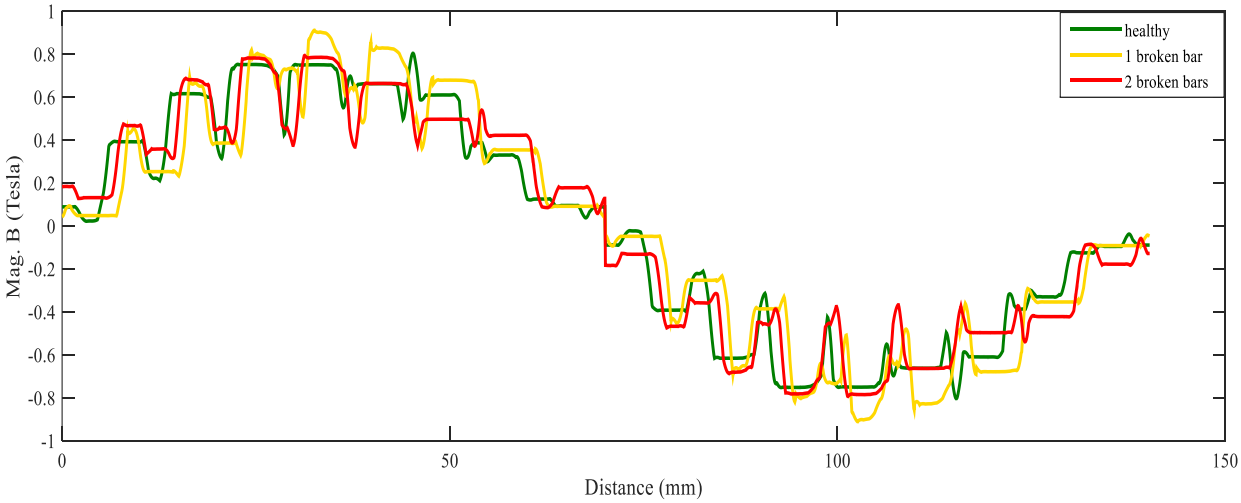

Fig. 10. Flux density distribution curve in healthy and defective conditions

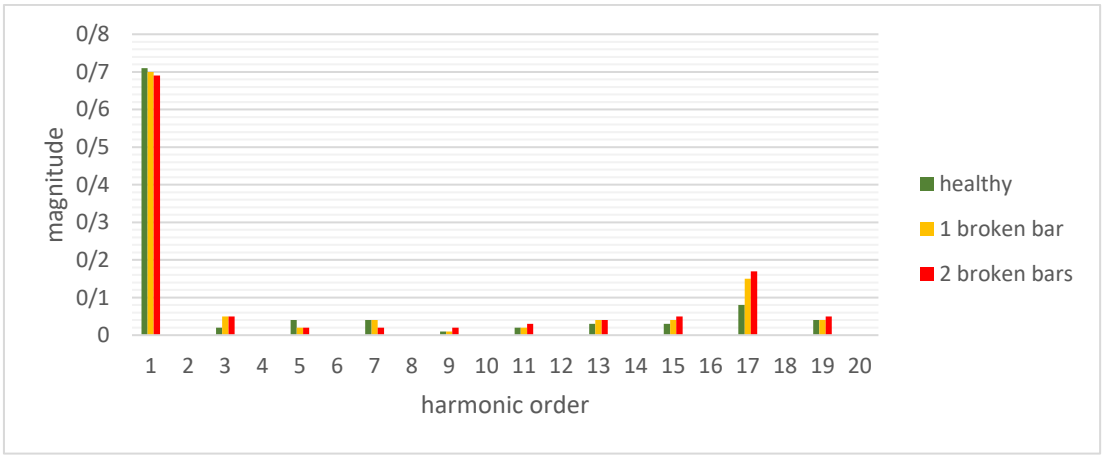

Fig. 11. Comparison of harmonic components of flux density in healthy and defective conditions

number of broken bars, the values of speed and torque decrease. The torque ripple in healthy conditions, with a rotor having 1 broken bar, and with a rotor having 2 broken bars, was measured as ±0.4, ±0.5, and ±0.7, respectively

.

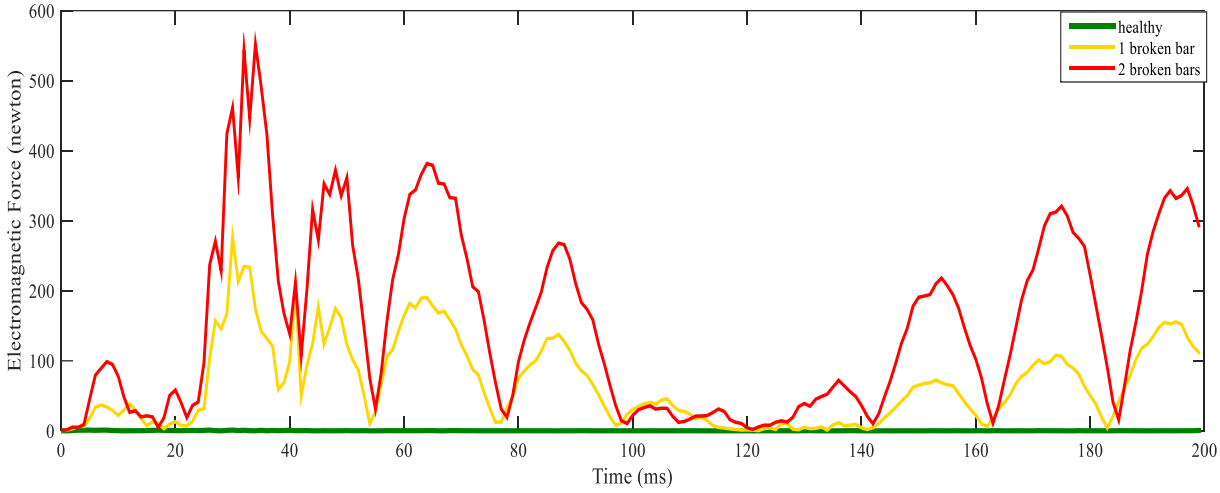

Fig. 12. Radial electromagnetic force in healthy and defective conditions

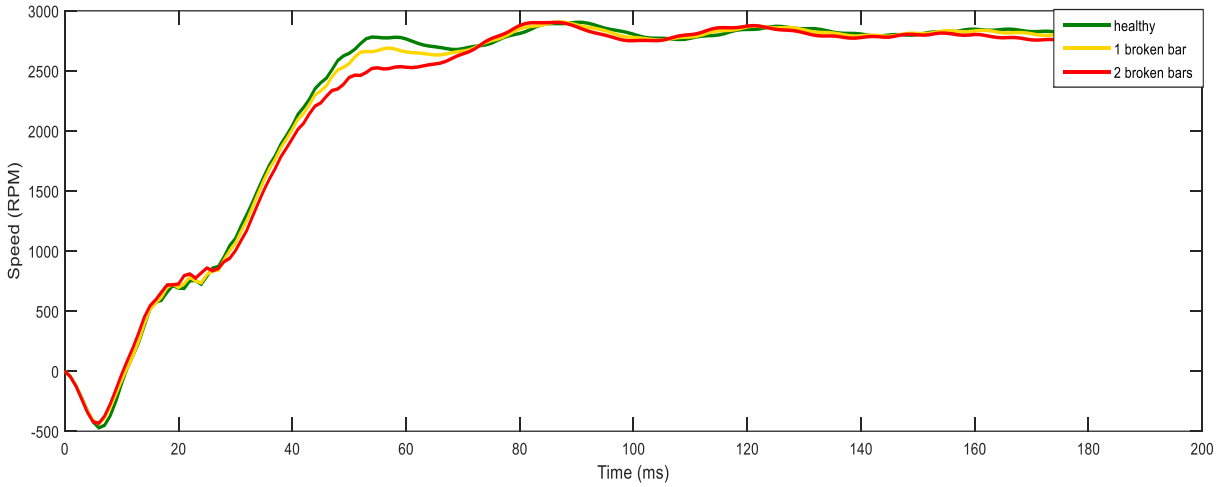

Fig. 13. Rotor speed in healthy and defective conditions

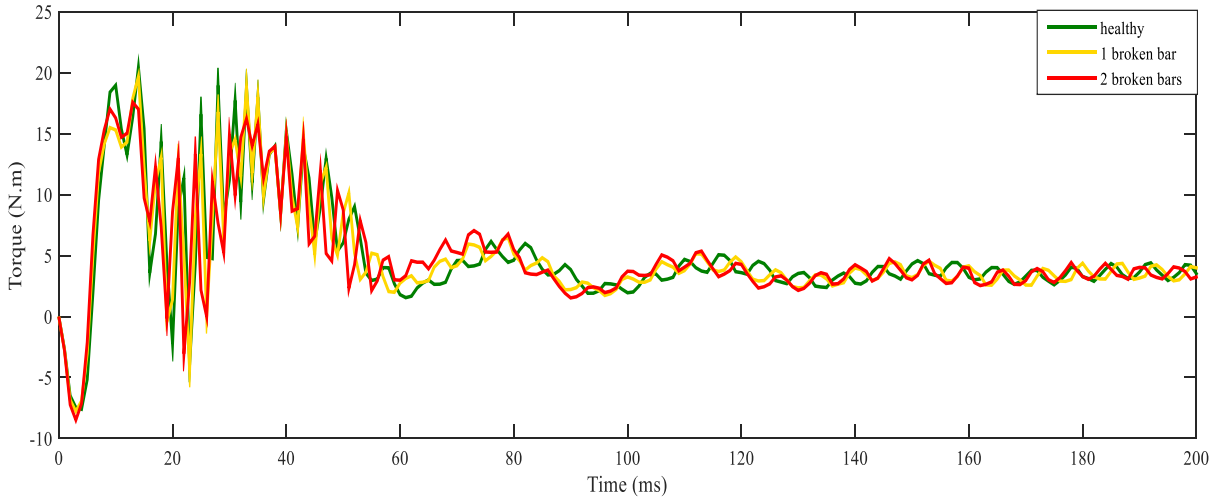

Fig. 14. Torque in healthy and defective conditions

VI. Losses in the BRB fault

The losses in an IM include constant losses and variable losses. Constant losses are those that remain constant in the normal operating range of the motor, and their value does not change. These losses include iron losses (core losses), friction losses, and windage losses, which can be calculated by performing a no-load test. Variable losses are also referred to as copper losses. These losses include stator copper losses and rotor copper losses. Copper losses can also be calculated by performing a blocked rotor test. A no-load test (Figure 15) and a blocked rotor test (Figure 16) have been performed on the studied motor. By using the DC test, the resistance of each stator phase can be calculated. The results of these tests on a healthy motor under nominal conditions are presented below. It is important to note that the presence of a BRB can have a significant effect on the efficiency of an SCIM. Due to broken bars, the motor losses increase, and some of the rotor bars may become overloaded. This overload can cause an increase in inter-bar currents that flow from the rotor core between the broken bar and adjacent bars. This can compromise the motor's efficiency. However, there is limited literature available on this particular effect [32-33]. It's worth exploring the effects of non-adjacent bar breaking in addition to other factors. While this is a less common occurrence, some studies have found that non-adjacent bars in the rotor cage can break under certain conditions [34-35]. In such situations, diagnosing the fault becomes challenging, as existing techniques like motor current analysis may not be effective. This is because the impacts of different breaks can be compensated for to some extent, depending on the relative position of the bars that have broken.

According to the DC test, the results of the no-load and blocked rotor tests of the Y-connected motor are presented in Tables IV and V, respectively. Based on the results of the DC test, no-load test, and blocked rotor test, motor losses are calculated and shown in Table VI. Additionally, the efficiency of the motor under healthy and BRB fault conditions are calculated and presented in Table VII. As can be seen, depending on the severity of the fault, the efficiency is affected, and this value decreases. Furthermore, iron and copper losses are compared in Table VIII.

In Table IX, experimental and simulation results are compared. In this table, the currents of rotor bars numbers 8 and 16, obtained from experimental and simulation results, have been compared. Rotor bar number 8 is the farthest from the BRBs (rotor bars numbers 1 and 2), while rotor bar number 16 is located near the BRBs. Additionally, the losses and efficiency of the motor under different conditions have been compared.

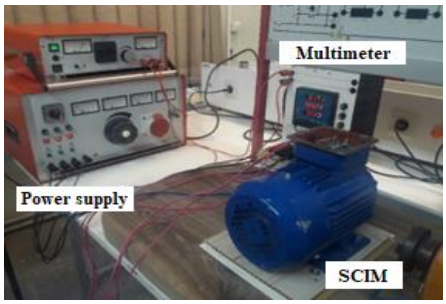

Fig. 15. No-load test laboratory set

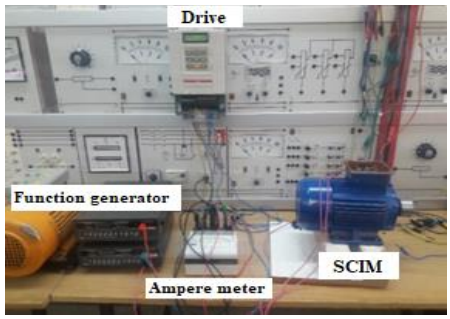

Fig. 16. Blocked rotor test laboratory set

TABLE IV NO LOAD TEST RESULTS

Parameter	Phase A	Phase B	Phase C
Active power (W)	70	65	50
Reactive power (VAR)	168	145	150
Voltage (V)	380	380	380
Current (A)	1.17	1	1.1
Power factor	0.27	0.24	0.19

TABLE V BLOCKED ROTOR TEST RESULTS

Parameter	Active power (W)	Reactive power (VAR)	Voltage (V)	Current (A)	Frequency (Hz)
Specifications	40	20	85	2.46	12

TABLE VI BLOCKED ROTOR TEST RESULTS

Parameter	Active power (W)	Reactive power (VAR)	Voltage (V)	Current (A)	Frequency (Hz)
Specifications	40	20	85	2.46	12

TABLE VII LOSSES OF THE STUDIED MOTOR

Losses	Core losses	Stator copper loss	Rotor copper loss
Specifications	85	136	48

TABLE VIII ELECTROMECHANICAL CHARACTERISTICS OF THE MOTOR IN THE DIFFERENT OPERATING CONDITIONS UNDER NOMINAL CONDITIONS

Conditions	Phase voltage (V)	Phase current (A)	Power factor	Torque (Nm)	Speed (RPM)	Mechanical power (kW)	Electrical power (kW)	Efficiency (%)
Healthy	220	2.5	0.92	3.5	2795	1.03	1.30	80.02
1 BRB	220	3.12	0.91	3.5	2740	1	1.33	75.18
2 BRBs	220	3.28	0.91	3.5	2720	0.996	1.38	71.73

TABLE IX LOSSES IN THE DIFFERENT OPERATING CONDITIONS UNDER NOMINAL CONDITIONS

Conditions	Stator copper loss (W)	Rotor copper loss (W)	Core losses + Windage losses (W)
Healthy	136	48	85
1 BRB	170	54	105
2 BRBs	197	71	112

TABLE X COMPARISON OF EXPERIMENTAL AND SIMULATION RESULTS

Parameter	Experimental results			Simulation results		
	Healthy	1 BRB	2 BRBs	Healthy	1 BRB	2 BRBs
stator current(A)	3.3	3.8	3.9	3.45	3.92	4.07
current bar number 16 (A)	230	260	310	235	268	312
current bar number 8 (A)	230	240	260	235	242	263
Torque ripple(N.m)	± 0.4	± 0.5	± 0.7	± 0.6	± 0.8	±1.1
Losses (W)	270	329	380	230	303	253
Efficiency (%)	79.23	75.18	72.46	83.57	82.35	80.55

VII. Conclusion

In this paper, a method for calculating the RBC in an SCIM under healthy and faulty conditions was presented. A key strength of the proposed approach is that it enables direct and precise estimation of individual rotor bar currents using the MCC model, which provides deeper insight into motor behavior under broken bar faults compared with conventional analysis. The results demonstrated that the presence of one or two broken bars significantly alters the motor's performance. The stator current increased from about 3.3 A in the healthy case to nearly 3.9 A with two broken bars, while efficiency dropped from approximately 80% to 72%. Furthermore, rotor and stator copper losses increased noticeably, and the motor speed decreased slightly (around 75 RPM). These variations indicate higher thermal and electrical stress on the remaining healthy bars and the overall motor. Finally, the close agreement between experimental measurements and simulation results confirms the accuracy of the MCC model and the reliability of the proposed analysis.

Conflicts of Interest: The authors declare that there is no conflict of interest regarding the publication of this paper.

References

[1] Shadfar, Hamed, and Hamid Reza Izadfar. "A New Squirrel Cage Rotor Structure to Improve the Dynamic Performance of the Single Phase Induction Motor." *International Journal of Industrial Electronics Control and Optimization, Vol.* 5, No. 4, pp. 279-286, 2022.

[2] Niaz Azari, Milad, Vasiye Lohrasbi, and Seyed Abdolah Mousavi. "Optimum design of high-temperature superconducting induction/synchronous motor to increase torque density using collective decision optimization algorithm." International Journal of Industrial Electronics Control and Optimization, Vol. 3, No. 2, pp. 137-145, 2020.

[3] Prasad, Kapu V. Sri Ram, and Varsha Singh. "Fault Diagnosis of Induction Machine for Rotor Cage Damage Using MCSA for Industrial Application." Electric Power Components and Systems, pp. 1-13, 2024.

[4] Bahgat, Bahgat Hafez, E. A. Elhay, Tole Sutikno, and Mahmoud M. Elkholy. "Revolutionizing motor maintenance: a comprehensive survey of state-of-the-art fault detection in three-phase induction motors." *International Journal of Power Electronics and Drive Systems,* Vol.15, No. 3, pp. 1968-1989, 2024.

[5] Dehnavi, Vahid Safari, and Masoud Shafiee. "Fault diagnosis of induction motors using novel measurement techniques and data fusion." *Measurement* (2025): 118135.

[6] Wang, Bingnan. "Induction Motor Fault Classification with Topological Data Analysis." In *2024 IEEE Energy Conversion Congress and Exposition (ECCE)*, pp. 5381-5386, 2024.

[7] Sheikh, Muhammad Aman, Sheikh Tahir Bakhsh, Muhammad Irfan, Nursyarizal bin Mohd Nor, and Grzegorz Nowakowski. "A review to diagnose faults related to three-phase industrial induction motors." *Journal of Failure Analysis and prevention,* Vol.22, No. 4, pp. 1546-1557, 2022.

[8] Gundewar, Swapnil K., and Prasad V. Kane. "Condition monitoring and fault diagnosis of induction motor." *Journal of Vibration Engineering & Technologies,* Vol. 9, pp. 643-674, 2021.

[9] Kavitha, M. "Hybrid AI-Mathematical Modeling Approach for Predictive Maintenance in Rotating Machinery Systems." *Journal of Applied Mathematical Models in Engineering*, pp. 1-8, 2025.

[10] AlShorman, Omar, Muhammad Irfan, Ra'ed Bani Abdelrahman, Mahmoud Masadeh, Ahmad Alshorman, Muhammad Aman Sheikh, Nordin Saad, and Saifur Rahman. "Advancements in condition monitoring and fault diagnosis of rotating machinery: A comprehensive review of image-based intelligent techniques for induction motors." *Engineering Applications of Artificial Intelligence*, Vol. 130, p. 107724, 2024.

[11] Konuhova, Marina. "Induction Motor Dynamics Regimes: A Comprehensive Study of Mathematical Models and Validation." *Applied Sciences*, Vol. 15, No. 3, p. 1527, 2025.

[12] Benninger, M., M. Liebschner, and C. Kreischer. "Automated Parameter Identification for Multiple Coupled Circuit Modeling of Induction Machines." In *2022 International Conference on Electrical Machines (ICEM)*, pp. 1307-1313. IEEE, 2022.

[13] Zhu, Xinkai, Guangyu Qi, Ming Cheng, Wei Qin, Yabin Liu, and Jiwei Huang. "Equivalent magnetic network model of electrical machine based on three elements: magnetic flux source, reluctance and magductance." *IEEE Transactions on Transportation Electrification,* 2024.

[14] Olarinoye, G. A., and I. Abdulwahab. "Comparative analysis and simulation of the dq reference frame model of the three phase induction motor and its modification." *Arid Zone Journal of Engineering, Technology and Environment,* Vol. 18, No. 1, pp. 41-52, 2022.

[15] Prasad, Kapu V. Sri Ram, K. Dhananjay Rao, and Faisal Alsaif. "Induction motor structure design to reduce vibrations with numerical (fea) and experimental (va) techniques." *IEEE Access,* 2024.

[16] X. Luo, Y. Liao, H. Toliyat, A. El-Antably, T. Lipo.: Multiple coupled circuit modeling of induction machines, IEEE Trans. Ind. Appl. Vol. 31, No. 2, pp. 311–318, 1995.

[17] Benninger, M., M. Liebschner, and C. Kreischer. "Automated Parameter Identification for Multiple Coupled Circuit Modeling of Induction Machines." In *2022 International Conference on Electrical Machines (ICEM)*, pp. 1307-1313. IEEE, 2022.

[18] Yang, Yi, Niaoqing Hu, Zhe Cheng, Jiangtao Hu, and Jiao Hu. "Coupled electromagnetic-dynamic modelling of induction motor with a broken rotor bar." In *Ninth International Symposium on Sensors, Mechatronics, and Automation System*, Vol. 12981, pp. 1176-1181, 2024.

[19] Fu, Qiang, Qing Guo, Wei Zhang, Weimin Cui, and Ling Zhao. "An analytical model for squirrel cage induction machine with broken rotor bars derived based on the multiple coupled circuit theory and the winding function approach." *International Journal of Circuit Theory and Applications*, Vol. 49, No. 6, pp. 1633-1658, 2021.

[20] Yu, Xinyi, Stefan Quabeck, Stephan Schüller, and Rik W. De Doncker. "Modelling of broken rotor bars and eccentricity faults in squirrel cage induction machines." In *2021 IEEE 13th International Symposium on Diagnostics for Electrical Machines, Power Electronics and Drives (SDEMPED)*, vol. 1, pp. 133-139. IEEE, 2021.

[21] Wei, C. H., L. Yan, W. H. Tang, and Q. H. Wu. "Detection of broken bars in induction motor based on multiple coupled circuit model with optimized parameters." In *2013 IEEE PES Asia-Pacific Power and Energy Engineering Conference (APPEEC)*, pp. 1-6. IEEE, 2013.

[22] Abdulkareem, Ademola, Tochukwu Anyim, Olawale Popoola, John Abubakar, and Agbetuyi Ayoade. "Prediction of induction motor faults using machine learning." *Heliyon* , Vol.11, No. 1, 2025.

[23] M.S.R. Krishna, K. S. Ravi, "Fault diagnosis of induction motor using motor current signature analysis", in 2013 International Conference on Circuits, Power and Computing Technologies (ICCPCT), pp. 180-186, 2013.

[24] Hussain, Syed Nazim, and Syed Sajjad Haider Zaidi.: Modeling and analysis of a three-phase induction motor with a broken rotor bar. In 17th IEEE International Multi Topic Conference, pp. 488-493, 2014.

[25] Nait-Said, N. "Rotor resistance estimation of an induction motor to detect broken bars fault using HH method." Electric Power Components and Systems, Vol. 32, No. 2, pp. 149-161, 2004.

[26] C. Kral, A. Haumer, and C. Grabner.: Modeling and Simulation of Broken Rotor Bars in Squirrel Cage Induction Machines, Proceedings of the World Congress on Engineering, pp.1 - 3, 2009.

[27] Pezzani, C., G. Bossio, and C. De Angelo.: Winding distribution effects on induction motor rotor fault diagnosis. Mechatronics, Vol. 24, No.8, pp.1050-1058, 2014.

[28] Khalifa, Fahim A., Sobhy Serry, Mohamed M. Ismail, and Basem Elhady. "Effect of temperature rise on the performance of induction motors." In 2009 International Conference on Computer Engineering & Systems, pp. 549-552. IEEE, 2009.

[29] A. Tessarolo, R. Menis, "Influence of Skewing on the Harmonic Content of Induction Machine Torque", Electric Power Systems Research, pp.45-56, 2018.

[30] Yektaniroumand, T., M. Niaz Azari, and M. Gholami. "Optimal rotor fault detection in induction motor using ppaper-swarm optimization optimized neural network." International Journal of Engineering, Vol.31, No.11, pp.1876-1882, 2018.

[31] El Idrissi, Abderrahman, Aziz Derouich, Said Mahfoud, Najib El Ouanjli, Ahmed Chantoufi, and Youness El Mourabit. "Acoustic characterization of a three-phase asynchronous machine under stator unbalance defects." *e-Prime-Advances in Electrical Engineering, Electronics and Energy*, Vol. 12, p. 100958, 2025.

[32] Imaouchen, Yacine, Samira Chekkal Ait Ouaret, Djamal Aouzellag, and Kaci Ghedamsi. "The Effect of Stator and Rotor Faults on the Dual-star Induction Motor Behavior." *Periodica Polytechnica Electrical Engineering and Computer Science*, Vol. 69, No. 2, pp. 111-121, 2025.

[33] Drobnič, Klemen, Mitja Nemec, Henrik Lavrié, Vanja Ambrožié, and Rastko Fižer. "Detection of Broken Rotor Bars in Presence of Load Oscillations." *IEEE access*, 2025.

[34] G. Y. Sizov, A. Sayed-Ahmed, Y. Chia-Chou, N. A. O. Demerdash.: Analysis and diagnostics of adjacent and nonadjacent broken rotor bar faults in squirrel-cage induction machines. IEEE Trans. Ind. Elec., Vol.56, No.11, pp.4627–4641, 2009.

[35] M. Riera-Guasp, M. F. Cabanas, J. A. Antonino-Daviu, M. Pineda-Sanchez, C. H. R. Garcia.: Influence of nonconsecutive bar breakages in motor current signature analysis for the diagnosis of rotor faults in induction motors, IEEE Trans. Energy Convers., Vol. 25, pp. 80-89, 2010.

Hamed Shadfar received his M.Sc. degree from Semnan University, Semnan, Iran, in 2018 with First class distinction. He is working toward a Ph.D. in the Faculty of Electrical and Computer Engineering, Semnan University, Semnan, Iran. His major research interests include design, modeling, condition monitoring, and fault diagnosis of electric machines.

Hamid Reza Izadfar is currently an Associate Professor in the Electrical and Computer Engineering Department of Semnan University. His main research interests are the design and analysis of electric machines and drives.

IECO

This page intentionally left blank.

International Journal Of
Industrial Electronics Control and Optimization
Print ISSN: 3517-2645
Online ISSN: 3568-2645
Homepage: https://ieco.usb.ac.ir/

Novel Low-Power OTA using New Block to Eliminate Common-Mode Signal

Khalil Monfaredi[1] | Mousa Yousefi[2]

Faculty of Engineering, Azarbaijan Shahid Madani University, Tabriz, Iran.[1,2]
Corresponding author's email: khmonfaredi@azaruniv.ac.ir

Article Info

Article type:
Research Article

Article history:
Received: 27-November-2024
Received in revised form: 22-April-2025
Accepted: 21-May-2025
Published online: 21-March-2026

Keywords:
CMRR Enhancement,
High gain,
Low power,
Trans-conductance amplifier.

ABSTRACT

In this paper, a trans-conductance amplifier based on Common Mode Rejection Ratio (CMRR) enhancement block is presented. The proposed block is capable of eliminating common mode signals at input stage. This feature improves the gain and CMRR of the amplifier substantially. The Cascode structure is also eliminated in proposed architecture, which resulted in favorably reduced power consumption due to low supply voltage requirements. The presented OTA is simulated in 180nm CMOS technology at Cadence Spectre environment with 1.5 v supply voltage proving it appropriate for low-voltage applications. The bias current of the proposed circuit is very low value of 3.9 µA. Gain and phase margin for this block are achieved to be 83.96 dB and 61.68 degree, respectively. These results achieved while the circuit drive a 5pF load at its output. The power consumption of the proposed amplifier is interestingly very low value of 5.9 µW which makes the block suitable for low-power applications.

I. Introduction

Operational amplifiers are one of the most important and widely used blocks in many analog circuits such as data converters, switched capacitor circuits and filters and medical circuits [1-3]. In switched-capacitor circuits, CMOS OTAs are widely used to transfer the charge between the capacitors with the targeted accuracy [4, 5]. Due to the rapid development of CMOS technology and the rapid growth of portable electronic devices, the demand for power-efficient integrated circuits has been increased [6]. On the other hand, down-scaling the device sizes along with smaller power supply requirements has forced the designers to make use of low-voltage, low-power techniques [7]. Meanwhile, decreasing the power supply voltage can reduce the voltage dynamic range and impose other restrictions such as current trasfer inefficiency on the circuit [8, 9]. Thus performance enhancement of advanced recycling folded cascode is always on demand [10].

Single stage amplifiers, such as Folded Cascode (FC) and telescopic amplifiers are more appropriate for low power applications compared with the two stage amplifiers due to their lower power consumption. Folded Cascode amplifiers have higher gain-bandwidth and higher output voltage swing, in comparison with their telescopic counterparts, and have therefore been widely used in recent years [11]. Meanwhile, easily connecting the output to input in folded cascode amplifier to build a buffer is another advantage of these amplifiers [12]. In Folded Cascode amplifiers, bias current sources have no role at improving the amplifier performance, so recycling bias current has been introduced as a technique to improve the gain and power consumption of amplifiers by handling the bias current source values [13].

RFC structure originally proposed at [14], in which the RFC scheme is thoroughly scrutinized and its benefits over the conventional FC structure approved by mathematical calculations and CAD tool simulations.

To improve the performance of Folded Cascode amplifier, the RFC structure is proposed in [15]. The relative isolation of the AC current path from the DC one, has lead to a significant increase in the gain and the slew rate of the amplifier compared with the conventional Folded Cascode amplifier, imposing no increase in surface area and power

consumption of the structure. The fact that the AC and DC paths are not full isolation from each other in this structure, leads to the amplifier trans-conductance being limited, which this problem has been fixed by the use of IRFC and the full isolation of AC and DC current paths [16].

In this paper, a new amplifier based on RFC structure is represented which includes the new CMRR enhancement block at its input stage. This block is capable to strictly remove the common mode current. The proposed amplifier, possesses the requirements for optimum performance, including very lower power consumption, bias current and supply voltage, higher gain and the reliably sufficient phase margin. Using compensation resistor, certain phase margin for the circuit is obtained [17].

This article includes the following sections: in section II the proposed amplifier is analyzed and discussed. Section III contains various parameters and simulation results obtained for the circuit. And finally, the article ends with conclusions in Section IV.

II. Principle of Operation

As shown in Fig. 1, the proposed amplifier has two stages, namely, the input and output stages. The CMRR enhancement block which is incorporated at input stage of the proposed amplifier, makes it possible to eliminate the common mode currents at input stage. This leads to a significant improvement of the amplifier's CMRR. In the conventional RFC structures, the Cascode structures are used in order to increase the accuracy of the signal transmission and thereby improving at CMRR. However, due to the Cascode structures utilized, this circuit requires a relatively high supply voltage, which will increase the overall power consumption. But, in the proposed circuit due to the fundamental role of the CMRR strengthening blocks in eliminating the common mode signals, simple current mirrors are efficiently utilized, interestingly reducing the minimum required supply voltage. This block is shown in Fig. 1 with dashed line. Also, in proposed amplifier the Cascode stage DC bias voltage that is required for the performance of transistors of the amplifiers is eliminated. A pair of PMOS transistors is used at the input of the amplifier because of lower common mode voltage input and flicker noise and higher non-dominant pole compared to the NMOS pair. Likewise, in the output stage, a low-voltage Cascode current mirror is placed that creates the bias voltage for the transistors of Cascode utilizing the input current.

The CMRR enhancement performance of the block at eliminating the common mode signal will be discussed below, by equivalent small-signal analysis of the proposed amplifier. In Fig. 2, half equivalent small-signal circuit of the amplifier is shown. Analyzing this circuit, it appears that due to a large equivalent resistance at node C_1, the current delivered to the output stage will be accompanied by a trivial error.

In Fig. 2, resistors and voltages of the M_n transistor connected to CMRR enhancement block, are called R_n and V_n, respectively and is defined by small signal analysis as follows:

$$R_{14} = \frac{h.rds_0(1+\mu_{2a}) + rds_{2a} + rds_{14}}{1+\mu_{14}} \quad (1)$$

$$R_{15} = \frac{h.rds_0(1+\mu_{1b}) + rds_{1b} + rds_{15}}{1+\mu_{15}} \quad (2)$$

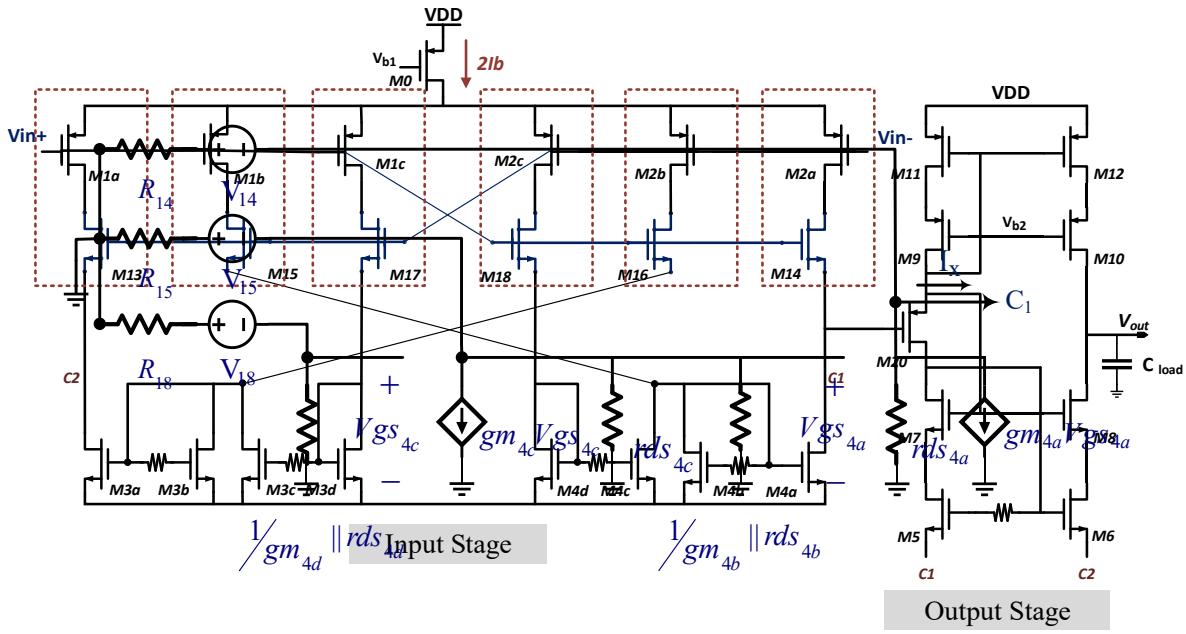

Fig. 2. The equivalent half circuit for input stage of OTA
Fig. 1. The proposed OTA based on CMRR enhancement block

$$R_{18} = \frac{h.rds_0(1+\mu_{2c}) + rds_{2c} + rds_{18}}{1+\mu_{18}} \quad (3)$$

$$V_{14} = \frac{Vin_1\mu_{2a} - Vin_2\mu_{14}}{1+\mu_{14}} \quad (4)$$

$$V_{15} = \frac{Vin_2\mu_{1b} - Vin_1\mu_{15}}{1+\mu_{15}} \quad (5)$$

$$V_{18} = \frac{Vin_1\mu_{2c} - Vin_2\mu_{18}}{1+\mu_{18}} \quad (6)$$

$$\begin{matrix} Vin_1 = Vin_- \\ Vin_2 = Vin_+ \end{matrix} \quad (7)$$

Parameter, h, is zero for differentional mode and is one for common mode. gm_i is ith mosfet transconductance, rds_i is ith mosfet output intrinsic impedance and $\mu_i = gm_i \times rds_i$.

Considering the Fig. 1, it can be seen that currents are passed from the input stage through nodes C_1 and C_2 to the output one.
where

The half equivalent circuit includes node C_1, whoes current is named I_x. According to Fig. 2, I_x can written as:

$$I_x = gm_{4a}Vgs_{4a} + \frac{Vin_1\mu_{2a} - Vin_2\mu_{14}}{\boldsymbol{h}.rds_0(1+\mu_{2a}) + rds_{2a} + rds_{14}} \quad (8)$$

Where V_{gs4a}, is gate-source voltage of transistor M_{4a} and can be calculated by small signal analysis of the Figure 2 as follows:

$$Vgs_{4a} = [\frac{1}{gm_{4b}} || rds_{4b} || rds_{4c} || R_{15}] \times (gm_{4c}Vgs_{4c} + \frac{Vin_2\mu_{1b} - Vin_1\mu_{15}}{h.rds_0(1+\mu_{1b}) + rds_{1b} + rds_{15}}) \quad (9)$$

$$Vgs_{4c} = [\frac{1}{gm_{4d}} || rds_{4d} || R_{18}] \times (\frac{Vin_1\mu_{2c} - Vin_2\mu_{18}}{h.rds_0(1+\mu_{2c}) + rds_{2c} + rds_{18}}) \quad (10)$$

By calculating the value of the parameter gate-source voltage of the transistor and putting it in Eq. (8), I_x is obtained as:

$$I_x = Vin_1(F) - Vin_2(G) \quad (11)$$

where F and G, are coefficients of V_{in1} and V_{in2}, respectively and can be calculated as follows:

$$F = [\frac{gm_{4a}}{gm_{4b}}(\frac{gm_{4c}\mu_{2c}}{gm_{4d}\,\mathrm{h.rds}_0(1+\mu_{2c}) + (rds_0(1+\mu_{2c}) + rds_{2c} + rds_{18}} - \frac{\mu_{15}}{rds_0(1+\mu_{1b}) + rds_{1b} + rds_{15}}) + \frac{\mu_{2a}}{rds_0(1+\mu_{2a}) + rds_{14} + rds_{2a}}] \quad (12)$$

$$G = [\frac{gm_{4a}}{gm_{4b}}(\frac{gm_{4c}\mu_{18}}{gm_{4d}\,\mathrm{h}.rds_0(1+\mu_{2c}) + rds_{2c} + rds_{18}} - \frac{\mu_{1b}}{rds_0(1+\mu_{1b}) + rds_{1b} + rds_{15}}) + \frac{\mu_{14}}{rds_0(1+\mu_{2a}) + rds_{14} + rds_{2a}}] \quad (13)$$

It can be observed that for equal values of the F and G, the voltages V_{in1} and V_{in2} in common mode have same sign and value of I_x will be zero, and as a consequence the CMRR approaches to infinite. Due to the opposite sign of the differential mode input voltages, the input stage current will be transferred to the output stage with doubled amplification.

For the coefficients F and G in node C_1 being equal, Eq. (14) must apply.

$$\begin{cases} \mu_{18} = \mu_{2c} \\ \mu_{15} = \mu_{1b} \\ \mu_{14} = \mu_{2a} \end{cases} \quad (14)$$

If we name the current transferred from node C_2 to the output stage, I_y, then for another half equivalent circuit similar to the one exhibited above its value can be calculated. Detailed equations related to I_y is neglected to avoid paper enlarment.

$$I_y = Vin_2(N) - Vin_1(M) \quad (15)$$

where M and N, are coefficients of V_{in1} and V_{in2}, respectively and can be calculated as follows:

$$M = [\frac{gm_{3a}}{gm_{3b}}(\frac{gm_{3c}\mu_{17}}{gm_{3d}\,\mathrm{h}.\mathrm{rds}_0(1+\mu_{1c}) + (rds_{1c} + rds_{17})} - \frac{\mu_{2b}}{rds_0(1+\mu_{2b}) + rds_{2b} + rds_{16}}) + \frac{\mu_{13}}{rds_0(1+\mu_{1a}) + rds_{1a} + rds_{13}}] \quad (16)$$

$$N = [\frac{gm_{3a}}{gm_{3b}}(\frac{gm_{3c}\mu_{1c}}{gm_{3d}\,\mathrm{h}.\mathrm{rds}_0(1+\mu_{1c}) + (rds_{1c} + rds_{17})} - \frac{\mu_{16}}{rds_0(1+\mu_{2b}) + rds_{2b} + rds_{16}}) + \frac{\mu_{1a}}{rds_0(1+\mu_{1a}) + rds_{1a} + rds_{13}}] \quad (17)$$

For the coefficients M and N in node C_2 being equal, Eq. (18) must apply.

$$\begin{cases} \mu_{17} = \mu_{1c} \\ \mu_{16} = \mu_{2b} \\ \mu_{13} = \mu_{1a} \end{cases} \quad (18)$$

Further scrutinizing the equations in differential and common mode CMRR can be achieved as follows:

$$CMRR = \frac{A_d}{A_c} = \frac{A(F+G) - B(M+N)}{A(F-G) - B(M-N)} \quad (19)$$

where A and B are defined as follows:

$$A = R_z(K_2\, gm_8 + K_1 R_K gm_6) + K_2 gm_{12}(R_K + rds_8) \quad (20)$$

$$B = R_K . R_z$$

$$R_z = \frac{rds_{12} + rds_{10}}{1 + \mu_{10}} \quad (21)$$

$$R_K = (R_{13} || rds_{3a} || rds_6)(1 + \mu_8) \quad (22)$$

$$K_1 = \frac{[\frac{\mu_7}{gm_5} - \frac{\mu_{20}}{rds_{20} + R(1+\mu_{20})}]}{1 - gm_5[\frac{\mu_7}{gm_5} - \frac{\mu_{20}}{rds_{20} + R(1+\mu_{20})}]} \quad (23)$$

$$K_2 = \frac{\frac{1}{gm_5}}{1 - \mu_7 + \frac{\mu_{20}}{gm_5(rds_{20} + R(1+\mu_{20})}} \quad (24)$$

Theoretically, for F=G and M=N upon establishment of the Eq. (14) and Eq. (18), the required circumstances of the proposed block placed in the input stage of amplifier are fulfilled and the role of this block in eliminating the common mode signal and increasing the CMRR is achieved. In this circumstance, the denumerator becomes zero and CMRR approaches infinite values.

One way to relax the phase margin of the amplifier, is to put a compensation resistance between NMOS current mirror transistors to separate their parasitic capacitances. By placing this resistor, as shown in Fig. 3, the first order transfer function current mirror becomes a second order transfer function current mirror. The transfer function of the current mirror shown in Fig. 3, can be written as follows to obtain its zero/poles

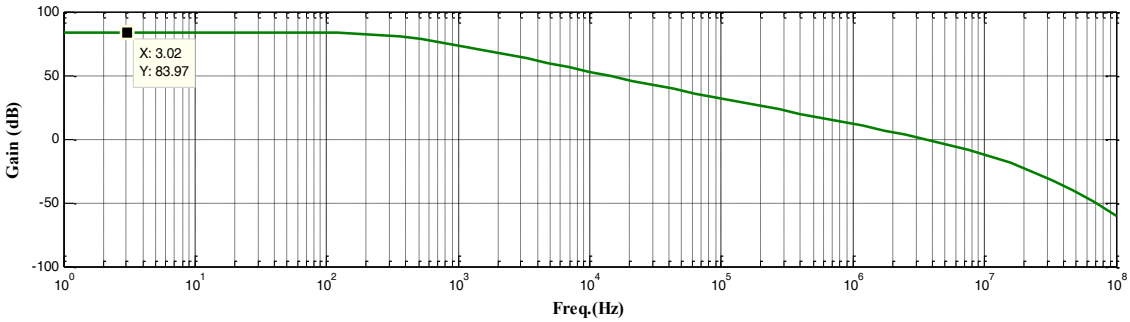

(a)

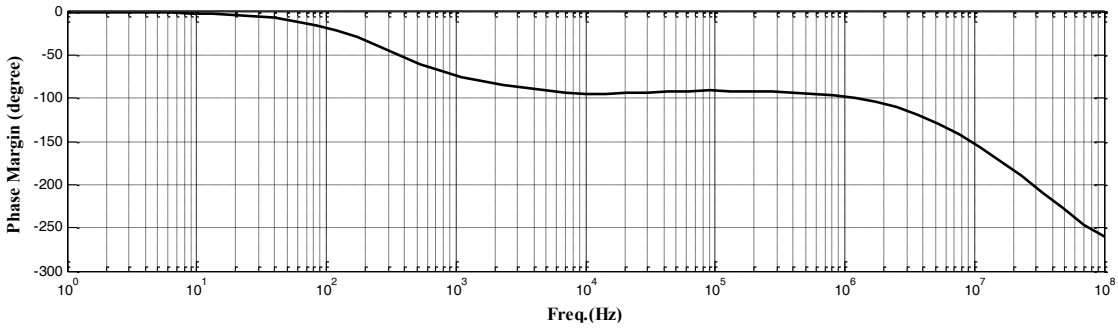

(b)

Fig. 4. (a) DC gain and (b) phase margin's curve of the proposed OTA

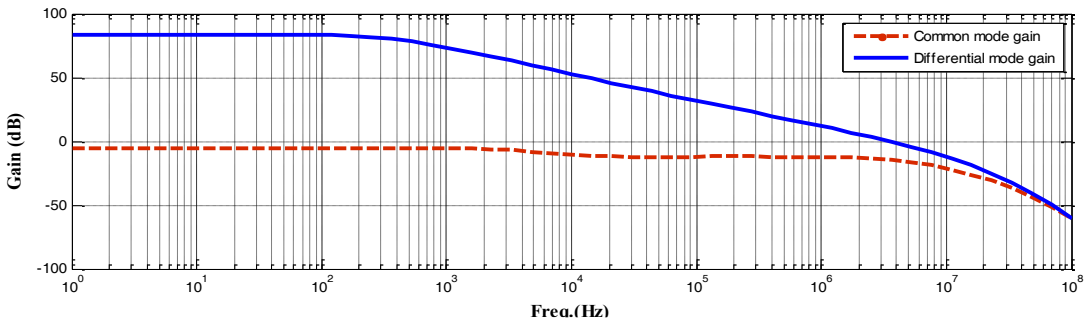

Fig. 5. Differential and common mode gain

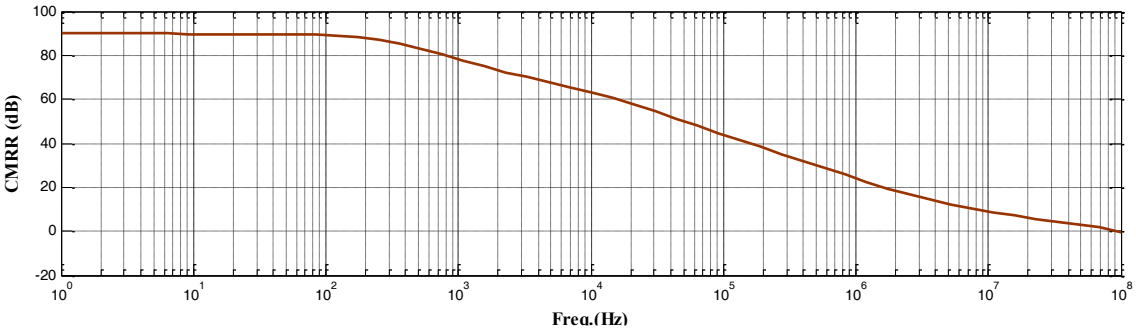

Fig. 6. CMRR curve of the proposed OTA

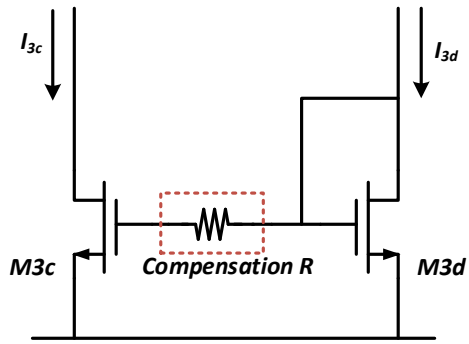

Fig. 3. Current mirror used in the proposed amplifier with compensation resistance

$$H(s) = \left(\frac{gm_{3c}}{gm_{3d}}\right)\frac{sRCgs_{3d}+1}{s^2\frac{RCgs_{3d}Cgs_{3c}}{gm_{3d}}+s\frac{Cgs_{3d}+Cgs_{3c}}{gm_{3d}}+1} \quad (25)$$

The current mirror transfer function zero/poles are obtained as below:

$$z = -\frac{1}{RCgs_{3d}} \quad (26)$$

$$p_{1,2} = \frac{Cgs_{3d}+Cgs_{3c}}{2RCgs_{3d}Cgs_{3c}}\left[-1 \pm \sqrt{1-\frac{4RCgs_{3c}Cgs_{3d}gm_{3d}}{(Cgs_{3c}+Cgs_{3d})^2}}\right] \quad (27)$$

Considering these equations, one can see that the first order transfer function current mirror is modified to yield a second order transfer function current mirror including a zero and two poles. The zero incorporated to the transfer function of the proposed amplifier, makes the system to operate faster. For each specific application and system the design must be customized to achieve the optimum performance. Modifying the value of aforementioned compensation resistance can reshape zero-pole pattern of the transfer function to yield optimum performance for any custom design and/or application.

III. Simulation Results

To prove the performance of the proposed amplifier, this circuit is simulated at Cadence software with 180nm CMOS technology while driving a 5pF load at its output. The Cascode structure which is commonly used at conventional RFC amplifiers has been removed because it requires a high supply voltage. Hence, the power supply voltage and accordingly the power consumption have been relatively diminished. The bias current of the proposed circuit is obtained 3.9μA for supply voltage of 1.5v. The power consumption is achieved to be 5.9μw which is suitable for low voltage and low power applications.

The DC gain and phase margin of the proposed amplifier are shown in Fig. 4. The gain and the phase margin of the circuit are 83.97 dB and 61.68 degrees, respectively. The amplifier's bandwidth is measured to be 3.7MHz. Differential mode and common mode gain are shown at Fig.

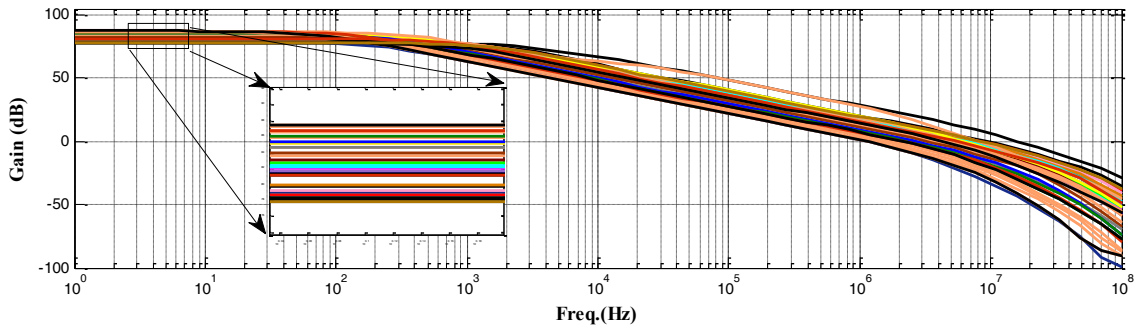

Fig. 7. Monte Carlo analysis for 40 times runs

5. Figure 6 shows the CMRR of the proposed amplifier which is derived almost 90dB

TABLE II PERFORMANCE OF THE OTA UNDER PVT VARIATIONS

parameter		GBW [MHz]	PM [degree]	DC Gain [dB]
corner	FF	3.95	56.4	82.87
	SS	2.8	60.6	83.74
	SF	3.4	62.35	84.15
	FS	3.1	61.23	83.64
	TT	3.7	61.68	83.96
VDD	-10%	3.4	64.2	81.59
	+10%	4.1	58.3	85.12
Temp	-40	3.5	65.4	84.7
	+125	3.9	57.6	82.17

Monte Carlo analysis of amplifier gain with 40 times run is shown at Fig. 7. This analysis verifies the qualitative performance of the proposed amplifier and approves its performance accuracy.

Table I includes the specifications obtained by simulations which is utilized to compare the performance of the proposed amplifier with its other counterparts. Higher gain and CMRR, lower power consumption and bias current and the reliably sufficient phase margin are of the most outstanding features of the proposed circuit. Performance of the OTA under PVT variations are shown at Table II.

IV. Conclusion

In this paper, an amplifier is represented which is based on the CMRR enhancement block. This block eliminates the common mode input and magnifies the differential mode current twice as before and hence increases the DC gain of the amplifier. The proposed amplifier does not require a high supply voltage to provide the optimum performance. Hence, the power consumption is significantly reduced due to low supply voltage along with low bias current incorporated at the amplifier. The suitable specification of the amplifier makes it interestingly suitable for low-voltage, low-power applications.

TABLE III PERFORMANCE SUMMARY AND COMPARISON WITH OTHER WORKS

Parameters	Proposed	[4]	[6]	[18]	[19]	[20]
Technology [µm]	0.18	0.065	0.18	0.35	0.25	-
Supply Voltage [v]	1.5	1.2	1.8	1.5	1.9	±2.5
DC Gain [dB]	83.96	68.9	84.18	82	44.7	82
PM [degree]	61.68	61.0	67.05	86	52	65
GBW [MHz]	3.7	6.4	1.37	1.5	0.81	5
CMRR [dB]	90	-	-	-	88	-
DC Power [µw]	5.949	977.6	19.76	47.25	62	37.8
Bias current [µA]	3.96	814.7	10.4	31.5	32.6	-
Input Voltage Noise @1Hz [$\mu V/Hz^{1/2}$]	4.8	32	31.86	-	-	-
Input Referred Noise [$\mu V/Hz^{1/2}$]	129	-	-	484.7	35	-
C_{load} [pF]	5	5	70	1.2	-	5

REFERENCES

[1] M. Akbari, "Single-stage fully recycling folded cascode OTA for switched-capacitor circuits," *Electronics Letters,* vol. 51, no. 13, pp. 977-979, 2015.

[2] P. J. Ilagan Matibag, "Design and test of a CMOS folded cascode OTA with current recycling," Universitat Politècnica de Catalunya, 2024.

[3] M. P. Garde, A. Lopez-Martin, R. G. Carvajal, and J. Ramírez-Angulo, "Super class-AB recycling folded cascode OTA," IEEE Journal of Solid-State Circuits, vol. 53, no. 9, pp. 2614-2623, 2018.

[4] M. Yavari and M. Mohtashamnia, "A fully-differential improved recycling folded-cascode amplifier for fast-settling switched-capacitor applications," Engineering Science and Technology, an International Journal, vol. 59, p. 101886, 2024.

[5] F. Gagliardi, A. Catania, M. Piotto, P. Bruschi, and M. Dei, "Parallel Slew-Rate Enhancer With Current-Recycling Core for Switched-Capacitors Circuits," IEEE Transactions on Circuits and Systems II: Express Briefs, 2024.

[6] C. Wu, P. Cai, J. Li, J. Xie, and Z. Luo, "Power-Efficient Recycling Folded Cascode Operational Transconductance Amplifier Based on Nested Local Feedback and Adaptive Biasing," Sensors, vol. 25, no. 8, p. 2523, 2025.

[7] M. Alioto, "Understanding DC behavior of subthreshold CMOS logic through closed-form analysis," IEEE Transactions on Circuits and Systems I: Regular Papers, vol. 57, no. 7, pp. 1597-1607, 2010.

[8] S. J. Azhari, K. Monfaredi, and H. F. Baghtash, "A novel ultra low power high performance atto-ampere CMOS current mirror with enhanced bandwidth," Journal of Electronic Science and Technology, vol. 8, no. 3, pp. 251-256, 2010.
[9] X. Zhao, Y. Wang, and L. Dong, "Super current recycling folded cascode amplifier with ultra-high current efficiency," Integration, vol. 62, pp. 322-328, 2018.
[10] A. S. Khade, V. Vyas, and M. Sutaone, "Performance enhancement of advanced recycling folded cascode operational transconductance amplifier using an unbalanced biased input stage," Integration, vol. 69, pp. 242-250, 2019.
[11] S. Kumaravel and B. Venkataramani, "An improved recycling folded cascode OTA with positive feedback," WSEAS Trans. Circuits Syst, vol. 13, pp. 85-93, 2014.
[12] B. Razavi, Design of analog CMOS integrated circuits. McGraw-Hill Higher Education, 2001.
[13] K. Monfaredi and Y. Belghisazar, "Improved low voltage low power recycling folded fully differential cascode amplifier," TABRIZ Journal of electrical Engineering, vol. 48, no. 1, pp. 327-334, 2018.
[14] R. S. Assaad and J. Silva-Martinez, "The recycling folded cascode: A general enhancement of the folded cascode amplifier," IEEE Journal of Solid-State Circuits, vol. 44, no. 9, pp. 2535-2542, 2009.
[15] P. Patra, P. K. Jha, and A. Dutta, "An enhanced recycling folded cascade OTA with a positive feedback," in 2013 IEEE Asia Pacific Conference on Postgraduate Research in Microelectronics and Electronics (PrimeAsia), 2013, pp. 153-157: IEEE.
[16] Y. Li, K. Han, X. Tan, N. Yan, and H. Min, "Transconductance enhancement method for operational transconductance amplifiers," Electronics letters, vol. 46, no. 19, pp. 1321-1323, 2010.
[17] T. Voo and C. Toumazou, "High-speed current mirror resistive compensation technique," Electronics Letters, vol. 31, no. 4, pp. 248-250, 1995.
[18] Z. Yan, P.-I. Mak, and R. P. Martins, "Two stage operational amplifiers: Power and area efficient frequency compensation for driving a wide range of capacitive load," IEEE Circuits and Systems Magazine, vol. 11, no. 1, pp. 26-42, 2011.
[19] J. Ramirez-Angulo, A. Lopez-Martin, A. Garimella, L. M. Kalyani-Garimella, and R. Carvajal, "Low-voltage, low-power rail-to-rail two stage op-amp with dynamic biasing and no Miller compensation," in 2007 50th Midwest Symposium on Circuits and Systems, 2007, pp. 25-28: IEEE.
[20] J. Mahattanakul, "Design procedure for two-stage CMOS operational amplifiers employing current buffer," IEEE Transactions on Circuits and Systems II: Express Briefs, vol. 52, no. 11, pp. 766-770, 2005.

Khalil Monfaredi received the B.Sc., M.Sc., and PhD degrees from Tabriz University in 2001 and Iran University of Science and Technology in 2003 and 2011, respectively. He is currently with Electrical and Electronics Engineering Faculty, Azarbaijan Shahid Madani University, Tabriz, Iran. He is the associate dean of engineering faculty, Azarbaijan Shahid Madani University since 2017. He is the author or coauthor of more than thirty national and international papers and also collaborated in several research projects. His current research interests include current mode integrated circuit design, low voltage, low power circuit and systems and analog microelectronics and data converters. Khalil Monfaredi is associate professor with Department of Electrical and Electronic Engineering, Engineering Faculty, Azarbaijan Shahid Madani University, Tabriz, Iran

Mousa Yousefi received the B.Sc. degree from Urmia University, M.Sc., and PhD degrees from Tabriz University. He was with Electronic Research Center Group, during 2008 to 2011 and was also an academic staff with Islamic Azad University, Ilkhechi Branch from 2008 to 2012. He is currently with Electrical and Electronics Engineering Faculty, Azarbaijan Shahid Madani University, Tabriz, Iran. His current research interests include current mode integrated circuit design, low voltage, low power circuit, design RF circuit and systems and analog microelectronics and data converters. Mousa Yousefi is assistant professor with Department of Electrical and Electronic Engineering, Engineering Faculty, Azarbaijan Shahid Madani University, Tabriz, Iran